




Characterization and Analysis of Lithium Plating on Silicon/Graphite negative electrodes in Lithium ion batteries

Kumulative Dissertation

zur Erlangung des Doktorgrades Dr. rer. nat.

der Fakultät für Naturwissenschaften

der Universität Ulm

vorgelegt von

Marius Flügel

aus Fulda

2023

Tag der Promotionsprüfung: 21.02.2024

Amtierender Dekan:

Prof. Dr. Thorsten Bernhardt

Erstgutachter:

Prof. Dr. Markus Hölzle, Universität Ulm, Fakultät für Naturwissenschaften / Leiter ZSW Standort Ulm

Zweitgutachter:

Prof. Dr. Mika Lindén, Universität Ulm, Fakultät für Naturwissenschaften

Wenn man immer nur an die Schwierigkeiten denkt, dann tut man überhaupt nichts.

*Konrad Adenauer, * 05.01.1876; † 19.04.1967*

German statesman and first chancellor of the Federal Republic of Germany

Declaration of Authorship

This dissertation was prepared from March 2020 to August 2023 at the Center of Solar Energy and Hydrogen Research Baden-Württemberg (ZSW).

I, Marius Flügel, herewith declare that the presented dissertation is solely my original work without external assistance. Furthermore, I declare, that all data, facts and figures taken from any literature, literally or figuratively, have been clearly identified as such. This thesis in the presented form and version has not been submitted to any other examination board.

Ulm, October 09, 2023

Marius Flügel

I. Executive Summary

The importance of electric vehicles has increased dramatically with the EU's decision to allow only zero-emission car production from 2035 [1]. In addition to powering millions of new cars, electrochemical energy storage systems, i.e. batteries, will also be used for stationary storage of renewable energy in the future. To further improve existing batteries, new materials are being explored constantly, mainly to further increase energy density and to lower specific costs. Silicon (Si) as a new anode active material provides several times the specific capacity of graphite, the most widely used anode active material today, however the aging processes are more severe and therefore more work is necessary to make Si the anode standard in the future. The focus of this work is the occurrence and detection of Li plating on Si/graphite anodes. Better understanding of this phenomena is essential to increase the share of Silicon in graphite anodes without suffering lifetime and safety of such batteries.

The energy density of graphite-based Lithium ion batteries (LIBs) correlates with the anode coating thickness [2]. The addition of Si as anode active materials offers the possibility to reduce the anode coating thickness at constant energy density. Based on this finding, three commercial 18650 cells with Si-containing anodes were selected for this work. With these cells as substrates, a new Glow discharge optical emission spectroscopy (GD-OES) method for the quantification of Li deposition on Si/graphite anodes was developed and validated using complementary in-situ and ex-situ techniques. During low temperature cycling ageing, Li plating appeared first in the high energy cells with rather thick and dense anode coating and at lower temperatures also in the high power cell with thinner anodes. The aging mechanism in the first life significantly influences the occurrence of Li plating in the second life aging. Once the mechanism of ageing at 45 °C had been conclusively elucidated, the cells were firstly aged at 45 °C to 80% SOH and then subjected to a second ageing at the conditions that led to Li plating of the fresh cells. In the case of loss of Li inventory (LLI), Li deposition ceased, whereas cells aging by loss of anode active material (LAAM), in this particular case by partial loss of the Si compound, remained susceptible to Li deposition.

The second study showed that anodes with higher Si contents and simultaneously lower anode thickness were less susceptible to Li plating [3]. This relationship has been systematically investigated by studying five pilot-scale anodes with different Si contents and very similar areal capacities with respect to Li plating. Cathodes that compensate for the irreversible anode losses with additional areal capacity have been used to build five series of pouch cells with very similar anode capacity despite decreasing anode thickness and fixed N/P ratio. Analysis of the voltage

relaxation after charging at different C-rates was used to observe the voltage plateau caused by the re-intercalation of reversibly deposited Li. With increasing Si content and corresponding decrease in layer thickness, the C-rate at which reversible Li plating was firstly detected increases. Ex-situ techniques GD-OES, scanning electron microscopy (SEM), and optical microscopy confirmed these results.

Finally, the quantified GD-OES Li depth profiles of four differently aged anodes were validated using neutron depth profiling (NDP) [4]. The sputter rate of Li is higher than the carbon (C) sputter rate, which results in a non-uniform sputtering of samples with Li plating on the anode surface. GD-OES and NDP have consistently shown that Li plating occurs only on the anode surface. A new method has been developed which takes into account the changing sputter rate and allows a more accurate depth calculation for samples with Li plating. Due to the higher Li sputter rate, the width of the Li plating peak on the anode surface increases. For aged anodes, the amount of Li irreversibly bound in the anode increases with the degree of aging. The amount of Li in the anode decreases from the surface of the electrode in the direction of the current collector. Due to the high sputter rate of Li, the Li-rich solid-electrolyte interphase (SEI) is preferentially sputtered off, resulting in increased Li detection at the anode surface. The effect of preferential sputtering increases with advanced degree of aging.

II. List of Abbreviations

Ah / mAh	Ampere hour / milliampere hour
ASSB	All solid state battery
BEV	Battery electric vehicle
C n^{-1}	C-rate, n corresponds to the operation time
CCD	charge coupled device
CEI	Cathode-electrolyte interphase
DEC	Diethylcarbonate
EC	Ethylencarbonate
EoL	End of life
FEC	4-Fluoroethylenecarbonate
GD-OES	Glow Discharge Optical Emission Spectroscopy
H/H_2	Hydrogen
HOMO	Highest occupied molecule orbital
IEA	International Energy Agency
LAAM	Loss of anode active material
Li/Li^+	Lithium / lithium cation
LIB	Li-ion Battery
LFP	Lithium Iron phosphate $LiFePO_4$
$LiPF_6$	Lithiumhexafluorophosphate
LLI	Loss of Lithium inventory
LMNO	Lithium-Nickel-Mangenese-Oxide spinel
LUMO	Lowest unoccupied molecule orbital
NCA	Lithium-Nickel-Cobalt-Aluminium-Oxide
NDP	Neutron depth profiling
NG	Natural Graphite

NMC	Lithium-Nickel-Manganese-Cobalt-Oxide $LiNi_xMn_yCo_zO_2$
N/P ratio	Ratio of the electrochemical capacity between negative and positive electrode, usually greater than 1
PMT	Photomultiplier tube
PVDF	Polyvinylidendifluoride
SBR	Styrene-butadiene-rubber
SEI	Solid electrolyte interphase
SG	Synthetic Graphite
SHE	standard hydrogen electrode
Si	Silicon
SOC	State of Charge
SOH	State of Health
V / mV	Volt / Millivolt
VC	Vinylene carbonate

III. Contents

Declaration of Authorship iii

I. Executive Summary v

II. List of Abbreviations vii

III. Contents ix

1. Introduction 1

1.1. Li-Ion Battery Functionality 2

1.2. Physicochemical fundamentals 4

1.3. Negative electrode materials 5

1.3.1. Graphite 6

1.3.2. Silicon-based anode materials 8

1.4. Positive electrode materials 10

1.5. Electrolyte 12

1.6. Aging mechanisms in LIBs 13

1.7. Characterization Methods for Li plating 16

1.7.1. Glow Discharge optical emission spectroscopy 16

1.7.2. Neutron depth profiling 20

1.7.3. Voltage Relaxation Analysis 21

2. Objective 23

3. Publications 24

3.1. Detection of Li Deposition on Si/Graphite Anodes from Commercial Li Ion Cells: A Post-Mortem GD-OES Depth Profiling 24

3.2. Onset Shift of Li Plating on Si/Graphite Anodes with increasing Si content 38

3.3. Observation of preferential sputtering on Si/Graphite anodes for Li-ion cells by GD-OES and its validation by neutron depth profiling 52

3.4. Aging mechanism for calendar aging of Li-ion cells with Si/Graphite anodes 67

3.5. 3D-Printed Testing Plate for the Optimization of High C-Rates Cycling Performance of Lithium-Ion Cells 82

4. Conclusion 95
5. References 101
6. List of figures 112
IV. Appendix 114
a) Curriculum vitae 114
b) List of Publications 115
i. Articles in Peer-Reviewed Scientific Journals 115
ii. Contribution to conferences and meetings 117
V. Acknowledgement 120

1. Introduction

The development of energy storage systems gained momentum during the 1970s under the impact of the first oil crisis, when the price of fossil fuels increased dramatically. [5]. Among the known and potentially promising electrochemical energy storage systems, Li ion batteries in particular have attracted the attention of researchers because the low mass of Li in combination with the highest redox potential of all metals promise high energy densities. In addition, the small atomic radius provides high diffusivity and therefore high power densities.

The development of LIBs began with the discovery of metal dichalcogenides such as TiS_2 by Stanley Whittingham as promising cathode host-materials due to their ability to store Li^+ ions in their atomic interstitials at a voltage around 2 Volt. [6,7]. In 1980, John B. Goodenough successfully increased this potential to ~4 V by the use of layered transition metal oxide $LiCoO_2$ [8]. These early LIBs used metallic Li as anode material, which posed a safety risk due to its tendency to form dendrites, potentially leading to short circuits, heat generation, and even spontaneous combustion and explosions in extreme cases [6–8]. Only when Akira Yoshino described graphite as stable negative electrode material due to its ability to store Li between its graphene layers, higher reversibility was achieved [9]. In 2019, these three scientists were awarded the Nobel Prize for their outstanding achievements in the field of LIBs [10].

Since the commercialization of LIBs in 1991 by Sony Corporation [11], LIBs become increasingly important in mobile devices, electric vehicles, and renewable energy storage. Scientific advances more than doubled the specific energy / energy density since 1991 from Wh kg^{-1} / 254 Wh L^{-1} [12] to more than 230 Wh kg^{-1} / 670 Wh L^{-1} today in commercially available cells [13], while simultaneously mass production reduced the cost by 97% since 1991 [14].

This development has opened many new applications for LiB and therefore also has multiplied the demand for LIBs from 30 GWh/a (2011) to 492 GWh/a (2021) [15] and is projected to reach 2 - 3.5 TWh/a (2030) annual capacity in the foreseeable future, according to the international energy agency (IEA) [16]. The electrification of transport is a major contributor to the growing demand for LIBs, as shown in Figure 1 [16]. Sales of electric vehicles have tripled between 2020 and 2022, accounting for 14% of the global car sales in 2022 and are expected to increase further to 23% in 2025 and 36% in 2030 [16].

To enhance the widespread adoption of LIB and LIB-powered vehicles, multiple considerations must be taken into account. Firstly, the energy density should be augmented to enable extended ranges. Secondly, it is crucial to achieve adequate fast-charging capability to minimize charging

station dwell time. Finally, cost and safety factors are also significant for the end-users. The use of new materials with higher specific capacities has the potential to further increase the energy density and to lower the specific costs. However, these new materials also sometimes come with unique ageing mechanisms that need a thorough understanding before using them in new battery generations.

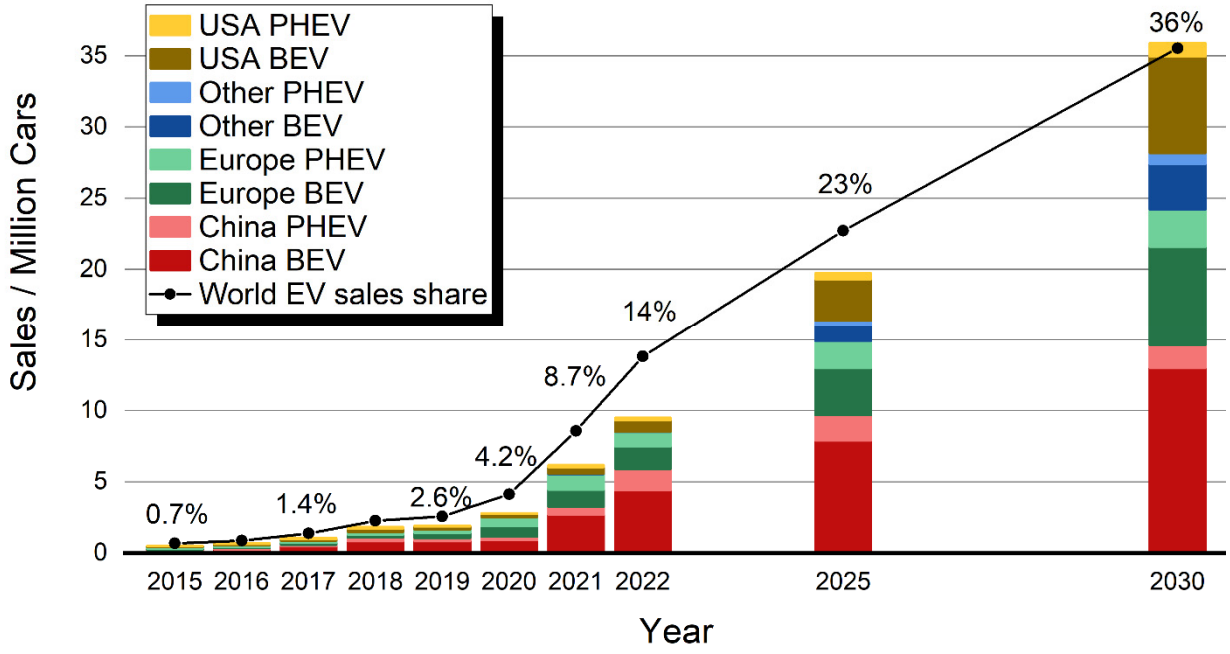

Figure 1: Historical development and projection of global sales of battery electric vehicles (BEV) and plug-in hybrid electric vehicles from 2015 to 2030. Reproduced with data adapted from reference [16].

In this introduction, the fundamental aspects of LIBs will be reviewed including the state of the art positive and negative electrode materials and their corresponding aging mechanisms. Additionally, the methods used in this thesis to uncover the aging mechanism of Li deposition will be described.

1.1. Li-Ion Battery Functionality

In general, an electrochemical cell comprises two electrodes, anode and cathode, an electrolyte, and a separator [17,18]. A galvanic cell is an electrochemical cell that converts chemical energy in a spontaneous reaction into electrical energy. If several cells are connected together, they constitute a battery, which can be categorized as primary or secondary. Secondary batteries exhibit a highly reversible discharge process and can be recharged through the application of electric energy. They have been designed for multiple discharge and recharge cycles without significant loss of capacity. During discharge, the negative electrode (anode) undergoes an oxidation reaction releasing electrons. Simultaneously, the positive electrode (cathode) undergoes a reduction

reaction, accepting the electrons released by the negative electrode. The electron flow through the external circuit form the negative to the positive electrode provides electrical energy needed for various applications. During charging, the electrochemical processes are reversed. The negative electrode is reduced, accepting electrons from the external circuit, while the positive electrode is oxidized, releasing electrons to the external circuit. Although the roles of the negative and positive electrodes are reversed during discharging and charging, the negative electrode during discharge is commonly referred to as the anode, and the positive electrode as the cathode [19].

The electrolyte in an electrochemical cell facilitates ionic conduction between the two electrodes. It is a solution or solid material which contains ions and allows them to move between the anode and cathode. This movement of ions maintains electrical neutrality during the redox reaction and allows charge to flow in the form of ions.

Additionally, the electrochemical cell contains a porous separator that physically isolates the two electrodes, preventing electrical contact, while allowing ionic contact.

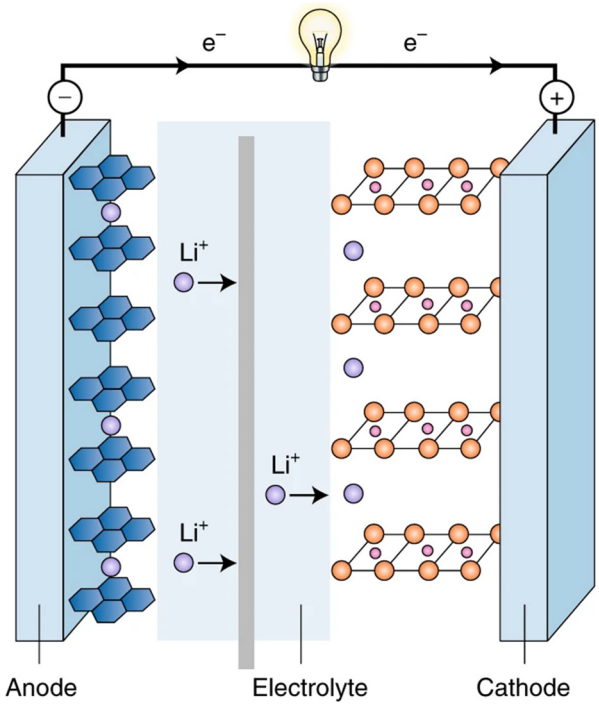

Figure 2: Schematic battery cell based on a graphite anode and a layered oxide cathode during discharge. Reproduced with permission from Springer Nature: How we made the Li-ion rechargeable battery, J.B. Goodenough, Copyright (2018) [20].

Lithium ions are well suited as a charge carriers because of its low mass and small ion radius, resulting in high ionic mobility in the electrolyte. Lithium storage in electrodes is generally based on alloying [21], conversion [22] or intercalation [22,23]. Common examples of alloying materials include Si, SiO_x, and Sn. However, the large volume changes associated with alloying during cycling limit its practical capacity [24]. In contrast, conversion-based LIBs are rarely used because

of the low reversibility of the lithiation process. The predominant lithiation mechanism involves intercalation in both the anode and cathode. Cathode materials commonly consist of olivine structures like $LiFePO_4$ (LFP) with 1D Li^+ diffusion pathways, layered structures like $LiNi_xCo_yMn_zO_2$ (NMC) with 2D Li^+ diffusion pathways or spinel structures like $LiNi_{0.5}Mn_{1.5}O_4$ (LNMO) with 3D Li^+ diffusion pathways [25]. Graphite remains a frequently utilized anode material, as Li^+ ions are capable of intercalating into its planar two-dimensional structure [26].

Figure 2 shows a schematic battery cell based on a graphite anode and a layered oxide as cathode during discharge. During the discharge reaction ($LiC_6 + 2\ Li_{0.5}CoO_2 \rightarrow 2LiCoO_2 + C_6$), Li^+ cations deintercalate from the graphite anode to the cathode through the electrolyte, while electrons pass through an external circuit to the cathode to provide electro-neutrality. The reciprocating flow during charging and discharging is often referred to as “rocking chair principle” [27].

1.2. Physicochemical fundamentals

The basic electrochemical principles and characteristics of LIBs are described below. In a spontaneous, thermodynamically favored galvanic reaction between two materials of different standard reduction potentials, the Gibbs free energy Δ_rG takes negative values. The Gibbs free energy Δ_rG, as described in eq. (1), is derived from the potential difference ΔE of both materials and the number z of exchanged electrons, with F being the Faraday constant (96,485.33 C mol^{-1}) [28].

$$\Delta_r G = -zF\Delta E \quad (1)$$

The cathode is the electrode with the higher standard electrode potential, which undergoes a reduction reaction, in which the cathode takes up the electrons provided during the oxidation reaction of the anode, the electrode with the lower standard electrode potential. The difference between the electrode potential of the cathode $E_{cathode}$ and the anode E_{anode} is the theoretical cell voltage ΔE [28].

$$\Delta E = E_{cathode} - E_{anode} \quad (2)$$

The electrode potential is given relative to a reference electrode. In aqueous systems, the standard hydrogen electrode, which by convention has a potential of 0 V, is used as the reference electrode. The potential of LIB electrodes, on the other hand, is usually given relative to the Li metal electrode. Under non-standard conditions, the Nernst equation (eq. (3)) is used to determine the electrode potential E_{eq} as a function of temperature T and the chemical activity a of the species involved [28].

$$E_{eq} = E^0 + \frac{RT}{zF} \ln \frac{a_{Ox}}{a_{Red}} \quad (3)$$

, where R is the gas constant (8.314 J k^{-1} mol^{-1}), T is the temperature and "a" is the activity of the respective redox species.

An overpotential η describes the difference between the actual potential E and the equilibrium potential E_{eq} as calculated using the Nernst equation. Overpotentials may have different root-causes and cause a reduced current flow, typically at increased potentials [28]. The divergence of the current from the state of equilibrium-potential is called polarization. A part of the polarization in batteries is due to Ohmic resistances caused by low inter-particle and particle-to-collector contact. Further sources of polarization result from kinetic limitations of charge transfer reactions and solid diffusion of Li ions [28].

$$\eta = E - E_{eq} \quad (4)$$

The capacity of an electrode Q gives the quantity of electrical charge that can be reversibly stored in the electrode material. According to Faraday's law [29], Q is calculated from the number of electrons "z" transferred during the redox process, the Faraday's constant F, the gravimetric mass m and the molar mass M of the redox-active component involved in the reaction

$$Q = \frac{m}{M} zF \quad (5)$$

Combining eq. 2 and eq. 5 [28,29], the electrical energy provided by an electrode couple is determined by

$$Energy = Q \cdot \Delta E = \int_0^{nF} \Delta E \, dq \quad (6)$$

1.3. Negative electrode materials

To date, strong progress has been made in innovating the cathode side of LIBs. Drivers had been the rather high costs of cathode materials as well as the fact that cathode materials determine main characteristics of batteries such as energy content or safety. However, the use of graphite as the sole anode active material limits both the energy density and charging rate of today's LIBs. A primary goal of anode innovation is to overcome these limitations, e.g. by incorporating Si as an anode active material as its theoretical specific capacity is almost ten times that of graphite [26,30]. This innovation allows the use of thinner anodes, which, on one hand, reduces the bulk diffusion length in the anode, allowing for higher charging rates, and, on the other hand, provides space for thicker cathodes, enabling higher overall energy content in such batteries. The incorporation of Si

is of particular interest to battery manufacturers as it is considered a drop-in technology requiring minimal conversion in battery manufacturing. Si-containing anode materials with low Si content were recently introduced in commercial battery cells to get batteries with higher energy densities, faster charging rates, and comparable stability to graphite-based cells. However, Si undergoes significant volume expansion of almost 300% during lithiation [31], resulting in high mechanical stress and stability issues that will lead to rapid capacity degradation if untreated.

1.3.1. Graphite

The most commonly used anode active material still is graphite, which combines low cost with beneficial properties such as low lithiation potential, high Li diffusion coefficient, high electrical conductivity, and excellent reversibility of the Li intercalation [26,32,33]. Graphite is composed of parallel graphene layers, which consist of sp^2 hybridized C atoms [34]. The layers are connected by weak van der Waals forces and π-π interactions between the orbitals of the delocalized electrons [34] and are arranged in an ABAB order in their thermodynamically most stable state [35,36]. The layered structure of graphite enables the intercalation of Li^+ ions between the graphene layers via the prismatic surfaces at their edges [37] or via defects. Parallel diffusion of Li^+ between graphene layers (10^{-7} - 10^{-6} cm^2 s^{-1}) is significantly faster than diffusion along the grain boundaries, which is approximately 10^{-11} cm^2 s^{-1} [38]. In the fully lithiated stage (LiC_6), six C atoms host one Li atom, which results in a maximum capacity of 372 mAh g^{-1} or 815 mAh cm^{-3} [26,32]. The reversible intercalation/deintercalation reaction can thus be expressed by

$$C_6 + xLi^+ + xe^- \xrightarrow{charge} Li_xC_6\,, \qquad 0 \leq x \leq 1 \tag{7}$$

As the graphene interlayer distance reversibly increases from 0.335 nm to 0.370 nm during intercalation, the graphite volume expands by 10.4% without significant mechanical stress or structural changes [39]. Graphite is lithiated at potentials of 0.25 V – 0.01 V vs. Li/Li^+, whereby so-called stages are formed [40]. The stages are periodic arrangements of lithiated layers, whose formation mechanism is not completely understood, however, several possible mechanisms have been proposed, as shown in Figure 3.

In the staging mechanism proposed by Rüdorff and Hofmann, every n^{th} layer is intercalated in a periodic sequence in the nth intercalation stage, with n graphene layers separating the intercalant layers [41,42]. However, this model cannot explain the transition from one stage to the next, as it would require the complete deintercalation and rearrangement of entire intercalant layers. Daumas

and Herold proposed that the graphene layers are flexible and able to deform around intercalated species [43].

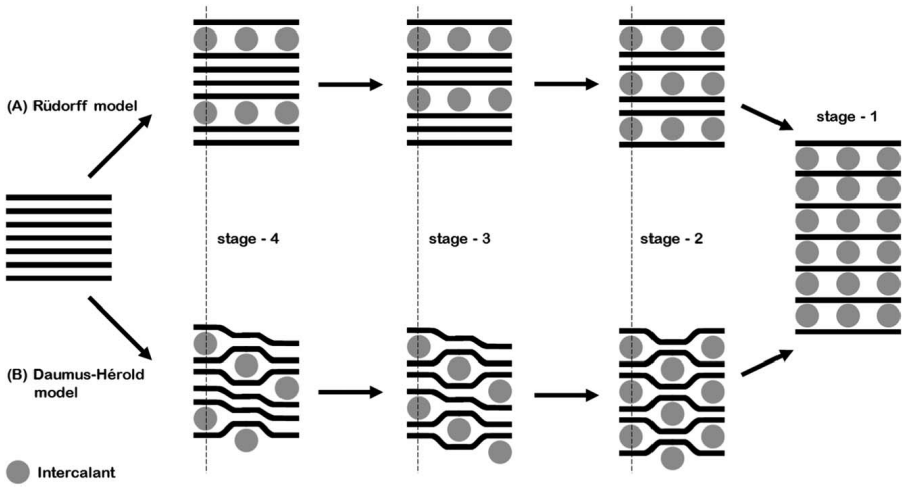

Figure 3: Schematic illustration of the (A) Rüdorff and (B) Daumas-Hérold models of Li intercalation in graphite. Reproduced with permission from Royal Society of Chemistry: In-situ Raman study of lithium-ion intercalation into microcrystalline graphite, C. Sole, N.E. Drewett, L.J. Hardwick, Copyright (2014) [44].

The theoretical voltage profile of graphite is characterized by the presence of potential plateaus, which indicate the presence of two distinct phases [40,45]. The lithiation process of graphite is associated with three main plateaus at the theoretical potentials of 218 mV vs. Li/Li^+ (1L→4L), 128 mV vs. Li/Li^+ (3L→2L/2), and 86 mV vs. Li/Li^+ , as seen in the potential profile of Figure 4 (2→1) [45,46]. The stages are named based on the order of the Li^+ ions in each nth interlayer. In addition, the character L refers to disordered, liquid-like Li arrangement in each nth interlayer. Corresponding to the change in the band structure caused by the varying lattice spacing, lithiated graphite changes its color from black in the delithiated state to blue (LiC_{18}, stage 3) to red (LiC_{12}, stage 2) to gold (LiC_6, stage 1). However, as the intercalation potentials are close to the potential of metallic lithium, side reactions such as lithium deposition may occur during the charging process at high current densities, which often causes inhomogeneous, local Li deposition, or at relatively low temperatures, at which homogeneous Li plating occurs, due to the occurrence of over-potentials [47,48].

Intrinsic challenges of graphite remain the limited fast charging capability and low initial coulombic efficiency, both of which depend on the particle size and morphology [49,50]. Solutions to these problems include surface modifications of the particles, spheroidization of the natural graphite (NG) or the use of synthetic graphite (SG). Surface modification of the graphite particles may consist of mild oxidation of the edge planes, which enables the SEI to bond more effectively, or in inorganic, organic or carbonaceous coatings [51–54]. Coating aims at facilitating SEI

formation and reducing charge transfer resistances while accelerating (de-) intercalation kinetics. Another approach is the use of special electrolyte additives, which will be discussed in a later chapter.

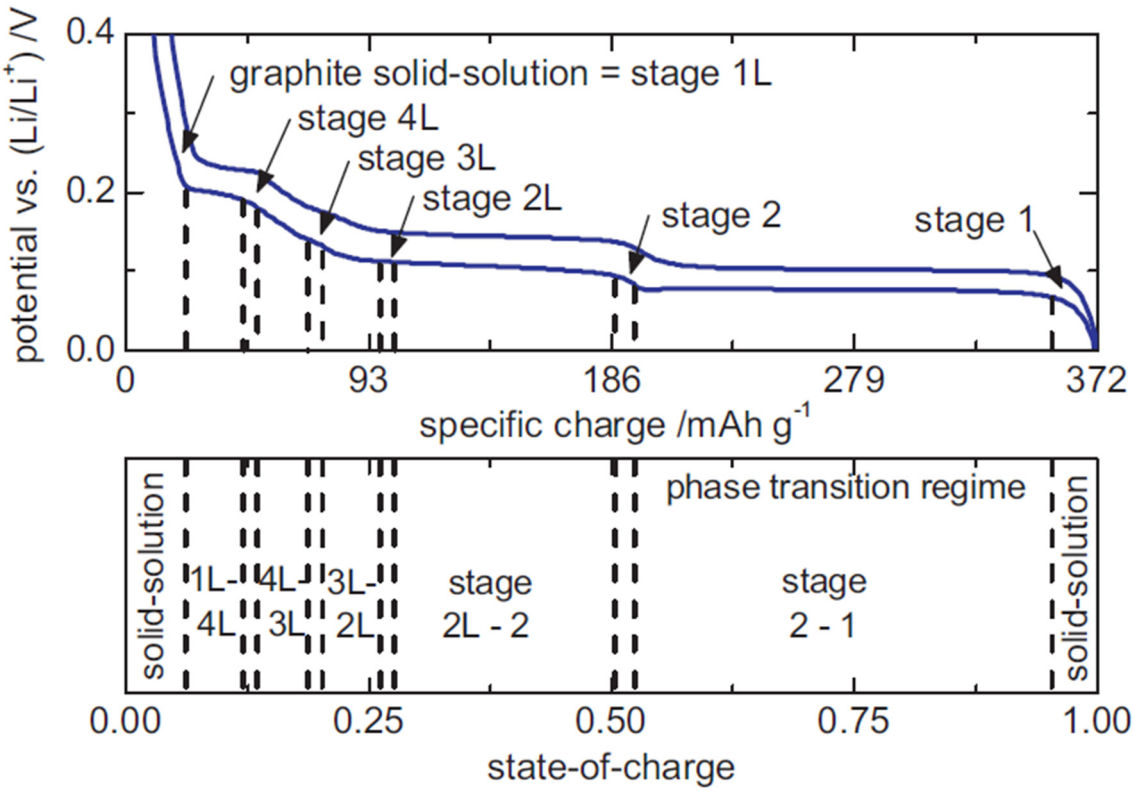

Figure 4: Lithium intercalation stages and stage transitions of graphite. Reprinted from Electrochimica Acta 106, M. Heß, P. Novák, Shrinking annuli mechanism and stage-dependent rate capability of thin-layer graphite electrodes for lithium-ion batteries, 149-158, Copyright (2013) with permission from Elsevier [46].

A more effective coating is achieved on spherical particles, which also reduces the amount of (inactive) coating material. Another benefit of the spheroidization of natural graphite is an improved (de-) intercalation kinetics, as the parallel alignment to the current collector of the flaky particle can be avoided [55,56]. In contrast to NG, which is mined from natural sources, synthetic graphite is produced by heat treatment of unsaturated carbon, usually petroleum coke, at 2,500 to 3,000 °C for several days [57]. The single crystals of SG are more anistropically oriented than the homogeneous orientation in NG, allowing enhanced (de)intercalation kinetics, although at the cost of lower ICE [57,58]. Another advantage of SG is the independence from natural deposits and a higher purity, whereas the long heat treatment makes SG more expensive than NG [57].

1.3.2. Silicon-based anode materials

Silicon (Si) has received considerable attention as a promising anode active material for LIBs because of its high theoretical specific capacity, low discharge potential and low cost [59,60]. Crystalline silicon has a cubic diamond structure with each atom being sp^3 hybridized and is an alloying material, which form stoichiometrically different intermetallic compounds depending on

the degree of lithiation [59]. Although Si could enable a large increase in energy density, the practical implementation of Si contents >4 wt.-% in the anodes of commercial cells has failed so far due to its drawbacks. Si undergoes a high volume alteration during (de-) lithiation, which causes rapid particle cracking and subsequent electrode degradation. For this reason, various mitigation strategies have been developed to reduce the volume expansion or increase the resilience of the Si particles.

High temperature lithiation of Si at around 400 °C results in the formation of the crystalline phases $Li_{12}Si_7$, Li_7Si_3, $Li_{13}Si_4$ and $Li_{22}Si_5$ [59]. Although, a theoretical gravimetric and volumetric capacity of 4,200 mAh g^{-1} and 2,386 mAh cm^{-3} can be achieved, the lithiation process is accompanied by a volume expansion of up to 320 % [31]. At room temperature, however, the maximum fully lithiated Si phase is $Li_{15}Si_4$, in which 3.75 Li atoms can be stored for each Si atom and which is accompanied by a volume expansion of 280 % [61]. This is equivalent to a theoretical specific and volumetric capacity of 3579 mAh g^{-1} and 2194 mAh cm^{-3}, respectively [30]. The voltage curve of a crystalline Si anode is characterized by a significantly larger hysteresis than that of a graphite anode. During initial lithiation, the anode potential falls sharply to a flat plateau at about 0.1 V vs. Li/Li^+ [62,63]. The voltage plateau corresponds to a two-phase region, in which crystalline Si particles alloy with Li to form amorphous a-Li_xSi [64,65]. During further lithiation below a potential of 50 mV vs. Li/Li^+, partially lithiated amorphous a-Li_xSi recrystallizes into metastable $Li_{15}Si_4$ [21,62–64,66,67]. In the following delithiation process, the two-phase reaction of crystalline $Li_{15}Si_4$ into amorphous a-Li_xSi causes a voltage plateau at 0.45 V vs. Li/Li^+. During the first cycle, the initially crystalline Si is transformed irreversibly into amorphous Si and remains amorphous in subsequent cycles [21,62], expect at anode potentials below 50 mV vs Li/Li^+, when crystalline $Li_{15}Si_4$ is formed [21,66]. The voltage curve of the second lithiation is characterized by the occurrence of two quasi-plateaus.

Lithiation: $$c\text{-}Si \rightarrow a\text{-}Li_xSi \rightarrow c\text{-}Li_{15}Si_4 \quad (8)$$

Delithiation: $$c\text{-}Li_{15}Si_4 \rightarrow a\text{-}Li_xSi \rightarrow a\text{-}Si \quad (9)$$

Various strategies have been developed to mitigate the detrimental volume expansion and improve the electrochemical properties of Si in LIBs. Among these, nano-sized Si particles [68], Si nano-tubes [69], micro-structured embedding of Si-nano particles (watermelon-inspired) [70], Si-nanolayer-embedded graphite [71] have been the most effective approaches, while simultaneously increasing the electrical conductivity of the semi-conducting Si. Si nano-particles have a critical diameter of 150 nm, below which the Si particles do not rupture or crack during lithiation [68]. In addition, a variety of porous network structures or yolk shell nanostructures, have been used to

create stable structures and interphases, that can endure the high volume expansion [72–75]. Although high capacities and excellent fast-charging capability have been achieved with such structures [69–75], the complexity of the preparation and the active material surface area are increasing significantly.

More relevant approaches include the use of SiO_x and Si/graphite blends, in which graphite buffers the volume expansion and protects the electrode from fracturing. During the lithiation of SiO_x, Li_2O and Li-silicates are formed in the first cycles, which attenuate the volume expansion of Si and increase the cycling stability [76,77]. Major challenges of SiO_x remain the low intrinsic conductivity and the high irreversible losses during the first cycle, as the Li-silicates and Li_2O are irreversibly formed [77,78]. Jung et al. found in simulations that Li_2O has a by two magnitudes higher Li^+ diffusivity than Li silicates, however, Li silicates dominate over Li_2O [79].

The current state of the art anode in LIBs are composites of graphite and SiO_x. However, as the amount of SiO_x is increased, the cycling performance of the anode deteriorates due to the volume change of SiO_x and the high irreversible capacity. As a result, optimizing the SiO_x/graphite ratio and suppressing the irreversible capacities through a pre-lithiation process are critical challenges for the negative electrode in LIBs.

1.4. Positive electrode materials

In state-of-the-art LIBs, the positive electrode incorporates Li-containing active materials and therefore represents the Li inventory. The currently most employed material classes are layered oxides $LiMO_2$, spinels LiM_2O_4 and olivines $LiMM'O_4$, whose crystal structure is shown in Figure 5 [25]. The element M is usually a transition metal which possesses partially filled d-orbitals and therefore rather easily can undergo changes in oxidation stage. The layered oxide $LiMO_2$, sometimes referred to as “ordered rock-salt structure”, has a high theoretical specific capacity of about 300 mAh g^{-1} based on the $M^{3+/4+}$ redox couple [80]. The cations are layered in slightly distorted O octahedra, which allows Li to diffuse two-dimensionally, enabling rapid lithium transport and high rate capability. The $LiCoO_2$ and $LiNiO_2$ families are of particular importance. Reversible deintercalation of $LiCoO_2$ is only possible for 50-60% of the Li, as complex phase transitions occur which drastically reduce the lifetime [81,82]. $LiNiO_2$, on the other hand, can be reversibly delithiated nearly completely, achieving high capacities [81]. However, the thermal stability of $LiNiO_2$ at elevated temperatures is worse than that of $LiCoO_2$, as oxygen release and exothermic decomposition reactions already start at lower temperatures. To improve the thermal

stability of high nickel containing materials, part of the Ni is substituted by Co and Mn [83,84]. Co restricts the phase transition, improving the cycling stability, while Mn restricts the oxygen release and therefore improves the thermal stability [83]. In state-of-the-art LIBs, $LiNi_{0.6}Co_{0.2}Mn_{0.2}O_2$, referred to as NMC622, is employed with a trend towards NMC811, $LiNi_{0.8}Co_{0.1}Mn_{0.1}O_2$, which have high capacities of up to 210 mAh g^{-1} and superior thermal stability compared to $LiNiO_2$ [84].

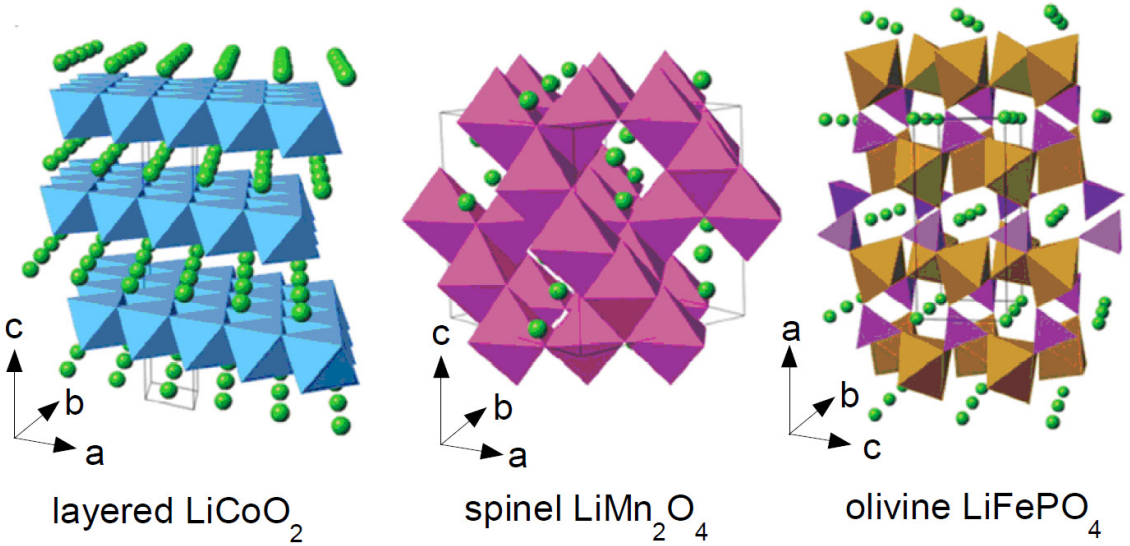

Figure 5: Crystal structure of the layered oxide $LiCoO_2$, the spinel $LiMn_2O_4$ and the olivine $LiFePO_4$. Reprinted with permission from MDPI, Comparative Issues of Cathode Materials for Li-Ion Batteries, C.M. Julien, A. Mauger, K. Zaghib, H. Groult, Copyright (2014) [25].

The spinel LiM_2O_4 has three-dimensional Li pathways, enabling excellent rate capability [85]. However, it offers only half of the layered oxide capacity based on the $M^{3.5+/4+}$ redox couple and because the potential difference to the $M^{3+/3.5+}$ redox couple is too high to be effectively used in batteries. The most prominent representative of this family is $LiMn_2O_4$[86]. Substitution of Mn by Ni leads to the formation of $LiNi_{0.5}Mn_{1.5}O_2$ with a potential of 4.7 V vs. Li/Li^+ [83,87]. Although high voltage spinels are highly attractive for automotive applications, those materials exceed the electrochemical stability window of current electrolytes, which requires further research.

The third material class worth mentioning includes the olivine structure $LiMM'O_4$ with its most prominent representative $LiFePO_4$ [88]. It consists of a divalent cation M and a quintvalent cation M', the polyanion $M'O_4^{3-}$. Li is contained in the octahedral sites of the hexagonal arrangement of closely packed oxygen atoms, thus only one-dimensional Li transport is possible. Due to its low prize and high safety, $LiFePO_4$ is now experiencing its renaissance despite low specific capacity of 150 mAh g^{-1} and low voltage of 3.4 V vs. Li/Li^+.

1.5. Electrolyte

The electrolyte in LIBs provides ionic conductivity between the positive and negative electrode and is electronically insulating [89]. In addition, the electrolyte forms a solid-electrolyte interphase (SEI) layer on the anode surface, which protects the electrolyte from further degradation and improves the battery safety [89,90]. The high cell voltage of 4.2 V in fully charge LIBs necessitates the use of electrolyte systems with a wide electrochemical stability window. Additionally, an ideal electrolyte has a high dielectric constant to enable the dissolution of high concentrations of conductive salt, a high ionic conductivity, which determines the Li^+ transport between anode and cathodes, a low viscosity to facilitate ion migration and minimize concentration gradients, and a high thermal stability to withstand high temperatures without evaporation or degradation. The common liquid electrolyte for LIBs comprises a mixture of two or three solvents, a lithium conductive salt and additives, with the ionic conductivity depending on both the composition of the solvents and the lithium salt [89,91,92]. Organic electrolytes consist of alkyl carbonates, usually a mixture of cyclic and linear carbonates. Cyclic carbonates, such as ethylene carbonate (EC), enable the dissolution of the electrolyte salt and its dissociation due to their dipole moment and their permittivity. Linear carbonates, such as diethylcarbonate (DEC), have a lower viscosity and permittivity and promote fast ion transport. The maximum ionic conductivity of these electrolyte solutions is at a $LiPF_6$ concentration of 0.8 - 1.2 M, therefore the electrolyte salt is usually added at a concentration of 1M [89,93,94]. The most commonly used electrolyte salt is $LiPF_6$, other salts in use, depending on the cell chemistry, are $LiBF_4$, LiTFSI, and LiBOB [95–97].

The SEI is made up of both organic and inorganic compounds, which formed from the degradation products of the electrolyte and Li ions, causing a loss of capacity in the initial cycle [89,98]. However, the SEI serves as an electrically insulating and especially chemical passivation layer on the anode, which prevents further electrolyte reduction and self-discharge, and is therefore crucial for a stable and effective battery operation [99,100]. The SEI should possess a high ionic conductivity to allow fast Li^+ transport and reduce over-potential build-up. As the active material volume changes during (de-) lithiation, the SEI should have mechanically flexibility, which is provided by the organic component. Figure 6 illustrates the energetic perspectives of the SEI formation and electrolyte decomposition, with the electrolyte stability window (E_g) approximated between HOMO (highest occupied molecule orbital) and LUMO (lowest unoccupied molecule orbital) [98].

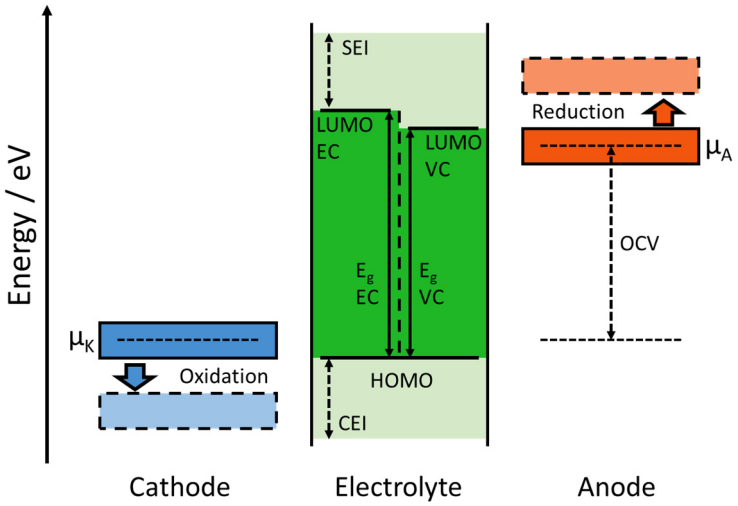

Figure 6: Energetic illustration of the decomposition of the electrolyte and formation of the SEI and CEI. Illustration based on [98].

The green area represents the electrochemical stability window of the electrolyte, with the red and blue bars representing the electrochemical potential μ_a and μ_k of anode and cathode, respectively. As μ_a is lower than LUMO, the electrolyte on the anode side undergoes reduction during lithiation to form the SEI, while the electrolyte on the cathode side is oxidized in a similar manner, forming the cathode-electrolyte interphase (CEI) [89].

SEI stability can be improved by adding specific additives, such as vinylene carbonate (VC), which stabilizes the SEI on graphite particles, and fluoroethylene carbonate (FEC), which helps form a stable but flexible SEI on Si particles [89,101]. VC has a positive reduction potential of ~1.1 V and generates poly-carbonates, oligomers and Li alkyl dicarbonates, which improve cycling stability. In contrast, EC is only reduced at 0.7 - 0.8 V vs Li/Li^+, so VC is reduced first, as indicated by Figure 6. FEC is already reduced at 1.3 V vs. Li and is primarily used in Si-containing anodes. It almost completely prevents the reduction of other electrolyte components and reduces the crack formation of Si particles [101,102].

1.6. Aging mechanisms in LIBs

Cycling and calendar ageing are the unwanted but unavoidable deterioration of the electrochemical properties of a LIB during use and storage, respectively. Degradation manifests itself as a decrease in capacity and/or an increase in internal resistance over time and cycles on the cell level [103,104]. The state of health (SOH) refers to the remaining discharge capacity of a cell relative to its initial discharge capacity and is an indicator of the aging progress of the cell [105]. Reaching a SOH below 80% is typically considered to be the end of life (EoL) of a battery [104,105]. Aging in LIBs

is uncaused by a number of complex chemical and physical processes, which can occur at the electrode-electrolyte interface, in the active materials, and in the electrode composites. Capacity loss can be caused by either LLI [106,107], by LAAM, or by loss of cathode active material (LCAM) [108,109]. In general, anode and cathode degrade by a variety of aging mechanisms as illustrated in Figure 7 [108]. The main mechanisms are often found on the anode side [103,104,110]. External factors affecting ageing rate are the temperature, the SOC range in which the cell is cycled, and the C-rate at which the cell is charged and discharged [110,111].

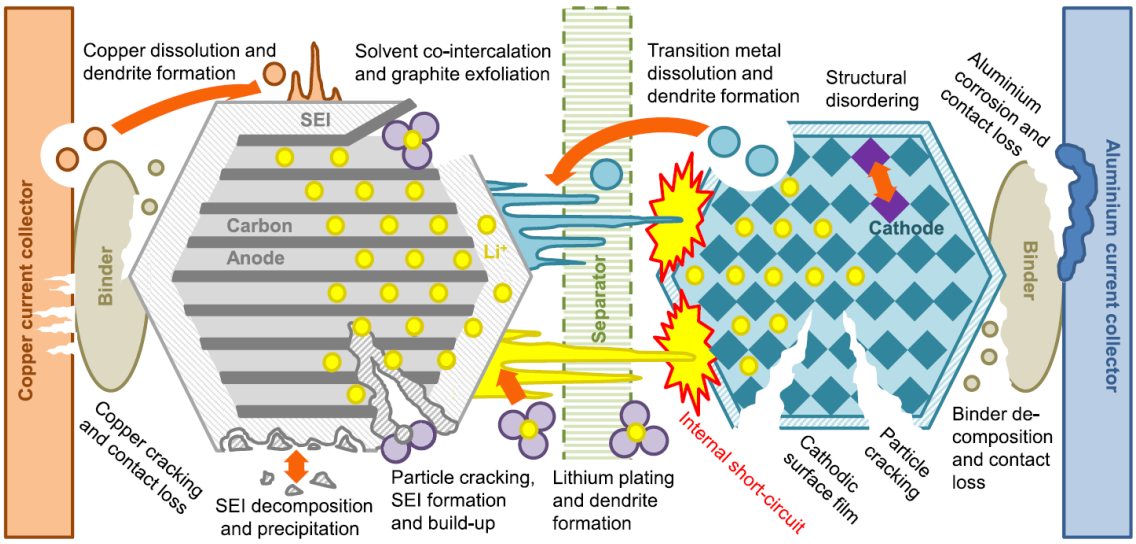

Figure 7: Side-reactions inside a LIB. Reprinted from Journal of Power Sources 341, C.R. Birkl, M.R. Roberts, E. McTurk, P.G. Bruce, D.A. Howey, Degradation diagnostics for lithium ion cells, 373-386, Copyright (2016) with permission from Elsevier [108].

The ageing rate r of Lithium ion batteries often exhibits an Arrhenius-like temperature dependence with a minimum ageing rate at about 25 °C [105]

$$r = A \exp\left(-\frac{E_A}{k_B T}\right) \tag{10}$$

A is the pre-exponential factor, E_A the activation energy and k_B the Boltzmann constant.

The increase in the ageing rate at higher and lower temperatures can be attributed to two different ageing mechanisms. At higher temperatures, SEI growth dominates, while at low temperatures the cells undergo predominantly Li plating. However, the crossover point of both ageing mechanisms depends, among other factors, on the C-rate and the anode coating thickness and may therefore be shifted [112,113].

Generally, the aging rate is strongly influenced by the active material employed [110], the depth of discharge (DOD) range in which the cell is aged [114], the charging and discharging C-rate [115] and the temperature [105], at which the cell is aged. By limiting the lower and upper cut-off voltage, the volume change of the anode active material can be reduced and the cathode

degradation can be mitigated [114]. At high temperatures, side reactions at the anode and cathode are promoted, while at low temperatures the intercalation kinetics are reduced, which favors the deposition of metallic Li [105,116]. High charging and discharging C-rate accelerate the aging rate of LIBs, as high C-rates can cause SEI and electrode fracture and Li deposition on the anode surface [117].

Li plating/deposition refers to the process in which lithium is deposited on the geometric surface of graphite particles as a parallel reaction to intercalation during the charging of a battery. This phenomenon occurs due to the low potential of graphite vs. Li/Li^+ during lithiation in combination with overpotentials (eq. 4), and has negative effects on the lifespan and safety of the battery. Various conditions can fulfill the criteria for Li plating, including fast charging [118], overcharging [119], and low-temperature charging [120–123]. These conditions limit the kinetics of intercalation, mass transfer, and diffusion of Li^+ [124]. During fast charging, the rate at which lithium is reaching the graphite electrode surface surpasses the bulk diffusion and intercalation processes, leading to Li deposition on top of the graphite particles. Fast charging often promotes an uneven distribution of charge across the electrode plane, particularly in large-format cells, which can cause local Li deposition even at high cycling temperatures [125–127]. In contrast, Li plating occurring during low-temperature charging tends to homogeneously cover the entire electrode plane due to hindered mass transfer [103,125,126,128,129]. The anode-cathode capacity ratio (N/P ratio) in cell design influences the probability of Li plating, requiring an excess capacity on the anode side to prevent Li plating.

Li electrodeposition exhibits a dendritic or mossy morphology, the former being attributed to its high adsorption and self-diffusion barriers [130–133]. The porous morphology of Li deposition provides additional active surface area for electrolyte decomposition reactions and the formation of a solid electrolyte interface (SEI), which accelerates capacity fading [105]. This can contribute to micropore clogging and increased resistance, creating a self-enhancing mechanisms that can promote further Li deposition [105]. In rare cases, Li dendrites can grow through the separator and cause internal short circuits, although this is primarily observed very few field incidents and difficult to observe in laboratory studies due to the very large amount of cells that would be needed. An additional safety concern associated with Li plating is the accelerated self-heating of very well insulated cells, which reduces the onset temperature and increases the susceptibility to thermal runaway [134].

1.7. Characterization Methods for Li plating

The characterization methods presented in this chapter have been used to detect Li plating on graphite and Si/graphite anodes. These are two quantitative methods, GD-OES and NDP, which can determine Li concentration versus depth, and an electrochemical method, voltage relaxation analysis, which provides in-situ hints of Li plating.

1.7.1. Glow Discharge optical emission spectroscopy

Glow discharge optical emission spectroscopy (GD-OES) is a method that couples glow discharge with an optical emission spectroscope for the qualitative and quantitative investigation of the elemental composition and depth profile of the surface and bulk volume of a solid [135,136]. Originally introduced by Grimm in 1968, who wanted to reduce the disadvantages of atmospheric arc and spark excitation by use of low-pressure plasma excitation, GD-OES was already used in the 1970s for the characterization of metals and alloys [137]. Starting with bulk analysis, further development led to the introduction of depth resolved elemental analysis in the 1980s, allowing the study of galvanized metals and metal coatings [138,139]. In the 1990s, the introduction of radio-frequency excitation opened the door to the characterization of non-conductive materials [140]. Since then, GD-OES-based methods have been successfully established for characterizing porous electrodes in LIBs and has been applied to the study of graphite and Si/graphite anodes [126,141–148].

A schematic of the glow discharge source and the spectroscopic detector is shown in Figure 8. The sample is electrically connected to the GD-OES cathode and physically separated from the hollow cylindrical GD-OES anode by a seal ring [136,149]. The glow discharge source is filled with low-pressure discharge gas, usually high purity Ar, before applying a high voltage. Electrons released from the sample surface are accelerated towards the GD-OES anode and collide inelastically with Ar atoms, ionizing them and therefore producing free electrons. These electrons cause the dissociation of further Ar atoms in an avalanche-like process, eventually forming a stable electrically conductive discharge plasma consisting of neutral Ar atoms, Ar^+ ions, and free electrons. The positively charged species are accelerated to the sample surface by the high negative potential of the GD-OES cathode, atomizing the sample and sputtering sample atoms into the Ar plasma.

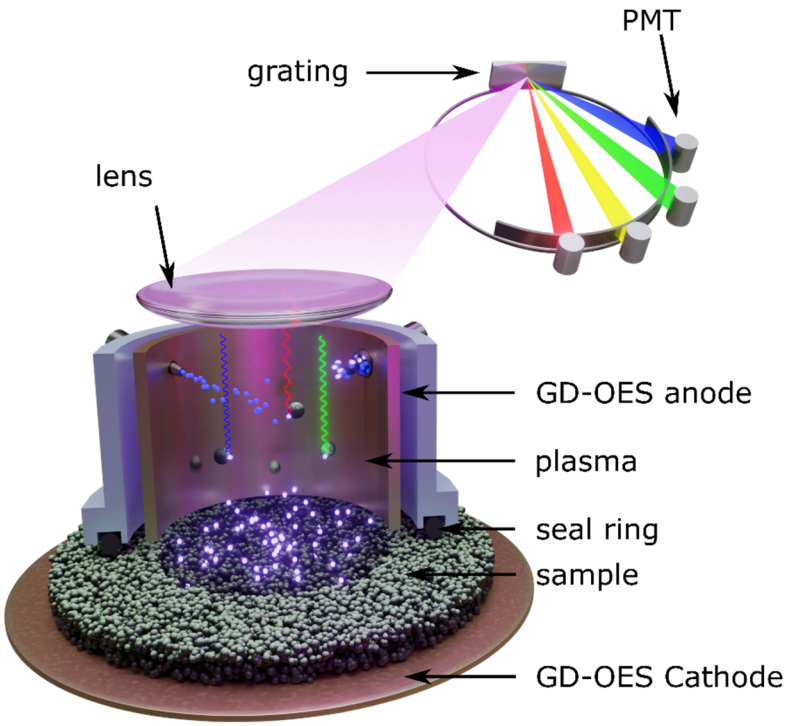

Figure 8: Schematic representation of the glow discharge source and the Rowland circle.

In the plasma, the sample atoms are energetically excited by collision mostly with electrons or Ar atoms. Upon energy release by emission of a photon of characteristic wavelength, the excited atoms return to their more energetically favorable ground state. From the glow discharge chamber, the emitted light passes through a lens and a slit into the spectrometer, where it is split into its spectral components on a concave grating located on a Rowland circle. These are then detected and quantified wavelength dispersive by dedicated photomultiplier tubes (PMT) or simultaneously by a charge-coupled device (CCD) camera [136,149].

The glow-discharge plasma is characterized by low pressure, low ionization energy, and overall electrical neutrality. Its spatial distribution can be categorized into several regions, progressing from the sample towards the GD-OES anode. Electrons are accelerated from the sample surface towards the anode by the electrical potential. The GD-OES cathode surface is covered by what is known as the cathode glow, where the electrons have gained enough energy to excite atoms. Excited atoms rapidly emit light and fall back to the ground state. The cathode glow is followed by the cathode dark space, in which the electrons have built up sufficient energy to ionize rather than excite argon atoms in collisions. As most of the potential drop takes place in the cathode dark space, the negative glow region, which follows the cathode dark space region, is almost field-free. In the cathode dark space region, the electron density increases strongly due to ionization. The electrons move relatively slowly in the negative glow region due to the low potential difference and can therefore excite atoms or recombine with ions [136,149].

Sputtering can be mathematically described as a binary collision where the proportion η of the energy is transferred to the sample atom according to [149]

$$\eta = \frac{(m_i + m_t)^2}{4\, m_i m_t} \tag{11}$$

where m_i is the mass of the sputter ion and m_t the mass of the target atom. As the energy of the incoming particle is not transferred to only one sample atom, several sample atoms can be ejected. The required minimum energy E_0 for sputtering can be estimated using [149]

$$E_0 = \frac{16 U_s}{\eta} \tag{12}$$

where U_s is the heat of sublimation and can be used to estimate the average bond strength.

Due to the distribution of the sputtering energy in the sample, a sputtered atom receives on average only 1/16 of the energy of the incoming atom.

Eq. (13) describes the sputter rate q_M on a sample consisting of different elements [149]. The sample will be enriched with the element that is more slowly sputtered. The sputter rate is then determined by this element, whose concentration is given by c_i according to

$$\frac{1}{q_M} = \frac{1}{100} \sum_i \left(\frac{c_i}{C_{Q_i}}\right) \tag{13}$$

The excitation processes in a glow discharge plasma are complex as atoms can be excited in several ways. In collisional excitation, an electron or neutral atom collides with an atom or molecule, transferring energy and exciting the atom or molecule. The excited species can then emit light as they return to their lower energy states. Alternatively, a photon with sufficient energy can be absorbed by an atom or molecule in the plasma, thus exciting it. Furthermore, excited or metastable atoms can collide with another atom or molecule in the plasma, transferring energy and causing ionization. This process, also known as Penning ionization, is important in gas mixtures where the excited species can transfer energy to other species with higher ionization energies [136,149,150].

GD-OES measurements provide relative intensities for each element measured, which can be quantified after calibration with reference samples of known composition. The intensity of a spectroscopic peak depends on the concentration of an element c_i, the sputter rate q_m, at which the sample is ablated, the emission yield R_i of the excited element in the plasma, and the detection efficiency k_i, with which the element is detected. The intensity is proportional to both the concentration and the sputter rate, since both affect the sample atom density in the plasma, which itself is proportional to the intensity. Mathematically, this relationship is described by [151,152]

$$I_i = k_i S_i R_i c_i q_m + b_i \quad (14)$$

which also takes into account the self-absorption rate S_i and the background intensity b_i.
For analytical purposes, it is more convenient to use relative sputter rates, resulting in eq. (15) [151,152]. By inverting the terms, as indicated by the suffix '. $c_i \frac{q_m}{q_{ref}}$ is the relative atomic number of a given element entering the plasma per second and is calculated using

$$c_i \frac{q_m}{q_{ref}} = k_i' S_i' R_i' I_i - b_i' \quad (15)$$

The hydrogen effect is known to be an interfering factor in analytical GD-OES requiring additional corrections [153–155]. However, the hydrogen effect has beneficial effects on the analysis of porous negative electrodes, so 1 vol.-% H_2 is commonly added to the high purity Ar gas used as sputter gas. Those beneficial effects include reduced intensity of lines of heavy elements such as Fe and Cr and increased intensity of light elements like O and Li. Furthermore, the hydrogen positively affects the crater shape and the sputter rate [144].

In 2007, Saito et al. demonstrated that GD-OES could be used to investigate aging phenomena over the entire depth of aged NCA cathodes [141]. Later in 2012, Takahara *et al.* developed a method to qualitatively determine the elemental distribution in graphite anodes and LFP cathodes in various aging stages [142]. They then optimized the depth profiling parameters by evaluating the effect of adding hydrogen and oxygen to the Ar [144]. A small amount of hydrogen proved beneficial for the sputter rate and sensitivity towards light elements. Still using Ar as discharge gas, Takahara *et al.* first quantified Li in NMC and graphite electrodes at different SOCs [143]. Finally, they investigated the SEI formation and Mn deposition on aged graphite anodes and found an increasingly inhomogeneous Li and Mn distribution caused by the aging process [145]. Ghanbari *et al.* investigated the aging phenomena of Li deposition on graphite anodes with GD-OES and developed a method to quantify the amount of metallic Li [126,146]. Due to the introduction of Si as anode active material in commercial cells, new aging mechanisms occur, which have been studied by Richter *et al.* [147,148]. Using a combination of GD-OES and neutron diffraction, they observed re-intercalation and re-distribution of Li in anodes charged at subzero temperatures [148]. At the start of this research work, there were no studies on the detection and quantification of Li deposition on Si/graphite anodes known in the accessible literature.

1.7.2. Neutron depth profiling

Neutron depth profiling (NDP) is a non-destructive technique for measuring the isotope concentrations versus depth [156,157]. Neutron-induced reactions with certain light elements are used to probe the surfaces of solids in the first few micrometres. The reaction of neutrons with atoms is proportional to the cross-section of the nuclides. As the reaction cross-section of most nuclides is rather small, cold neutrons with energies below 10^{-2} eV mostly pass through the sample without interacting. However, some elements including Na, Li, B, and Be have isotopes with a large reaction cross-section, making NDP a very good technique for studying these elements [157].

^{6}Li isotopes undergo an exoergetic reaction with thermal neutrons, in which an alpha particle with 2055 keV and a triton particle with 2727 keV energy are produced [157]:

$$^{6}Li + n \rightarrow \ ^{4}He(2055\ keV) + \ ^{3}H(2727\ keV) \tag{16}$$

As only 7.5% of all Li atoms are ^{6}Li isotopes, the results have to be extrapolated [157].Each reaction of an isotope with a neutron produces charged particles of equal energy. The energy of the particle decreases as it passes through the sample due to the stopping power of the sample. The relationship between the depth of the particle's origin and its residual energy [157] is described according to

$$x = \int_{E(x)}^{E_0} \frac{1}{S(E)}\, dE \tag{17}$$

S(E) is the stopping power of the material, E(x) is the residual energy of the particle, E_0 is the initial energy and x is the distance traveled by the particle in the material.

For multi-elemental compounds, the stopping power can be calculated using Bragg's law [158]. The stopping power is mostly independent of the chemical and electrical state of the matrix.

The reaction cross-section is inversely proportional to the square root of the neutron energy [157]. Therefore, the reaction rate increases with decreasing neutron energy. A moderator such as water can be used to reduce the energy of the neutrons to the temperature equilibrium with their environment. The energy of the neutrons can be further reduced by cooling the moderator. By filtering the neutron beam through single-crystal sapphire, epithermal neutrons and gamma radiation are removed. Due to the low energy of the neutrons, no beam or thermal damage is induced in the sample [157].

Due to the large reaction cross-section of Li and the limited number of methods capable of measuring Li depth profiles, NDP is employed in the field of LIBs. Nagpure et al. used NDP to

monitor the Li concentration profile in fresh and aged graphite anodes and found an accumulation of Li in the SEI of aged anodes [159]. Operando NDP measurements were made possible by a new cell design that allowed the distinction between reversibly intercalated Li into graphite and irreversibly bound Li in the SEI [160]. Later, Wetjen et al. applied NDP to observe reversible and irreversible processes in Si/graphite anodes and gained insight into the SEI formation and depth-dependent Li concentration profiles [161]. In a study containing Si/graphite anodes with varying Si contents, Moyassari et al. investigated the lithiation into the anodes at different SOCs [162]. More recently, NDP application has been extended to the investigation of Li concentration profiles and charging/discharging behaviour of all-solid-state-batteries (ASSB) [163,164]. A comparison between GD-OES depth profiling and NDP was carried out in this thesis for the first time.

1.7.3. Voltage Relaxation Analysis

Detecting Li plating in full cells is challenging, due to the scarcity of externally measurable parameters. However, the cell voltage can give an indication of the onset and dissolution of Li metal deposition. If the anode potential falls below 0 V vs. Li/Li^+ during charging, the deposition of Li metal on the anode is thermodynamically favored over the intercalation of Li into the active material. Large diffusion and charge transfer over-potentials during high charging currents or low temperatures are often responsible for negative anode potentials vs. Li/Li^+.

The Gibbs phase rule specifies the number of degrees of freedom (F) in a system in thermodynamic equilibrium depending on the number of components (C) present and the number of phases (P) existing at the same time [28]:

$$F = C - P + 2 \tag{18}$$

In the case of a Li metal electrode, the number of components is 1, as is the number of phases. If the temperature and the pressure are kept constant, the remaining degrees of freedom are 0. For this reason, the chemical potential μ(p, T), which is a function of pressure and temperature, and the electrical potential are constant [28]. Consequently, when metallic Li is deposited on a current collector, the anode potential remains constant, and likewise when the deposited metallic Li dissolves.

In practice, a voltage plateau is observed during relaxation after the deposition of metallic Li on the anode surface [165–167], as the Li dissolves and intercalates into the anode active material, where it is energetically more stable. Since the first publications of Uhlmann et al. in half cells [167], Petzl et al. in full cells [165], and von Lüders et al. in full cells in combination with operando

neutron scattering [166], voltage relaxation analysis has been used in several studies [168–170] to non-destructively detect Li plating in full cells. In this thesis, voltage relaxation was applied to get hints for Li plating.

2. Objective

This thesis was carried out within the project “CharLiSiKo – Charakterisierung von Lithium-Abscheidungen auf Graphit und Silicium-Graphit-Kompositanoden“ funded by the Federal ministry of Education and Research (BMBF) under grant agreement n° 03XP0333A. The focus of this project is on detecting Li depositions on graphite and Si/graphite composite anodes, and validating the methods for reproducibility and comparison with other methods. The objective of the project further is to develop efficient workflows and strategies to prevent or weaken the deposition of Li metal on anodes, which will increase the service life and safety of high-energy cells, reduce costs, improve sustainability, and reduce dependencies to critical raw materials.

The scientific objectives of this work are (i) to develop a method for the quantification of Li plating on Si/graphite anodes, (ii) to improve the depth accuracy of GD-OES measurements, particularly for anodes with surface Li deposition, and (iii) to investigate the correlation between reduced anode thickness due to the addition of Si and the occurrence of Li plating.

(i) Few techniques are capable of detecting and quantifying Li, and even fewer techniques can produce Li depth profiles over the entire depth of an electrode. This makes GD-OES a valuable instrument for the analysis of aged anodes. The previously existing GD-OES method for the quantification of Li [126,146] is only applicable to graphite anodes, therefore a new method is needed to determine the amount of metallic Li on Si containing anodes.

(ii) The accuracy of the depth for GD-OES measurements is affected by the limitation that the depth can only be measured after the GD-OES measurement has been completed. As a result, the sputter rate must be assumed to be constant throughout the measurement. This assumption has been verified experimentally for fresh and aged anodes with homogeneously distributed elements. In the case of Li plating, however, the elements are non-uniformly distributed and show different sputter rates. A method comparison with NDP, another method that can quantify Li versus depth, should provide an opportunity to improve the depth calculation.

(iii) Due to its high specific capacity, Si offers the possibility of reducing the anode thickness while maintaining a constant areal capacity. This property has the potential to reduce the susceptibility to Li plating due to reduced diffusion pathways in the pores of the anode. However, a lower Li diffusion coefficient has been found for Li in the Si particles, which increases the susceptibility to Li plating. Due to these contradictions, it remains uncertain how susceptible Si-containing anodes are to Li plating compared to graphite anodes.

3. Publications

3.1. Detection of Li Deposition on Si/Graphite Anodes from Commercial Li Ion Cells: A Post-Mortem GD-OES Depth Profiling

Reprinted with permission from:

M. Flügel, K. Richter, M. Wohlfahrt-Mehrens, T. Waldmann, 2022 *J. Electrochem. Soc.* **169** 050533

© 2022 The Author(s). Published on behalf of The Electrochemical Society by IOP Publishing Limited. This is an open access article distributed under the terms of the Creative Commons Attribution 4.0 License (CC BY, http://creativecommons.org/licenses/by/4.0/), which permits unrestricted reuse of the work in any medium, provided the original work is properly cited.

DOI: https://doi.org/10.1149/1945-7111/ac70af

Individual Contribution

M. Flügel	Conceptualization, Methodology, Validation, Formal Analysis Investigation, Writing - Original Draft, Visualization
K. Richter	Formal Analysis, Investigation, Visualization
M. Wohlfahrt-Mehrens	Supervision, Writing – Review & Editing
T. Waldmann	Conceptualization, Writing – Review & Editing, Supervision, Project administration, Funding acquisition

Summary

In the first publication of this thesis, an investigation was conducted on three commercially available cylindrical cells that utilize Si as part of the anode active material. Si is chosen as active material for its higher specific capacity compared to graphite at similar low working potentials, allowing for higher specific energy at cell level.

One key aspect of this research focused on developing a novel method to quantify Li plating on the surface of Si-containing anodes. Unlike the quantification of Li plating on graphite anodes, where all oxygen (O) detected is assumed to be bound as Li_2O in the solid electrolyte interface (SEI), some of the O in Si-containing anodes is bound in SiO_x particles. Due to uncertainty in the oxygen content of SiO_x particles, a corridor representing the minimum amount of metallic Li is determined.

The initial characterization revealed that one cell type is designed for high-power applications due to its low anode thickness and high porosity, while the other two are designed for high-energy applications due to their high anode coating thickness and low porosity. The Si content of the anodes in all three cells was quantified using GD-OES, ranging from approximately 2.5% to 4.0% by weight. However, these Si contents contribute 11.5% to 19.5% of the anode capacity of fresh cells, as determined using DVA. The cell types were subjected to three different aging procedures 1) at low temperature ageing to promote and to induce Li plating, 2) at 45 °C to promote SEI growth and 3) at 45 °C to 80% to its initial capacity and subsequent 100 cycles aging at low temperature (procedure 1).

While the high-energy cells exhibited Li plating during aging at 0 °C and experienced a rapid decline in capacity, the high-power cell only exhibited Li plating at -20 °C. Li plating on the anode surfaces was detected through SEM, which revealed the presence of Li dendrites, and GD-OES, which showed high Li concentration. The newly-developed GD-OES method confirmed the presence of metallic Li on the anode surface in each cell type.

Aging at 45°C was intended to investigate if the use of Si as an active material would result in a different aging mechanism. Similar to the fresh cells, the anodes of the aged cells were assembled in half coin cells against a Li metal counter-electrode. Comparing the voltage profiles with fresh anodes, it was observed that the capacity contribution of Si decreased in two cell types, while graphite did not exhibit aging in any of the cell types. Anodes with minimal capacity loss during aging showed a high bulk Li content in the GD-OES depth profile, indicating lithium loss inside the anode (LLI) as the aging mechanism. In contrast, anodes with high capacity loss displayed

thick SEI films around the Si particles, indicating Si deacitvation (LAAM) as the aging mechanism.

As the active Li inventory diminishes, the tendency to Li plating decreases with subsequent low-temperature aging after the initial aging period. The conditions that induced Li plating in fresh cells no longer triggered Li plating in aged cells. However, the cell type that primarily aged due to LAAM exhibited an unchanged tendency for Li plating in the aged state. These findings are valuable for evaluating the potential use of aged cells in second-life applications.

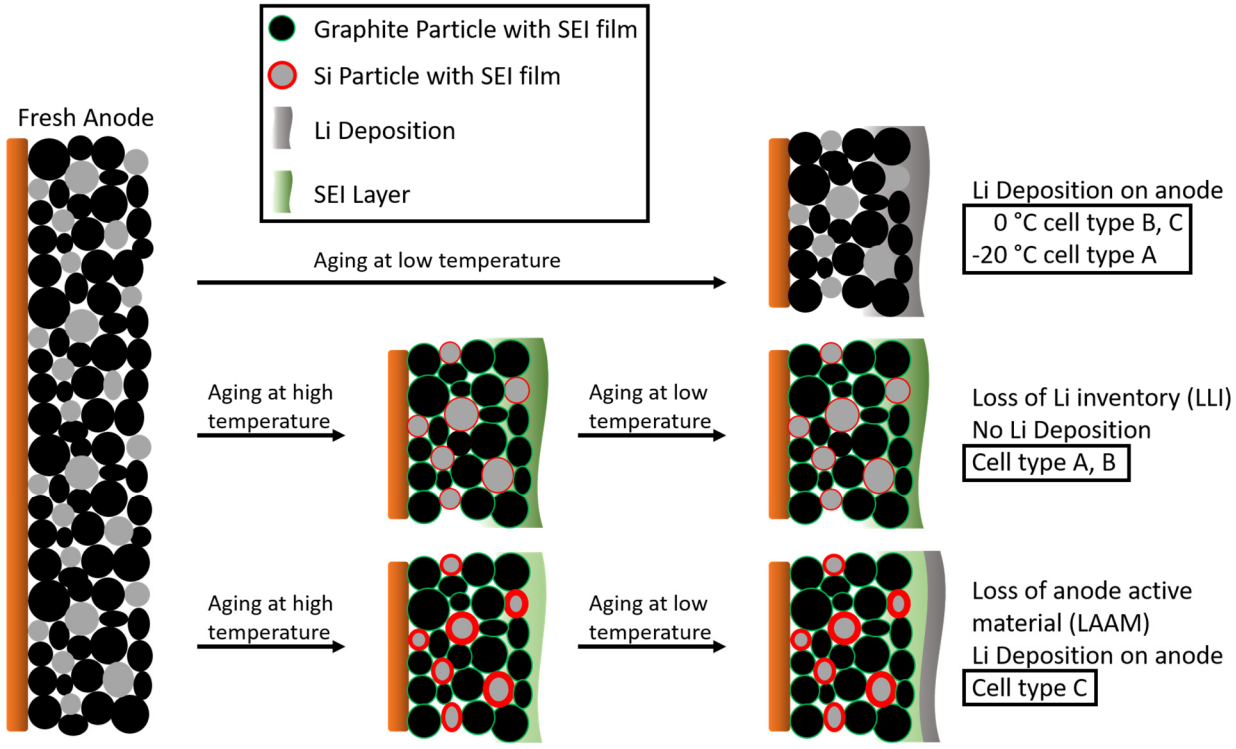

Figure 9: Schematic illustration of the results obtained in the publication [2].

Journal of The Electrochemical Society, 2022 **169** 050533

Detection of Li Deposition on Si/Graphite Anodes from Commercial Li-Ion Cells: A Post-Mortem GD-OES Depth Profiling Study

Marius Flügel, Karsten Richter, Margret Wohlfahrt-Mehrens, and Thomas Waldmann[z]

ZSW—Zentrum für Sonnenenergie- und Wasserstoff-Forschung Baden-Württemberg, Helmholtzstrasse 8, D-89081 Ulm, Germany

A new semi-quantitative method was developed to detect Li deposition on Si/graphite anodes. This method is based on Post-Mortem glow discharge optical emission spectroscopy (GD-OES) depth profiling. Based on the contents of Si, Li, and O in the GD-OES depth profiles, we define a corridor, in which the minimum amount of metallic Li on the anode is located. This method was applied to three types of commercial 18650 cells with Si/graphite anodes in the fresh state and with Li plating intentionally produced by cycling at low temperatures. Additional cells were cycling aged at 45 °C to 80% SOH. The main aging mechanisms at 45 °C were determined using differential voltage analysis (DVA), SEM, and half cell experiments. Subsequently, the cells aged at 45 °C were further cycled under the conditions that had led to Li deposition for the fresh cells. Furthermore, the anode coating thickness for 18 types of commercial Li-ion cells are correlated with the specific energy, while distinguishing between graphite anodes and Si/graphite anodes. Our extensive Post-Mortem study gives deep insights into the aging behavior of state-of-the-art Li-ion cells with Si/graphite anodes.

© 2022 The Author(s). Published on behalf of The Electrochemical Society by IOP Publishing Limited. This is an open access article distributed under the terms of the Creative Commons Attribution 4.0 License (CC BY, http://creativecommons.org/licenses/by/4.0/), which permits unrestricted reuse of the work in any medium, provided the original work is properly cited. [DOI: 10.1149/1945-7111/ac70af]

Manuscript submitted March 29, 2022; revised manuscript received May 6, 2022. Published May 27, 2022.

The theoretical capacity of graphite is limited to 372 mAh g^{-1}, therefore the use of alloying materials like Si or SiO_x is considered to increase the capacity of anodes.[1] However, the cyclic stability of pure Si is very poor,[2,3] therefore, Si/graphite composite anodes were developed as they show a better cycling stability than Si and a higher capacity than graphite.[4] Si-graphite composites are already used as anode active material in commercially available state-of-the-art Li-ion batteries (LIBs).[5–9]

Different groups conducted research regarding the improvement of the cycle life and capacity of such anodes.[10–12] The SEI on Si particles does not withstand the high volume expansion, so the SEI is partially reformed in each cycle. This irreversible consumption of Li is called loss of Li inventory (LLI).[13–16] During aging, however, the Si particles can fracture and lose electrical contact. This results in a loss of anode active material (LAAM).[17–19]

A severe aging mechanism in LIBs is Li plating/deposition, since it can lead to fast aging as well as to a decrease of safety.[20–25] Most research on Li deposition focusses on graphite anodes.[26] However, there is a lack of knowledge on Li deposition on Si/graphite anodes. Li deposition can occur as a parallel reaction to intercalation of Li ions into graphite and is favoured by low temperatures and high charging C-rates.[20,21,26,27] Si has a higher working potential than graphite,[28] however, Li has a lower diffusion coefficient in Si than in graphite.[29] Due to these opposite influences on Li deposition, more detailed investigations are necessary.

We recently observed reversible Li deposition indirectly by operando neutron diffraction in commercial Li-ion cells.[7] The relaxation mechanism after Li deposition on Si containing anodes is different from graphite anodes.[7] Deposited Li re-intercalates into graphite and the Si compound.[7] Furthermore, redistribution of Li can lead to lithiation of the Si compound from lithiated graphite until an equilibrium is reached.[7]

A semi-quantitative method was developed by our group to detect Li deposition on graphite anodes using glow discharge optical emission spectroscopy (GD-OES).[30,31] In this method, it was assumed that all detected O is bound as Li_2O in the SEI (Eq. 1). Li_2O is the SEI compound with the highest percentage of Li, therefore the result of this method corresponds to the minimum amount of metallic Li.[30,31] The detected amount of Li is reduced by the amount of Li in the calculated amount of Li_2O (Eq. 2). Metallic Li was deposited on the anode surface if the resulting amount of metallic Li is positive.

$$O_{det} = O_{SEI} = O_{Li_2O} \quad [1]$$

$$Li_{met} = Li_{det} - Li_{Li_2O} \quad [2]$$

GD-OES is a destructive method and, moreover, can only be applied to disassembled cells. In contrast, with a 3-electrode setup,[32] operando XRD,[33,34] and in situ solid state ^{7}Li NMR[35,36] Li deposition can be detected during operation. Using the 3-electrode setup, however, it is only possible to reliably determine the onset of Li deposition, however, quantification is difficult. With operando XRD, the depth resolution is only 3 μm, furthermore, depth resolution is not possible with cylindrical cells. The cells used in this study are cylindrical cells in a metal housing, which makes measurement with the strong magnet needed for in situ solid state ^{7}Li NMR very difficult. Li deposition can also be determined by titration.[37] However, the chemicals used to extract metallic lithium are carcinogenic and mutagenic. Furthermore, no depth-dependent determination of Li deposition can be carried out by titration.

The GD-OES method for graphite cannot be applied on Si-containing anodes, since in Si/graphite anodes, O is present in Li_2O in the SEI and in SiO_x in the anode active material.[6] Therefore, in this publication, we present a further development of our method that allows quantification of Li deposition on Si/graphite anodes. We apply the method to anodes from three types of commercial 18650 cells whose anode active material varies in Si content, particle size, porosity, and coating thickness. We investigate how aging differs among these three cell types at both low temperatures and high temperatures. Finally, we investigate the effect of aging at 45 °C before cycling under conditions which had lead to Li deposition for the fresh cells.

Experimental

Three types of 18650 cells (A–C) were investigated. Each cell type was purchased in a batch of 30 cells. Upon arrival of the cells, each cell was weighed and the voltage and internal resistance (Hioki 3554, 1 kHz) were determined. The standard deviations are similarly low as for other cell types and therefore suitable for further investigations.[38] Cell parameters for all three cell types are summarized in Table I.

[z]E-mail: thomas.waldmann@zsw-bw.de

Journal of The Electrochemical Society, 2022 **169** 050533

Table I. Overview on the three investigated cell types on this study, test conditions, and results of the initial cell testing. The values for cell resistance, voltage, and weight are mean values and standard deviations.

Cell	A	B	C
Format	18650	18650	18650
Number of cells	30	30	30
Nominal capacity	3.0 Ah	3.35 Ah	3.5 Ah
Voltage Range	2.0–4.2 V	2.65–4.2 V	2.5–4.2 V
Max. charging-Rate	5 A (1.6C)	2 A (0.6C)	3.5 A (1C)
C-Rate during aging	1C (3 A)	0.5C (1.675 A)	0.85C (3 A)
Anode	Si/C	Si/C	Si/C
Cathode	NCA	NCA	$LiNi_{0.824}Mn_{0.053}Co_{0.124}O_2$
Cell resistance	14.4 ± 0.2 mΩ	20.8 ± 0.2 mΩ	29.1 ± 0.4 mΩ
Cell voltage	3.479 ± 0.001 V	3.549 ± 0.003 V	3.600 ± 0.001 V
Cell weight	47.10 ± 0.05 g	47.10 ± 0.05 g	46.67 ± 0.11 g
Application	High Power	High Energy	High Energy

Table II. Summary of the detailed examination of the cells used in this study.

	Cell A	Cell B	Cell C
Si-content	~3.5–4 wt%	~2.5–3.0 wt%	~2.0–2.5 wt%
Si-particle size	< 10 μm	> 10 μm	< 10 μm
Gr particle size	> 10 μm	> 10 μm	> 10 μm
Coating thickness	60 μm	80 μm	82 μm
Specific Energy	236 Wh	254 Wh	270 Wh
Rev. Capacity RT at C/20	3.15 Ah	3.38 Ah	3.49 Ah
Porosity	28.7% ± 0.2	19.8% ± 0.4%	19.3% ± 0.4%
Li in fresh anode (ICP-OES)	1.49 wt%	1.35 wt%	0.64 wt%

The electrochemical measurements were conducted with Basytec CTS systems and climate chambers (Vötsch). Three cycling aging procedures were performed with two cells each. Low temperature aging took place at 0 °C for cell B and C and at −20 °C for cell A. The aging at elevated temperature was conducted at 45 °C for all cells. Cells tested for second-life viability were aged at 45 °C to SOH 80% and then at low temperature for an additional 100 cycles. The C-rate and corresponding current of each cell is listed in Table I. During the control cycle (every 25 cycles), the cells were charged with 0.1C (CCCV, I < 0.05C) to 4.2 V and discharged with 0.1C (CC) to the end of discharge voltage. The control cycles were done at the respective aging temperature.

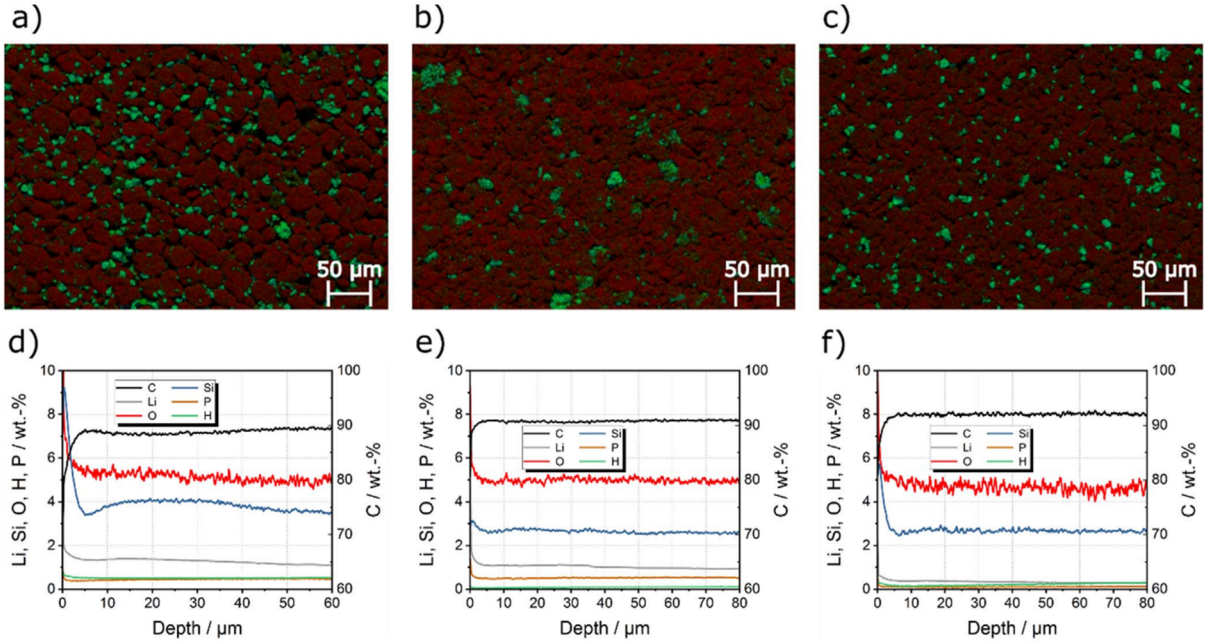

Figure 1. EDX mappings of the fresh anodes of (a) cell type A, (b) cell type B, and (c) cell type C show graphite particles in red and Si particle in green, (d)–(f) show the GD-OES depth profiles of the anodes shown above.

Journal of The Electrochemical Society, 2022 **169** 050533

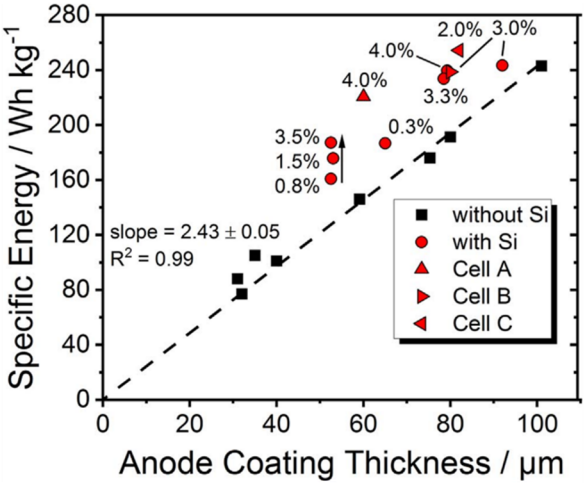

Figure 2. Correlation between the anode coating thickness and the specific energy for 18 commercial cylindrical cell types which were opened in our lab. The anodes were measured by GD-OES depth profiling to determine the Si content. Cell types A–C investigated in detail in this study are represented by red triangles.

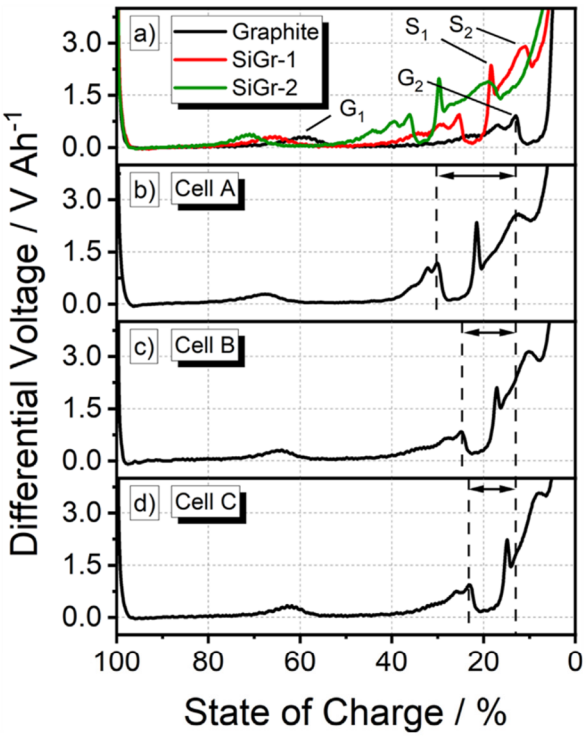

Figure 3. DVA of cell types A, B and C. The position of Gr-2 was compared with a reference graphite anode and two reference Si/graphite coatings.

Cell disassembly was performed in an Ar-filled glovebox (O_2 < 0.1 ppm, H_2O < 0.1 ppm) after discharge at 0.1C to the respective end-of-discharge voltage (see Table I) at the temperature, at which the cells were aged. The electrodes were washed three times for 1 min each in DMC before drying under Ar atmosphere and under vacuum for 1 h each.

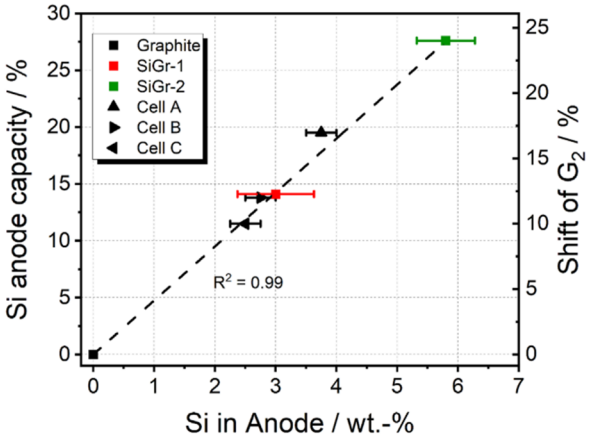

Figure 4. Linear correlation between the Si content in the anodes and the share of the anode capacity provided by Si.

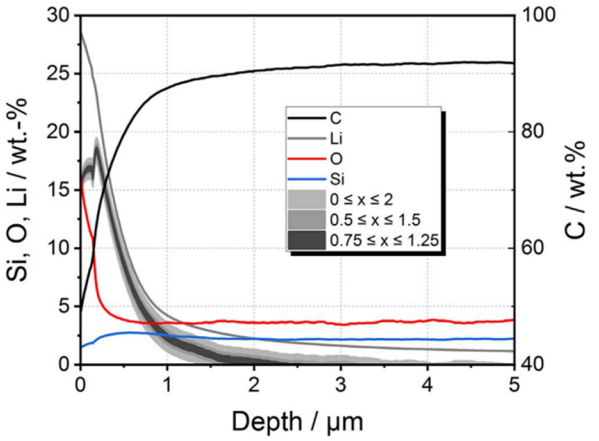

Figure 5. GD-OES depth profile with corridor of the minimum amount of metallic Li depending on the oxygen content of the Si particles.

Electrodes, which were utilized to build them into coin half cells, were transferred in a container with Ar atmosphere to the dry room (dew point −60 °C). In the dry room, the coating of one side of the electrodes was removed by laser blanking like in one of our previous studies.[39] Under dry air, the single-side coated electrodes were transferred to an Ar-filled glovebox, in which round electrodes with a diameter of 12 mm were punched out. CR2032 half cells consisting of one prepared electrode from the original 18650 cell, 2 GFA separators, one Li counter electrode (diameter 16 mm), and 150 μl electrolyte (1 M $LiPF_6$ in EC: DEC (3:7) wt% + 10 wt% FEC) were built. After a soaking time of 12 h, the coin half cells were cycled three times at 0.1C between 0.01 V − 1.5 V at room temperature.

GD-OES analyses were conducted using a GDA750 device (Spectruma) on electrode samples of 2.5 mm diameter. The measurements were performed in radio frequency (RF) mode at a frequency of 2501 Hz, at a discharge voltage of 550 V and a pressure of 2 hPa. A mixture of 1% H_2 in Ar (both 6.0 purity) was used as sputtering gas. The following element specific emission lines were used for detection: H (121.6 nm), O (130.2 nm), C (156.1 nm), P (178.3 nm), Si (288.1 nm), Li (670.7 nm).

Scanning electron microscopy (SEM) of electrodes was carried out with a secondary electron (SE) detector at 5 kV using a LEO 1530 VP (Zeiss) equipped with a Gemini thermal field emission column. EDX mappings were recorded at an acceleration voltage of

Journal of The Electrochemical Society, 2022 **169** 050533

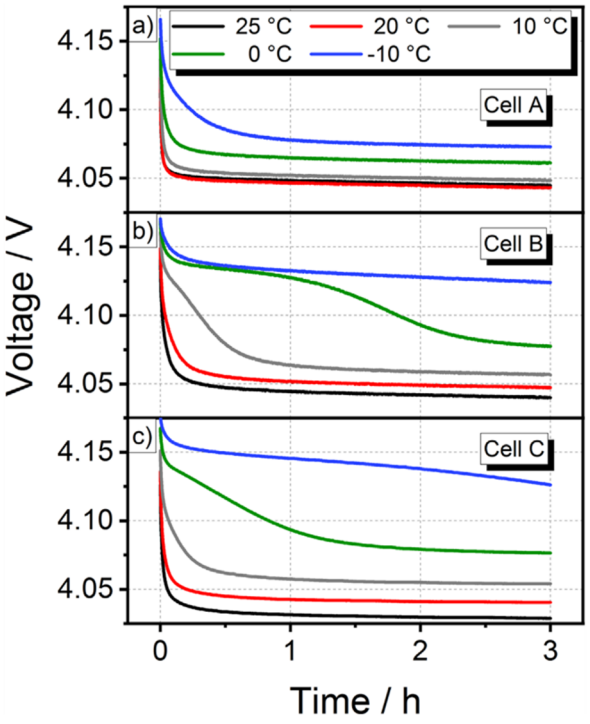

Figure 6. Voltage relaxation at different temperatures during a 3 h rest time of cells A–C after charging the cells at a charging current of 2 A to SOC = 80%.

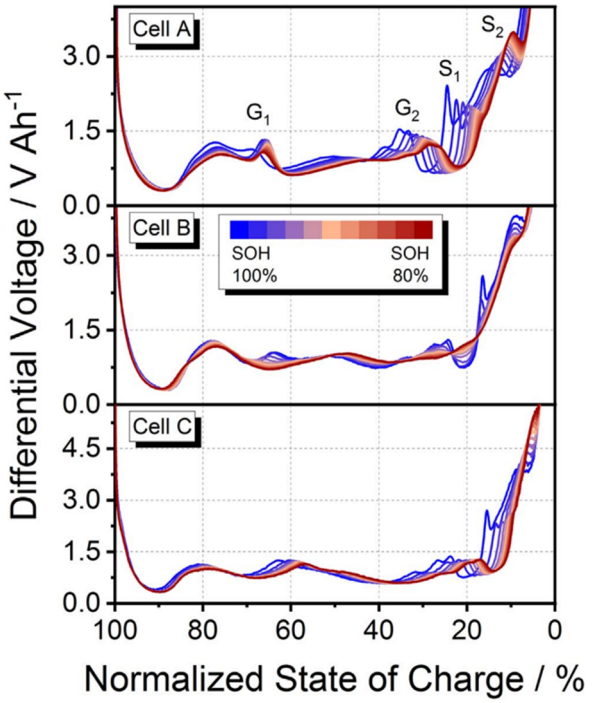

Figure 7. DVA of full cells A–C of control cycles every 25 cycles during aging of cells from SOH = 100% to SOH = 80%.

10 kV. Cross-sections of anodes were generated with a Hitachi IM4000Plus broad-beam argon ion milling system, using an ion beam voltage of 5 kV. During sample preparation for SEM (top view and cross section), the samples were exposed to air. Since air contact could potentially have an impact on the samples, aged cells were always compared to fresh cells as a reference.

For the Hg porosimetry measurements, a 20 cm long electrode piece was provided on which a double determination of porosity was performed (PASCAL 140-440 Series from Porotec).

The active material, graphite and two already mixed Si/graphite composites, was purchased from Iopsilion (China). All three electrodes consist of 94 wt% active material, 2 wt% CMC (TIMCAL, Switzerland) and 2 wt% SBR (ZEON, Japan) as binder and 2 wt% SuperC65 (Nippon paper Industries, Japan) as conductive additive. An aqueous binder solution containing 2 wt% CMC was prepared in a planetary mixer and then the SuperC65 was added. After homogenization of the conductive additive, the active material and SBR were added to the slurry and stirred in for another 120 min. The slurry was coated onto Cu foil using a pilot coater on a width of 80 mm at a speed of 1.5 m min^{-1} and with a target loading of 3 mAh cm^{-2}. The electrodes were calandered at 40 °C with a slot width of 35 μm.

Results and Discussion

Basic characterization of the cells.—In order to determine the chemistries of the commercial cells, they were investigated by Post-Mortem analysis. The electrodes were characterized by SEM/EDX, GD-OES, ICP-OES, Hg porosimetry, and electrochemical characterization. The results of this examination are summarized in Table II.

Figures 1a–1c show EDX mappings of the surfaces of anodes from cells A–C. The amount of Si particles visible on anode A is higher than that on anode B or C. Si particles seen on anodes A and C are typically smaller than 10 μm. In contrast, Si particles with a diameter larger than 10 μm can be seen on anode B. It is also apparent from the SEM images corresponding to Figs. 1a–1c that the porosity of anode A is higher than that of the other two anodes. This is consistent with Hg porosity measurements revealing that the porosity of the fresh anode A is ~29%, whereas anode B and C each have a porosity of ~19%.

To quantify Si and determine its distribution within the anode, GD-OES depth profiles were recorded. Cell A has the highest Si content of ~4 wt%, compared to ~3 wt% for cell B, and ~2.5 wt% for cell C. The Si distribution in the anodes of the three cells is very homogeneous. In accordance with ICP-OES measurements, a comparably high Li content is also noticeable in the GD-OES depth profiles, even though the cells were fully discharged (see Table II).

Lain investigated the correlation between power density and electrode design.[9] The authors found that lower coating thicknesses and smaller particles were chosen for cells with higher power density.[9] This observation is also consistent with our results from Post-Mortem analysis.

Figure 2 shows the correlation of the specific energy of 18 types of commercial cylindrical cells with the anode coating thickness. The three cells from this study are marked as red triangles. The additional data points originate from Quinn et al.[38] and further disassembled cells. Quinn et al. had already found a correlation between energy density and anode coating thickness, however, at the time of that study were not able to differentiate between graphite and Si containing anodes.[38] However it was pointed out that the active material type could have influences on the specific energy of the cell.[38]

In the work of Richter et al., it became possible to measure the Si content of anodes from commercial cells.[5] This allows distinguishing between cells with graphite (black squares) and with Si content (red circles and triangles) in Fig. 2. The differentiation of the data according to the Si content leads to an improved fitting for the data points from the graphite anodes. As expected, the slope of the fit through the data points of the graphite cells and its error (2.43 ± 0.05 Wh kg^{-1} μm^{-1}) is lower than determined by Quinn et al. (2.81 ± 0.12 Wh kg^{-1} μm^{-1}).[38]

Journal of The Electrochemical Society, 2022 **169** 050533

We note that Fig. 2 represents an overview considering the Si contents in anodes of state-of-the-art cells only. However, some scattering can be expected in this plot, e.g. from variations of anode porosity between cells which is neglected here.

In Fig. 2, higher amounts of Si in the anodes result in lower anode coating thicknesses at a given specific energy. For instance, with a constant anode coating thickness of 53 μm, the specific energy can be increased from 130 Wh kg^{-1} to 160 Wh kg^{-1} by adding 0.8 wt% Si, to 175 Wh kg^{-1} by adding 1.5 wt% Si and to approximately 190 Wh kg^{-1} by adding 3.5 wt% Si (see arrow in Fig. 2). On the other hand, to achieve a specific energy of 190 Wh kg^{-1}, the anode coating thickness of 80 μm of a graphite anode can be reduced to 53 μm by adding 3.5 wt% Si.

For cylindrical cells, a lower coating thickness leads to longer electrodes and more windings in the jellyroll and thus to a higher energy content.[40] Due to the different Si contents in the anodes of the different cell types, the spread of the data points is higher than that of the graphite anodes. Setting the cells investigated in this paper into the context of other commercial cells shows their accordance with the general trend.

Three Si/graphite electrodes were prepared with 0 wt% Si, 3.0 wt% Si (SiGr-1) and 5.8 wt% Si (SiGr-2) for comparison. The peaks in Fig. 3a appearing at state-of-charge (SOC) 60% and 13% at the graphite cell were named G_1 and G_2. Si operates at higher working potentials, therefore the characteristic Si peaks S_1 and S_2 appear at low SOC.[41] Similarly, the peak caused by Si appearing at higher SOC was named S_1 and the Si peak appearing at low SOC S_2. With increasing Si content, G_1 and G_2 shift to higher SOC.[41]

Figures 3b–3d shows the differential voltage analysis (DVA) of anodes from cells A–C rebuilt into coin half cells. In the anode SiGr-1, Si accounts for 14.1% of the total anode capacity and in the anode SiGr-2, Si accounts for 27.6%. The Si percentage of the anode capacity is 19.5% in cell A, 13.8% in cell B, and 11.5% in cell C.

Plotting the Si fraction of the anode capacity against the Si content in the anode reveals a linear relationship (Fig. 4). The error in x-direction is caused by the analysis method to determine the Si content. The fit result of $R^2 = 0.99$ indicates that the data from the anodes from the commercial cells agrees well with the linear relationship between the Si content in the anode and the capacity percentage that is stored in the Si compound, which was found for the in-house made electrodes.

GD-OES method development.—The method developed in our group to estimate the amount of metallic Li on graphite anodes assumes Li_2O as being the sole SEI species.[30] Several groups found that inorganic and organic SEI is also formed on Si particles.[42–44] Therefore, Li_2O can also be assumed as the dominant SEI species for Si particles. The formation of Li silicates during the lithiation of SiO_x ($0 < x \leqslant 2$), which is beneath the SEI layer, is frequently reported in the literature.[45,46] However, most known silicates have the characteristic of being composed of Li_2O and SiO_2.[47] Therefore, the model can also be applied despite Li silicate formation.

A critical issue is the unknown amount of O bound in SiO_x particles. We therefore introduce a corridor inside which the minimum amount of metallic Li is found. The boundaries of the corridor are defined by the lower limit x_{min} and upper limit x_{max} of SiO_x (Eq. 3). In this way, the model can be applied with modified limits on (i) pure Si particles that are only slightly oxidized during aging, on (ii) stoichiometric SiO and on (iii) SiO_x.

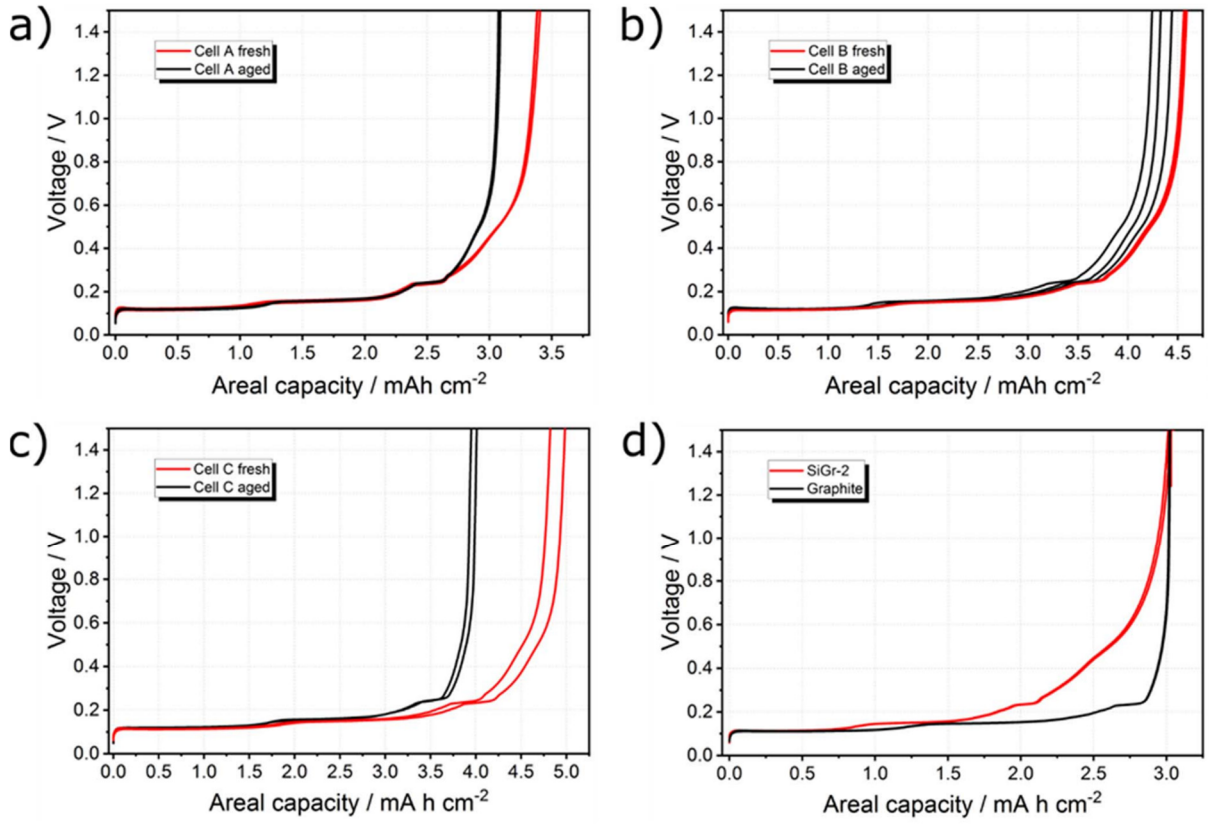

Figure 8. Half-cell potentials of anodes taken from fresh cells (red) and from cells aged to SOH = 80% (black) of (a) cell type A, (b) cell type B, and (c) cell type C; (d) graphite anode (black) and SiGr-2 anode (red) for comparison to indicate the potential range of Si and graphite.

Journal of The Electrochemical Society, 2022 **169** 050533

$$Li_{met} = Li_{det} - \left(O_{det} - Si_{det} \frac{x \bullet M(O)}{M(Si)} \right) \bullet \frac{2 \bullet M(Li)}{M(O)} \qquad [3]$$

where Li_{met} is the weight percentage of metallic and Li, Li_{det}, O_{det}, and Si_{det} are the weight percentages of detected Li, O and Si, respectively. M(Li), M(O) and M(Si) are the molar mass of Li, O, and Si, respectively.

In the case of no Si in the anode, accordingly $Si_{det} = 0$, the equation corresponds to the one used by Ghanbari et al. for detecting Li depositions on graphite anodes.[30]

Figure 5 shows the GD-OES depth profile of a Si containing anode with Li deposition on the surface. The corridor was plotted for three different limits of O content in SiO_x. As the width of the O interval is reduced, the corridor in which minimal Li deposition can be found decreases. As the amount of O available for the formation of Li_2O varies for different oxygen contents in SiO_x, the depth to which metallic Li can be present also varies between 1.5 and 4 μm in the different scenarios. The depth to which metallic Li is detected decreases with a decreasing O amount in SiO_x. The amount of metallic lithium increases with higher O content in SiO_x.

A low O content in SiO_x can be assumed when pure Si is part of the active material. During aging, Li silicates are formed, and it should hence be considered that Si will bind O. A higher O content must be considered for SiO, which has most likely a higher a cycling stability at the expense of intial Coulombic efficiency.

In the y-direction of Fig. 5, i.e. the corridor representing the amount of Li deposition is comparably narrow. In contrast, the depth of the Li deposition (x-direction of Fig. 5) shows a larger error. The amount of Li can therefore most likely be detected much more accurately than the depth distribution.

Li deposition behaviour on anodes of fresh cells.—The differences in the three cell types shown in the previous section cause the cells to suffer from Li plating under different operating conditions. One method to get a hint on reversible Li plating on graphite anodes is the evaluation of the voltage relaxation after charging.[22,48,49] After deposition of Li on the anode surface, a mixed anode potential develops which leads to a shoulder in the relaxation curve during re-intercalation of Li metal into graphite.[22,48–51]

Figures 6a–6c show the voltage relaxation for temperatures from 25 °C to −10 °C for cells A-C. All cells were charged with 2 A at

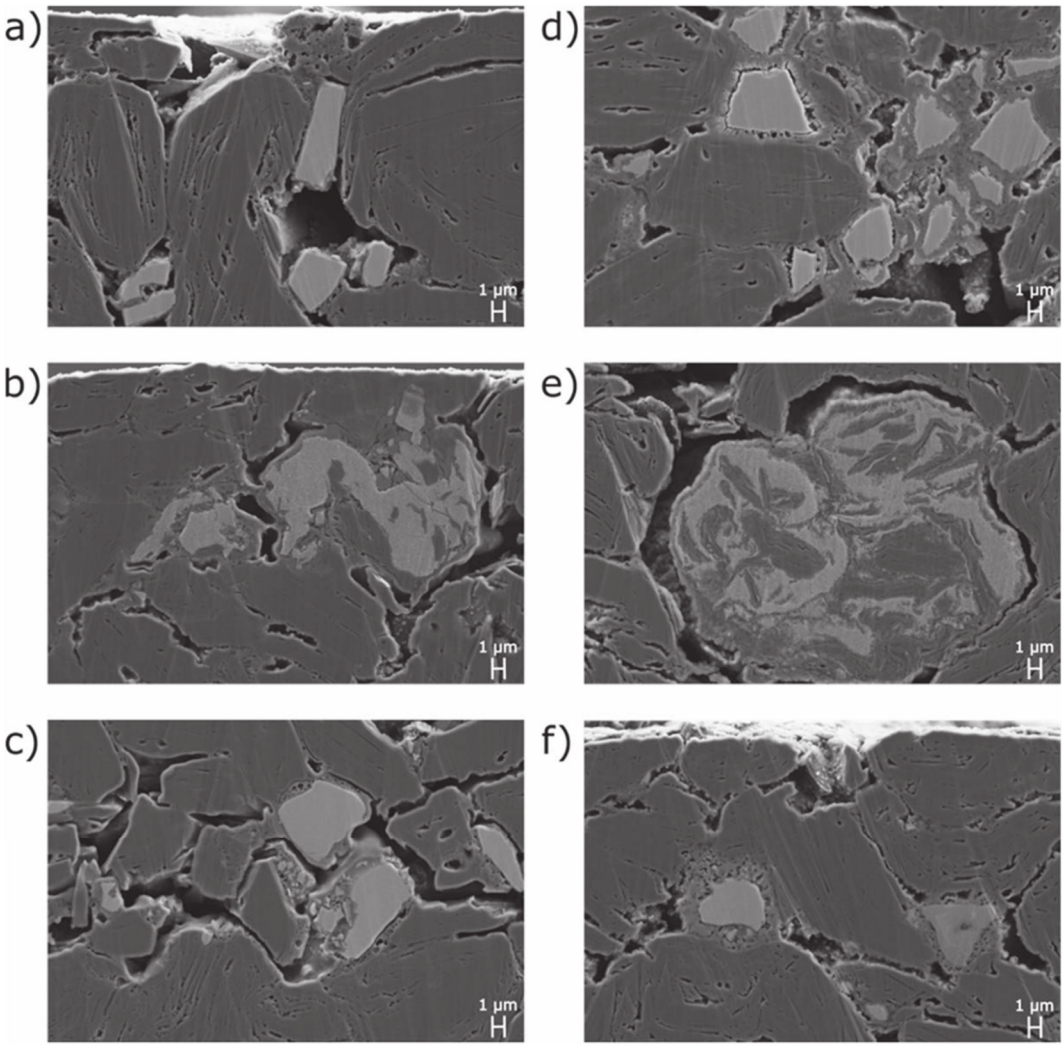

Figure 9. SEM of cross-sections from anodes (a)–(c) from fresh cells and (d)–(f) cells aged at 45 °C. (a), (d) cell type A, (b), (e) cell type B, (c), (f) cell type C. Representative Si and graphite particles were shown in detail to demonstrate SEI growth after aging. No particle cracking was observed in any of the Si particles studied. Furthermore, none of the graphite particles showed delamination.

Journal of The Electrochemical Society, 2022 **169** 050533

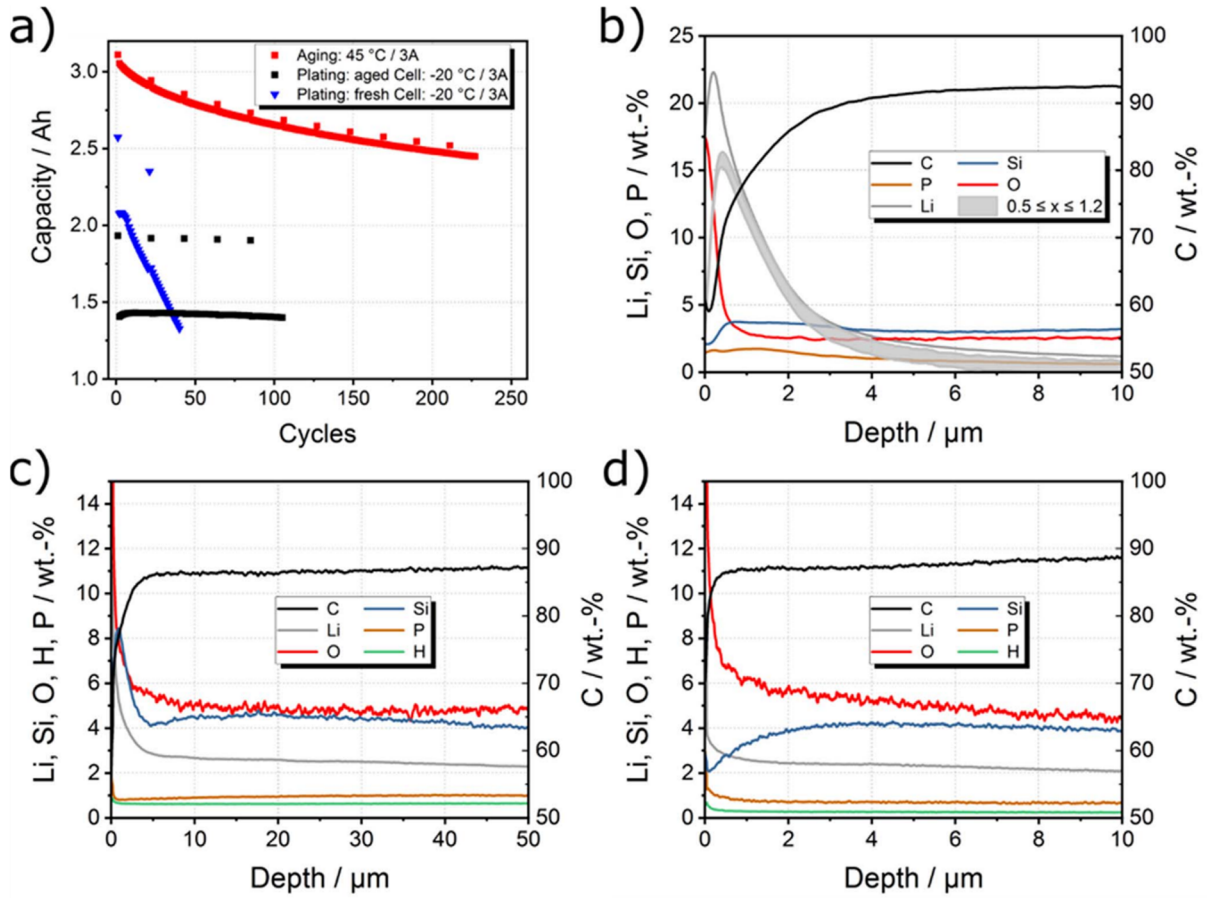

Figure 10. (a) Electrochemical aging of cell type A and (b)–(d) GD-OES depth profiles of the anodes; (b) aging at −20 °C (blue) shows linear capacity loss and metallic Li is detectable on anode surface; (c) aging at 45 °C shows logarithmic decrease in capacity and increase in Li amount in anode bulk; (d) after aging at 45 °C and −20 °C (black) no Li deposition was observed.

CC–CV until SOC = 80%. After each charging step, the cells were subjected to a three-hour relaxation at the respective temperature.

Cell A, which is designed for high charging currents due to a high porosity, low anode coating thickness, and small Si particles, has only a small voltage plateau even at temperatures of −10 °C indicating a very low amount of reversible Li plating. In contrast, cells B and C show pronounced Li plating at −10 °C, which could not completely re-intercalate during a 3 h rest time. Both cells also show a voltage plateau at 0 °C, which indicates reversible Li plating. Cell B exhibits a voltage plateau due to Li re-intercalation at 0 °C, which is completed only after ∼2 h.

Aging behaviour of the fresh cells at 45 °C and at low temperatures.—Figure 7 shows the DVAs of cell A–C during cycling aging at 45 °C. The capacities were normalized to a SOC of 100% in each step to illustrate the respective capacity with respect to Si. The peaks G_1, G_2, S_1, and S_2, which have already been assigned to graphite and Si by DVA with half cells in Fig. 3, can be clearly identified for cell types A–C.

Again, it is observed that in cell type A, Si has the highest share of the cell capacity. During cycling at 45 °C of cell A, G_2 and S_1 shift to lower SOCs and the intensity of S_1 decreases. S_2 also shifts to lower SOCs, however, the peak height increases, indicating that the anode potential rises more steeply at low SOC. The fraction of capacity provided by Si decreases not only in absolute terms, however, also in relation to graphite.

For cell type B, the quantification of the Si capacity fraction decrease during aging is not possible. At the beginning, no reduction in capacity of Si is detectable. While S_1 shifts to lower SOCs in cell types A and C during the first check-up cycles, it remains at the same SOC in cell type B. However, the DVA becomes increasingly diffuse during aging, so that G_2 and S_1 are no longer discernible.

The capacity fraction of Si in cell type C decreases rapidly within the first 60 cycles to such an extent that S1 is barely detectable after the 60th cycle. For both cell types A and C, there is a logarithmic decrease of the capacity, with the greatest losses occurring within the first 60 cycles. The DVA shows that in cell types A and C a decrease in Si capacity occurs, therefore, in both cells LAAM is part of the aging mechanism. In cell type B, however, the capacity seems to decrease predominantly due to LLI.

For further investigation, coin half cells were built from fresh and aged anodes of cell types A–C. The potential curves of a graphite anode and the SiGr-2 composite anode, which both have an areal capacity of 3 mAh cm^{-2}, are shown in Fig. 8d. The potential profile of graphite displays the intercalation steps in the voltage range of 0.01 − 0.2 V vs Li/Li^+. At higher potentials, graphite is hardly electrochemically active, thus the potential increases sharply. The Si content in the active material of the SiGr-2 composite is 5.8%. Si is mainly electrochemically active in the potential range of 0.2 V − 1.0 V vs Li/Li^+, therefore the SiGr-2 composite anode provides high capacity in this potential range. The fact that graphite and Si are active in different potential ranges can be used to study the aging of the anodes.

Journal of The Electrochemical Society, 2022 **169** 050533

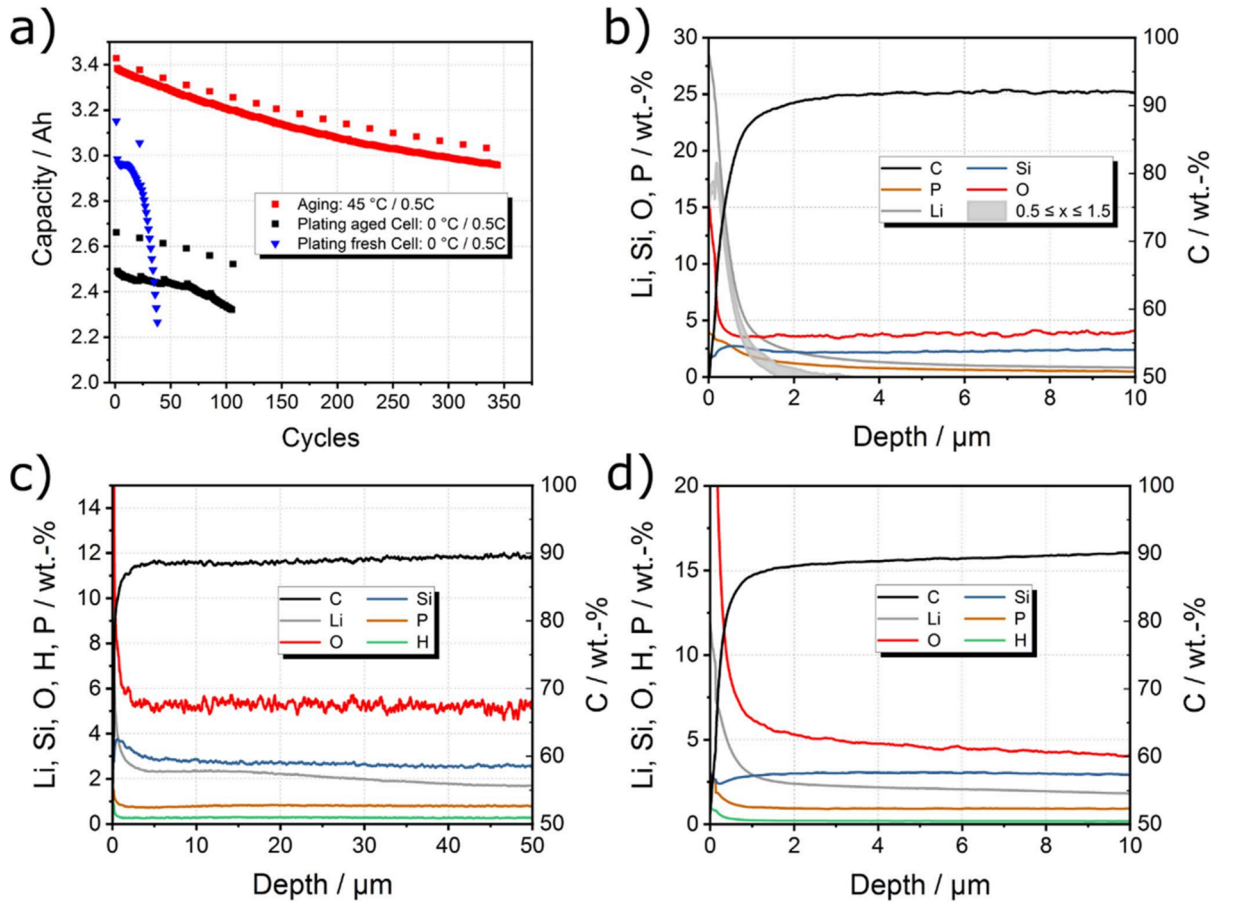

Figure 11. (a) Electrochemical aging of cell type B and (b)–(d) GD-OES depth profiles of the anodes; (b) aging at 0 °C (blue) shows exponential capacity loss and metallic Li is detectable on anode surface; (c) aging at 45 °C shows linear decrease in capacity and increase in Li amount in anode bulk; (d) after aging at 45 °C and 0 °C (black) no Li deposition is detected.

In Figs. 8a–8c, the potential curves of the fresh anodes harvested from opened cells A–C are shown in red and those of the aged anodes in black. The anode from the aged cell A provides the same areal capacity in the potential range 0.01 − 0.2 V vs Li/Li^+ as the fresh anode as indicated by coinciding black and red curve until ∼2.7 mAh cm^{-2} (Fig. 8a). However, the capacity in the range 0.2 − 1.0 V vs Li/Li^+ has decreased during aging, resulting in a total capacity loss of 10%. However, the potential rise of the aged anode from 0.2 V is less steep than that of the graphite anode in Fig. 8d, indicating that not all Si capacity is lost. DVA of cell type A in Fig. 7 also shows that Si capacity, visible at peak position S_1 and S_2, decreases during aging. However, both peaks are still detectable at SOH = 80%, which indicates a remaining capacity of the Si as well.

For cell B (Fig. 8b), the capacity of the anode from the aged cell decreased only marginally compared to the anode from the fresh cell. Small losses of graphite capacity as well as losses of Si capacity are observable. The total capacity loss of the anode from the aged cell is only 5.5%. The DVA of cell type B gives little indication of the aging of the anode due to the peaks becoming indistinct. Therefore, the aging mechanism can be more accurately determined with the Post-Mortem built coin half-cells.

In contrast, Si in the aged cell C is hardly electrochemically active anymore (Fig. 8c). The potential curve of the anode from the aged cell C is very similar to that of graphite (Fig. 8d). The anode from the aged cell C still contains 81% of the capacity of the fresh anode. Since the cell capacity of the aged full cell is only 80% of the original capacity, any loss of anode capacity of less than 20% implies that a loss of available Li must have occurred as well. Almost all of the capacity loss in cell C can be accounted for by LAAM. The results found with coin half cells at cell type C can be confirmed with DVA of the full cell. In this cell, too, the Si capacity decreases sharply, so that peaks S_1 and S_2 are barely detectable after aging. In cell type A, on the other hand, LAAM and LLI contribute approximately in equal parts to capacity losses, and in cell B LLI is almost exclusively responsible for the capacity loss.

Additionally, cross-sections of the anodes from the fresh cells and cells aged at 45 °C were examined in SEM (Fig. 9). No particle cracking was observed in any of the Si particles studied. Furthermore, none of the graphite particles showed exfoliation. Si incorporated in the graphite matrix most likely serves as a buffer during charging, resulting in less mechanical stress on the Si particles.

Si particles in the anodes from cell types A and C show significantly increased film formation with almost 1 μm layer thickness after aging (Figs. 9d, 9f). These thick films could be SEI layers which cause an increased charge transfer impedance. Thicker SEI films impede lithiation and de-lithiation of Si particles, resulting in LAAM. We note that the anode samples were exposed to air during the transfer from the glovebox to the SEM. However, since the anodes from the fresh cells do not show significant film formation on the Si particles in contrast to the anodes from the aged cells, the air did most likely have no significant effect on these results.

Cell type B, which showed LAAM to a small extent in half cell tests, also shows only a very thin SEI layer and no particle cracking

Journal of The Electrochemical Society, 2022 **169** 050533

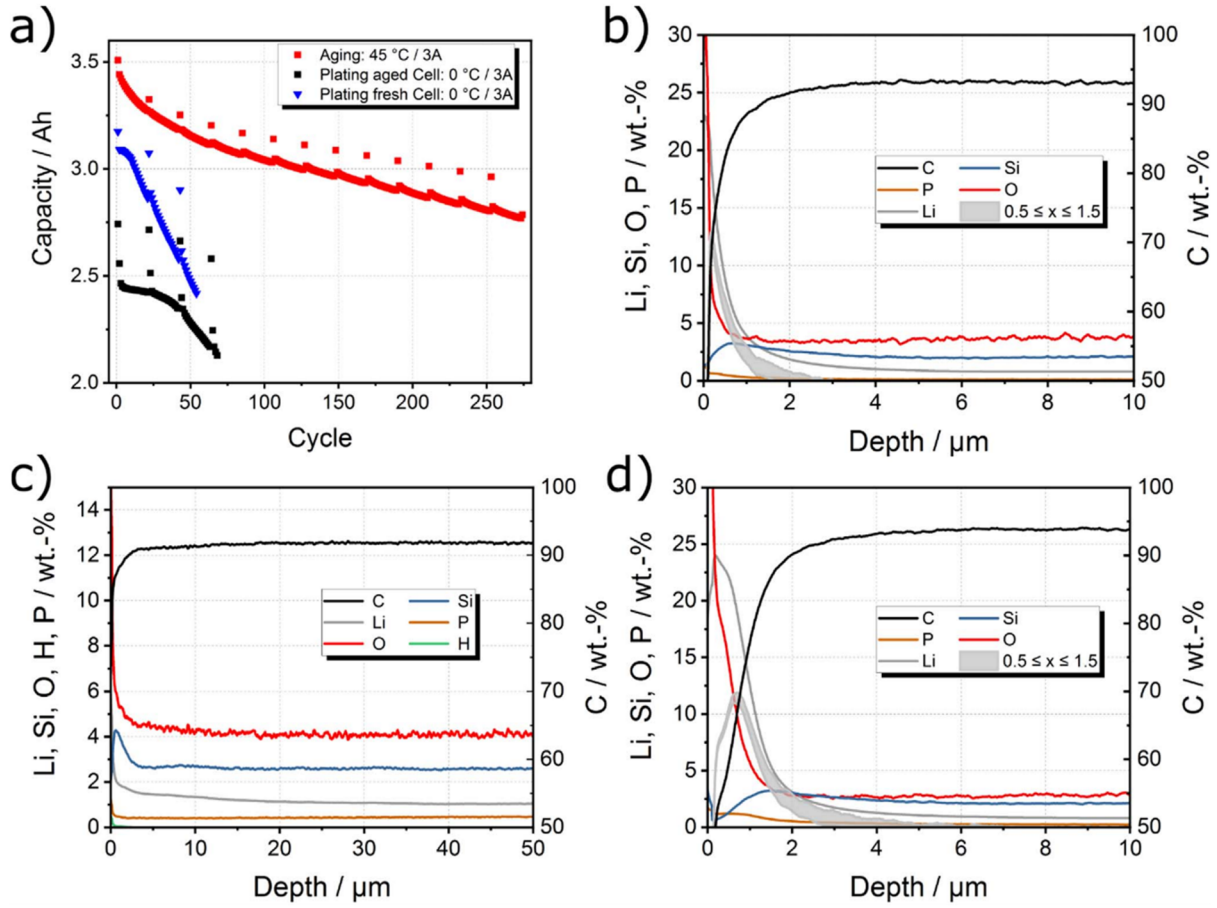

Figure 12. (a) Electrochemical aging of cell type C and (b)–(d) GD-OES depth profiles of the anodes; (b) aging at 0 °C (blue) shows linear capacity loss and metallic Li is detectable on anode surface; (c) aging at 45 °C shows logarithmic decrease in capacity and increase in Li amount in anode bulk; (d) after aging at 45 °C and 0 °C (black) Li deposition is observed on the anode surface.

in cross-section (Fig. 9e). The capacity profile of the fresh cells during aging at low temperature is shown in Figs. 10a, 11a, and 12b (blue). In all cases, the cell capacity drops sharply within 50 cycles. While cells A and C have a linear capacity decrease, the aging of cell B is accelerated most likely due to pore clogging.[52]

Figures 10b, 11b, 12b show the depth profiles of the anode surface of cells A, B and C, which were obtained after opening the cells cycled at low temperatures. The depth profiles show a high amount of detected Li for each cell. Using the method developed in the present study, the amount of metallic Li is plotted as a corridor in the respective depth profiles. Due to the different conditions under which the cells start to show irreversible Li deposition, a direct comparison of the GD-OES depth profiles is not possible.

GD-OES depth profiles of the anodes from the cells A–C cycled at 45 °C are shown in Figs. 10c, 11c, 12c, respectively. On the anodes from all aged cells, the total amount of Li in the electrode, obtained by integration of the GD-OES depth profile, is higher than in the anodes from the fresh cells. This result is confirmed by ICP-OES analysis. Due to irreversible Li consumption during aging by SEI formation and loss of Si particles containing Li, the amount of Li in the anode increases steadily. This is consistent with 1.5 Ah 18650 cells and 16 Ah pouch cells where the amount of Li increased in the anodes while it decreased in the cathodes with aging.[53,54]

From the half cell tests (Fig. 8) and the cross sections of the anodes (Fig. 9), it can be concluded that cell type B predominantly suffers from loss of capacity due to irreversible Li consumption. Cell A and C lose capacity due to the electrochemical inactivity of the Si. This is most likely caused by the pronounced layer formation, which hinders Li diffusion into the particles and consumes Li.

Susceptibility to Li plating of pre-aged cells.—To investigate susceptibility to Li plating of cells pre-aged at 45 °C, pre-aged cells were subjected to the low-temperature aging that resulted in Li deposition in the unaged cells.

The capacity profiles during cycling of the pre-aged cells are shown as black squares in Figs. 10a–12a. The GD-OES depth profiles of the second-life anodes are shown in subfigure Figs. 10d–12d.

Cell type A, which could only be brought to Li deposition at −20 °C, shows no capacity losses during second-life aging at −20 °C after previous aging at 45 °C (black data points in Fig. 10a). GD-OES depth profiling does not show Li deposition on the anode surface (Fig. 10d), however, the Li content in the anode bulk is similarly high as that of the cell aged at 45 °C (Fig. 10c). This suggests Li plating cannot be provoked in cell type A anymore due to high irreversible Li consumption in the anode after cycling at 45 °C.

In the pre-aged cell type B, the difference compared to cell A is the slow decrease in capacity during cycling at 0 °C (Fig. 11a). Nevertheless, the cell can withstand 100 cycles at 0 °C without a sharp capacity drop. In GD-OES depth profiling, a high Li content could only be detected in the anode bulk but not on the anode surface (Fig. 11d).

During the cycling at low temperature of the pre-aged cell type C, the cell capacity of cell C dropped faster so that the test was terminated prematurely (Fig. 12a). The GD-OES depth profile shows

Journal of The Electrochemical Society, 2022 **169** 050533

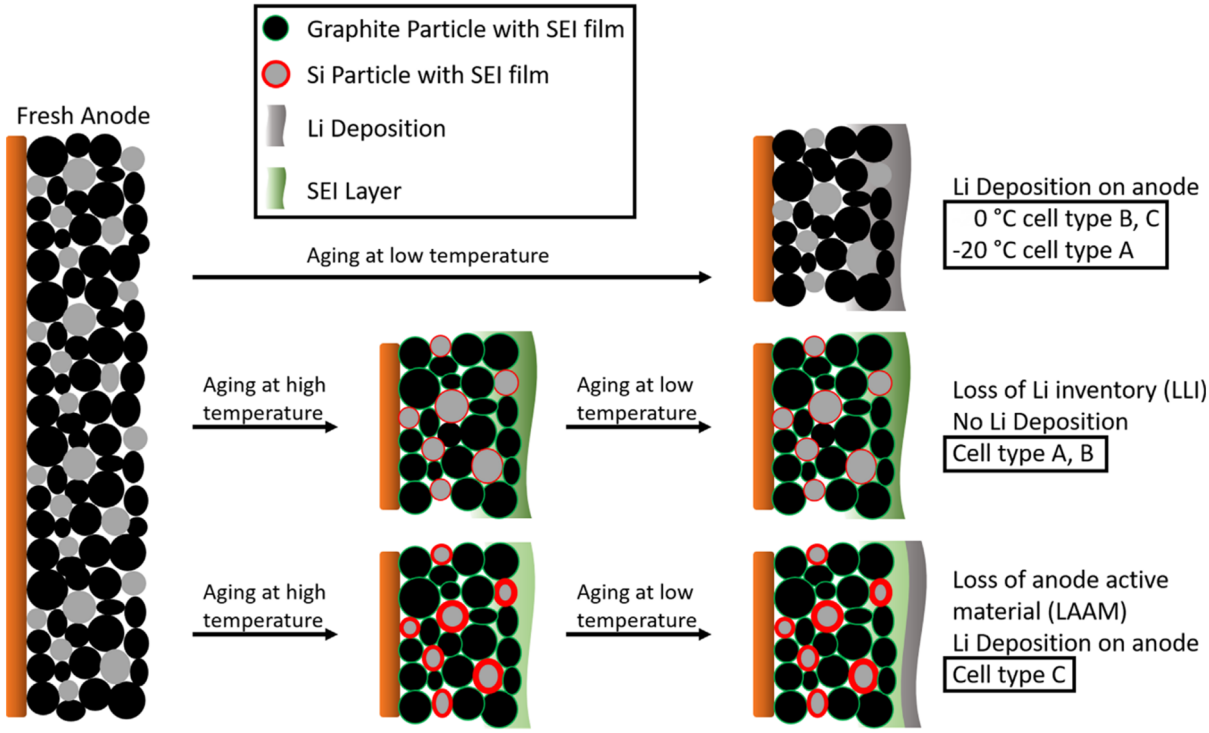

Figure 13. Schematic representation of Li deposition on fresh anodes (top), aging at high temperatures where LLI occurs and Li deposition does not occur in subsequent aging at low temperatures (middle), and loss of anode active material during aging at high temperatures causing Li deposition to occur in subsequent aging at low temperatures (bottom).

Li deposition on the anode surface (Fig. 12d). In contrast to cell A and B, during aging at 45 °C the Si component was significantly degraded for cell type C. Due to the inactivity of Si, the anode potential decreased faster, and went below 0 V vs Li/Li^+, allowing Li plating thermodynamically.

A schematic summary the results of this work is shown in Fig. 13. Cell type A, which showed Li deposition on the anode only at very low temperatures due to high anode porosity, thin anode coating, and small Si particles, showed no further capacity decrease under Li deposition conditions after irreversible Li loss at 45 °C. Cell type B, which showed mainly LLI and hardly any LAAM during aging, still showed tendencies to Li deposition at low temperatures, however, the cycling stability was significantly prolonged compared to fresh cell B at 0 °C. Cell type C exhibited the most pronounced LAAM during aging. Cycling at low temperatures showed only minor differences between the fresh and the aged cell with regard to their tendencies to Li plating on the anode.

Conclusions

A new Post-Mortem GD-OES depth profiling method was developed which is able to determine the minimum amount of metallic Li on Si/graphite anodes. Due to the unknown O content in the SiO_x particles, which is included in our calculation, a corridor was defined within which the minimum Li metal amount of an anode containing a Si compound is located.

The anode coating thicknesses from 18 types of commercial cylindrical Li-ion cells showed clear trends with the specific energies of the respective cells. Distinguishing between cells with graphite anodes and Si/graphite anodes showed that higher Si amounts lead to thinner anodes and therefore to more windings and higher specific energies in cylindrical cells.

Three types of commercial 18650 cells with Si/graphite anodes were characterized in detail regarding their cell chemistry and electrode properties. The cells were cycling aged at 45 °C and the aging behavior was analyzed using SEM, DVA, GD-OES, and coin half cells. GD-OES depth profiling did not show Li plating on the anodes of the cells cycled at 45 °C, however, for cells cycled at low temperatures. Li deposition occurs in high power cells as low as −20 °C, while high energy cells exhibit Li deposition as low as 0 °C. A higher anode porosity, smaller Si particles, and a thinner anode coating were observed in the high power cell.

After cycling aging at 45 °C, all three cell types were subsequently cycled under conditions which had lead to Li deposition in case of the fresh cells. We found that cells whose anode active material is partly deactivated (e.g. by film growth on the Si particles) during aging at 45 °C (LAAM) are still at risk of Li deposition in the aged state. Cells whose anode active material remains intact, however which suffer from loss of cyclable lithium (LLI), show a significantly reduced tendency to Li deposition. In contrast to anodes without Si, our results indicate that the Si compound can be responsible a change of the susceptibility to Li plating by loss of anode active material. We stress that knowledge of the aging mechanism and the tendency of the cell to Li deposition is critical to the operating condition of a cell in second-life applications. Therefore, it is very important that the aging mechanisms are known.

Our new GD-OES based method in combination with complementary methods results yielded deep insights into the aging behavior of state-of-the-art Li-ion cells with Si/graphite anodes. Further studies into this direction and further method validation are underway in our labs.

Acknowledgments

Funding of the project CharLiSiKo by the German Federal Ministry of Education and Research (BMBF) under contract n° 03XP0333A and project management by Forschungszentrum Jülich

(PTJ) are gratefully acknowledged. We thank C. Pfeifer (ZSW) for SEM/EDX and G. Arnold (ZSW) for ICP-OES measurements.

ORCID

Marius Flügel https://orcid.org/0000-0002-9792-0414
Margret Wohlfahrt-Mehrens https://orcid.org/0000-0002-5118-5215
Thomas Waldmann https://orcid.org/0000-0003-3761-1668

References

1. F. Luo, B. Liu, J. Zheng, G. Chu, K. Zhong, H. Li, X. Huang, and L. Chen, *J. Electrochem. Soc.*, **162**, A2509 (2015).
2. X. H. Liu, L. Zhong, S. Huang, S. X. Mao, T. Zhu, and J. Y. Huang, *ACS Nano*, **6**, 1522 (2012).
3. J. Li, A. K. Dozier, Y. Li, F. Yang, and Y.-T. Cheng, *J. Electrochem. Soc.*, **158**, A689 (2011).
4. G. G. Eshetu, H. Zhang, X. Judez, H. Adenusi, M. Armand, S. Passerini, and E. Figgemeier, *Nat. Commun.*, **12**, 1 (2021).
5. K. Richter, T. Waldmann, M. Memm, M. Kasper, and M. Wohlfahrt-Mehrens, *J. Electrochem. Soc.*, **165**, A3602 (2018).
6. K. Richter, T. Waldmann, M. Kasper, C. Pfeifer, M. Memm, P. Axmann, and M. Wohlfahrt-Mehrens, *J. Phys. Chem. C*, **123**, 18795 (2019).
7. K. Richter, T. Waldmann, N. Paul, N. Jobst, R.-G. Scurtu, M. Hofmann, R. Gilles, and M. Wohlfahrt-Mehrens,, *ChemSusChem*, **13**, 529 (2020).
8. P. Kuntz, O. Raccurt, P. Azaïs, K. Richter, T. Waldmann, M. Wohlfahrt-Mehrens, M. Bardet, A. Buzlukov, and S. Genies, *Batteries*, **7**, 48 (2021).
9. M. J. Lain, J. Brandon, and E. Kendrick,, *Batteries*, **5**, 64 (2019).
10. M. Wetjen, D. Pritzl, R. Jung, S. Solchenbach, R. Ghadimi, and H. A. Gasteiger, *J. Electrochem. Soc.*, **164**, A2840 (2017).
11. M. Wetjen, S. Solchenbach, D. Pritzl, J. Hou, V. Tileli, and H. Gasteiger, *J. Electrochem. Soc.*, **7**, 1503 (2018).
12. V. Müller, R.-G. Scurtu, K. Richter, T. Waldmann, M. Memm, M. A. Danzer, and M. Wohlfahrt-Mehrens, *J. Electrochem. Soc.*, **166**, A3796 (2019).
13. M. M. Kabir and D. E. Demirocak, *Int. J. Energy Res.*, **41**, 1963 (2017).
14. T. Joshi, K. S. Eom, G. Yushin, and T. F. Fuller, *J. Electrochem. Soc.*, **161**, A1915 (2014).
15. M. Dubarry, B. Y. Liaw, M.-S. Chen, S.-S. Chyan, K.-C. Han, W.-T. Sie, and S.-H. Wu, *J. Power Sources*, **196**, 3420 (2011).
16. M. Dubarry, V. Svoboda, R. Hwu, and B. Y. Liaw, *Electrochem. Solid-State Lett.*, **9**, A454 (2006).
17. C. R. Birkl, M. R. Roberts, E. McTurk, P. G. Bruce, and D. A. Howey, *J. Power Sources*, **341**, 373 (2017).
18. J. Christensen and J. Newman, *J. Solid State Electrochem.*, **10**, 293 (2006).
19. R. Deshpande, M. Verbrugge, Y.-T. Cheng, J. Wang, and P. Liu, *J. Electrochem. Soc.*, **159**, A1730 (2012).
20. T. Waldmann, M. Wilka, M. Kasper, M. Fleischhammer, and M. Wohlfahrt-Mehrens, *J. Power Sources*, **262**, 129 (2014).
21. J. C. Burns, D. A. Stevens, and J. R. Dahn, *J. Electrochem. Soc.*, **162**, A959 (2015).
22. T. Waldmann, J. B. Quinn, K. Richter, M. Kasper, A. Tost, A. Klein, and M. Wohlfahrt-Mehrens, *J. Electrochem. Soc.*, **164**, A3154 (2017).
23. M. Fleischhammer, T. Waldmann, G. Bisle, B.-I. Hogg, and M. Wohlfahrt-Mehrens, *J. Power Sources*, **274**, 432 (2015).
24. T. Waldmann and M. Wohlfahrt-Mehrens, *Electrochim. Acta*, **230**, 454 (2017).
25. A. A. Abd-El-Latif, P. Sichler, M. Kasper, T. Waldmann, and M. Wohlfahrt-Mehrens, *Batter. Supercaps*, **4**, 1135 (2021).
26. T. Waldmann, B.-I. Hogg, and M. Wohlfahrt-Mehrens, *J. Power Sources*, **384**, 107 (2018).
27. M. Weiss et al., *Adv. Energy Mater.*, **11**, 2101126 (2021).
28. K. P. C. Yao, J. S. Okasinski, K. Kalaga, J. D. Almer, and D. P. Abraham, *Adv. Energy Mater.*, **9**, 1803380 (2019).
29. N. Ding, J. Xu, Y. X. Yao, G. Wegner, X. Fang, C. H. Chen, and I. Lieberwirth, *Solid State Ion.*, **180**, 222 (2009).
30. N. Ghanbari, T. Waldmann, M. Kasper, P. Axmann, and M. Wohlfahrt-Mehrens, *J. Phys. Chem. C*, **120**, 22225 (2016).
31. N. Ghanbari, T. Waldmann, M. Kasper, P. Axmann, and M. Wohlfahrt-Mehrens, *ECS Electrochem. Lett.*, **4**, A100 (2015).
32. S. P. Rangarajan, Y. Barsukov, and P. P. Mukherjee, *J. Mater. Chem. A*, **7**, 20683 (2019).
33. P. P. Paul et al., *Energy Environ. Sci.*, **14**, 4979 (2021).
34. D. P. Finegan et al., *Energy Environ. Sci.*, **13**, 2570 (2020).
35. H. Ge, T. Aoki, N. Ikeda, S. Suga, T. Isobe, Z. Li, Y. Tabuchi, and J. Zhang, *J. Electrochem. Soc.*, **164**, A1050 (2017).
36. J. Arai, Y. Okada, T. Sugiyama, M. Izuka, K. Gotoh, and K. Takeda, *J. Electrochem. Soc.*, **162**, A952 (2015).
37. C. Birkenmaier, B. Bitzer, M. Harzheim, A. Hintennach, and T. Schleid, *J. Electrochem. Soc.*, **162**, A2646 (2015).
38. J. B. Quinn, T. Waldmann, K. Richter, M. Kasper, and M. Wohlfahrt-Mehrens, *J. Electrochem. Soc.*, **165**, A3284 (2018).
39. T. Waldmann, B.-I. Hogg, M. Kasper, S. Grolleau, C. Gutiérrez Couceiro, K. Trad, B. P. Matadi, and M. Wohlfahrt-Mehrens,, *J. Electrochem. Soc.*, **163**, A1232 (2016).
40. T. Waldmann, R.-G. Scurtu, K. Richter, and M. Wohlfahrt-Mehrens, *J. Power Sources*, **472**, 228614 (2020).
41. J. Schmitt, M. Schindler, and A. Jossen, *J. Power Sources*, **506**, 230240 (2021).
42. B. T. Young, D. R. Heskett, C. C. Nguyen, M. Nie, J. C. Woicik, and B. L. Lucht, *ACS Appl. Mater. Interfaces*, **7**, 20004 (2015).
43. C. Cao, I. I. Abate, E. Sivonxay, B. Shyam, C. Jia, B. Moritz, T. P. Devereaux, K. A. Persson, H.-G. Steinrück, and M. F. Toney, *Joule*, **3**, 762 (2019).
44. Q. Li, X. Liu, X. Han, Y. Xiang, G. Zhong, J. Wang, B. Zheng, J. Zhou, and Y. Yang, *ACS Appl. Mater. Interfaces*, **11**, 14066 (2019).
45. B. Philippe, R. Dedryvère, M. Gorgoi, H. Rensmo, D. Gonbeau, and K. Edström, *Chem. Mater.*, **25**, 394 (2013).
46. S. C. Jung, H.-J. Kim, J.-H. Kim, and Y.-K. Han, *J. Phys. Chem. C*, **120**, 886 (2016).
47. A. Nakagawa, N. Kuwata, Y. Matsuda, and J. Kawamura, *J. Phys. Soc. Jpn.*, **79**, 98 (2010).
48. C. Uhlmann, J. Illig, M. Ender, R. Schuster, and E. Ivers-Tiffée, *J. Power Sources*, **279**, 428 (2015).
49. C. von Lüders, V. Zinth, S. V. Erhard, P. J. Osswald, M. Hofmann, R. Gilles, and A. Jossen, *J. Power Sources*, **342**, 17 (2017).
50. C. Hogrefe, S. Hein, T. Waldmann, T. Danner, K. Richter, A. Latz, and M. Wohlfahrt-Mehrens, *J. Electrochem. Soc.*, **167**, 140546 (2020).
51. F. Holtstiege, P. Bärmann, R. Nölle, M. Winter, and T. Placke, *Batteries*, **4**, 4 (2018).
52. X.-G. Yang, Y. Leng, G. Zhang, S. Ge, and C.-Y. Wang, *J. Power Sources*, **360**, 28 (2017).
53. T. Waldmann, N. Ghanbari, M. Kasper, and M. Wohlfahrt-Mehrens, *J. Electrochem. Soc.*, **162**, A1500 (2015).
54. A. Iturrondobeitia, F. Aguesse, S. Genies, T. Waldmann, M. Kasper, N. Ghanbari, M. Wohlfahrt-Mehrens, and E. Bekaert, *J. Phys. Chem. C*, **121**, 21865 (2017).

3.2. Onset Shift of Li Plating on Si/Graphite Anodes with increasing Si content

Reprinted with permission from:

M. Flügel [a], M. Bolsinger [b], M. Marinaro [a], V. Knoblauch [b], M. Hölzle [a], M. Wohlfahrt-Mehrens [a], T. Waldmann [a], 2023 *J. Electrochem. Soc.* **170** 060536

[a] ZSW – Zentrum für Sonnenenergie- und Wasserstoff-Forschung, Baden-Württemberg, Helmholzstraße 8, 89081 Ulm, Germany

[b] Aalen University of Applied Sciences (AU), Materials Research Institute, Beethovenstraße 1, 73430 Aalen, Germany

© 2023 The Author(s). Published on behalf of The Electrochemical Society by IOP Publishing Limited. This is an open access article distributed under the terms of the Creative Commons Attribution 4.0 License (CC BY, http://creativecommons.org/licenses/by/4.0/), which permits unrestricted reuse of the work in any medium, provided the original work is properly cited.

DOI: https://doi.org/10.1149/1945-7111/acdda3

Individual Contribution

M. Flügel	Conceptualization, Methodology, Validation, Investigation, Writing - Original Draft, Visualization
M. Bolsinger	Investigation, Resources, Visualization, Writing – Review & Editing
M. Marinaro	Methodology, Writing – Review & Editing
V. Knoblauch	Writing – Review & Editing, Supervision
M. Hölzle	Writing – Review & Editing, Supervision
M. Wohlfahrt-Mehrens	Writing – Review & Editing, Supervision
T. Waldmann	Conceptualization, Writing – Review & Editing, Supervision, Project administration, Funding acquisition

Summary

The second publication focuses on the impact of the Si content in anodes on their susceptibility to Li plating. Five different series of anodes with varying Si contents, along with corresponding cathodes, were coated on a pilot scale. The reversible anode areal capacities were kept constant, resulting in reduced coating thickness for higher Si contents. To account for irreversible capacity losses in the anodes and to achieve pouch full cells with different Si contents and fixed N/P ratios, the cathode areal capacities were adjusted to match those of the anodes. The porosity and tortuosity of the anodes were closely matched to exclude their influence on the results.

During the study, a linear relationship between the Si capacity contribution to the total anode capacity and the irreversible capacity losses during the formation cycles was observed. The fast charging performance of the cells was compared at temperatures of 25 °C and 0 °C. At 25 °C, cells with low Si content and a graphite cell filled with VC-containing electrolyte exhibited the best performance, with capacity retention declining with increasing Si content. However, at 0 °C, the cell with the highest Si content, along with the graphite cell, showed the highest capacity retention at the highest charging rate of 2C. Cells with lower Si contents demonstrated lower capacity retention, indicating that reducing the anode thickness is most beneficial for charge rate capability.

Voltage relaxation experiments conducted after charging at 0 °C revealed a critical charging rate at which reversible Li plating could first be detected, except for the SiG20.8 cell. The critical charging rate increased with higher Si content, indicating that cells with higher Si content and thinner anodes were more resistant to Li plating at low temperatures. To further investigate irreversible Li plating, a brief aging procedure at 0 °C was followed by post-mortem analysis using GD-OES and SEM. The results from voltage relaxation, Li stripping, SEM measurements, and GD-OES depth profiling were in agreement and demonstrated clear trends in the reduced susceptibility of Si/graphite anodes to Li plating at 0 °C for the same anode areal capacities as Si content increased.

Optical microscopy under an inert gas atmosphere was employed to examine the presence of Li deposition at different SOC levels. The trend observed at 0°C, where higher Si contents and thinner anodes resulted in increased resistance to Li plating, was also observed at 23°C.

This study provides evidence that Si compounds in graphite anodes can have a positive effect by inhibiting Li plating, although higher Si contents accelerate aging at higher C-rates. The Si content is likely to shift the temperature of the minimum aging rate in Arrhenius plots. Additionally, the thinner electrode coatings resulting from Si in the anodes reduce the impedance of battery cells by providing additional available electrode surface within a given cell size.

Overall, the findings of this research provide valuable insights into the relation between Si content in anodes and the susceptibility to Li plating, as well as the impact on fast charging performance and aging characteristics of battery cells. These results can contribute to the development of improved battery technologies and guide future investigations in this field.

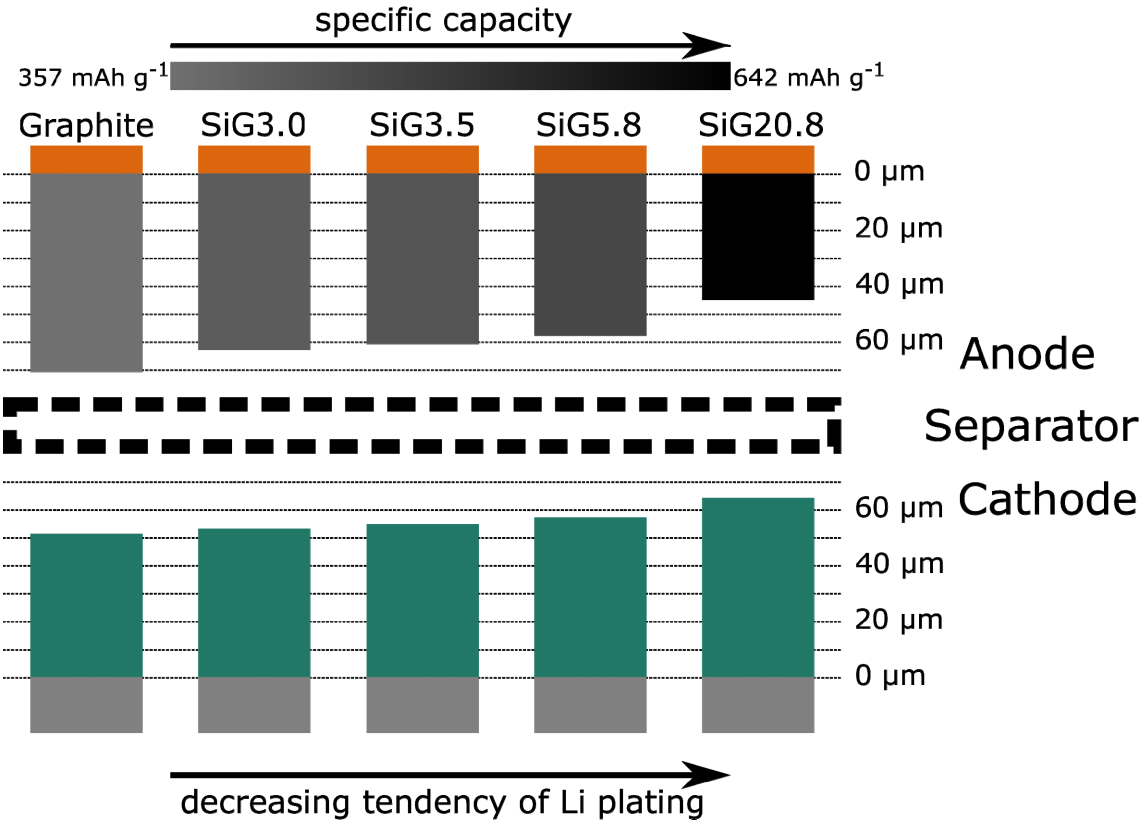

Figure 10: Schematic illustration of the thicknesses of the anodes and cathodes which have been paired together [3].

Journal of The Electrochemical Society, 2023 **170** 060536

Onset Shift of Li Plating on Si/Graphite Anodes with Increasing Si Content

Marius Flügel,[1] Marius Bolsinger,[2] Mario Marinaro,[1] Volker Knoblauch,[2] Markus Hölzle,[1] Margret Wohlfahrt-Mehrens,[1,3] and Thomas Waldmann[1,3,z]

[1]*Zentrum für Sonnenenergie- und Wasserstoff-Forschung Baden-Württemberg (ZSW), D-89081 Ulm, Germany*
[2]*Aalen University of Applied Sciences (AU), Materials Research Institute, D-73430 Aalen, Germany*
[3]*Helmholtz Institute Ulm for Electrochemical Energy Storage (HIU), Helmholtzstraße 11, D-89081 Ulm, Germany*

Mixing graphite with Si particles in anodes of Li-ion batteries provides increased specific energy. In addition, higher Si contents lead to thinner anode coatings at constant areal capacity. In the present study, we systematically investigated the influence of the Si content on the susceptibility of Li plating on Si/graphite anodes. Si/graphite anodes with Si contents from 0 to 20.8 wt% combined with NMC622 cathodes were manufactured on pilot-scale. After initial characterization in coin half cells and by SEM, pouch full cells with fixed N/P ratios were built. Rate capability at different temperatures, and Post-Mortem analysis were carried out. Results from voltage relaxation, Li stripping, SEM measurements, glow discharge optical emission spectroscopy (GD-OES) depth profiling, and optical microscopy were validated against each other. A decreasing susceptibility to Li plating with increasing Si content in the anodes could be clearly observed. A critical C-rate was defined, at which Li plating was detected for the first time. It was also found that at 0 °C the critical C-rate increases with increasing Si contents. At 23 °C the SOC at which Li dendrites were first observed on the anode also increased with higher Si content.
© 2023 The Author(s). Published on behalf of The Electrochemical Society by IOP Publishing Limited. This is an open access article distributed under the terms of the Creative Commons Attribution 4.0 License (CC BY, http://creativecommons.org/licenses/by/4.0/), which permits unrestricted reuse of the work in any medium, provided the original work is properly cited. [DOI: 10.1149/1945-7111/acdda3]

Manuscript submitted February 23, 2023; revised manuscript received May 25, 2023. Published June 22, 2023.

Since the initial days of Li-ion batteries, the specific anode capacity was limited to a theoretical value of 372 mAh g^{-1},[1] as graphite was the only material of choice and can only reversibly store one Li atom per six C atoms. Silicon as an anode material, however, allows the storage of nearly four Li atoms per Si atom in $Li_{15}Si_4$, resulting in a theoretical capacity of 3,579 mAh g^{-1} at room temperature.[2] However, the highest possible alloying level of Si is accompanied by a strong volume expansion of almost 300%,[3] which leads to particle cracking, repeated SEI formation, and even electrode delamination.[4–6] Blending lower amounts with Si with graphite is one elegant way to mitigate these issues.[7–10]

Recent studies have proven that Si compounds are already incorporated in the anodes of commercially available cells.[11,12] After the method development by Richter et al., it became possible to determine the Si content with glow discharge optical emission spectroscopy (GD-OES) depth profiling measurements of anodes from Post-Mortem analysis.[13,14] Our recent study with Post-Mortem analysis of 18 cylindrical cells showed that commercial cells contain up to 4 wt% Si in the anode.[15] Si compounds in the anode can either lead to higher specific energy when the thickness of the electrode is kept constant or to thinner anode coatings at the same anode areal capacity.[15] For example, the anode coating thickness at a desired energy density of 190 Wh kg^{-1} can be reduced from 80 μm for a pure graphite coating to 53 μm in case of a Si/graphite coating with 3.5 wt% Si. Alternatively, the specific energy can be increased from 160 to 190 Wh kg^{-1} at a constant anode thickness of 53 μm by increasing the Si content from 0.8 wt% to 3.5 wt%.[15]

Studies on the aging mechanisms of Si/graphite anodes have identified either loss of anode active material (LAAM)[13,15–17] or loss of Li inventory (LLI) as main causes of capacity loss.[15,18–20] LAAM can occur during particle fracture and electronic isolation of Si particles by an excessively thick SEI. LLI often takes place simultaneously due to Li being stuck in fractured or isolated particles as a result of Li consumption in the SEI.[21,22]

As of today, few studies had been performed on Li plating on Si/graphite anodes,[15,23] what basically might be a similar process compared to pure graphite anodes at low temperatures and high charge rates.[24] Using neutron diffraction experiments and cells that suffered from Li plating, Richter et al. found that deposited Li first is re-intercalating into graphite before redistributing from graphite into Si.[23] We investigated the Li plating conditions of several cylindrical Si containing cells, which were classified as high-energy or high-power cells.[15] Si/graphite anodes in high-energy cells show a stronger susceptibility to Li plating compared to high-power cells due to their higher coating thickness and lower porosity.[15] Furthermore, we found that the tendency for Li plating increases after aging when LAAM in the form of loss of the Si compound is the main aging mechanism.[15] Similarly, in case of LLI as main aging mechanism, the susceptibility to Li plating decreases.[15]

Since Li plating presents a significant safety risk due to internal short circuits[25,26] and lower onset temperatures for exothermic reactions and the thermal runaway,[27,28] identifying Li plating in an early stage is essential for safe battery operation. Several literature reviews have already been published summarizing the established methods for in situ and Post-Mortem detection of Li plating.[24,29,30] In situ methods for Li plating metal detection are the use of a reference electrode between anode[31,32] and cathode as well as observing the voltage relaxation profile (VRP) after charging.[33,34] At anode potentials below 0 V vs Li/Li^+, Li plating is thermodynamically favored over Li intercalation into the active material.[35] Once Li plating has occurred, Li metal can re-intercalate into the anode, thus keeping the anode potential constant and resulting in a flat voltage plateau.[33,34]

Post-Mortem methods for detection of Li plating on anodes in disassembled cells include XPS,[36] GD-OES[15,28,37] and SEM.[28,38] The minimum amount of metallic Li can be quantified on graphite[37] and Si/graphite anodes[15] using GD-OES. Li plating can be qualitatively detected by SEM due to the characteristic dendrites.[38,39]

In this study, we investigate changes in Li plating on anodes with increasing Si content. Anodes were coated with identical areal capacity, resulting in lower coating thickness at higher Si contents. Higher irreversible capacities of anodes with higher Si content were compensated by higher areal capacities of the cathode. Since the N/P ratio, defined as the ratio of the areal capacity of the anode relative to the cathode, also influences the occurrence of Li plating, the required cathode capacities were selected in a way that all cells have an N/P ratio of 1.1. Furthermore, this study includes a method validation for voltage relaxation, Li stripping, SEM measurements, and GD-OES depth profiling. Another aim of this study is to reveal general trends on aging and susceptibility to Li plating.

[z]E-mail: thomas.waldmann@zsw-bw.de

Journal of The Electrochemical Society, 2023 **170** 060536

Experimental

Electrode manufacturing.—Graphite active material and four Si/graphite composite active materials with different Si contents were purchased from Iopsilion (China). The Si content in the active material was 0 wt% (Graphite), 3.2 wt% (SiG3.0), 3.7 wt% (SiG3.5), 6.2 wt% (SiG5.8) and 23.1 wt% (SiG20.8), as determined with total carbon (TC)-analysis. Anode coatings were prepared using active material, CMC binder (TIMCAL, Switzerland), SBR binder (ZEON, Japan), and SuperC65 conductive additive (Nippon paper Industries, Japan) with a weight ratio of 94:2:2:2 (Graphite, SiG3.0—SiG5.8) and 90:3:3:4 (SiG20.8).

A 2 wt% binder solution was prepared in a planetary mixer in which carbon black firstly was homogenized before adding active material and SBR. The anode slurry was coated onto Cu foil using a pilot coater a width of 80 mm at a speed of 1.5 m min^{-1}. Calendering to a target density of 1.3 g cm^{-3} was done at roll temperatures of 40 °C.

Cathode coatings are prepared by coating N-methyl pyrrolidone (NMP) based slurries with 94 wt% active material (BASF, Germany), 2 wt% PVDF (Solvay, Belgium), 2 wt% carbon black (TIMCAL, Switzerland), and 2 wt% graphite (TIMCAL, Switzerland) onto Al foil. The cathodes were calendered at 100 °C roll temperature to a density of 3.2 g cm^{-3}.

Electrode compositions and active material loadings are summarized in Table I.

Cell manufacturing.—Reversible and irreversible capacities of the electrodes were determined with CR2032 coin half cells at ZSW. They were built with a 12 mm diameter working electrode, 2 layers of separator (Whatman, GF/A), and a 16 mm diameter Li counter electrode. Graphite cells were filled with 150 μl of 1 M $LiPF_6$ in EC: DEC (3: 7 wt%) + 2 wt% VC (Gotion, USA) and Si containing cells were filled with 150 μl of 1 M $LiPF_6$ in EC: DEC (3: 7 wt%) + 10 wt% FEC (Gotion, USA). Graphite and Si/Gr coin half cells were operated in the voltage window of 0.01–1.5 V and NMC622 coin half cells in the voltage window of 3.0–4.3 V.

Pouch full cell were assembled at ZSW using one double-sided coated anode with an area of 26 cm^2 and two single-sided coated cathodes with an area each of 24 cm^2, and Celgard 2325 separator. Graphite pouch full cells were filled with 1.5 mL of VC or FEC containing electrolyte and Si pouch cells were filled with 1.5 mL of FEC containing electrolyte. The pouch full cells were operated in the voltage window of 3.0–4.2 V.

Cells used for ex situ light microscopy imaging at Aalen University of Applied Sciences (AU) were built in an Ar-filled glove box (GS Glovebox Systemtechnik; <1.0 ppm O_2 & <1.0 ppm H_2O). The half cell setup consists of a 15 mm diameter anode mm and a 14 mm diameter Li foil electrode (Sigma Aldrich, 750 μm thickness), with a 16 mm diameter GF/A separators and a Celgard 2325 in between. 150 μl electrolyte (1 M $LiPF_6$ in EC: DEC (3: 7 wt %) + 10% FEC) was added to each coin cell.

Electrochemical tests.—EIS measurements to determine the tortuosity were performed on a BioLogic VMP 3 in a symmetrical coin cell set-up at room temperature. The EIS measurements were performed in multi-sine mode within a frequency range of 500 kHz to 10 mHz with a sinusoidal potential amplitude of 10 mV. Tortuosity values were calculated by fitting of the experimental data using ZView (Scribner Associates, Inc.). The symmetrical setup was used to avoid a mixed impedance between different working and counter electrodes and to simulate blocking conditions. Electrodes from the same anode with an area of 1.131 cm^{-2} and 2.011 cm^{-2} were punched out and dried 16 h under vacuum at 130 °C. The coin cells were then assembled in an argon filled glovebox using two layers of GF/A and 150 μl of electrolyte. Graphite cells were filled with 150 μl of 1 M $LiPF_6$ in EC: DEC (3 : 7 wt%) + 2 wt% VC and Si containing cells were filled with 150 μl of 1 M $LiPF_6$ in EC: DEC (3 : 7 wt%) + 10 wt% FEC.

The electrochemical measurements were conducted with MACCOR systems and cells positioned in climate chambers (CTS). The formation cycles started after 12 h soaking time by charging at 0.1 C to 4.2 V in CC–CV (constant current - constant voltage) mode and discharging at 0.1 C to 3.0 V in CC mode. During charge rate capability tests the cells were charged three times in CC mode to 4.2 V at charging rates of 0.1 C, 0.2 C, 0.33 C, 0.5 C, 1 C, 1.5 C, and 2 C. After reaching 4.2 V, the cells rested for 1 h (Si/graphite cells) or 3 h (Graphite cells) before discharged at 0.2 C to 3.0 V. All tests were performed with 3 cells each at 25 °C ± 1 °C and at 0 °C.

The amount of Li deposited on the anodes was quantified by fully charging two cells of each cell type in CC mode at 0 °C and immediately discharging the cells at 0.05 C to 3.0 V. The capacity charged into the cells at each C-rate is equal to the capacity charged into the cells at 0.1 C (CC) to 4.2 V. Metal plates were attached to the cells for better heat dissipation.

For a short aging of 5 cycles, 2 cells of each cell type were charged at 0 °C at 0.2 C and 0.33 C (graphite), 0.33 C and 0.5 C (SiG3.0 and SiG3.5), and 0.5 C and 1 C (SiG5.8 and SiG20.8), respectively, and discharged at 0.2 C.

Testing of the half cells for ex situ light microscopy was done with a BASYTEC CTS-Lab battery tester and all cells were set up in a climate chamber (Binder) at 23 °C. Formation was conducted by three charge / discharge cycles at a current rate of C/10. Charging was performed in CC-CV mode and discharging in CC mode. The half cells were cycled between 1.5 V and 0.01 V. Lithiation is terminated by reaching the <C/40 criteria. The theoretical capacity based on the electrodes mass loading was used for the charge and discharge current calculations. After formation, the cells were charged in CC mode with 1 C to different SOCs (50%–100%).

Table I. Summary of physico-chemical anode properties.

	Graphite	SiG3.0	SiG3.5	SiG5.8	SiG20.8
Si in AM	0 wt%	3.2 wt%	3.7 wt%	6.2 wt%	23.1 wt%
AM	94 wt%	94 wt%	94 wt%	94 wt%	90 wt%
CB	2 wt%	2 wt%	2 wt%	2 wt%	4 wt%
CMC	2 wt%	2 wt%	2 wt%	2 wt%	3 wt%
SBR	2 wt%	2 wt%	2 wt%	2 wt%	3 wt%
Si in Anode	0 wt%	3.0 wt%	3.5 wt%	5.8 wt%	20.8 wt%
AM Loading Anode	8.7 mg cm^{-2}	7.7 mg cm^{-2}	7.4 mg cm^{-2}	6.9 mg cm^{-2}	5.3 mg cm^{-2}
AM Loading Cathode	15.4 mg cm^{-2}	15.9 mg cm^{-2}	16.5 mg cm^{-2}	17.1 mg cm^{-2}	19.3 mg cm^{-2}
Density	1.3 g cm^{-3}	1.3 g cm^{-3}	1.3 g cm^{-3}	1.3 g cm^{-3}	1.3 g cm^{-3}
Porosity	42.4 ± 0.3%	43.5 ± 0.1%	44.1 ± 0.2%	42.7 ± 0.2%	42.9 ± 0.1%
Tortuosity	7.92	6.08	7.57	7.04	6.71
D_{50} value	14.77 μm	14.50 μm	14.12 μm	13.18 μm	13.16 μm

Journal of The Electrochemical Society, 2023 **170** 060536

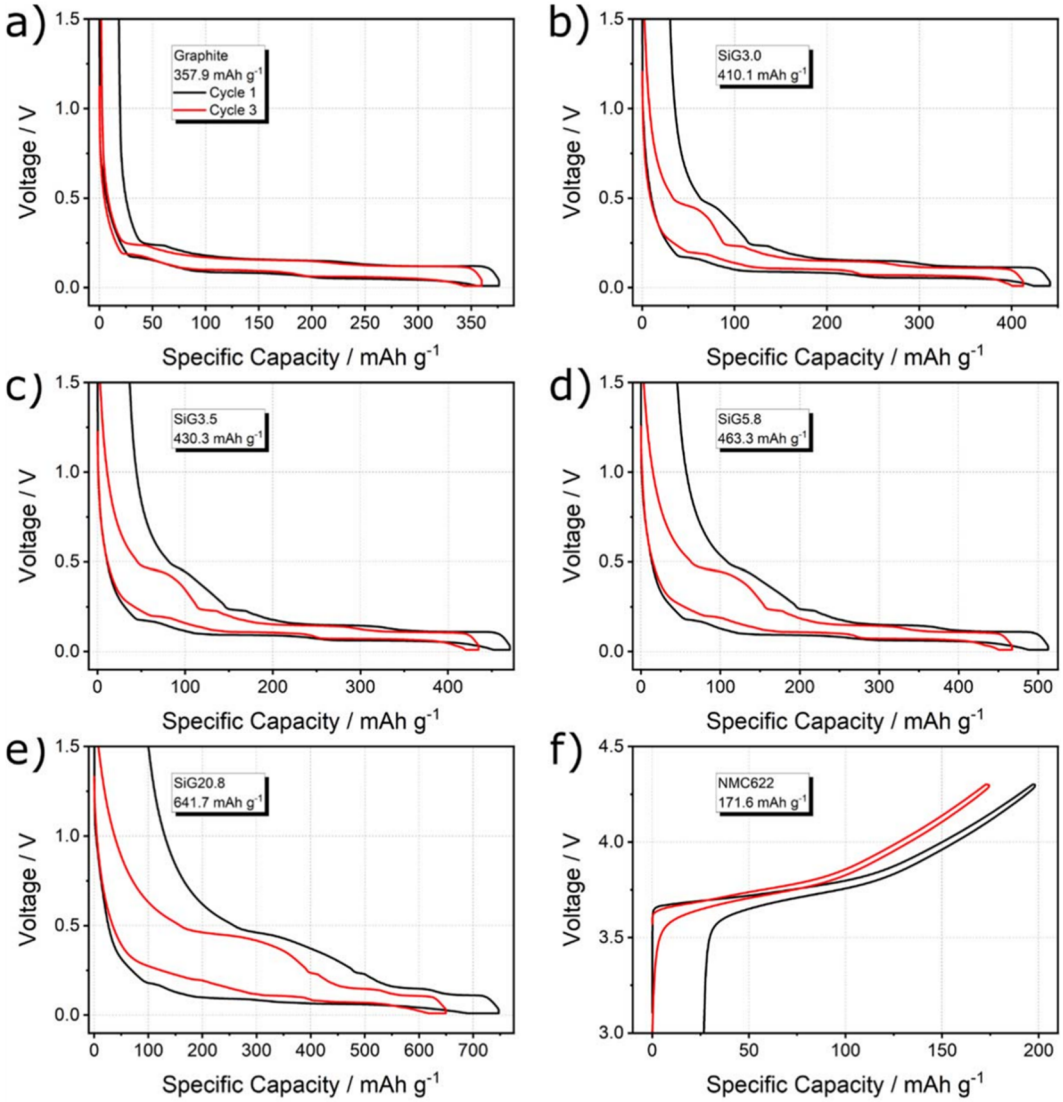

Figure 1. (a)–(e) Voltage profiles of the five anodes and (f) the NMC622 cathode showing the first formation cycle in black and the third formation cycle in red. The discharge capacity of the third formation cycle is shown in the box below the electrode name.

Post-mortem characterization.—GD-OES depth profiling analyses were conducted at ZSW using a GDA750 measurement device (Spectruma, Germany). The measurements were performed in radio frequency (RF) mode at a frequency of 2501 Hz, at a discharge voltage of 550 V and a pressure of 2 hPa. A mixture of 1% H_2 in Ar (both 6.0 purity) was used as sputtering gas. The following specific emission lines for individual elements were used for detection: H (121.6 nm), O (130.2 nm), C (156.1 nm), P (178.3 nm), Si (288.1 nm), Li (670.7 nm).

Scanning electron microscopy (SEM) of electrodes was performed with a secondary electron (SE) detector at 5 kV using a LEO 1530 VP (Zeiss) equipped with a Gemini thermal field emission column at ZSW. Cross-sections of anodes were generated with a Hitachi IM4000Plus broad-beam argon ion milling system, using an ion beam voltage of 5 kV. During sample preparation for SEM (top view and cross-section), the samples were exposed to air.

For Hg porosimetry measurements at ZSW, a 20 cm long electrode piece was used and a double determination of porosity was performed. Hg porosimetry was performed using a PASCAL 140–440 Series from Porotec. The pressure was slowly increased until the instrument detected Hg intrusion into the sample. The pressure increase was then reduced and stopped until Hg intrusion has taken place. Afterwards, the pressure was increased again and the process was repeated. The pressure was increased at 6–19 MPa min^{-1} up to a maximum pressure of 374 MPa.

High-resolution light microscopy was performed with a ZEISS Axio Observer 7 with an EC Epiplan-Neofluar 100x objective using a neutral white (3200 K) LED and an extended depth of field mode inside the glovebox at AU. The images were taken in the center of the electrode.

Results and Discussion

Electrode and cell characterization.—For this work, we purchased four already blended Si/graphite powders as well as the pure graphite powder used in the blends with Si. The specific capacities of the active materials were listed by the manufacturer as 355 mAh g^{-1} (Graphite), 400 mAh g^{-1} (SiG3.0), 420 mAh g^{-1} (SiG3.5), 450 mAh g^{-1} (SiG5.8) and 650 mAh g^{-1} (SiG20.8).[40] The particle size

Journal of The Electrochemical Society, 2023 **170** 060536

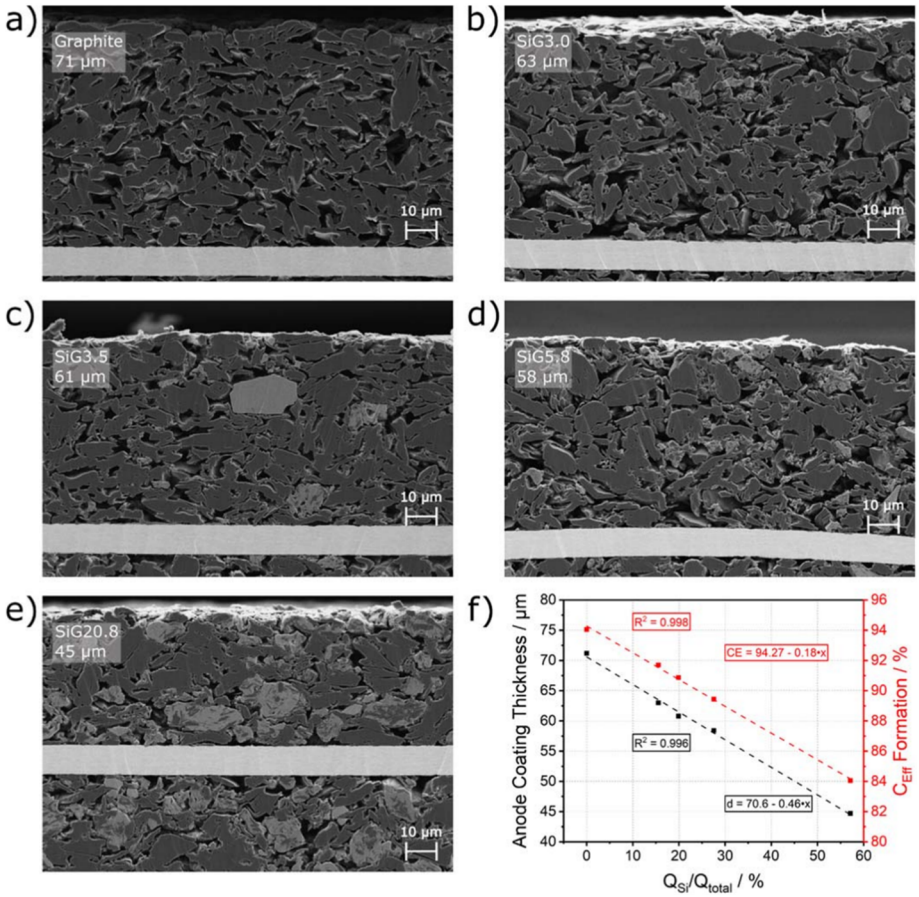

Figure 2. (a)–(e) SEM images of one side of the double-sided anodes taken with the SE detector; (f) plot of the anode coating thickness vs. Si capacity contribution (black) and initial coulombic efficiency vs Si capacity contribution (red).

Table II. Summary of electrochemical cell properties, which were determined experimentally in half cells as well as the theoretical capacity specified by the manufacturer. The reported irreversible capacity includes the irreversible capacity losses of all three formation cycles.

	NMC622	Graphite	SiG3.0	SiG3.5	SiG5.8	SiG20.8
Theoretical Capacity specified by the manufacturer [mAh g^{-1}]		355	400	420	450	650
Reversible Capacity [mAh g^{-1}]	171.6	357.9	410.1	430.3	463.3	641.7
Irreversible Capacity [mAh g^{-1}]	26.5	22.6	37.1	43.3	54.7	121.2
C_{eff} Formation [%]	86.62	94.05	91.70	90.87	89.44	84.06
Areal Capacity [mAh cm^{-2}]	2.63–3.30	3.11	3.16	3.18	3.20	3.40
N/P Ratio [-]		1.10	1.11	1.10	1.09	1.13
Q_{Si}/Q_{total} [%]		0	15.52	19.90	27.54	57.11

distribution reveals that the D_{50} value (Table I) of the powder mixtures decreases with higher Si content, which is in agreement with the SEM observations. However, SEM investigations have also revealed that the Si microparticles are secondary particles consisting of Si nanoparticles in a C matrix. By TC analysis, the Si content was determined to be 3.2 wt% Si (SiG3.0), 3.7 wt% Si (SiG3.5), 6.2 wt% (SiG5.8), and 23.1 wt% (SiG20.8) of the respective active material.

The porosities of the anodes were determined by Hg intrusion and the tortuosity by EIS. The values listed in Table I are very similar, and therefore effects of differences in porosity or tortuosity on fast-charge capability and Li plating can be excluded in this study.

Figure 1 shows the cell voltage during the first (black line) and third (red line) lithiation and de-lithiation cycle. As expected, the experimental specific capacity of the anode increases with the amount of Si in the anode due to its higher specific capacity. Experimentally determined irreversible capacity losses also increase with the amount of Si in the anode, which is consistent with literature and the intrinsically higher first cycle capacity loss of Si.[41] The irreversible capacities refer to the total irreversible losses of the three formation cycles. All experimental reversible and irreversible capacities are listed in Table II. The voltage profiles of the different anodes are comparable during lithiation. However, during de-lithiation the voltages of the cells with Si-containing anodes are higher, most likely due to the hysteresis of Si.[42]

We used the Si mass fractions ω of the respective active materials as well as the specific capacities q to calculate the overall capacity contribution of Si (Q_{Si}/Q_{total}) to the anode active material (Table II)

Journal of The Electrochemical Society, 2023 **170** 060536

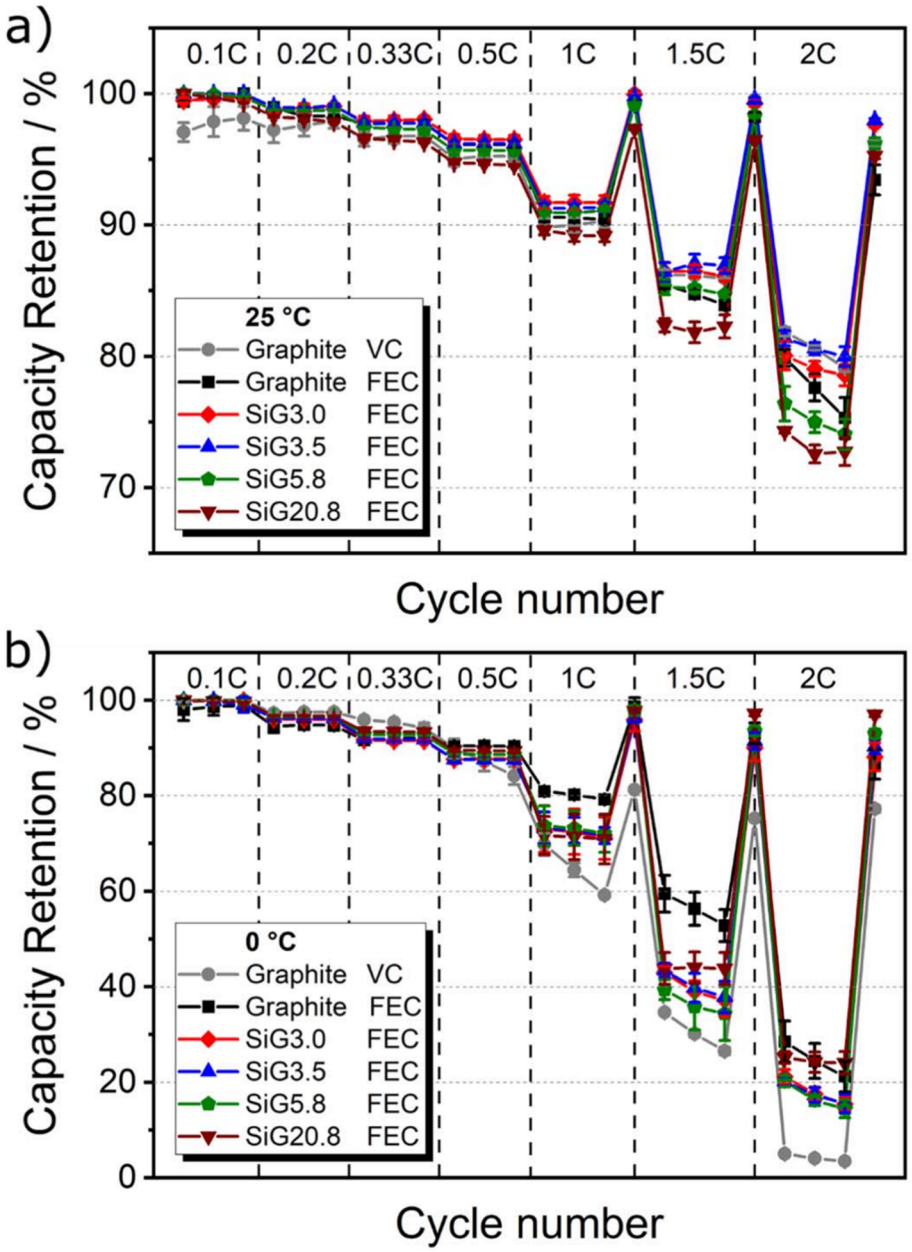

Figure 3. Charge rate capability tests at (a) 25 °C and (b) 0 °C, in which the cells were charged to 4.2 V in CC mode and discharged at 0.2 C to 3.0 V. After charging three times at 1 C, 1.5 C, and 2 C, a check-up cycle at 0.1 C was inserted.

Table III. Capacity charged into the cells at 0.1 C (CC) to 4.2 V (row 1) and the capacities obtained from the dissolution of the deposited Li during discharge at 0.05 C. The first column gives the charging C-rate.

	Graphite 10% FEC	SiG3.0 10% FEC	SiG3.5 10% FEC	SiG5.8 10% FEC	SiG20.8 10% FEC
Charged Capacity	103 mAh	107 mAh	108 mAh	113 mAh	115 mAh
0.2 C	0 mAh	0 mAh	0 mAh	0 mAh	0 mAh
0.33 C	0.7 mAh	0 mAh	0 mAh	0 mAh	0 mAh
0.5 C	3.6 mAh	1.4 mAh	0.7 mAh	0.7 mAh	0 mAh
1 C	7.6 mAh	4.4 mAh	3.9 mAh	3.5 mAh	—

Journal of The Electrochemical Society, 2023 **170** 060536

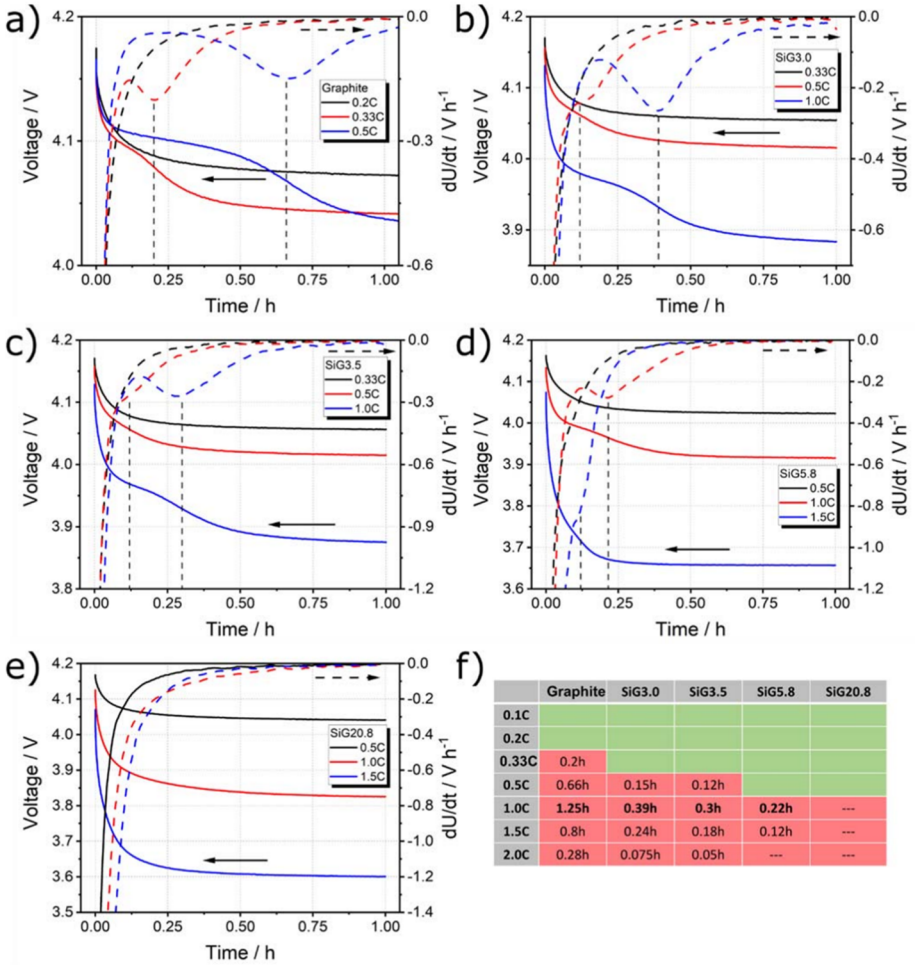

f)

	Graphite	SiG3.0	SiG3.5	SiG5.8	SiG20.8
0.1C					
0.2C					
0.33C	0.2h				
0.5C	0.66h	0.15h	0.12h		
1.0C	1.25h	0.39h	0.3h	0.22h	---
1.5C	0.8h	0.24h	0.18h	0.12h	---
2.0C	0.28h	0.075h	0.05h	---	---

Figure 4. (a)–(e) Voltage curves during the rest step after fast charging (solid line) are shown for the highest uncritical C-Rate (black), the critical C-rate (red) and the next highest C-rate tested (blue). The first derivative of the voltage curves are shown in dashed lines. (f) The matrix illustrates for each anode whether Li plating occurs (red) or whether no Li re-intercalation was detected (green). The values correspond to the duration until Li re-intercalation is completed.

using Eqs. (1) and (2). We noticed a linear relationship between the Si capacity share and the irreversible capacity losses, which is shown in Fig. 2f. This allows calculating the irreversible capacity losses of the anode with any Si content between 0 wt% and 20.8 wt%.

$$Q_{total} = \omega_{Gr} \cdot q_{Gr} + \omega_{Si} \cdot q_{Si} = Q_{Gr} + Q_{Si} \quad [1]$$

$$\frac{Q_{Si}}{Q_{total}} = \frac{Q_{total} - Q_{Gr}}{Q_{total}} \quad [2]$$

In these equations, ω is the mass fraction, q_{Gr} and q_{Si} are the experimental specific capacities of graphite and Si.

Anodes with different Si contents were coated with areal capacities in the narrow range of 3.25 mAh cm^{-2} ± 0.15 mAh cm^{-2}. At such constant areal capacity the anode coating thickness decreases with increasing Si content. Figures 2a–2e show the SEM cross-sections at the same magnification of the five anodes and the anode coating thickness clearly decreases. In these SEM image, Si particles are shown in a brighter shade of grey due to their higher atomic mass. Further, there is a linear relationship between the anode thickness and the Si capacity contribution, which is also shown in Fig. 2f.

It must be noted that thinner anode coatings will lead to larger electrode surface areas in a given cell volume. For example, in 21700 cells, the jellyrolls will then have additional windings.[43] Since larger electrode areas lower the cell impedance,[44] thinner electrodes as achieved by increasing Si content, could lead to cells with lower impedance and therefore to benefits of such cells in view of fast charging/discharging.

Based on the reversible and irreversible capacities of the anode and cathode active materials, we targeted a N/P ratio of 1.10. Cathode loading (mg cm^{-2}), and therefore cathode areal capacity (mAh cm^{-2}), was adjusted in order to compensate for the different irreversible capacity losses of anodes, hence having full-cells with a similar N/P ratio of 1.1. Details on the cathode and anode loadings are given in Table I. Table II shows that all the N/P ratios are very similar and therefore the cells are suitable for further experiments. This cell design results in anodes with identical areal capacity and therefore the same amount of Li inventory being in the cell. In addition, all anodes have a similar porosity and tortuosity. Therefore, any differences in the occurrence of Li plating on the anodes are solely due to different anode thicknesses resulting from the different Si contents.

Journal of The Electrochemical Society, 2023 **170** 060536

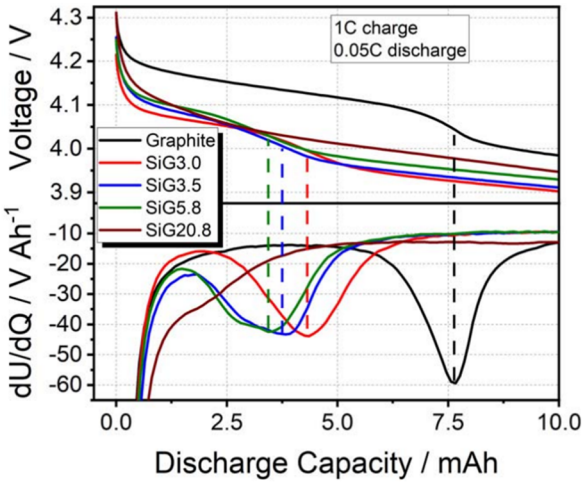

Figure 5. Stripping discharge experiment showing the voltage curve during discharge and the first derivative of the voltage vs the discharge capacity. The minimum in the first derivative marks the end of the stripping of deposited Li and the beginning of de-lithiation of the anode.

Fast-charging capability and low temperature charging.—Cells with different Si contents in the anodes were subjected to fast charging experiments at ambient temperatures of 25 °C as well as 0 °C. Charging was carried out in CC mode to observe potential Li re-intercalation during the voltage relaxation during resting-time after charging, which may have been masked by the CV phase. Charge rate capability tests for graphite were separately done with both available electrolytes to exclude any effect of the VC or FEC,[45–47] which are added as electrolyte additives to form a stable SEI on graphite and Si, respectively.

Figure 3a shows the charge rate capability at 25 °C, in which all cells were charged three times at each individual C-rate. Starting after 1 C charging, a C/10 check-up cycle between each C-rate was included to observe irreversible capacity losses. Until a charging rate of 1 C, little differences in the capacity retention were observed between the different cell types. The capacity retention at 1 C is close to 90%, most likely due to the low anode density of 1.3 g cm^{-3}, which facilitates fast diffusion pathways. From a C-rate of 1 C, the SiG20.8 cell type shows a lower capacity retention than the other cell types with lower Si content. Furthermore, high irreversible losses of SiG20.8 are already visible in the first check-up cycle. At even higher C-rates, the capacity retention further decreases and the irreversible losses continue to grow. SiG5.8 also shows lower capacity retention and higher irreversible losses compared to cells with a lower Si content. Even though the anode thickness decreases due to the higher Si content, cells with high Si content showed the lowest capacity retention. This result indicates, that Si is not beneficial towards the charge rate capability, most likely due to higher diffusion barriers of Li in Si (0.47–0.62 eV)[48–52] compared to Li diffusion in lithiated graphite (~0.2–0.4 eV).[53,54] However, we note that barriers are to best of our knowledge only available for single Li atoms in Si and not for higher lithiated alloys. This result indicates that the anode thickness is not the limiting factor for fast charging capability. Since the porosity in all anodes is very high, the better kinetics of the graphite most likely dominate. Irreversible capacity losses in the graphite cell and cells with Li contents of 3.0 wt% and 3.5 wt% firstly occurred after charging at 2 C. Deposition of Li on the anode surface of each cell type was confirmed by visual inspection after cell opening during the Post-Mortem analysis.

At 25 °C (Fig. 3a), the graphite cells with VC as electrolyte additive show better capacity retentions compared to graphite cells with FEC. In addition, the graphite cells containing FEC suffer from higher irreversible losses at high C-rates. However, at 0 °C the FEC containing graphite cells have a much better capacity retention compared to graphite cells with VC (Fig. 3b). Those findings are in agreement with literature, as VC as electrolyte additive was reported to increase the coulombic efficiency and cycle life of graphite based cells.[47] However, it also increases the charge transfer resistance of graphite anodes,[47] making it less suitable for fast charging, especially at low temperatures. FEC instead of VC was used as electrolyte additive for Si containing cells, as FEC forms a more flexible SEI.[45,46]

Figure 3b indicates that the Graphite (FEC) and SiG20.8 cell type, which had the lowest fast charging capability at 25 °C, shows the highest fast charging capability at 0 °C. In addition, SiG20.8 has the lowest irreversible capacity losses, which is obvious during the 0.1 C check-up cycle. Up to 1.5 C, Graphite (FEC) has the highest capacity retention, though from 1.5 C it decreases with every cycle. The capacity retention of the check-up cycles decreases most likely due to irreversible Li plating.

Cells with Si contents between 3.0 wt% and 5.8 wt% have the lowest capacity retention of all FEC containing cells at 0 °C. The capacity retention of these three cell types are too close in order to identify any trend related to Si content. The superior performance of graphite suggests that at low temperatures, lithiation of graphite is faster than the lithiation of Si (see discussion on Li diffusion barriers above). In addition, the stable capacity retention of SiG20.8 at 0 °C, which does not exhibit any irreversible capacity loss indicates that the reduction of the anode thickness by the addition of Si has a pronounced positive effect to the fast charging capability.

Reversible Li plating on the anode surface caused by fast charging can be observed during the rest step, since the re-intercalation of deposited Li into the anode causes a voltage plateau.[28,33,34,55,56] After each charging step, cells were given 1 h—3 h rest time for voltage relaxation. The cell voltage was differentiated versus time to determine the end of re-intercalation into the anode[33] in Figs. 4a–4e.

Cells tested at 25 °C exhibited visible Li deposition on the anode surface after cell opening, which was found during the Post-Mortem analysis, however, no voltage plateau was observed during voltage relaxation at this temperature. The amount of reversibly deposited Li might be either too small to detect, it re-intercalates too quickly into the anode, or it potentially reacts with the electrolyte instead of re-intercalating at 25 °C.

At 0 °C higher amounts of Li plating, as well as slowed down re-intercalation into graphite and reaction with the electrolyte can be expected compared to 25 °C. Such differences between the five different cell types were observed during the voltage relaxation at 0 °C (Fig. 4). Superior performance of the graphite cell with FEC as electrolyte additive compared to VC was decisive to study only the voltage relaxation of the graphite cell with FEC.

Voltage relaxation was used to determine a critical C-rate at which Li plating was observed for the first time. Figure 4 shows the voltage profiles in red color and its derivatives after charging at the critical C-rate, the next highest C-rate in blue color and the highest uncritical C-rate in black. Figure 4f summarizes the results of a total of 105 voltage relaxation measurements from Figs. 4a–4e. The matrix in Fig. 4f displays the critical C-rates in red and shows the time span, after which re-intercalation is completed.

Interestingly, the graphite cells already exhibit reversible Li plating at 0.33 C, although they have excellent fast charging behavior up to 1 C without irreversible capacity losses. Re-intercalation is completed after 0.2 h at 0.33 C, after 0.66 h at 0.5 C and not until 1.25 h at 1 C. At even higher C-rates, the re-intercalation time decreases, indicating that due to high overpotentials, the cut-off voltage is reached faster and less Li is deposited on the anode surface.

In Si containing cells reversible Li plating occurs at higher C-rates. For SiG3.0 and SiG3.5, which have Si contents of 3 wt% and 3.5 wt% respectively, the critical C-rate for Li-plating is 0.5 C. Re-intercalation time slightly decreases form SiG3.0 to SiG3.5,

Journal of The Electrochemical Society, 2023 **170** 060536

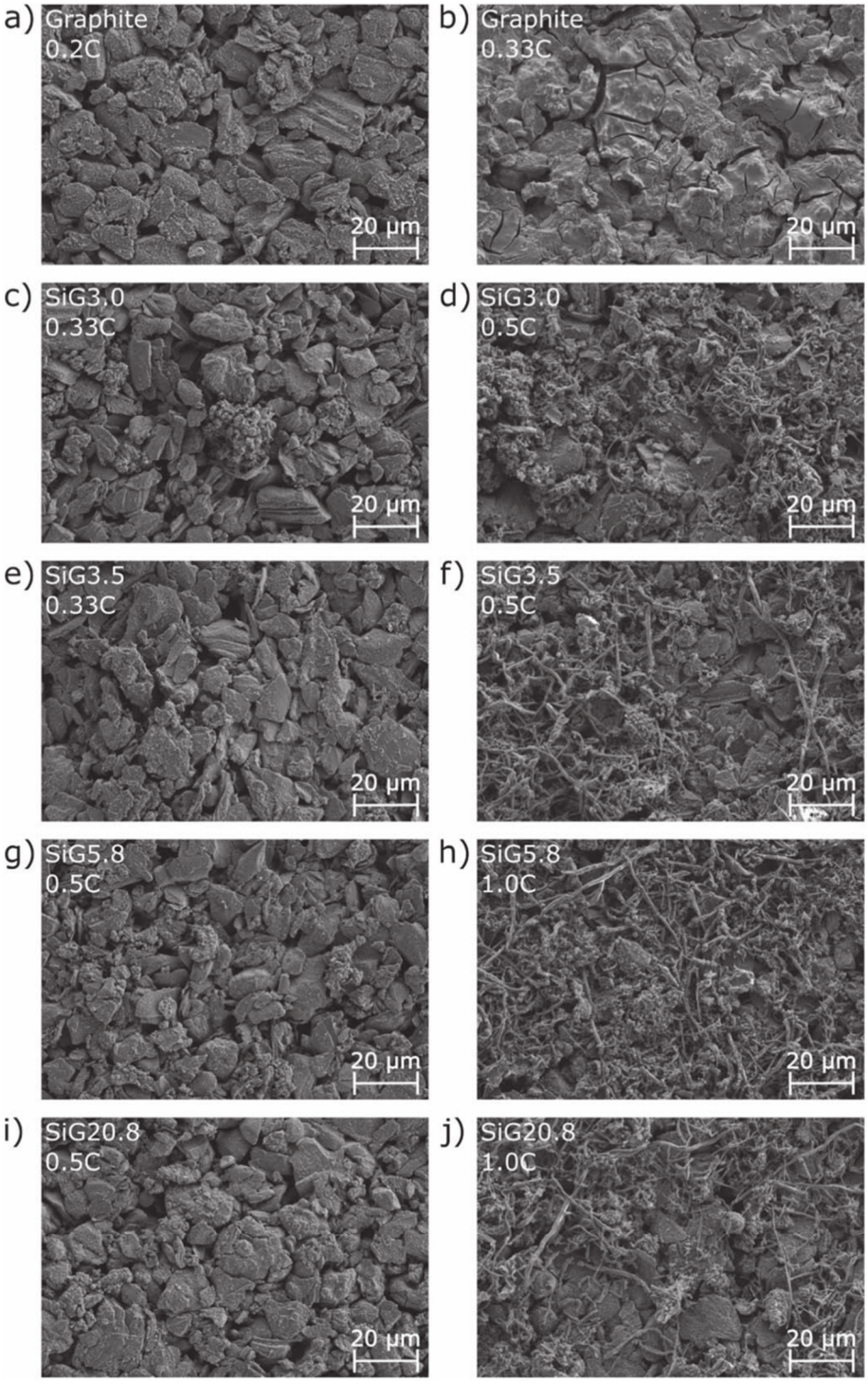

Figure 6. SEM images of the anodes after aging at the highest uncritical C-rate (left column) and the lowest critical C-rate (right column). Li plating was only measurable after aging at a critical C-rate.

indicating that less Li was deposited on the anode of SiG3.5 (compare Figs. 4b, 4c) The SiG5.8 cell type, which contains 5.8 wt% Si in the anode, first shows reversible Li plating at 1 C (Fig. 4d). In each of these four cell types (Graphite, SiGr3.0, SiGr3.5, SiG5.8), the maximum re-intercalation time is observed after charging at 1 C. In contrast, no voltage plateau could be observed in the relaxation profiles of SiG20.8. Post-Mortem analysis, however, proved that irreversible Li plating occurs as early

Journal of The Electrochemical Society, 2023 **170** 060536

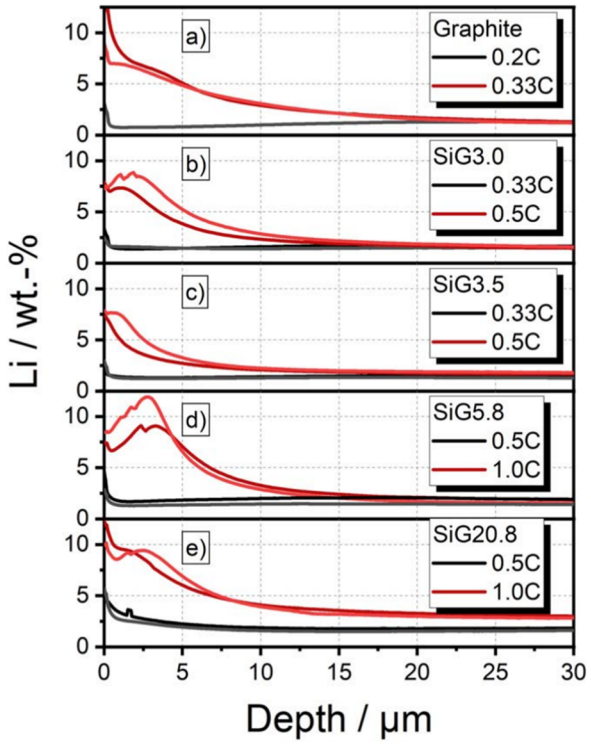

Figure 7. GD-OES measurements of the anodes aged at the highest uncritical C-rate (black and gray) and the critical C-rate (red and orange) show that the Li concentration on the anode surface is increased after critical aging. The graphs in a lighter shade show the reproduced measurements.

as 1 C for the cells with SiG20.8 anodes. Therefore, these fields in the matrix in Fig. 4f are marked red, pointing out that Li plating already occurred.

We clearly observed a trend towards higher critical C-rates for Li plating with higher Si contents (Fig. 4f). Based on this observation, the minimum in an Arrhenius plot of aging rates[57–60] will most likely shift to lower temperatures with higher Si content.

Additionally, the stripping discharges of the cells can be compared.[61–63] For this purpose, the cells were charged at 0 °C with constant current and immediately afterwards discharged at a low rate of 0.05 C (Fig. 5). The capacity charged into the cells at each C-rate is equal to the capacity charged into the cells at 0.1 C (CC) to 4.2 V. Thereby, it was ensured that the same capacity was charged into the cells at each C-rate. The mixed potential of plated Li and lithiated graphite and Si leads to a plateau in the discharge curve.[61] The minimum in the derivative of the voltage curve is caused by the voltage drop as the dissolution of deposited Li (Li stripping) is completed (Fig. 5).[63] Table III lists the amount of charge which originates from the stripping of deposited Li.

Reversible Li plating on graphite anodeswas first detected after charging at a C-rate between 0.2 C and 0.33 C, as was observed with voltage relaxation. In contrast, SiG3.0 to SiG5.8 first show Li stripping at charging C-rates between 0.33 C and 0.5 C. On the anode with the highest Si content (SiG20.8), no voltage plateau could be observed during stripping discharge.

With higher C-rates, the amount of Li that is stripped from the anode increases. However, the amount of Li that is stripped from Si/graphite anodes decreases with higher Si content.

The results from Fig. 5 show that with higher Si content, less Li is plated on the anode. In addition, the measurements are consistent with voltage relaxation experiments (Fig. 4), where the re-intercalation time, and thus most likely the amount of plated Li, decreases with higher Si content.

In this section, we primarily focused on Li plating at 0 °C. We have seen that although graphite cells have the best fast charging capability, they suffer from Li plating at lower C-rates at 0 °C. The cells become more tolerant to higher charging C-rates with higher Si content without showing Li plating. Additionally, the amount of Li plating at the same C-rate seems to decrease with higher Si content, i.e. with thinner anode coatings for very similar anode areal capacities, porosity, tortuosity, and N/P ratios.

Post-Mortem analysis of cells to detect Li plating.—Post-Mortem methods were applied to investigate whether Li fully re-intercalates into the anode materials or if Li is also deposited irreversibly as Li metal. For this reason, an aging procedure of five cycles at 0 °C at the respective critical C-rate and highest uncritical C-rate was started, before these cells were opened and investigated with SEM and GD-OES depth profiling. The critical C-rate refers to the charging C-rate, at which reversible Li deposition was observed in the voltage relaxation profile at 0 °C after fast-charging, whereas no re-intercalation could be observed after charging at an uncritical C-rate. SEM can detect the presence of Li deposits on the anode surface facing the separator,[38,39] while GD-OES depth profiling is used to create quantitative element profiles to determine the Li amount at the anode surface.[13,37] The aging procedure was deliberately kept short to avoid thick Li coverage of the anode surface, which would have impeded the GD-OES measurements.

SEM measurements of anodes in Fig. 6 display anodes after uncritical aging in the left column and after critical aging in the right column. The respective charging C-rates during aging are shown in the upper left corner. These SEM images confirm the electrochemical findings that no Li is deposited reversibly or irreversibly on the anode surface below the critical charging C-rate. In contrast, either a thick film (Fig. 6b) or dendrites (Figs. 6d, 6f, 6h) are evident on aged anodes cycled at the critical charging C-rates. This is fully consistent with the voltage relaxation experiments of Fig. 4.

In addition to the SEM images, GD-OES measurements were performed to detect Li plating on the anode surfaces. Figure 7 shows GD-OES depth profiles where a depth of 0 µm corresponds to the beginning of the measurements and therefore to the anode surface. Again, no Li plating was observed on the anode surfaces after aging at the highest uncritical C-rate. However, aging at the critical C-rate leads to a distinct increase of the Li concentration at the anode surface after only five cycles. The finding that Li plating happens mainly on the anode surface is consistent with previous GD-OES depth profiling studies with graphite[37] and Si/graphite [15,23] anodes, in situ optical microscopy experiments[64] from our group and simulations by Latz's group.[65,66] We noticed that compared to our previous GD-OES measurements mostly using strongly aged cells, Li plating can also be detected after few aging cycles.

Li plating detected with SEM and GD-OES arises from irreversibly deposited Li, while voltage relaxation and stripping discharge detects reversible deposited Li. The observation of irreversibly lost Li demonstrates that the deposited Li does not re-intercalate completely but undergoes side-reactions or must have lost electrical contact to the anode. Overall, the critical C-rates found by GD-OES in Fig. 7 are fully consistent with the SEM measurements in Fig. 6 and with the voltage relaxation curves in Fig. 4. These results are also mostly consistent with those from the Li stripping experiments in Fig. 5. The only deviation was found in case of SiG20.8 where Li plating was not evident in the voltage relaxation curves.

In order to assess the Li deposition behavior on the anodes at 23 °C, half cells were opened immediately after charging and investigated with high-resolution light microscopy under inert gas atmosphere (Fig. 8). The anodes graphite, SiG3.0, SiG5.8 and SiG20.8 were charged in half cell setup at 1 C to 50%, 60%, 70%, 80%, 90%, and 100% SOC and the presence of Li depositions was compared. Due to the very similar Si content of the anodes SiG3.0 and SiG3.5, only the anode SiG3.0 was investigated with ex situ microscopy. The short time-span of 2 min between end of charging and cell opening and the fast evaporation of the electrolyte most likely prevent the re-intercalation of Li into the anode.

Journal of The Electrochemical Society, 2023 **170** 060536

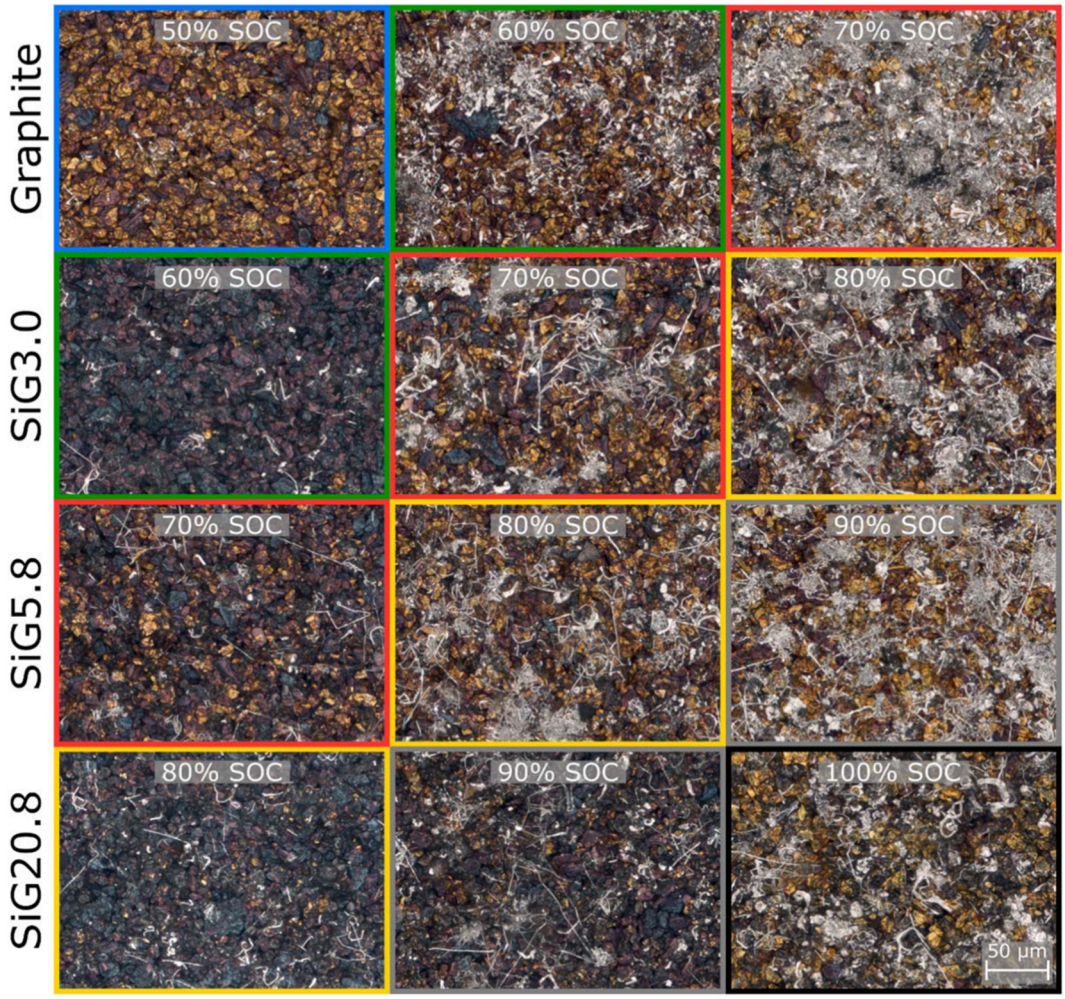

Figure 8. Light microscopy images of the anode surfaces at different SOCs. The images show that with increasing Si content the SOC, at which Li is deposited on the anode surface, increases.

Figure 8 includes images of each anode at three different SOCs, at which Li deposition is hardly visible (left column), locally visible (middle column) or covering the anode surface (right column). Images at the same SOC are framed by the same color. A general trend was observed toward higher SOC to observe more Li on the anode surface.

Li deposition on graphite anodes first appeared at 50% SOC and at 70% SOC the anode surface was fully covered with Li. The anode SiG3.0 showed isolated Li dendrites at 60% SOC, however, at 70% SOC the amount of Li dendrites has increased significantly. Similarly, the anode SiG5.8 exhibited Li plating at 80% SOC, however, few Li dendrites were already visible at 70% SOC. Full coverage of the anode SiG20.8 was only visible at 100% SOC, with local Li deposits already visible at 90% SOC. These findings demonstrate that also at ambient temperatures Li plating is less pronounced with increasing Si content. This trend is consistent with the results obtained at 0 °C using voltage relaxation and stripping discharge.

Conclusions

We investigated the effect of Si content in anodes on their susceptibility to Li plating. Therefore, five types of anodes with different Si contents and corresponding cathodes were coated on pilot scale. The anode areal capacities were kept constant to reduce the anode coating thickness for anodes with higher Si contents. The areal capacity of the cathodes were tailored to compensate the irreversible capacity losses of the anodes and to obtain pouch full cells with different Si contents and very similar N/P ratios. Furthermore, the porosity and tortuosity of the anodes were almost identical, so that their influence could be excluded. We observed a linear relationship between the Si capacity contribution to the total anode capacity and the irreversible capacity losses of the anodes during the three formation cycles.

The fast charging performance of all cells was compared in charge rate capability tests at 25 °C and 0 °C. We found that at 25 °C cells with low Si content and the graphite cell filled with VC containing electrolyte performed best. The capacity retention declined with increasing Si content. At 0 °C, however, the cell with the highest Si content along with the graphite cell filled with FEC containing electrolyte have the highest capacity retention at the highest C-rate. Lower Si contents have a lower capacity retention indicating that the reduction of the anode thickness is most beneficial for the charge rate capability.

Voltage relaxation experiments after charging at 0 °C were conducted to detect reversible Li plating at 0 °C. For each cell type except SiG20.8 a critical C-rate was found, at which reversible Li plating could be detected for the first time. The critical C-rate increases with Si-content, making cells with high Si content at similar areal capacity and therefore thinner anodes more resistant to Li plating at low temperatures.

A short aging procedure at 0 °C followed by Post-Mortem analysis with GD-OES and SEM was carried out to determine if irreversible Li plating occurs at the critical C-rate. Consistent with operando methods, Li plating has been detected at the critical C-rate, however, no Li plating occurs below the critical C-rate. Voltage relaxation, Li stripping, SEM measurements and GD-OES depth profiling are validated against each other and revealed clear trends on the susceptibility of Si/graphite anodes at 0 °C for the same anode areal capacities with Si increasing content.

Optical microscopy under inert gas atmosphere was used to investigate the presence of Li deposition at defined SOC levels. Similarly, the same trend as found at 0 °C, that high Si contents and thus thinner anodes make the cells more resistant to Li plating, was also found at 23 °C.

Overall, our results clearly showed that Si compounds in graphite anodes can have a positive effect by hindering Li plating, however, they can also increase the aging rate at 25 °C. The Si content will most likely shift the temperature of the minimum aging rate in Arrhenius plots. The thinner electrode coatings arising from Si in the anodes will furthermore decrease the impedance of battery cells, e.g. by additional available electrode surface in a given battery cell size. Further experiments into these directions are ongoing in our labs.

Acknowledgments

Funding of the project CharLiSiKo (AQua-Cluster) by the German Federal Ministry of Education and Research (BMBF) under contract n° 03XP0333A and project management by Projektträger Jülich (PTJ) are gratefully acknowledged. The authors are indebted to the ZSW members C. Pfeifer for SEM/EDX, G. Arnold for ICP-OES measurements, K. Fischinger for Hg porosimetry measurements, as well as M. Feinauer (ZSW) and C. Weisenberger (AU) for fruitful discussions.

ORCID

Marius Flügel https://orcid.org/0000-0002-9792-0414
Mario Marinaro https://orcid.org/0000-0002-5954-0357
Thomas Waldmann https://orcid.org/0000-0003-3761-1668

References

1. J. R. Dahn, T. Zheng, Y. Liu, and J. S. Xue, *Science*, **270**, 590 (1995).
2. F. Luo, B. Liu, J. Zheng, G. Chu, K. Zhong, H. Li, X. Huang, and L. Chen, *J. Electrochem. Soc.*, **162**, A2509 (2015).
3. L. Y. Beaulieu, T. D. Hatchard, A. Bonakdarpour, M. D. Fleischauer, and J. R. Dahn, *J. Electrochem. Soc.*, **150**, A1457 (2003).
4. J. Li, A. K. Dozier, Y. Li, F. Yang, and Y.-T. Cheng, *J. Electrochem. Soc.*, **158**, A689 (2011).
5. X. H. Liu, L. Zhong, S. Huang, S. X. Mao, T. Zhu, and J. Y. Huang, *ACS Nano*, **6**, 1522 (2012).
6. Y. Wang, Y. Liu, J. Zheng, H. Zheng, Z. Mei, X. Du, and H. Li, *Nanotechnology*, **24**, 424011 (2013).
7. Y. Hu, B. Yu, X. Qi, B. Shi, S. Fang, Z. Yu, and J. Yang, *J. Mater. Sci.*, **55**, 10155 (2020).
8. W. An, B. Gao, S. Mei, B. Xiang, J. Fu, L. Wang, Q. Zhang, P. K. Chu, and K. Huo, *Nat. Commun.*, **10**, 1447 (2019).
9. S. Y. Kim, J. Lee, B.-H. Kim, Y.-J. Kim, K. S. Yang, and M.-S. Park, *ACS Appl. Mater. Interfaces*, **8**, 12109 (2016).
10. H. Jia, X. Li, X. Zhang, L. Luo, Y. He, B. Li, Y. Cai, S. Hu, X. Xiao, C. Wang, K. Rosso, R. Yi, R. Patel, and J.-G. Zhang, *Nat. Commun.*, **11**, 1474 (2020).
11. P. Kuntz, O. Raccurt, P. Azaïs, K. Richter, T. Waldmann, M. Wohlfahrt-Mehrens, M. Bardet, A. Buzlukov, and S. Genies, *Batteries*, **7**, 48 (2021).
12. B. Lain, J. Brandon, and E. Kendrick, *Batteries*, **5**, 64 (2019).
13. K. Richter, T. Waldmann, M. Kasper, C. Pfeifer, M. Memm, P. Axmann, and M. Wohlfahrt-Mehrens, *J. Phys. Chem. C*, **123**, 18795 (2019).
14. K. Richter, T. Waldmann, M. Memm, M. Kasper, and M. Wohlfahrt-Mehrens, *J. Electrochem. Soc.*, **165**, A3602 (2018).
15. M. Flügel, K. Richter, M. Wohlfahrt-Mehrens, and T. Waldmann, *J. Electrochem. Soc.*, **169**, 50533 (2022).
16. M. Schindler, J. Sturm, S. Ludwig, A. Durdel, and A. Jossen, *J. Electrochem. Soc.*, **168**, 60522 (2021).
17. J. Schmitt, M. Schindler, and A. Jossen, *J. Power Sources*, **506**, 230240 (2021).
18. D. Anseán, G. Baure, M. González, I. Cameán, A. B. García, and M. Dubarry, *J. Power Sources*, **459**, 227882 (2020).
19. K. Kalaga, M.-T. F. Rodrigues, S. E. Trask, I. A. Shkrob, and D. P. Abraham, *Electrochim. Acta*, **280**, 221 (2018).
20. X. Li, A. M. Colclasure, D. P. Finegan, D. Ren, Y. Shi, X. Feng, L. Cao, Y. Yang, and K. Smith, *Electrochim. Acta*, **297**, 1109 (2019).
21. T. Waldmann, N. Ghanbari, M. Kasper, and M. Wohlfahrt-Mehrens, *J. Electrochem. Soc.*, **162**, A1500 (2015).
22. A. Iturrondobeitia, F. Aguesse, S. Genies, T. Waldmann, M. Kasper, N. Ghanbari, M. Wohlfahrt-Mehrens, and E. Bekaert, *J. Phys. Chem. C*, **121**, 21865 (2017).
23. K. Richter, T. Waldmann, N. Paul, N. Jobst, R.-G. Scurtu, M. Hofmann, R. Gilles, and M. Wohlfahrt-Mehrens, *ChemSusChem*, **13**, 529 (2020).
24. T. Waldmann, B.-I. Hogg, and M. Wohlfahrt-Mehrens, *J. Power Sources*, **384**, 107 (2018).
25. Y. Jiang et al., *Energy Storage Mater.*, **28**, 17 (2020).
26. T. Yang, Y. Sun, T. Qian, J. Liu, X. Liu, F. Rosei, and C. Yan, *Energy Storage Mater.*, **26**, 385 (2020).
27. T. Waldmann and M. Wohlfahrt-Mehrens, *Electrochim. Acta*, **230**, 454 (2017).
28. T. Waldmann, J. B. Quinn, K. Richter, M. Kasper, A. Tost, A. Klein, and M. Wohlfahrt-Mehrens, *J. Electrochem. Soc.*, **164**, A3154 (2017).
29. Y. Tian, C. Lin, H. Li, J. Du, and R. Xiong, *Appl. Energy*, **300**, 117386 (2021).
30. Z. Li, J. Huang, B. Yann Liaw, V. Metzler, and J. Zhang, *J. Power Sources*, **254**, 168 (2014).
31. S. S. Zhang, K. Xu, and T. R. Jow, *J. Power Sources*, **160**, 1349 (2006).
32. T. Waldmann, B.-I. Hogg, M. Kasper, S. Grolleau, C. G. Couceiro, K. Trad, B. P. Matadi, and M. Wohlfahrt-Mehrens, *J. Electrochem. Soc.*, **163**, A1232 (2016).
33. C. von Lüders, V. Zinth, S. V. Erhard, P. J. Osswald, M. Hofmann, R. Gilles, and A. Jossen, *J. Power Sources*, **342**, 17 (2017).
34. S. Schindler, M. Bauer, M. Petzl, and M. A. Danzer, *J. Power Sources*, **304**, 170 (2016).
35. N. Legrand, B. Knosp, P. Desprez, F. Lapicque, and S. Raël, *J. Power Sources*, **245**, 208 (2014).
36. D. Aurbach, I. Weissman, A. Schechter, and H. Cohen, *Langmuir*, **12**, 3991 (1996).
37. N. Ghanbari, T. Waldmann, M. Kasper, P. Axmann, and M. Wohlfahrt-Mehrens, *J. Phys. Chem. C*, **120**, 22225 (2016).
38. H. Honbo, K. Takei, Y. Ishii, and T. Nishida, *J. Power Sources*, **189**, 337 (2009).
39. A. Friesen, F. Horsthemke, X. Mönnighoff, G. Brunklaus, R. Krafft, M. Börner, T. Risthaus, M. Winter, and F. M. Schappacher, *J. Power Sources*, **334**, 1 (2016).
40. E. Moyassari, T. Roth, S. Kücher, C.-C. Chang, S.-C. Hou, F. B. Spingler, and A. Jossen, *J. Electrochem. Soc.*, **169**, 10504 (2022).
41. M. Jiao, Y. Wang, C. Ye, C. Wang, W. Zhang, and C. Liang, *J. Alloys Compd.*, **842**, 155774 (2020).
42. Y. Jiang, G. Offer, J. Jiang, M. Marinescu, and H. Wang, *J. Electrochem. Soc.*, **167**, 130533 (2020).
43. T. Waldmann, R.-G. Scurtu, K. Richter, and M. Wohlfahrt-Mehrens, *J. Power Sources*, **472**, 228614 (2020).
44. T. Waldmann, S. Rössler, M. Blessing, R. Schäfer, R.-G. Scurtu, W. Braunwarth, and M. Wohlfahrt-Mehrens, *J. Electrochem. Soc.*, **168**, 090519 (2021).
45. E. Markevich, G. Salitra, and D. Aurbach, *ACS Energy Lett.*, **2**, 1337 (2017).
46. C. Xu, F. Lindgren, B. Philippe, M. Gorgoi, F. Björefors, K. Edström, and T. Gustafsson, *Chem. Mater.*, **27**, 2591 (2015).
47. J. C. Burns, R. Petibon, K. J. Nelson, N. N. Sinha, A. Kassam, B. M. Way, and J. R. Dahn, *J. Electrochem. Soc.*, **160**, A1668 (2013).
48. H. Kim, K. E. Kweon, C.-Y. Chou, J. G. Ekerdt, and G. S. Hwang, *J. Phys. Chem. C*, **114**, 17942 (2010).
49. C.-Y. Chou, H. Kim, and G. S. Hwang, *J. Phys. Chem. C*, **115**, 20018 (2011).
50. O. I. Malyi, T. L. Tan, and S. Manzhos, *Appl. Phys. Express*, **6**, 27301 (2013).
51. W. Wan, Q. Zhang, Y. Cui, and E. Wang, *Journal of physics: Condensed matter*, **22**, 415501 (2010).
52. Z. Wang, Q. Su, H. Deng, W. He, J. Lin, and Y. Q. Fu, *J. Mater. Chem. A*, **2**, 13976 (2014).
53. K. Persson, V. A. Sethuraman, L. J. Hardwick, Y. Hinuma, Y. S. Meng, A. van der Ven, V. Srinivasan, R. Kostecki, and G. Ceder, *J. Phys. Chem. Lett.*, **1**, 1176 (2010).
54. K. Persson, Y. Hinuma, Y. S. Meng, A. van der Ven, and G. Ceder, *Phys. Rev. B*, **82**, 125416 (2010).
55. V. Zinth, C. von Lüders, M. Hofmann, J. Hattendorff, I. Buchberger, S. Erhard, J. Rebelo-Kornmeier, A. Jossen, and R. Gilles, *J. Power Sources*, **271**, 152 (2014).
56. C. Uhlmann, J. Illig, M. Ender, R. Schuster, and E. Ivers-Tiffée, *J. Power Sources*, **279**, 428 (2015).
57. T. Waldmann, M. Wilka, M. Kasper, M. Fleischhammer, and M. Wohlfahrt-Mehrens, *J. Power Sources*, **262**, 129 (2014).
58. X.-G. Yang and C.-Y. Wang, *J. Power Sources*, **402**, 489 (2018).
59. M. Bozorgchenani, G. Kucinskis, M. Wohlfahrt-Mehrens, and T. Waldmann, *J. Electrochem. Soc.*, **169**, 30509 (2022).
60. G. Kucinskis, M. Bozorgchenani, M. Feinauer, M. Kasper, M. Wohlfahrt-Mehrens, and T. Waldmann, *J. Power Sources*, **549**, 232129 (2022).
61. R. V. Bugga and M. C. Smart, *ECS Trans.*, **25**, 241 (2010).
62. C. von Lüders, J. Keil, M. Webersberger, and A. Jossen, *J. Power Sources*, **414**, 41 (2019).
63. M. Petzl and M. A. Danzer, *J. Power Sources*, **254**, 80 (2014).
64. C. Hogrefe, T. Waldmann, M. Hölzle, and M. Wohlfahrt-Mehrens, *J. Power Sources*, **556**, 232391 (2023).
65. S. Hein and A. Latz, *Electrochim. Acta*, **201**, 354 (2016).
66. T. Danner, M. Singh, S. Hein, J. Kaiser, H. Hahn, and A. Latz, *J. Power Sources*, **334**, 191 (2016).

3.3. Observation of preferential sputtering on Si/Graphite anodes for Li-ion cells by GD-OES and its validation by neutron depth profiling

Reprinted with permission from:

I. Pivarníková [a,b,=], **M. Flügel** [c,=], N. Paul [a], A. Cannavo [d], G. Ceccio[d], J. Vacík[d], P. Müller-Buschbaum [a,b], M. Wohlfahrt-Mehrens [c], R. Gilles [a], T. Waldmann[c], 2024 *J. Power Sources* **594** 233972

[=] equal contribution

[a] Heinz Maier-Leibnitz Zentrum (MLZ), Technical University of Munich, Lichtenbergstr.1, 85748 Garching, Germany

[b] Technical University of Munich, TUM School of Natural Sciences, Department of Physics, Chair for Functional Materials, James-Franck-Str. 1, 85748 Garching, Germany

[c] ZSW – Zentrum für Sonnenenergie- und Wasserstoff-Forschung, Baden-Württemberg, Helmholzstraße 8, 89081 Ulm, Germany

[d] Nuclear Physics Institute, Academy of Sciences of the Czech Republic, CZ-25068 Řež, Czech Republic

© 2023 Elsevier B.V. All rights reserved.

DOI: https://doi.org/10.1016/j.jpowsour.2023.233972

Individual Contribution

I. Pivarníková	Conceptualization, Methodology, Validation, Investigation, Writing - Original Draft, Visualization
M. Flügel	Conceptualization, Methodology, Validation, Investigation, Writing - Original Draft, Visualization
N. Paul	Conceptualization, Methodology, Validation, Investigation, Linguistic support, Writing – Review & Editing
A. Cannavo	Investigation
G. Ceccio	Investigation
J. Vacík	Investigation
P. Müller-Buschbaum	Writing – Review & Editing, Supervision
M. Wohlfahrt-Mehrens	Supervision
R. Gilles	Conceptualization, Writing – Review & Editing, Supervision
T. Waldmann	Conceptualization, Writing – Review & Editing, Supervision, Project administration, Funding acquisition

Summary

In this publication, Li depth profiles of four differently aged Si/graphite anodes were measured and compared using Glow Discharge Optical Emission Spectroscopy (GD-OES) and Neutron Depth Profiling (NDP) techniques. GD-OES is a destructive method that involves sputtering off the sample in layers using an Ar plasma. The emitted light from the excited sample atoms in the plasma is then analyzed using optical emission spectroscopy to detect element-specific wavelengths. In contrast, NDP is a non-destructive method based on the reaction of ^{6}Li isotopes with neutrons, with the detection of the fission products ^{4}He and ^{3}H and their energy using detectors. The aim of this comparison was to enhance the accuracy of the GD-OES method for depth profiling of Li in electrodes.

The measurements were performed on the following four types of anodes: A) Aged at 0 °C to 60% SOH, which induced Li plating, B) Fresh anode at 100% SOH, C) aged at 45 °C to 90% SOH and D) aged at 45 °C to 76% SOH.

In the case of the sample with Li plating on the anode surface, the sputter rate of the Li layer was found to exceed that of graphite. Consequently, due to the accelerated removal of Li, its layer thickness in the GD-OES depth profile was incorrectly determined to be too low. A new method based on the proportionality of Ar intensity to sputter rate was introduced to accurately convert sputter time to sputter depth. Due to the higher sputter rate, the sample atom density in the plasma increases, resulting in increased excitation of Ar atoms by collisions. As the concentration of Ar is kept constant, the intensity increase corresponds to the increase of the sputter rate. Excellent agreement was obtained between the Li depth profiles of GD-OES and NDP using the adapted method.

As described in the previous publication, the Li content in the anodes can increase sharply with progressive aging, especially due to SEI thickening of Si particles. The calibration range of Li is narrow since Li compounds are limited in incorporation into calibration samples due to low solubility or high reactivity. To validate the quality of the calibration, the depth profiles were measured for samples whose bulk Li content exceeds the calibration range. A good agreement of the Li depth profiles between GD-OES and NDP was determined for the bulk. As expected, the Li content increases with increasing state of aging. However, a higher Li concentration with GD-OES compared to NDP was determined at the surface to a depth of about 10 µm. As a result of preferential sputtering, the Li rich SEI layer is sputtered faster than graphite and Si due to the higher sputter rate of Li.

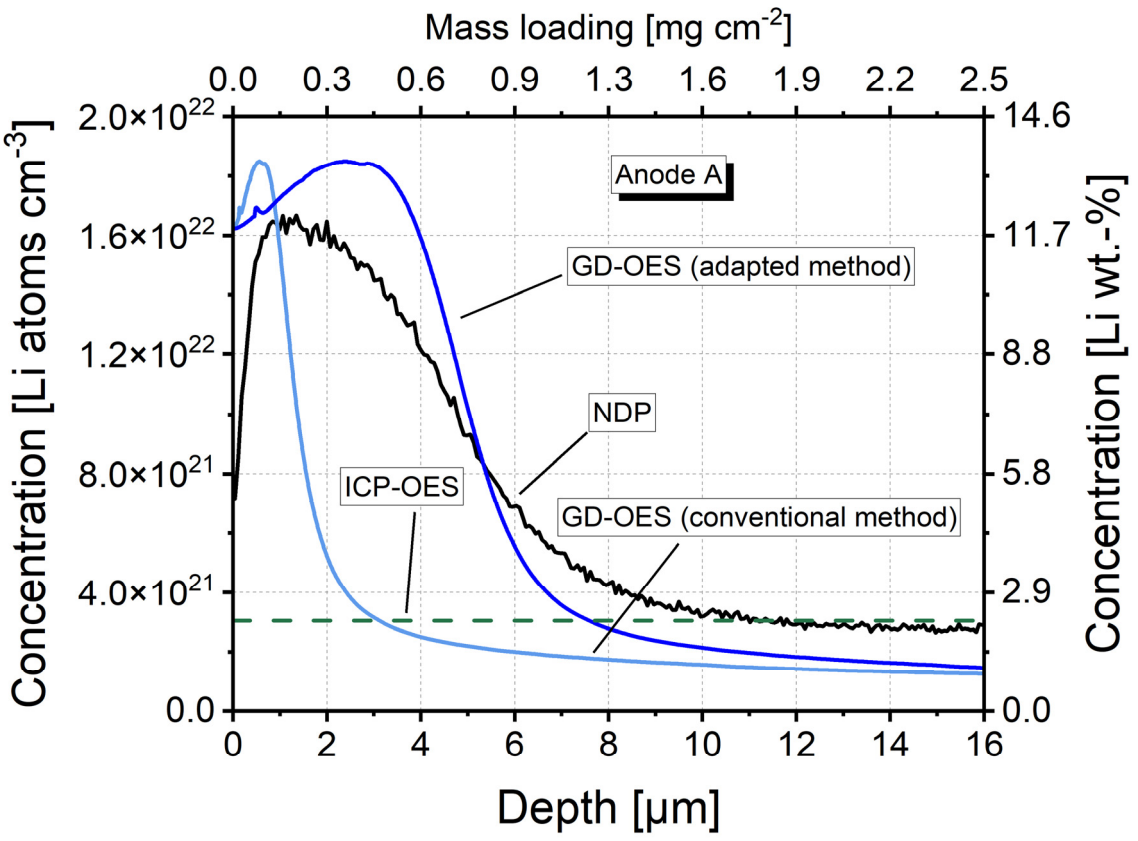

Figure 11: GD-OES and neutron depth profile of a Si/graphite anode with Li plating on the anode surface [4].

Journal of Power Sources 594 (2024) 233972

Contents lists available at ScienceDirect

Journal of Power Sources

journal homepage: www.elsevier.com/locate/jpowsour

Observation of preferential sputtering of Si/graphite anodes from Li-ion cells by GD-OES and its validation by neutron depth profiling

Ivana Pivarníková [a,b,1], Marius Flügel [c,1], Neelima Paul [a,*], Antonino Cannavo [d], Giovanni Ceccio [d], Jiří Vacík [d], Peter Müller-Buschbaum [a,b], Margret Wohlfahrt-Mehrens [c,e], Ralph Gilles [a], Thomas Waldmann [c,e]

[a] Heinz Maier-Leibnitz Zentrum (MLZ), Technical University of Munich, Lichtenbergstr.1, 85748, Garching, Germany
[b] Technical University of Munich, TUM School of Natural Sciences, Department of Physics, Chair for Functional Materials, James-Franck-Str. 1, 85748, Garching, Germany
[c] ZSW – Zentrum für Sonnenenergie- und Wasserstoff-Forschung, Baden-Württemberg, Helmholzstraße 8, 89081, Ulm, Germany
[d] Nuclear Physics Institute, Academy of Sciences of the Czech Republic, CZ-25068, Řež, Czech Republic
[e] HIU - Helmholtz Institute Ulm for Electrochemical Energy Storage, Helmholtzstrasse 11, 89081 Ulm, Germany

HIGHLIGHTS

- Li depth profiling of anodes by complementary methods of NDP and GD-OES.
- Determination of Li plating and SEI growth mostly on the anode surface.
- Characterization of preferential Li sputtering in GD-OES depth profiling.
- Method improvement for GD-OES including preferential sputtering via Ar lines.
- Method validation of NDP and GD-OES with Li depth profiles.

ARTICLE INFO

Keywords:
Lithium-ion batteries
Neutron depth profiling (NDP)
Glow discharge optical emission spectroscopy (GD-OES)
Post-mortem analysis
Lithium plating
SEI growth
Aging mechanism
Si/graphite anodes

ABSTRACT

Although the loss of Li inventory (LLI) is a common aging mechanism in Li-ion batteries, there are only few methods capable of comprehensive depth profiling within the bulk of the electrode to locate the residual Li. Two post-mortem analytical methods, which can be used to obtain quantified Li depth profiles to depths greater than 10 μm from the electrode surface are neutron depth profiling (NDP) and glow discharge optical emission spectroscopy (GD-OES). In this work, the validation of GD-OES using NDP by examining the Si/graphite anodes of cylindrical 21700 cells is presented. One anode was in a pristine/fresh state, two anodes were aged to the state of health (SOH) 90% and 76% at 45 °C respectively, and suffered from heavy solid electrolyte interphase (SEI) growth, and the fourth anode was aged to SOH 60% at 0 °C and exhibited Li plating. It is demonstrated that Li plating leads to a faster sputter rate of the Li-rich anode surface. An adapted method is introduced to incorporate the changing sputter rate into the depth profile calculation. For the aged anodes, the progressive aging of the anodes leads to a higher amount of irreversibly bound Li on the anode surface.

1. Introduction

Due to the increasing demand for lithium-ion batteries with high-energy density, many efforts have been made in recent decades to develop novel batteries. Thanks to their high theoretical capacity, low cost and abundant natural resources, silicon-based materials have been one of the best candidates to increase the capacity and performance of the battery anodes [1–3]. The Si/graphite composite anodes received much attention, because they combine the high capacity of silicon with the mechanical stability of conventional graphite [4,5]. Up to 4 wt.-% Si is used in anodes of commercial cells [6]. However, during (de-)lithiation, silicon particles undergo significant morphological changes,

* Corresponding author.
E-mail address: Neelima.Paul@frm2.tum.de (N. Paul).
[1] Equal contribution.

https://doi.org/10.1016/j.jpowsour.2023.233972
Received 15 March 2023; Received in revised form 29 November 2023; Accepted 10 December 2023
Available online 9 January 2024
0378-7753/© 2023 Elsevier B.V. All rights reserved.

which result in an ongoing decomposition of electrolyte at the solid electrolyte interface (SEI) [7]. To better understand the underlying reversible and irreversible degradation processes in Si/graphite electrodes, depth-resolved methods need to be used to obtain information on the decomposition products of the lithium-containing electrolyte across the electrode thickness.

Neutron depth profiling (NDP) is a non-destructive nuclear analytical method, which is used for obtaining quantitative depth specific information of relevant elements in various types of solid materials [8]. Upon irradiation of the material by thermal neutrons, specific isotopes of several light nuclides can emit charged particles after neutron capture: ^{3}He, ^{6}Li, ^{10}B, ^{14}N, ^{17}O, ^{33}S, ^{35}Cl and ^{40}K, including some radioactive nuclides such as: ^{7}Be, ^{22}Na and ^{59}Ni [8]. Because of its high sensitivity for ^{6}Li, NDP has become a well-established technique for the quantification of Li concentration depth profiles in battery electrodes [9]. The following nuclear reaction of a neutron with a ^{6}Li isotope takes place, producing alpha (α) and triton (^{3}H) particles at well-defined energies (Fig. 1a):

$$^{6}\mathrm{Li} + \mathrm{n} \rightarrow \alpha(2055.55\ \mathrm{keV}) + {}^{3}\mathrm{H}\ (2727.92\ \mathrm{keV}) \quad (1)$$

These charged particles gradually lose energy as they penetrate the material before emerging at the sample surface. The energy loss depends on their path length, material composition and the density. The Li concentration depth profile is obtained from the residual energy spectrum of emerged particles [10].

In contrast, glow discharge optical emission spectroscopy (GD-OES) is a spectroscopic method in which a selected area on the sample is sputtered off in a controlled manner and excited in the GD plasma to emit visible light. GD-OES can be used for both qualitative and, with suitable calibration, quantitative elemental analysis of almost all elements in solid samples as a function of depth. Fig. 1b schematically shows the measurement setup of the GD-OES. The sample is placed in electrical contact with the GD-OES cathode opposite to the GD-OES anode. The hollow anode is filled with the discharge gas, e.g. Ar. A high voltage between the sample and the anode releases electrons from the sample, which are accelerated to the anode. Ar atoms are ionized upon collision with the accelerated electrons and subsequently accelerated towards the sample due to their positive charge. Due to the impact of the Ar ions on the sample, the atoms of the sample are sputtered and migrate into the plasma. There they are electrically excited by collisions with electrons and Ar atoms and emit light during de-excitation. The light is focused by a lens onto a concave grating where it is split into individual wavelengths. Photons of element-specific wavelengths are detected with photomultiplier tubes (PMTs) [11].

Both methods have in common that they can perform quantitative depth profiling of Li and therefore can be used to analyze the Li distribution within electrodes from Li-ion batteries. Furthermore, both methods are complementary to each other since they are based on different measurement principles. In Table 1, the main advantages and disadvantages are listed to provide an overview of measuring principles and limitations for each method.

NDP is becoming widely used in Li-ion battery research, where it is applied to complement conventional electrochemical analysis [12–17]. It provides combined information about Li content originating from all lithium-containing compounds in the analyzed electrodes, such as SEI and the lithiated active materials. For example, Wetjen et al. provided insights into depth–resolved information on the reversible and irreversible processes occurring during the formation cycle of Si/graphite electrodes, where both initial SEI formation and ongoing electrolyte decomposition occur uniformly throughout the electrode thickness [12].

Table 1
List of main advantages and disadvantages for the comparison of NDP and GD-OES methods.

NDP	GD-OES
+ non-destructive: counting of particles arising from thermal neutron reaction with ^{6}Li, no external effect of beam/sample interaction	- destructive: effects caused by surface ablation, Ar plasma/sample interaction
- sensitive only to specific isotopes of a few light elements, such as ^{3}He, ^{6}Li, ^{10}B or ^{14}N	+ sensitive to more or less all elements, except F
- neutron facility/proposal needed: longer waiting times	+ laboratory technique: easily available
+ precise Li content determination possible with reference standards	- limited time dependent depth determination
- accessible depth decreases with increasing sample density	+ accessible depth independent on sample density
+ Li content information averaged over the entire sample area can be obtained in the single measurement (sample size up to 20 mm in diameter for battery materials)	- only small sample area is measured (2–4 mm in diameter for battery materials)

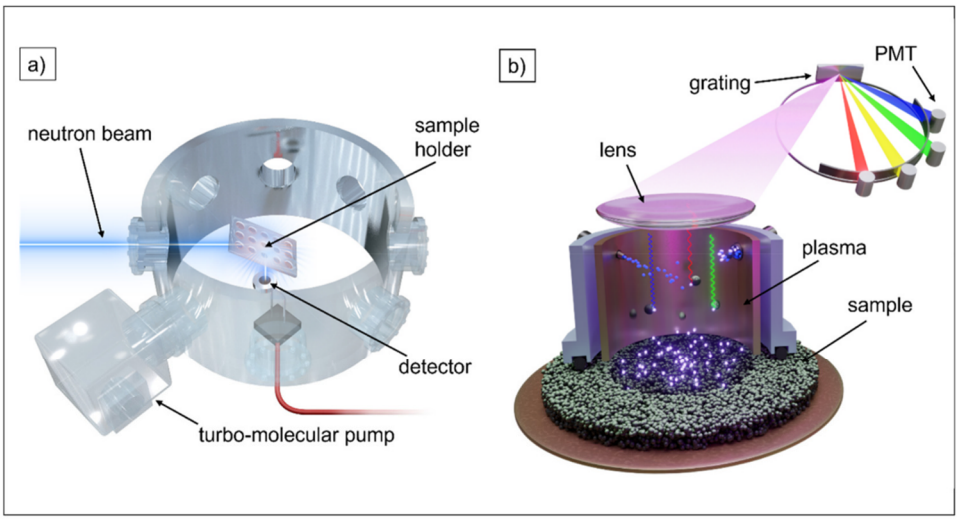

Fig. 1. Schematic comparison of neutron depth profiling (a) and glow discharge optical emission spectroscopy (b) methods: a) The sample is placed in the middle of the vacuum chamber and the detector collects charged particles arising from the ^{6}Li(n,^{4}He)^{3}H nuclear reaction. b) The sample is placed before the plasma chamber and Ar ions sputter off sample atoms. Those atoms are excited in the plasma and emit light, which is recorded with photomultiplier tubes (PMTs).

Moyassari et al. investigated the (de-)intercalation phenomena in Si/graphite porous anodes for the first time using ex-situ NDP during the initial discharge at defined depths of the discharge state [13]. Due to its non-destructive nature, the NDP can also be used for *operando* experiments. Linsenmann et al. developed a novel cell design to obtain information on lithium distribution across the electrode during battery operation [14]. Moreover, Lyons et al. performed *in situ* lithiation of micron-scale Sn foils at a constant potential using a customized Li-ion coin cell design. Lithium diffusion constants were calculated using Fick's 1st and 2nd laws, based on the temporal and spatial changes in Li concentration [15]. In addition, Tomandl et al. successfully investigated migration of Li during the lithiation/delithiation process in ceramic solid electrolytes [16,17].

GD-OES has also been successfully applied to battery electrodes, as well. However, it is a destructive method that creates a crater in the electrode by sputtering with Ar ions. Saito et al. performed the first studies with GD-OES on aged electrodes to investigate the power fading mechanism [18]. Later, Takahara et al. studied the distribution of elements both qualitatively and quantitatively in anodes [19,20]. Takahara et al. demonstrated the application of GD-OES for analysis of SEI and detection of Mn deposition, and studied the effect of small amounts of O_2 or H_2 added to the discharge gas [21,22]. Ghanbari et al. developed a method to detect Li deposition on graphite anodes and studied the inhomogeneous aging of graphite anodes [23,24]. Subsequently, Richter et al. extended the application of GD-OES to state-of-the-art Si/graphite anodes by developing a new calibration for Si content from 0 to 100 wt.-%. The new method was then used to study the aging of Si/graphite anodes and the formation of Si-rich films on the anode surface [25–27]. Recently, Flügel et al. presented a method to determine the minimum amount of elemental Li on Si/graphite anodes [6]. As in Ghanbari et al. [23,24], the method is based on the assumption that Li is bound in the SEI as Li_2O and additionally on the assumption of partially oxidized SiO_x [6]. With the help of all these semi-quantitative GD-OES methods, aging phenomena were detected on the anode surface, i.e. the SEI formation on graphite [23,28] and Si/Graphite anodes [6,26], Li plating on graphite [23,24,29,30] and Si/graphite anodes [6] and Cu re-deposition near the separator [31,32]. These results are consistent with the results obtained by other experimental methods such as cross-sectional *in situ* optical microscopy [33] and Nuclear Magnetic Resonance (NMR) [34], in the case of Li plating with the performed simulations [35]. In some samples, preferential sputtering in GD-OES can occur when different elements in the sample have varying sputter yields. Sputter yield refers to the number of atoms sputtered per incident ion [36]. If the sputter yield is higher for one element compared to another, the element with the higher sputtering yield will be preferentially sputtered, leading to changes in the elemental composition of the surface. So far, preferential sputtering has been studied most extensively in binary samples, in which preferential sputtering leads to a depletion on the surface of the element with the higher sputtering yield [36,37].

Most GD-OES calibration samples were fabricated in-house in a way similar to the fabrication of real electrodes to avoid matrix effects [38]. The calibration samples are graphite coatings with added Li-containing compounds synthesized by aqueous preparation. Due to the reactivity of many Li compounds, calibration samples are limited to 1.34 wt.-% Li, while the Li content in strongly aged anodes exceeds the calibration range.

Other methods commonly used in the elemental analysis of Li-ion batteries include inductively coupled plasma optical emission spectroscopy (ICP-OES), secondary ion mass spectroscopy (SIMS), X-ray photoelectron spectroscopy (XPS) and energy dispersive X-ray spectroscopy (EDX). However, compared to NDP and GD-OES in terms of quantitative analysis of Li depth profile, they have decisive disadvantages. Due to the method of sample collection, ICP-OES cannot provide depth-resolved information [39]. Cross-sections of samples can be obtained using an Ar-ion mill or a focused ion beam, however detection of Li with EDX is not yet possible [40]. XPS and SIMS are surface sensitive methods that can sputter off the samples, but only at a very low sputter rate of 1–10 nm/min [41,42]. In addition, quantification with both methods is very complicated due to the difficult preparation of the reference sample, the surface conditions of the sample and the influence of primary ions.

In this work, we focus on the comparison of the two methods, NDP and GD-OES, for the determination of Li concentration profiles in Si/graphite anodes. Measurements were performed on both fresh and aged Si/graphite anodes to address the GD-OES calibration accuracy issues beyond the calibration range, as well as the influence of their non-destructive (NDP) and destructive (GD-OES) properties on the experimental results.

2. Experimental section

2.1. Electrode characteristics

The studied electrodes are Si/graphite anodes from commercially available 21700 cells with a nominal capacity of 4.85 Ah, a voltage range of 2.5–4.2 V and the maximum charging rate of 0.7C. The thickness of the anode coating is 92 μm with a density of 1.58 g cm^{-3} and porosity is 25.8% in all anodes. The Si amount in the anodes is 3.5 wt.-%. The electrochemical investigations were carried out with Basytec CTS systems and climatic chambers (Vötsch) at ZSW. Aging details of cells, from which anodes A – D were extracted, are summarized in Table 2. The effect of aging on all anodes is schematically shown in Fig. 2. High-temperature aging causes increasing SEI formation for anodes B and C. Low-temperature aging is accompanied by Li plating in case of anode A.

The cells had a voltage of 3.6 V and were at the state of charge (SOC) of 30% when delivered. Formation cycle was performed by the manufacturer. Before cell opening, all cells were discharged at 0.1C at room temperature to 2.5 V (SOC 0%) to extract all anodes in their delithiated state. In this way, all cyclable Li was removed from the anode and the residual Li was expected to be the Li trapped within the SEI, which was also present both at the surface and within the anode bulk due to its porosity. The cell, from which the anode A was extracted, was opened in the glovebox under Ar atmosphere due to the expected Li plating on the anode, while cells, from which anodes B – D were extracted, were opened under ambient conditions. All electrodes were washed three times with dimethyl carbonate (DMC) for 1 min each to remove residual conducting salt.

A 16 mm sample was punched out of each anode from the same central position for NDP examination. GD-OES measurements were performed on electrode areas directly adjacent to the punched-out position. In addition, GD-OES measurements were performed only after the samples arrived at the NDP measurement site to ensure that there were no time dependent effects on the Li concentration measurements.

2.2. Neutron depth profiling

The NDP measurements were performed on the TNDP spectrometer of the NPI CANAM infrastructure at the nuclear research reactor LVR15 in Řež (operated by the Research Center Řež). The TNDP spectrometer is installed on a short vertically curved neutron guide (SwissNeutronics) filtering a beam of the well-thermalized parallel neutrons (Cd ratio ≈

Table 2
Summary of the aging programs of the four cells with the temperature of the climatic chamber, the charge and discharge rate, and the number of cycles until the SOH was reached.

Anode	Temperature	Charging	Discharging	Cycles	SOH
A	0 °C	1C (CCCV)	1C (CC)	34	60%
B	–	–	–	0	100%
C	45 °C	0.5C (CCCV)	0.5C (CC)	180	90%
D	45 °C	0.4C (CCCV)	0.5C (CC)	580	76%

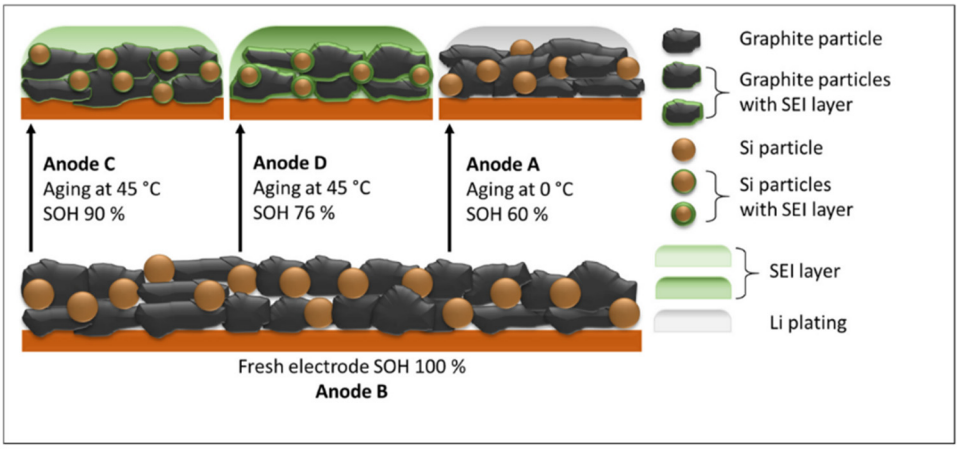

Fig. 2. Schematic summary of four types of analyzed anodes. High-temperature aging causes increasing SEI formation at the electrode shown as a green film. Low-temperature aging is accompanied by Li plating, which is displayed as a grey film on the electrode. (For interpretation of the references to colour in this figure legend, the reader is referred to the Web version of this article.)

10^4) with a neutron thermal flux of 6×10^7 n $cm^{-2}s^{-1}$. The TNDP spectrometer consists of a multipurpose vacuum chamber and a set of detection systems [43]. During the measurement the neutron beam irradiates the entire sample with an inclination of about 5° to avoid neutron self-shielding. The $^6Li(n,^4He)^3H$ nuclear reaction (with a high cross-section of 940 b) on the ^6Li atoms in the sample is induced. The reaction products (alpha and triton particles) that are isotropically emitted from the reaction sites are then registered by a fully depleted detector (a type of Canberra-Packard, F50143). The detector is positioned coaxially and parallel to the anode surface at a distance of 55 mm. The principle of the method is schematically shown in Fig. 1a.

The energy spectrum of triton (^3H) was used to determine the Li depth concentration profiles within the electrodes. Measurement time per sample was 8–35 h, depending on lithium content, in order to obtain sufficient statistics (of a few thousands counts per channel). The measurements of the reference standards with known composition were performed to determine the absolute amount of the Li in the anodes. For the energy calibration, i.e. to convert the channel numbers into an energy scale, a small amount (1.21 ± 0.12 μg/cm^2) of isotopically enriched ^6LiF sputtered on a thin Mylar foil was used. The signals of alpha and triton particles are well defined (see Equation (1)) and separated (see Fig. 3a), and therefore both can be used for energy calibration. For the quantity calibration, a round-robin standard with a well-defined ^{10}B content was used. The content of $1.904 \pm 0.015 \times 10^{16}$ $^{10}B/cm^2$ was determined after calibration to the SRM2137 standard [44]. For this reference sample, the monitored reaction is $^{10}B(n,^4He)^7Li$ and the energy spectra is shown in Fig. 3b. The peak positions are slightly down-shifted compared to the theoretical values due to the implantation of ^{10}B into the Si substrate. However, this does not affect the suitability of the standard for quantitative determination of the Li content in anodes. For the analysis of Li concentration in the anode samples, a natural abundance of ^6Li (7.59%) is taken into account [45]. A constant average density is assumed for each anode. The uncertainty in the final Li concentration measured by NDP is estimated to be 10% percent and the depth resolution is 30 nm. The energy loss of tritons in the anodes is calculated using the SRIM (Stopping and Range of Ions in Matter) software, which takes into account different material compositions [46]. The data evaluation was performed using the N4DP software [10,47].

2.3. GD-OES

Glow discharge optical emission spectroscopy (GD-OES) analyses

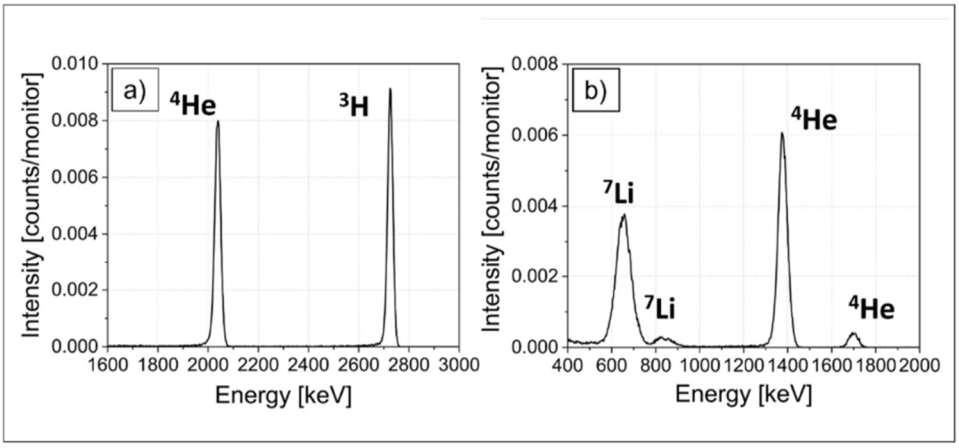

Fig. 3. a) Energy spectrum of $^6Li(n,^4He)^3H$ for the ^6LiF reference sample. b) Energy spectrum of $^{10}B(n,^4He)^7Li$ for the boron reference sample. In both cases, signals of ^4He and ^3H are well separated.

were conducted at ZSW using a GDA750 device (Spectruma) on anode samples. The measurements were performed in radio frequency (RF) mode at a frequency of 2501 Hz, at a discharge voltage of 550 V and at a pressure of 2 hPa. A mixture of 1% H_2 in Ar (both 6.0 purity) was used as a sputter gas. The following element specific emission lines were used for detection: H (121.6 nm), O (130.2 nm), C (156.1 nm), P (178.3 nm), Si (288.1 nm), Li (670.7 nm), Ar (476.5 nm), Ar (696.5 nm), Ar (706.7 nm), Ar (714.7 nm), Ar (727.9 nm). The depth of the crater was determined after a measurement with a Keyence confocal microscope. The Ar lines were detected with a charge-coupled device (CCD) camera while the other lines were detected with photomultiplier tubes (PMTs). The analyzed area has a diameter of 2.5 mm.

2.4. ICP-OES

The inductively coupled plasma optical emission spectroscopy (ICP-OES) measurements were performed at ZSW with an Arcos SOP (Spectro) with Ar 5.0 as carrier gas. For sample collection, the electrode coatings were carefully scraped off from the current collecting foil with a scalpel.

2.5. SEM

Scanning electron microscopy (SEM) of electrodes was carried out at ZSW with a secondary electron (SE) detector at 5 kV using a high-performance LEO 1530 VP (Zeiss) microscope equipped with a Gemini thermal field emission column. EDX mappings were recorded at an acceleration voltage of 10 kV. Cross-sections of anodes were generated with a Hitachi IM4000Plus broad-beam Ar ion milling system, using an ion beam voltage of 5 kV. During sample preparation for SEM top view and cross-section, the samples were exposed to air.

3. Results and discussion

The cell samples chosen were specifically selected to study the effects of anode aging. One cell was disassembled at 100% SOH to determine the Li distribution of a fresh anode. Based on the Li distribution in the unaged state, the changes in Li distribution were investigated after different aging mechanisms. At elevated temperatures, the solid-electrolyte interphase (SEI) decomposes, dissolves or undergoes structural changes, resulting in the reformation of the SEI and a continuous increase in SEI thickness [48]. This phenomenon occurs ubiquitously on the active material within the anode, resulting in an expected homogeneous increase in Li distribution. The SEI accumulates over a significant number of cycles, coinciding with a gradual depletion of the electrolyte. Consequently, as the electrodes dry out, there is a rapid decline in cell capacity. This is in contrast to aging at lower temperatures, at which the Li intercalation is kinetically slowed down. At high charge rates and lower temperatures, the anode potential drops below 0 V vs. Li/Li^+, thermodynamically favoring the deposition of elemental Li [49]. This results in a non-uniform lithium distribution due to the deposition of lithium on the anode surface. Deposited lithium is susceptible to reacting with the electrolyte or may experience electrical disconnection, leading to a decrease in lithium inventory and consequently a significant loss of capacity [50]. These two aging mechanisms were selected in order to be able to compare GD-OES and NDP for the most different anode aging phenomena.

3.1. Detection of Li plating

The comparison between NDP and GD-OES is intended to demonstrate the reliability and accuracy of GD-OES depth profiles. The challenge is the lack of suitable calibration samples with a high Li content. Many aged anode samples have an average Li content or show Li plating, which is beyond the calibration range of GD-OES.

Fig. 4 shows the Li depth profiles of anode A in the range of 0–16 µm

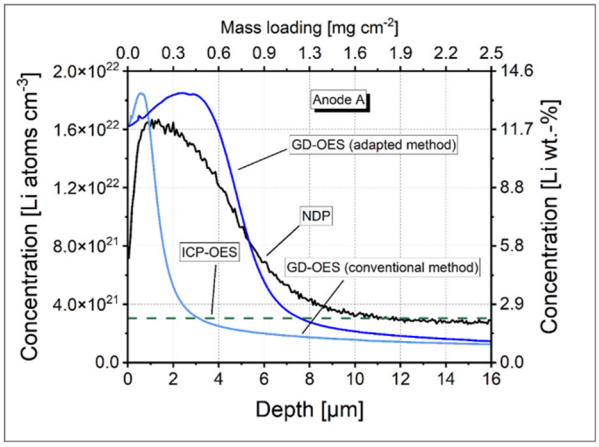

Fig. 4. Comparison of the NDP depth profile (black) with the GD-OES depth profiles of Li using both the conventional method (light blue) and the adapted method (dark blue) for depth calculation for anode A. (For interpretation of the references to colour in this figure legend, the reader is referred to the Web version of this article.)

measured by NDP (black) and GD-OES (light blue and dark blue), starting at 0 µm at the electrode/separator interface. Additionally, the green line indicates the average (i.e. depth independent) Li concentration of the electrode determined by ICP-OES. The graph shows two GD-OES depth profiles whose depth calculation was performed according to the so called "conventional method" (light blue) and with the so called "adapted method" (dark blue) described later.

ICP-OES analysis resulted in an average total Li content of 2.22 ± 0.09 wt.-% corresponding to $3.04 \times 10^{21} \pm 0.12 \times 10^{21}$ Li atoms cm^{-3} from the surface to the current collector. Since this sample was aged at low temperatures, a very inhomogeneous Li distribution can be expected along the depth of the anode. The NDP examination reveals a high Li value in the upper 8 µm from the anode surface, which decreases towards the bulk. The maximum content of the Li plating measured by NDP is 1.67×10^{22} Li atoms cm^{-3} or 12.2 wt.-% with a maximum depth of the Li plating of 6–8 µm. At the depth of 8–16 µm from the surface, the NDP depth profile shows a much lower Li content and is approaching the average value estimated by the ICP-OES in the bulk. Due to the very high Li content at the surface, the Li concentration is slightly below the average bulk Li concentration below a depth of 12 µm. The surface peak in the NDP measurements is in qualitative agreement with previous GD-OES measurements [6,19,20,23–26] and simulations [35] of anodes with Li deposition.

The GD-OES depth profile shows a similar pattern of Li distribution in the electrode. Near the surface the maximum concentration of 13.7 wt.-% (1.8×10^{22} Li atoms cm^{-3}) is found and it decreases rapidly towards the bulk. However, the depth profile of the deposited Li evaluated by the conventional method (light-blue curve in Fig. 4) significantly differs from the NDP measurement. Although the thickness of the Li plating layer is approximately 8 µm with NDP, only approximately 2 µm was determined with GD-OES with the conventional method.

During cycling at low temperatures, the intercalation kinetics decrease and the over-potentials increase. At anode potentials below 0 V vs. Li/Li^+ the deposition of metallic Li is favored over the intercalation of Li into the anode. Recently, we have shown that the addition of Si, which allows the reduction of the anode thickness at constant areal capacity, decreases the risk of Li plating. Anodes containing Si only showed Li plating at higher C-rates than graphite anodes with the same areal capacity. The amount of metallic Li found on this anode might have been reduced by the addition of Si as anode active material [51].

During GD-OES measurement, the mass fraction of each element

versus sputter time is recorded. The conventional method of calculating the sputter depth from the sputter time is based on the assumption that the sputter rate is constant. The sputter rate should be indeed constant if the elements present in the sample are homogeneously distributed and no preferential sputtering is occurring. However, because the sputter rate of the Li-rich layer in the anode is much higher than that of the graphite, the GD-OES analysis with the conventional method gives a thickness of only approximately 2 μm, while the actual thickness is about 8 μm.

In order to confirm the thickness of the Li plating layer determined by NDP using another method, we acquired SEM and EDX images of the cross-section of anode A. Fig. 5a shows the EDX mapping of the elements C, O and Si at the cross-section of anode A. Due to exposition to air during the sample preparation, the deposited Li could be oxidized, so we can get a hint on Li deposition through the O signal. The image shows that the Li deposition on the anode surface is most likely 6–10 μm thick. This observation is consistent with the NDP depth profile of anode A, in which the Li content drops sharply after 6 μm and the bulk concentration of Li is reached after about 10 μm. Due to the short aging of 34 cycles, no noticeable amount of SEI is seen around the Si particles in the bulk, confirming there is only low Li content in the bulk.

3.2. Further development of GD-OES depth profiling method

The use of complementary methods such as NDP and SEM of cross-sectioned anodes is a complex and expensive analytical approach and it is not available for every GD-OES measurement. Therefore, we were looking for a way to calculate the depth parameter more correctly using the data provided by GD-OES, which takes into account the different sputter rates.

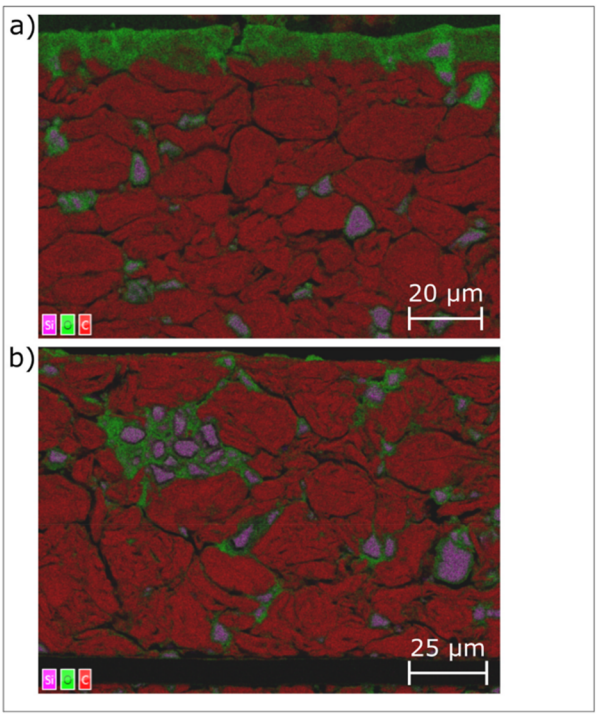

Fig. 5. Cross-sections of anode A (a) and anode D (b) recorded with EDX elemental mapping showing Si (magenta), O (green) and C (red). a) Due to the sample preparation, the Li deposition is oxidized, therefore Li deposition is indicated by the O signal. b) The Si particles exhibit distinctive SEI films due to aging. (For interpretation of the references to colour in this figure legend, the reader is referred to the Web version of this article.)

Here, we present a new adapted method of converting the sputter time into the respective sputter depth based on the intensity of Ar lines, which are simultaneously recorded during measurement with CCD cameras. Ar is used as a sputtering gas and plasma component in every measurement, and it emits light during the measurement. Fig. 6 shows the intensity of the Ar lines at 714.704 nm (red, "Ar715") and 727.294 nm (blue, "Ar727") as well as the Li intensity of anode A, which has Li plating, and anode B, the pristine/fresh anode, which is used as a reference here.

It is obvious that the Ar727, Ar715, and Li intensities behave similarly for both anodes A and B, respectively. Anode B shows a nearly uniform Ar intensity and a constant sputter rate (Fig. 6c). However, the Li-rich surface of anode A causes an increase in Ar intensity during the sputtering of this layer (Fig. 6a). After the Li has been sputtered off from the anode surface, recognizable by the decreasing Li intensity, the Ar intensity also decreases and reaches a stable value, which it maintains for the rest of the measurement. During measurements, sample atoms can be excited by collisions with Ar atoms in the plasma. In the same way, Ar atoms can also be excited by collisions with sample atoms [52]. Due to the increase of the sample concentration in the plasma, caused by the high sputter rate, the probability of collisions increases. In addition, the current increases during the high sputter rates, which also increases the excitation by elastic and inelastic collisions with electrons [53]. Consequently, there is a correlation between the sputter rate and the Ar intensity [54,55].

Parker et al. already found that the intensity of certain Ar lines shows a similar behavior as the sputter rate [54]. We assumed that the intensity of some Ar lines is proportional to the sputter rate for the measurement of porous electrodes. Therefore, the depth d at a point in time can be calculated by the term given in equation (2):

$$d = D\frac{\int_0^z I_{Ar}(t)dt}{\int_0^t I_{Ar}(t)dt} \tag{2}$$

where D is the total depth at the end of the measurement, z is the time, t is the total measurement duration, and I_{Ar} is the intensity of the Ar line. An example of the depth calculation is provided in the Supplementary Information (Fig. S1).

In Fig. 6c, the depth parameter of the anodes A and B is calculated using equation (2) and is plotted as a function of time. It can be seen that for anode A, which has Li plating on the surface, a sputter depth of ~6 μm is achieved in the first 200 s. From 200 s onwards, equilibrium is reached and the increase in depth with time is approximately linear, corresponding to a nearly constant sputter rate. Equilibrium is reached when the excess of Li due to Li plating is removed, and Li, which is still intercalated or present in the SEI can only be removed after being exposed to sputtering ions after the covering graphite is removed. In contrast, anode B shows a uniform sputter rate from the beginning with a crater depth of 2.5 μm achieved after 200 s.

Using the equation presented in equation (2), the depth of anode A is recalculated from the measurement time in Fig. 4 (dark blue curve). The adapted depth calculation provides a significantly improved agreement between the NDP and GD-OES measurements. The maximum Li amount is not affected by the recalculation, only the width of the Li plating peak is increased. This changes the amount of Li plating between 0 and 10 μm from 4.48×10^{22} Li atoms cm^{-3} to $9.99 \times 10^{22} \pm 0.03 \times 10^{22}$ Li atoms cm^{-3} and is very similar to the NDP result of 9.54×10^{22} Li atoms cm^{-3}. The deviation results from the use of the different Ar lines to calculate the depth. Since the results are very similar, any of the Ar lines listed (AR727 for dark blue curve in Fig. 4) can be used for the depth calculation. The amount of detected Li by GD-OES from the surface to the current collector foil is 2.2 wt.-%, compared to 2.22 wt.-% measured by ICP-OES. The reason that the Li content in the 8–16 μm range with GD-OES is below the concentration determined with NDP could be a measurement artifact of the preferential sputtering, which will be described later.

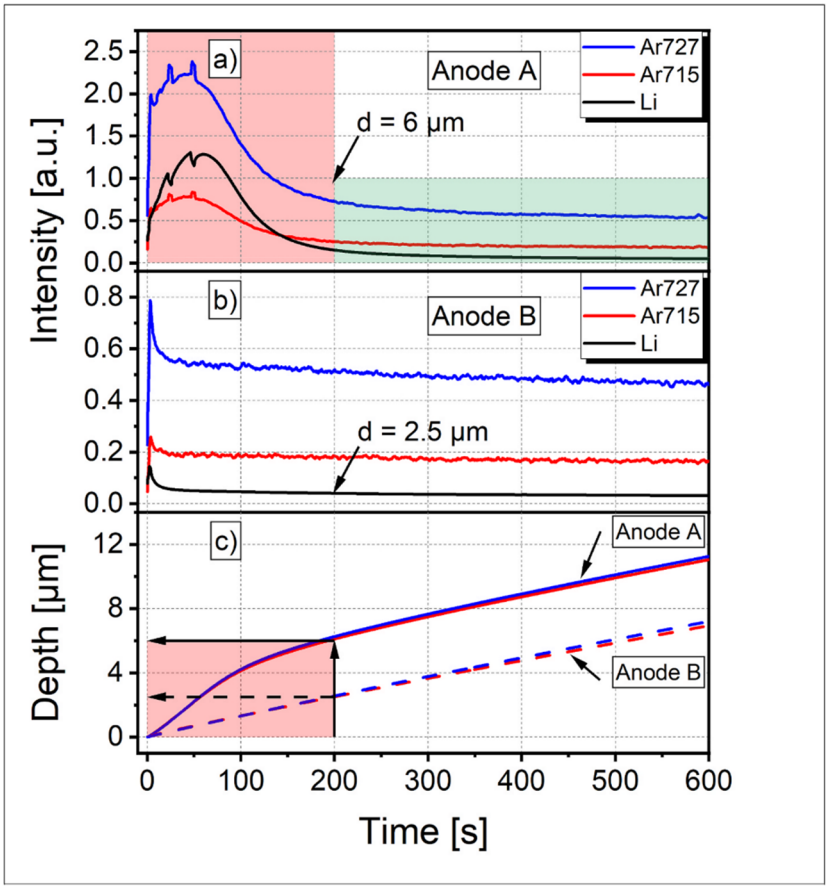

Fig. 6. Plot of Ar and Li intensity versus time for a) anode A and b) anode B, showing that Ar intensities behave similarly to the sputter rate; c) Sputter depth versus sputter time, demonstrating that in anode A a higher sputter depth is reached within the first 200 s before the sample sputter becomes constant.

We note that the previous results with GD-OES methods to quantify Li plating semi-quantitatively on graphite [23,24] and Si/graphite anodes [6] are still valid using the adapted depth calculation. Based on the detected amount of O and Si, these methods determine the minimum amount of elemental Li. However, with the improved depth calculation as presented here, the depth distribution is represented more accurately.

3.3. Detection of SEI growth

Fig. 7a–c shows the NDP and GD-OES depth profiles of anodes B, C, and D. Anode B is the anode of a pristine/fresh cell (100% SOH), while anodes C and D were aged at 45 °C until 90% and 76% SOH, respectively. All cells were fully discharged to the end-of-charge voltage before opening. Therefore, the detected Li corresponds to irreversibly lost Li inventory and residual intercalated Li. In addition to the NDP depth profile (black) and the two GD-OES depth profiles (blue), the average Li content determined by ICP-OES is also plotted as a dashed green line in the graphs. Due to the partial overlapping of alpha and triton particle energies, caused by higher electrode thickness, only the range 0–16 µm is examined using NDP. The ICP-OES analysis results in a Li content of the three samples: 1.56 wt.-% (anode B), 2.16 wt.-% (anode C) and 2.61 wt.-% (anode D). As can be seen, all contents are above the range of 0–1.34 wt.-% Li in the calibration samples of GD-OES. Due to the high irreversible loss of Li to the SEI during formation cycles, particularly due to presence of Si, the percentage of Li in a pristine/fresh, discharged cell is already above 1.35 wt.-%.

All NDP depth profiles show a Li peak on the anode surface and the Li content in the bulk continues to increase with aging. The increased Li content with aging is consistent with Waldmann et al., Iturrondobeitia et al. and Wetjen et al. [28,30,56]. This observation can be attributed to the irreversible binding of Li in the SEI and within the films around the active material particles, especially the Si particles [57,58]. Furthermore, it can be seen that the Li depth profile for anode B is very uniform, while for anode C it exhibits a slight decrease towards the anode bulk, and for anode D, on the contrary a slight increase starting at around 6 µm. Additionally, the Li concentration in the upper 16 µm of the anode are higher than the average Li-level of the electrode, which suggests that the Li gradient may continue even further towards the current collector.

Fig. 5b shows the EDX element mapping of the cross-section of anode D in which O is shown in green, Si in magenta, and C in red. Because the sample was in contact with atmospheric O during the preparation, a reaction with O_2 cannot be excluded. It can be very clearly seen that a thick layer of SEI is formed around the Si particles. The very thick SEI suggests that high amounts of Li are irreversibly bound in the anode, which has been reported in the literature [6,59,60]. Furthermore, it appears that the SEI layer of the particles near the anode surface is thicker than the SEI of the Si particles near the Cu collecting foil, as was already observed by Richter et al. [25,26].

GD-OES measurements are possible through the entire electrode coating up to the Cu current collector foil. Thus, the elemental distribution in the electrode can be measured, and by integration [23], the total amount of an element can be determined. Li concentrations

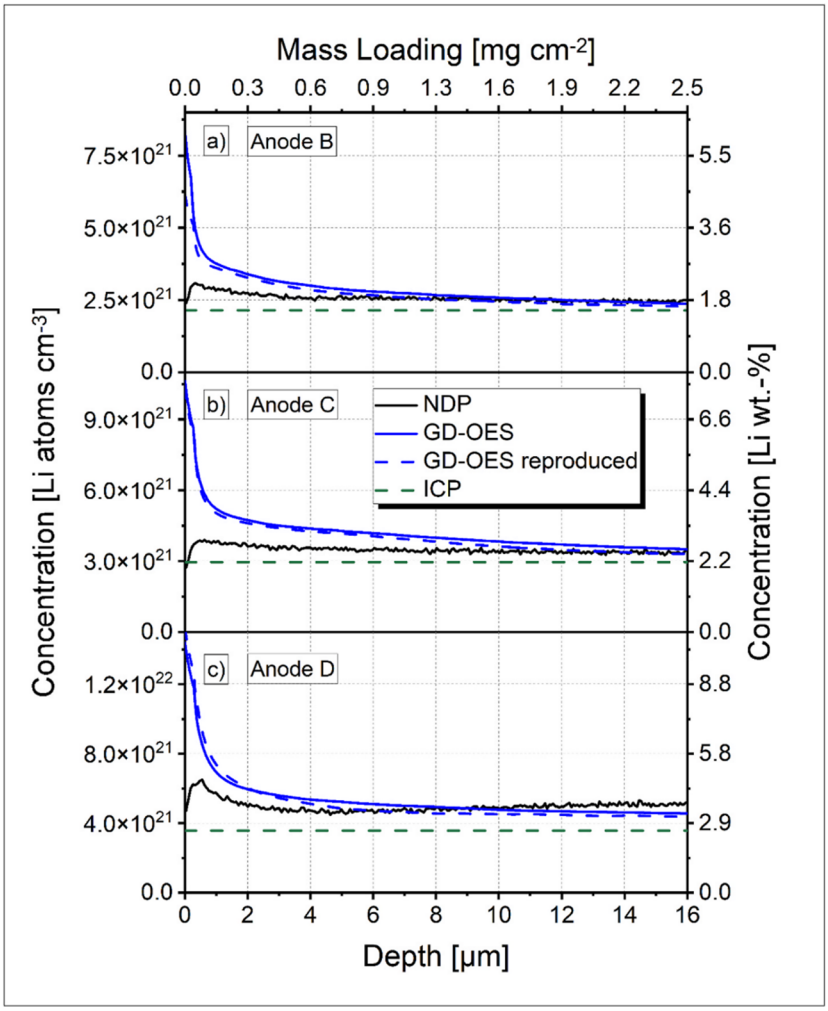

Fig. 7. NDP (black) and GD-OES (blue) depth profiles of anodes B, C and D at a depth of 0 µm (surface) to 16 µm; ICP-OES measurements (green) show the average Li content in the sample. (For interpretation of the references to colour in this figure legend, the reader is referred to the Web version of this article.)

obtained with GD-OES in anodes B, C and D are 1.58 ± 0.08 wt.-%, 2.21 ± 0.18 wt.-% and 2.76 ± 0.22 wt.-%, respectively. For low Li values such as in anode B, the Li concentration determined with GD-OES is close to that measured with ICP-OES. While the difference to the ICP-OES Li concentration increases with aging, the ICP-OES result is within the error range of the GD-OES measurement. Therefore, GD-OES calibration for Li has been shown to provide reliable results even outside its calibration range. For GD-OES measurements of aged anodes, which do not have Li deposition on the surface, the adapted method was not applied. Since Li is distributed in the anode and does not form a separate Li-rich layer on the anode surface, the sputter rate is the same as the carbon sputter rate and therefore is constant throughout the electrode.

In comparison with the NDP depth profiles, it can be seen that the Li peak on the anode surface is also evident in the GD-OES depth profiles, where the peak is more pronounced. In addition, the Li content at the electrode surface measured with GD-OES increases due to progressed aging. From the surface of the anode towards the electrode bulk, a slight difference in the Li concentration is observed in the profiles of both measurement methods. The GD-OES measurement yields higher concentrations in each measurement. The decrease in Li concentration from the surface towards the bulk, detected by NDP, is also observed by GD-OES. Since the decrease in the GD-OES measurements is steeper, the GD-OES and NDP profiling values converge to be equal from 12 µm depth onwards. The Li gradient is caused by the inhomogeneous distribution of Li in the anodes, with more Li found in the SEI near the anode surface. This result is consistent with the findings of Takahara et al., who observed inhomogeneous Li depth profiles in degraded anodes [22].

As discussed, GD-OES and NDP Li depth profiles show consistent results with regard to the Li prominent peak at the anode surface, a higher than average Li content (measured by ICP-OES) on the anode surface, increased Li content due to the aging mechanism, and the Li gradient from the surface toward the bulk.

However, the different Li concentration in the uppermost 10 µm of the anode surface measured with GD-OES and NDP is most likely caused by preferential sputtering [37], which is described and discussed below.

It is evident from Fig. 7a–c that GD-OES depth profiles reveal a higher Li concentration at the surface than NDP measurements. The difference between the NDP and GD-OES concentrations is 1×10^{21} Li atoms cm^{-3} at a depth of 0.5 µm for anode B, however, they both methods measure the same Li concentration at a depth of 6 µm. For anode C, the difference in the Li concentration between GD-OES and NDP is 2×10^{21} Li atoms cm^{-3} at a depth of 0.5 µm and both methods measure the same Li concentration only from a depth of 12 µm. The difference is most serious in anode D, where it is 3×10^{21} Li atoms cm^{-3}

at the anode surface, although even higher Li value can be observed for NDP from a depth of 10 µm.

During preferential sputtering, an element with a high sputter rate is sputtered faster than other elements with a lower sputter rate [37]. The occurrence of this phenomenon is known, for example, in metal oxides, where O is removed faster than the metal atom [61]. This leads to a relative enrichment of the element with a lower sputter rate at the anode surface and additional O can only be sputtered off when the metal atoms are sputtered off beforehand.

In contrast to metal oxides, Li-ion anodes consist of mainly graphite particles, which have a very low sputter rate, and which are covered with Li containing SEI. We found out in section 3.1, that Li has a much higher sputter rate than graphite. However, the anodes B, C and D do not consist of Li-rich layer on the anode surface, but Li is distributed much more uniformly in the anode.

The resulting sputtering process is schematically shown in Fig. 8. When the sputtering process starts, the SEI covering the anode is sputtered off. As the SEI has a high Li content, it results in the Li peak that is observed with GD-OES. Moreover, NDP and SEM confirm the presence of a Li-rich SEI, which is most pronounced at the surface. As the sputtering process proceeds, the anode surface is depleted of the SEI, which means that the SEI located between the graphite particles of the top layer can easily be sputtered off. As illustrated in Fig. 8, compared to the real composition in the anode, the plasma composition exhibits a higher Li content. This is most likely the reason for an increased Li concentration in the GD-OES depth profiles. In addition to the decreasing Li content towards the electrode bulk, we observe a Li depletion on the anode surface, resulting in a steeper Li gradient in the GD-OES depth profiles. Further Li can only be sputtered off when graphite is ablated to expose the SEI layer of the second graphite layer. This equilibrium is the reason why the Li concentration of GD-OES and NDP are the same below a depth of 12 µm as this is approximately the thickness of one graphite particle. The effect of preferential sputtering is more evident in highly aged cells with increasing SEI thickness.

Although we observe preferential sputtering for aged Si/graphite anodes, its consequence for the quality of the results is limited. The phenomenon of preferential sputtering does not lead to increased Li values, as evidenced by the comparison of GD-OES with ICP-OES. The trend of the Li distribution is similar for both methods GD-OES and NDP.

4. Conclusion

In this work, we successfully applied both methods, NDP and GD-OES, to measure depth profiles of Li in Si/graphite anodes after post-mortem analysis of Li-ion batteries. The comparison of the two complementary techniques has served to further improve the GD-OES method for depth profiling of Li in electrodes.

Due to the limited availability of suitable calibration samples with sufficiently high Li mass fraction, validation of the GD-OES method outside the calibration range is necessary. In this work, it is shown that by comparison with ICP-OES that GD-OES, we can reliably determine the Li content by data integration. In addition, by comparison with NDP, we have shown that the distribution of Li as a function of depth can be determined by GD-OES with sufficient accuracy. While the detected concentrations of most elements measured with GD-OES in LIB anodes are within the concentration range of the respective element, the concentrations measured for Li are outside the Li calibration range, as only calibration samples up to 1.34 wt.-% were prepared due to the high reactivity of many Li compounds. Even though the results of the comparison showed that the Li concentration could also be reliably measured outside the calibration range, an option for producing calibration samples with higher Li content is to use lithium compounds with atoms that are not present in LIB or are present in very low concentrations, such as Li chloride or Li nitrate.

We succeed in demonstrating the faster sputtering of Li plating from the anode and in establishing an equation to perform the depth calculation more accurately. The conventional method was based on the assumption of a homogeneous sputter rate, which led to uncertainty regarding the width of the Li plating peak in the GD-OES depth profiles. This bias can be eliminated using the adapted method developed in the present work, since in the case of Li-ion anodes it has been shown that the sputter rate can be approximately modelled by the Ar intensity.

Furthermore, we observe that the preferential sputtering can occur on the anode surface. This phenomenon is caused by the higher sputter rate of Li, as it is mainly present in the Li plating layer or in the SEI near the surface. Although this effect occurred and was observable through the differences in the GD-OES depth profiles from the NDP depth profiles, it did not affect the main results. The NDP measurements showed that the Li content has the highest value at the surface and decreases slightly with depth. This finding is consistent with previous GD-OES and

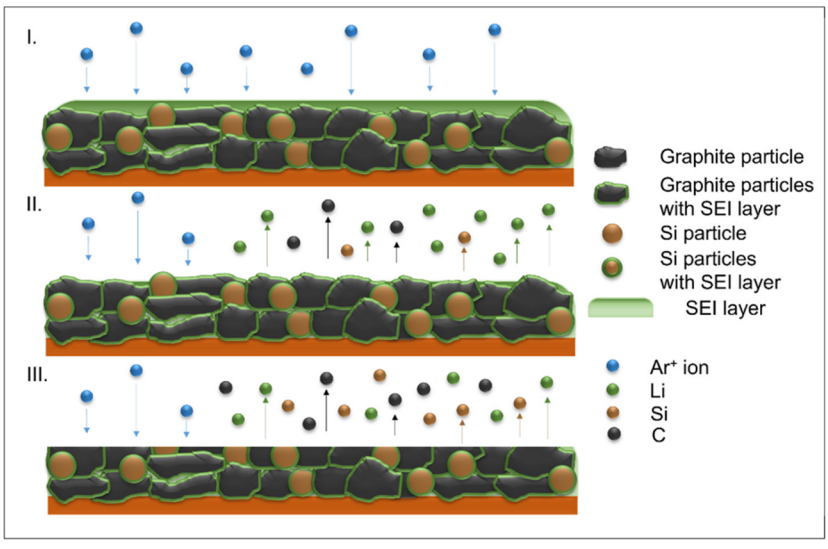

Fig. 8. Schematic explanation of the preferential sputtering phenomenon. I. The surface of the anode sample is bombarded by Ar ions. II. In a Li-containing SEI top layer, Li atoms are preferentially sputtered off. III. In the bulk, equilibrium is established and Li, C and Si atoms are sputtered at the same rates.

NDP results.

CRediT authorship contribution statement

Ivana Pivarníková: Formal analysis, Methodology, Writing – original draft, Writing – review & editing, Investigation. **Marius Flügel:** Formal analysis, Investigation, Methodology, Writing – original draft, Writing – review & editing. **Neelima Paul:** Conceptualization, Formal analysis, Investigation, Methodology, Supervision, Writing – original draft, Writing – review & editing. **Antonino Cannavo:** Methodology, Writing – review & editing. **Giovanni Ceccio:** Methodology, Writing – review & editing. **Jiří Vacík:** Methodology, Resources, Writing – review & editing. **Peter Müller-Buschbaum:** Funding acquisition, Supervision, Writing – review & editing. **Margret Wohlfahrt-Mehrens:** Funding acquisition, Supervision, Writing – review & editing. **Ralph Gilles:** Funding acquisition, Supervision, Project administration, Writing – review & editing. **Thomas Waldmann:** Conceptualization, Funding acquisition, Project administration, Resources, Supervision, Writing – review & editing.

Declaration of competing interest

The authors declare that they have no known competing financial interests or personal relationships that could have appeared to influence the work reported in this paper.

Data availability

Data will be made available on request.

Acknowledgement

I.P. and M.F. contributed equally to this work. The authors acknowledge the German Federal Ministry of Education and Research (BMBF) for funding the project CharLiSiKo (03XP0333A) within the AQua cluster and the project ExZellTUM III (03XP0255) within the ExcellBattMat cluster. Furthermore, the authors thank Reiner Müller (MLZ) for the creation of Fig. 1a, Emanuele Marini (ZSW) for the creation of Fig. 1b, Claudia Pfeifer (ZSW) for EDX measurements and Gisela Arnold (ZSW) for ICP-OES measurements. The NDP measurements were carried out at the NPI and RC infrastructures 'CANAM' and 'Reactors LVR-15 and LR-0' in Řež (CR) supported by Ministry of Education, Youth and Sports of the Czech Republic (projects No. LM2015056 and LM2015074).

Appendix A. Supplementary data

Supplementary data to this article can be found online at https://doi.org/10.1016/j.jpowsour.2023.233972.

References

[1] X.X. Zuo, J. Zhu, P. Muller-Buschbaum, Y.J. Cheng, Nano Energy 31 (2017) 113–143, https://doi.org/10.1016/j.nanoen.2016.11.013.
[2] J.R. Szczech, S. Jin, Energy Environ. Sci. 4 (2011) 56–72, https://doi.org/10.1039/C0EE00281J.
[3] G.G. Eshetu, H. Zhang, X. Judez, H. Adenusi, M. Armand, S. Passerini, E. Figgemeier, Nat. Commun. 12 (2021) 5459, https://doi.org/10.1038/s41467-021-25334-8.
[4] J. Asenbauer, T. Eisenmann, M. Kuenzel, A. Kazzazi, Z. Chen, D. Bresser, Sustain. Energy Fuels 4 (2020) 5387–5416, https://doi.org/10.1039/D0SE00175A.
[5] P. Li, H. Kim, S.-T. Myung, Y.-K. Sun, Energy Storage Mater. 35 (2021) 550–576, https://doi.org/10.1016/j.ensm.2020.11.028.
[6] M. Flügel, K. Richter, M. Wohlfahrt-Mehrens, T. Waldmann, J. Electrochem. Soc. 169 (2022) 050533, https://doi.org/10.1149/1945-7111/ac70af.
[7] J. Kim, O.B. Chae, B.L. Lucht, J. Electrochem. Soc. 168 (2021) 030521, https://doi.org/10.1149/1945-7111/abe984.
[8] R.G. Downing, G.P. Lamaze, J.K. Langland, S.T. Hwang, J. Res. Natl. Inst. Stand. Technol. 98 (1993) 109–126, https://doi.org/10.6028/jres.098.008.
[9] S. Whitney, S.R. Biegalski, Y.H. Huang, J.B. Goodenough, J. Electrochem. Soc. 156 (2009) A886–A890, https://doi.org/10.1149/1.3216033.
[10] M. Trunk, M. Wetjen, L. Werner, R. Gernhauser, B. Markisch, Z. Revay, H. A. Gasteiger, R. Gilles, Mater. Char. 146 (2018) 127–134, https://doi.org/10.1016/j.matchar.2018.09.030.
[11] R.K. Marcus, J.A. Broekaert, Glow Discharge Plasmas in Analytical Spectroscopy, Wiley Online Library, 2003, https://doi.org/10.1002/0470857854.
[12] M. Wetjen, M. Trunk, L. Werner, H.A. Gasteiger, R. Gernhauser, R. Gilles, B. Markisch, Z. Revay, J. Electrochem. Soc. 166 (2019) A1408–A1411, https://doi.org/10.1149/2.0581908jes.
[13] E. Moyassari, L. Streck, N. Paul, M. Trunk, R. Neagu, C.-C. Chang, S.-C. Hou, B. Märkisch, R. Gilles, A. Jossen, J. Electrochem. Soc. 168 (2021) 020519, https://doi.org/10.1149/1945-7111/ac4545.
[14] F. Linsenmann, M. Trunk, P. Rapp, L. Werner, R. Gernhäuser, R. Gilles, B. Märkisch, Z. Revay, H. Gasteiger, J. Electrochem. Soc. 167 (2020), https://doi.org/10.1149/1945-7111/ab9b20.
[15] D.J. Lyons, J.L. Weaver, A.C. Co, J. Mater. Chem. A 10 (2022) 2336–2351, https://doi.org/10.1039/D1TA09639G.
[16] I. Tomandl, J. Vacik, T. Kobayashi, Y. Mora Sierra, V. Hnatowicz, V. Lavreniev, P. Horak, G. Ceccio, A. Cannavo, M. Baba, R. Ye, Radiat. Eff. Defect Solid 175 (2020) 394–405, https://doi.org/10.1080/10420150.2019.1701471.
[17] I. Tomandl, T. Kobayashi, A. Cannavó, J. Vacík, G. Ceccio, T. Sassa, V. Hnatowicz, J. Power Sources 542 (2022) 231719, https://doi.org/10.1016/j.jpowsour.2022.231719.
[18] Y. Saito, M.K. Rahman, J. Power Sources 174 (2007) 877–882, https://doi.org/10.1016/j.jpowsour.2007.06.223.
[19] H. Takahara, H. Miyauchi, M. Tabuchi, T. Nakamura, J. Electrochem. Soc. 160 (2012) A272, https://doi.org/10.1149/2.061302jes.
[20] H. Takahara, M. Shikano, H. Kobayashi, J. Power Sources 244 (2013) 252–258, https://doi.org/10.1016/j.jpowsour.2013.01.109.
[21] H. Takahara, Y. Kobayashi, K. Shono, H. Kobayashi, M. Shikano, T. Nakamura, J. Electrochem. Soc. 161 (2014) A1716, https://doi.org/10.1149/2.1011410jes.
[22] H. Takahara, A. Kojyo, K. Kodama, T. Nakamura, K. Shono, Y. Kobayashi, M. Shikano, H. Kobayashi, J. Anal. Atomic Spectrom. 29 (2014) 95–104, https://doi.org/10.1039/c3ja50183c.
[23] N. Ghanbari, T. Waldmann, M. Kasper, P. Axmann, M. Wohlfahrt-Mehrens, J. Phys. Chem. C 120 (2016) 22225–22234, https://doi.org/10.1021/acs.jpcc.6b07117.
[24] N. Ghanbari, T. Waldmann, M. Kasper, P. Axmann, M. Wohlfahrt-Mehrens, ECS Electrochem. Lett. 4 (2015) A100–A102, https://doi.org/10.1149/2.0041509eel.
[25] K. Richter, T. Waldmann, M. Memm, M. Kasper, M. Wohlfahrt-Mehrens, J. Electrochem. Soc. 165 (2018) A3602, https://doi.org/10.1149/2.0071816jes.
[26] K. Richter, T. Waldmann, M. Kasper, C. Pfeifer, M. Memm, P. Axmann, M. Wohlfahrt-Mehrens, J. Phys. Chem. C 123 (2019) 18795–18803, https://doi.org/10.1021/acs.jpcc.9b03873.
[27] K. Richter, T. Waldmann, N. Paul, N. Jobst, R.G. Scurtu, M. Hofmann, R. Gilles, M. Wohlfahrt-Mehrens, ChemSusChem 13 (2020) 529–538, https://doi.org/10.1002/cssc.201903139.
[28] T. Waldmann, N. Ghanbari, M. Kasper, M. Wohlfahrt-Mehrens, J. Electrochem. Soc. 162 (2015) A1500–A1505, https://doi.org/10.1149/2.0411508jes.
[29] T. Waldmann, J.B. Quinn, K. Richter, M. Kasper, A. Tost, A. Klein, M. Wohlfahrt-Mehrens, J. Electrochem. Soc. 164 (2017) A3154, https://doi.org/10.1149/2.0961713jes.
[30] A. Iturrondobeitia, F. Aguesse, S. Genies, T. Waldmann, M. Kasper, N. Ghanbari, M. Wohlfahrt-Mehrens, E. Bekaert, J. Phys. Chem. C 121 (2017) 21865–21876, https://doi.org/10.1021/acs.jpcc.7b05416.
[31] M. Flügel, M. Kasper, C. Pfeifer, M. Wohlfahrt-Mehrens, T. Waldmann, J. Electrochem. Soc. 168 (2021) 020506, https://doi.org/10.1149/1945-7111/abdc5f.
[32] M. Flügel, T. Waldmann, M. Kasper, M. Wohlfahrt-Mehrens, ChemPhysChem 21 (2020) 2047–2050, https://doi.org/10.1002/cphc.202000333.
[33] C. Hogrefe, T. Waldmann, M. Hölzle, M. Wohlfahrt-Mehrens, J. Power Sources 556 (2023) 232391, https://doi.org/10.1016/j.jpowsour.2022.232391.
[34] B.P. Matadi, S. Geniès, A. Delaille, T. Waldmann, M. Kasper, M. Wohlfahrt-Mehrens, F. Aguesse, E. Bekaert, I. Jiménez-Gordon, L. Daniel, J. Electrochem. Soc. 164 (2017) A1089, https://doi.org/10.1149/2.0631706jes.
[35] S. Hein, A. Latz, Electrochim. Acta 201 (2016) 354–365, https://doi.org/10.1016/j.electacta.2016.01.220.
[36] R. Shimizu, Nucl. Instrum. Methods Phys. Res. Sect. B Beam Interact. Mater. Atoms 18 (1986) 486–495, https://doi.org/10.1016/S0168-583X(86)80074-X.
[37] H. Werner, N. Warmoltz, Surf. Sci. 57 (1976) 706–714, https://doi.org/10.1016/0039-6028(76)90356-3.
[38] R. Payling, T. Nelis, R.F. Browner, J.M. Chalmers, M.S. Cresser, J.J. Monaghan, A. Sanz Medel, R.D. Snook, F. Adams, M.J. Adams, B. Chase, B. Hoving, Glow Discharge Optical Emission Spectroscopy: A Practical Guide, The Royal Society of Chemistry, 2003, https://doi.org/10.1039/9781847550989.
[39] B. Vortmann-Westhoven, M. Winter, S. Nowak, J. Power Sources 346 (2017) 63–70, https://doi.org/10.1016/j.jpowsour.2017.02.028.
[40] I.D. Campbell, M. Marzook, M. Marinescu, G.J. Offer, J. Electrochem. Soc. 166 (2019) A725, https://doi.org/10.1149/2.0821904jes.
[41] Y. Feng, B.M. Koo, A. Seyeux, J. Swiatowska, C. Henry de Villeneuve, M. Rosso, F. Ozanam, ACS Appl. Mater. Inter. 14 (2022) 35716–35725, https://doi.org/10.1021/acsami.2c08203.
[42] S. Oswald, M. Hoffmann, M. Zier, Appl. Surf. Sci. 401 (2017) 408–413, https://doi.org/10.1016/j.apsusc.2016.12.223.

[43] J. Vacik, I. Tomandl, V. Hnatowicz, P. Horak, A. Cannavo, G. Ceccio, D. Fink, T. Kobayashi, Y. Rongbin, M. Baba, In: AIP Conference Proceedings, AIP Publishing LLC, 2019 030005, https://doi.org/10.1063/1.5127680.
[44] NIST, Certificate of Analysis Standard Reference Material 2137, 2010. https://ts apps.nist.gov/srmext/certificates/archives/2137.pdf.
[45] J. Meija, T.B. Coplen, M. Berglund, W.A. Brand, P. De Bièvre, M. Gröning, N. E. Holden, J. Irrgeher, R.D. Loss, T. Walczyk, Pure Appl. Chem. 88 (2016) 293–306, https://doi.org/10.1515/pac-2015-0503.
[46] J.F. Ziegler, M.D. Ziegler, J.P. Biersack, Nucl. Instrum. Methods Phys. Res. Sect. B Beam Interact. Mater. Atoms 268 (2010) 1818–1823, https://doi.org/10.1016/j.nimb.2010.02.091.
[47] M.A. Trunk, Determination of Isotope Concentration Profiles in Materials Science Applications Using Cold Neutrons, Dissertation, Technische Universität München, 2021.
[48] K. Jalkanen, J. Karppinen, L. Skogström, T. Laurila, M. Nisula, K. Vuorilehto, Appl. Energy 154 (2015) 160–172, https://doi.org/10.1016/j.apenergy.2015.04.110.
[49] T. Waldmann, B.-I. Hogg, M. Wohlfahrt-Mehrens, J. Power Sources 384 (2018) 107–124, https://doi.org/10.1016/j.jpowsour.2018.02.063.
[50] Q.Q. Liu, C.Y. Du, B. Shen, P.J. Zuo, X.Q. Cheng, Y.L. Ma, G.P. Yin, Y.Z. Gao, RSC Adv. 6 (2016) 88683–88700, https://doi.org/10.1039/c6ra19482f.
[51] M. Flügel, M. Bolsinger, M. Marinaro, V. Knoblauch, M. Hölzle, M. Wohlfahrt-Mehrens, T. Waldmann, J. Electrochem. Soc. 170 (2023) 060536, https://doi.org/10.1149/1945-7111/acdda3.
[52] L.M. Babcock, J. Am. Chem. Soc. 125 (2003) 12058–12059, https://doi.org/10.1021/ja033535b.
[53] B. Chapman, Glow Discharge Processes: Sputtering and Plasma Etching, Wiley, 1980.
[54] M. Parker, M.L. Hartenstein, R.K. Marcus, Spectrochim. Acta B Atom Spectrosc. 52 (1997) 567–578, https://doi.org/10.1016/S0584-8547(96)01659-X.
[55] A.B. Anfone, R.K. Marcus, J. Anal. Atomic Spectrom. 16 (2001) 506–513, https://doi.org/10.1039/b009874o.
[56] M. Wetjen, M. Trunk, L. Werner, R. Gernhauser, B. Markisch, Z. Revay, R. Gilles, H. A. Gasteiger, J. Electrochem. Soc. 165 (2018) A2340–A2348, https://doi.org/10.1149/2.1341810jes.
[57] A. Bordes, E. De Vito, C.d. Haon, A. Boulineau, A. Montani, P. Marcus, Chem. Mater. 28 (2016) 1566–1573, https://doi.org/10.1021/acs.chemmater.6b00155.
[58] N. Delpuech, N. Dupre, P. Moreau, J.S. Bridel, J. Gaubicher, B. Lestriez, D. Guyomard, ChemSusChem 9 (2016) 841–848, https://doi.org/10.1002/cssc.201501628.
[59] K. Richter, T. Waldmann, N. Paul, N. Jobst, R.-G. Scurtu, M. Hofmann, R. Gilles, M. Wohlfahrt-Mehrens, ChemSusChem 13 (2020) 529–538, https://doi.org/10.1002/cssc.201903139.
[60] N. Paul, M. Wetjen, S. Busch, H. Gasteiger, R. Gilles, J. Electrochem. Soc. 166 (2019) A1051–A1054, https://doi.org/10.1149/2.0781906jes.
[61] J. Malherbe, H. Martínez, B. Fernández, C. Pécheyran, O.F. Donard, Spectrochim. Acta B Atom Spectrosc. 64 (2009) 155–166, https://doi.org/10.1016/j.sab.2008.11.009.

3.4. Aging mechanism for calendar aging of Li-ion cells with Si/Graphite anodes

Reprinted with permission from:

K. Bischof, **M. Flügel**, M. Hölzle, M. Wohlfahrt-Mehrens, T. Waldmann, 2024 *J. Electrochem. Soc.* **171** 010510

© 2024 The Author(s). Published on behalf of The Electrochemical Society by IOP Publishing Limited. This is an open access article distributed under the terms of the Creative Commons Attribution 4.0 License (CC BY, http://creativecommons.org/licenses/by/4.0/), which permits unrestricted reuse of the work in any medium, provided the original work is properly cited.

DOI: https://doi.org/10.1149/1945-7111/ad1b7c

Individual Contribution

K. Bischof	Conceptualization, Methodology, Validation, Investigation, Writing - Original Draft, Visualization
M. Flügel	Conceptualization, Methodology, Validation, Investigation, Writing – Review & Editing
M. Hölzle	Writing – Review & Editing, Supervision
M. Wohlfahrt-Mehrens	Writing – Review & Editing, Supervision
T. Waldmann	Conceptualization, Writing – Review & Editing, Supervision, Project administration, Funding acquisition

Summary

In this publication, the influence of the Si content, the SOC, as well as the temperature on calendar aging is investigated. Cells with varying Si contents in the anode (0 wt.-%, 3.0 wt.-%, 5.8 wt.-% and 20.8 wt.-%) were aged at different SOC (30%, 60% and 100%) and different temperatures (25 °C, 45 °C and 60 °C) until 80% SOH. Regular check-up cycles were conducted at 25 °C to measure the decrease in cell capacity. After each check-up, the cells were recharged to the respective SOC and further aged. For all cell types, the capacity decrease over time follows a square root-like behavior and was fitted with a square root function with high R^2 values. The aging rate, determined by the derivative of the fitting function, followed an Arrhenius function.

The investigations revealed that the aging rate is increasing with higher amounts of Si in the anode, with higher SOC of the cells and at higher temperatures, at which the cells are aging. A square root dependence of the capacity fading over time is commonly associated with the formation and thickening of the SEI. A higher aging rate observed with increasing Si content indicates that SEI formation is more severe on Si particles than on graphite particles. In addition, since SEI is formed by the reductive decomposition of the electrolyte and conductive salt due to the low anode potential, a higher SOC, that is, lower anode potentials, promotes electrolyte decomposition. Lastly, a higher temperature will accelerate the reaction rate and thus also contribute to SEI development.

To further investigate the underlying aging mechanism and differentiate between LAAM and LLI induced aging, differential voltage analysis (DVA) and post-mortem analysis was employed. DVA results indicate that the Si capacity contribution is decreasing with aging, implicating LAAM as aging mechanism for the Si component. In addition, the capacity contribution of the anode and cathode and its change during aging can be quantified. In all cell types, the cathode contribution decreased with aging, indicating LLI as the underlying aging mechanism. However, with increasing Si content, the anode capacity slightly decreases, which is most likely caused by Si deactivation.

Post-Mortem analysis using SEM/EDX and GD-OES showed that aging is more severe in Si containing cells. The SEI thickness did not increase as severe as during cyclic aging, however, the P and F amount, as determined with EDX, and the Li amount, as determined with GD-OES, increase during aging.

The results of this study indicated that a combination of LLI and LAAM, which both seem to be caused by SEI formation, are the aging mechanism of calendar aging of Si containing cells.

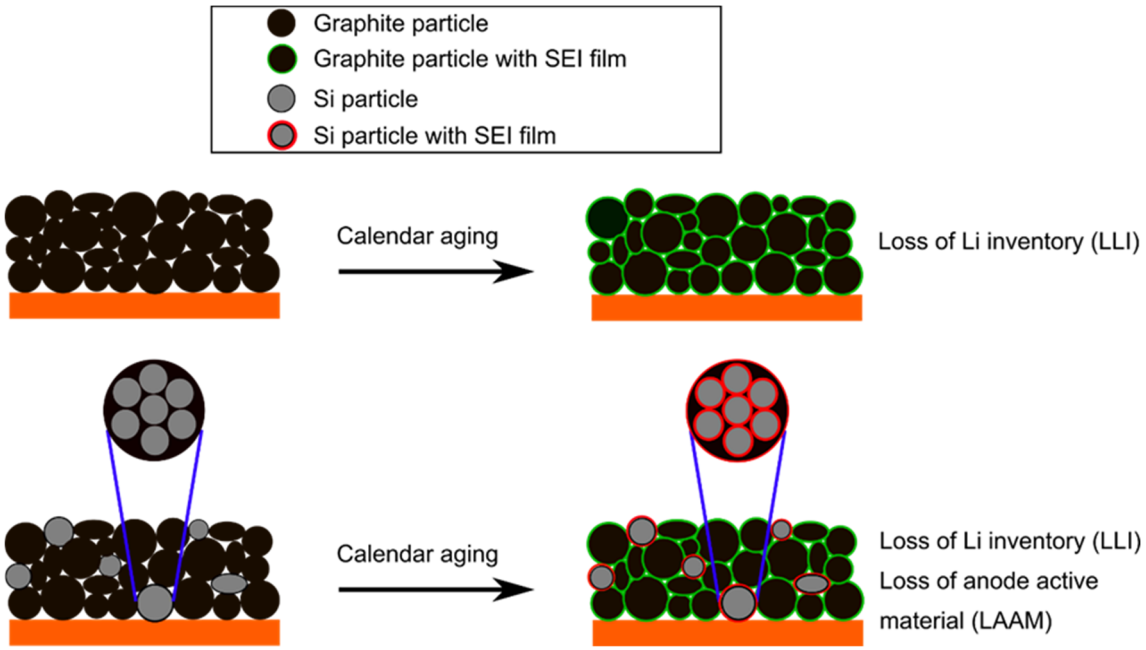

Figure 12: Illustration of the calendar aging mechanism of a graphite anode (left) and Si/graphite anode (right) [171].

Journal of The Electrochemical Society, 2024 **171** 010510

Aging Mechanism For Calendar Aging of Li-Ion Cells With Si/Graphite Anodes

Katharina Bischof,[1] Marius Flügel,[1] Markus Hölzle,[1] Margret Wohlfahrt-Mehrens,[1,2] and Thomas Waldmann[1,2,z]

[1]*ZSW—Zentrum für Sonnenenergie- und Wasserstoff-Forschung Baden-Württemberg, Helmholtzstrasse 8, D-89081 Ulm, Germany*
[2]*HIU—Helmholtz Institute Ulm for Electrochemical Energy Storage, Helmholtzstraße 11, D-89081 Ulm, Germany*

Calendar aging of Li-ion batteries with Si/graphite electrodes was investigated within this study. A total of 121 single-layer pouch full cells with either graphite or Si/graphite (3.0 wt−%, 5.8 wt−% and 20.8 wt−% Si) anodes and NMC622 cathodes with the same N/P ratio were built on pilot-scale. Calendar aging was studied at SoC 30%, 60%, and 100%, as well as temperature (25 °C, 45 °C, 60 °C) and time dependence. The aging data was analyzed in terms of capacity fade and a square-root behavior was observed. Differential voltage analysis (DVA) has been performed as a function of aging time. The observed temperature and time dependence is best described by time dependent, 3D Arrhenius plots. Post-Mortem analysis (SEM, EDX, GD-OES) is applied to investigate the changes on electrode and material level. Conclusions are drawn on the main aging mechanisms for calendar aging of Li-ion cells with Si/graphite anodes and differences between Si/graphite and pure graphite anodes are discussed. The Si-containing cells show a combination of lithium inventory loss and a loss of accessible Si active material, both caused by SEI growth.
© 2024 The Author(s). Published on behalf of The Electrochemical Society by IOP Publishing Limited. This is an open access article distributed under the terms of the Creative Commons Attribution 4.0 License (CC BY, http://creativecommons.org/licenses/by/4.0/), which permits unrestricted reuse of the work in any medium, provided the original work is properly cited. [DOI: 10.1149/1945-7111/ad1b7c]

Manuscript submitted August 11, 2023; revised manuscript received December 14, 2023. Published January 16, 2024.

Supplementary material for this article is available online

An adequate lifetime of the Li-ion batteries (LIBs) is critical to ensure market acceptance of such batteries in portable, mobile and stationary applications.[1] In addition, high energy density is another important factor that determines the competitiveness of LIBs. Especially for electric vehicles, further increase in battery energy density is of great interest to achieve longer driving ranges in combination with smaller batteries.[2,3] Silicon (Si) is considered as the most promising anode material that, due to its high theoretical capacity of 3,579 mAh g^{-1} at room temperature,[4] would enable a significant increase in both gravimetric and volumetric energy density as well as reducing raw materials costs.[2,5,6] However, the alloying reaction of Si with Li^+-ions leads to a large volume expansion of the anode, typically resulting in poor cycling stability and rapid capacity loss of pure Si electrodes.[2,6,7] As a consequence, neither pure graphite nor pure Si anodes can meet the stringent requirements of future electrical devices. Therefore, silicon/graphite composite (Si/graphite) anodes with up to 4 wt−% of Si[8] are currently used in commercially available state-of-the-art LIBs to improve both the capacity without suffering in cycle life of such batteries.[2,9]

Cycling aging of Li-ion cells with graphite and Si/graphite anodes was investigated in detail over the last years. Different groups have identified either loss of anode active material (LAAM)[8,10–12] or loss of Li inventory (LLI)[8,13–15] as the main root causes of capacity loss. LLI is caused by Li reacting irreversibly and forming SEI which can take place on both graphite[16,17] and Si/graphite anodes.[11] LAAM can occur for both graphite and Si particles by electronic isolation of particles e.g., resulting from electrode cracks. However, only Si particles can show particle fracture due to volume expansion[18] and SEI growth[8,11] which results in additional LAAM. We have recently shown for three types of commercial cells, that LAAM occurs only for certain types of Si components.[8]

As recently pointed out by McBrayer et al., there is a lack of understanding on the mechanisms of calendar aging in case of Si/graphite anodes,[5] since only few studies exist on this topic.[15,19–21] Zilberman et al. investigated calendar aging of commercial cylindrical cells (~3.5 wt−% Si).[19] The authors concluded that for the cell type investigated, LAAM regarding the Si component was the main cause of capacity fade.[19]

[z]E-mail: thomas.waldmann@zsw-bw.de

Therefore, we systematically investigated calendar aging of cells with Si/graphite anodes in comparison to pure graphite anodes, with the aim of a comprehensive picture for the trends regarding time, temperature, SoC, and Si content. For this purpose, 121 pouch cells were built and calendar aged at different storage conditions. The aging behavior is investigated in terms of capacity fade. Differential voltage analysis (DVA) on cell level is added to this investigation to gain further insight into electrode processes. The rate dependence of the capacity fade over time and temperature is best described by three-dimensional (3D) Arrhenius plots. Investigations on electrode and material level are performed by Post-Mortem analysis using SEM/EDX and glow discharge optical emission spectroscopy (GD-OES). Finally, we draw conclusions on the main aging mechanisms for calendar aging of Li-ion cells with Si/graphite anodes and thereby discuss differences between Si/graphite and pure graphite anodes.

Experimental

Electrode manufacturing.—Graphite active material and three Si/graphite composite active materials with different Si contents were purchased from Iopsilion (China). The Si contents in the anode electrodes were 0 wt−% (Graphite), 3.0 wt−% (SiG3.0), 5.8 wt−% (SiG5.8) and 20.8 wt−% (SiG20.8). Anode coatings were prepared using active material, CMC binder (TIMCAL, Switzerland), SBR binder (ZEON, Japan), and SuperC65 conductive additive (Nippon paper Industries, Japan) with weight ratios of 94:2:2:2 (Graphite, SiG3.0 and SiG5.8) and 90:3:3:4 (SiG20.8). Cathode coatings are prepared by coating N-methyl pyrrolidone (NMP) based slurries with 94 wt−% NCM622 active material (BASF, Germany), 2 wt−% PVDF (Solvay, Belgium), 2 wt−% carbon black (TIMCAL, Switzerland), and 2 wt−% graphite (TIMCAL, Switzerland) onto Al foil. The cathodes were calendered at 100 °C roll temperature to a density of 3.2 g cm^{-3}. Both, anodes and cathodes were produced on ZSW's pilot coating lines. These electrodes are from the same production batch as in our previous study by Flügel et al.[8,22] More details on the electrode production and their properties (density, porosity, tortuosity) can be found there.[8,22]

Cell manufacturing.—In total 121 single-layer pouch full cells were assembled at ZSW's pilot line with the four negative electrodes

Journal of The Electrochemical Society, 2024 **171** 010510

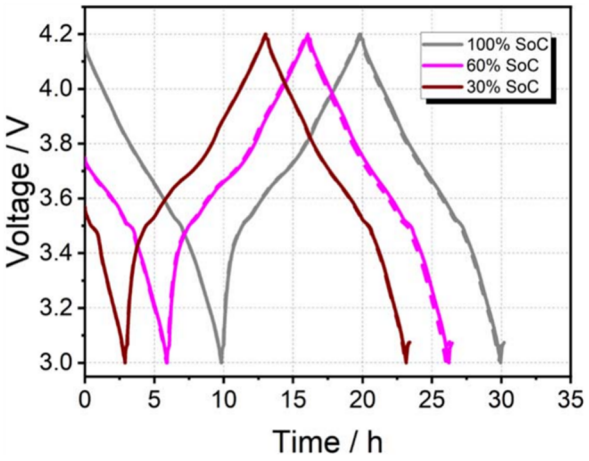

Figure 1. Exemplary representation of the time course of a check-up routine for all three SoCs examined. The dashed lines correspond to the reproduction of the voltage curve by a second cell aged under the same conditions (SiG5.8, 25 °C). The discharge capacity of the full cycle was used to determine the irreversible capacity loss caused by calendar aging.

and complementary NMC622 cathodes described above. The areal capacity of the cathodes is matched to the areal capacity of the respective anode in such a way that irreversible active material losses due to the Si component are compensated. As a result, a similar N/P ratio of 1.1 is achieved for all cell types.[8,22]

The pouch full cells were assembled using one single-sided coated anode with an area of 26 cm^2 and one single-sided coated cathode with an area of 24 cm^2, Celgard 2325 separator. Graphite pouch cells were typically filled with 900 μl of VC containing electrolyte (1.0 M $LiPF_6$ in EC:DEC (3:7 wt−%) + 2 wt−% VC) and Si pouch cells were filled with 900 μl of FEC containing electrolyte (1.0 M $LiPF_6$ in EC:DEC (3:7 wt−%) + 10 wt−% FEC). To exclude any effect of the electrolyte additive on the capacity fade behavior, 13 graphite cells were additionally filled with the FEC containing electrolyte. VC was chosen as the primary electrolyte additive for the graphite cells as it is considered to be the most effective additive to ensure a long lifetime of graphite cells.[23,24] Unless otherwise stated, graphite cells in the following always refer to these graphite cells with VC. As FEC is reported to form a more stable and flexible SEI on Si,[25,26] it was used as the electrolyte additive for the Si-containing cells.

Calendar aging procedure.—All electrochemical tests were conducted at ZSW with a MACCOR 4200 system at room temperature. Formation was performed after a rest period of 12 h with three cycles at 0.1 C in the voltage range from 2.8 V to 4.2 V. CC-CV (constant current - constant voltage) mode (CV until I < 0.05 C) was used for charging and CC mode for discharging.

To investigate calendar aging, the cells were charged to three different SoCs (100%, 60%, and 30%) at 0.1 C after formation and aged at three different temperatures (25 °C, 45 °C, and 60 °C). A SoC of 30% and 60% was achieved by first discharging the corresponding cells to a lower voltage limit of 3.0 V in a CC discharge step and then charging them for 3 h and 6 h, respectively, using CC mode. The cells with a target SoC of 100% were charged to 4.2 V using CC-CV mode without prior discharge. Subsequently, the cells were stored in climate chambers (Vötsch) at 25 °C and 45 °C and in a home-made thermobox at 60 °C. For the graphite-containing cells with FEC as electrolyte additive only the combinations of the aging parameters 60% SoC or 100% SoC and 45 °C or 60 °C were tested. In this case, the cells were placed in two different climate chambers (45 °C: Binder, 60 °C: CTS) than all other cells investigated. At least two cells with the same parameters were built for each of the three influencing factors: Si content, SoC, and temperature. If a deviating electrochemical behavior occurred between two cells of the same type, further cells were calendar aged under the same conditions.

The progress of calendar aging was monitored by regular electrochemical check-ups. For the cells stored at 25 °C and 45 °C, these took place approximately every four weeks. Since the fastest aging was expected at a temperature of 60 °C, check-ups for these cells were performed at bi-weekly intervals. For this purpose, cells aged at 45 °C and 60 °C were first cooled to room temperature for ∼1 h. The check-up routines (Fig. 1) then included a CC discharge step until a lower voltage limit of 3.0 V was reached, followed by a CC-CV charge and CC discharge cycle in the voltage range of 3.0 V to 4.2 V. To prevent the initiation of potential side reactions caused by the check-ups, a low C-rate of 0.1 C was used for all charge and discharge processes. Finally, the cells were charged to their original SoCs using the same protocols described above. The 0.1 C used for charging was always based on the discharge capacity from the full cycle of the most recent check-up. This means that this capacity was adjusted for each check-up routine to match the required SoCs to the current aging state of the cells.

To determine the current SoH of the cells at time t, the discharge capacity Q(t) from the full cycle of each check-up was referenced to the discharge capacity Q(t = 0) of the third formation cycle to 3.0 V according to equation

$$SoH(t) = \frac{Q(t)}{Q(t=0)} \quad [1]$$

After reaching SoH = 80%, which was defined as end-of-life (EoL) criterion, the aging was stopped.

Determination of aging rates.—To determine the aging rates, the SoHs of the cells were plotted versus time t. All time periods in which the cells were in check-ups were subtracted in order to consider only the real duration of the calendar aging. The capacity decrease curves were then fitted in Origin using the relationship

$$SoH = 100 + a\sqrt{t} \quad [2]$$

with the parameter a and the intercept SoH(t = 0) = 100%. The corresponding aging rates r were determined from the time derivative

$$r = -\frac{dSoH}{dt} = -\frac{a}{2\sqrt{t}} \quad [3]$$

For graphite-containing cells aged at a temperature of 25 °C, an increase in SoH was initially observed. To determine their aging rates analogously to the described procedure, the maximum SoH reached during aging was normalized to SoH(t = 0) = 100% in each case.

Post-mortem characterization.—SEM top view images of the anodes were measured at an accelerating voltage of 5 kV using a JSM-IT500 microscope (JEOL) equipped with a tungsten filament. EDX was performed at an accelerating voltage of 20 kV. A LEO 1530 VP microscope (Zeiss) equipped with a Gemini field emission column was used to characterize anodic cross-sections. Measurements were recorded at an accelerating voltage of 5 kV using a SE detector. Electrode cross-sections were prepared with a Hitachi IM4000Plus broad-beam argon ion milling system, using an ion beam voltage of 5 kV. During sample preparation for SEM (top view and cross-section), the samples were exposed to air.

GD-OES depth profiling analysis was performed with a GDA750 measurement device (Spectruma, Germany). Measurements were carried out in radio frequency (RF) mode at a frequency of 2501 Hz, at a discharge voltage of 550 V and a pressure of 2 hPa. The sputtering gas was a mixture of 1% H_2 in Ar (both 6.0 purity). The specific emission line of 670.7 nm was used for the detection of Li.

Journal of The Electrochemical Society, 2024 **171** 010510

Results and Discussion

Capacity fade during calendar aging.—Figure 2 shows the capacity decay during calendar aging at different temperatures vs time for 100% SoC. It is noted that the scattering of data of reproduced cells is comparable to commercial cells described by others.[27]

The capacity decrease in Fig. 2 is characterized by a strong temperature dependence, which is reflected in an increasing aging with increasing temperature. The cells aged at a temperature of 25 °C still exhibit a SoH > 80% after more than 200 d regardless of the Si content (blue data points in Fig. 2), while the cells at a storage temperature of 60 °C have already reached their EoL criterion (SoH = 80%) by this time (red data points in Fig. 2). Between the cells aged at 60 °C, a capacity loss increasing with increasing Si content can also be observed (red data points in Fig. 2). While the graphite based cells with VC as electrolyte additive (Fig. 2a) reached SoH < 80% only after more than 150 d (10 check-ups), the Si-containing cells with SiG3.0, SiG5.8 and, SiG20.8 anodes fell below the EoL criterion already after 59–91 days (4–6 check-ups), about 60 d (4 check-ups) and 40–52 d (2–3 check-ups), respectively. A similar trend can be observed for the other temperatures, but still the differences between the Si contents are the strongest at 60 °C aging. Compared to the pure graphite based cells (regardless of the electrolyte additive used), the capacity of the Si/graphite cells always decreases faster. This trend is similar to the deteriorated calendar lifetime of Si-containing LIBs compared to their pure graphite counterparts described by McBrayer et al. due to the presence of Si.[5]

Similar trends were also found for the SoCs of 60% and 30% (see Figs. S1 and S2). Only the SiG5.8 cells stored at 30% SoC appear to age at a similar rate within the scattering at 45 °C as at 60 °C. This finding is reproducible for two cells (see yellow data points which are bleached out in Fig. S2c). However, there was an extremely high internal resistance of >1000 mΩ measured before performing the check-ups of these two cells, possibly leading to the fast capacity decrease. In perspective to the overall data set, this behavior therefore seems to be an outlier. Overall, the capacity losses are smaller for the lower SoCs compared to 100% SoC, with only minor differences between 60% and 30% SoC (see Figs. S3, S4, and S5).

At 100% SoC the graphite cells with FEC as electrolyte additive show a similar capacity decay at 45 °C as well as at 60 °C compared to their VC containing counterparts (see Fig. 2a). In this case, the capacity fade curves seem to be little affected by the different additives. In contrast, at 60% SoC (see Fig. S1a) the capacity losses after around 50 d are smaller for the graphite cells with FEC

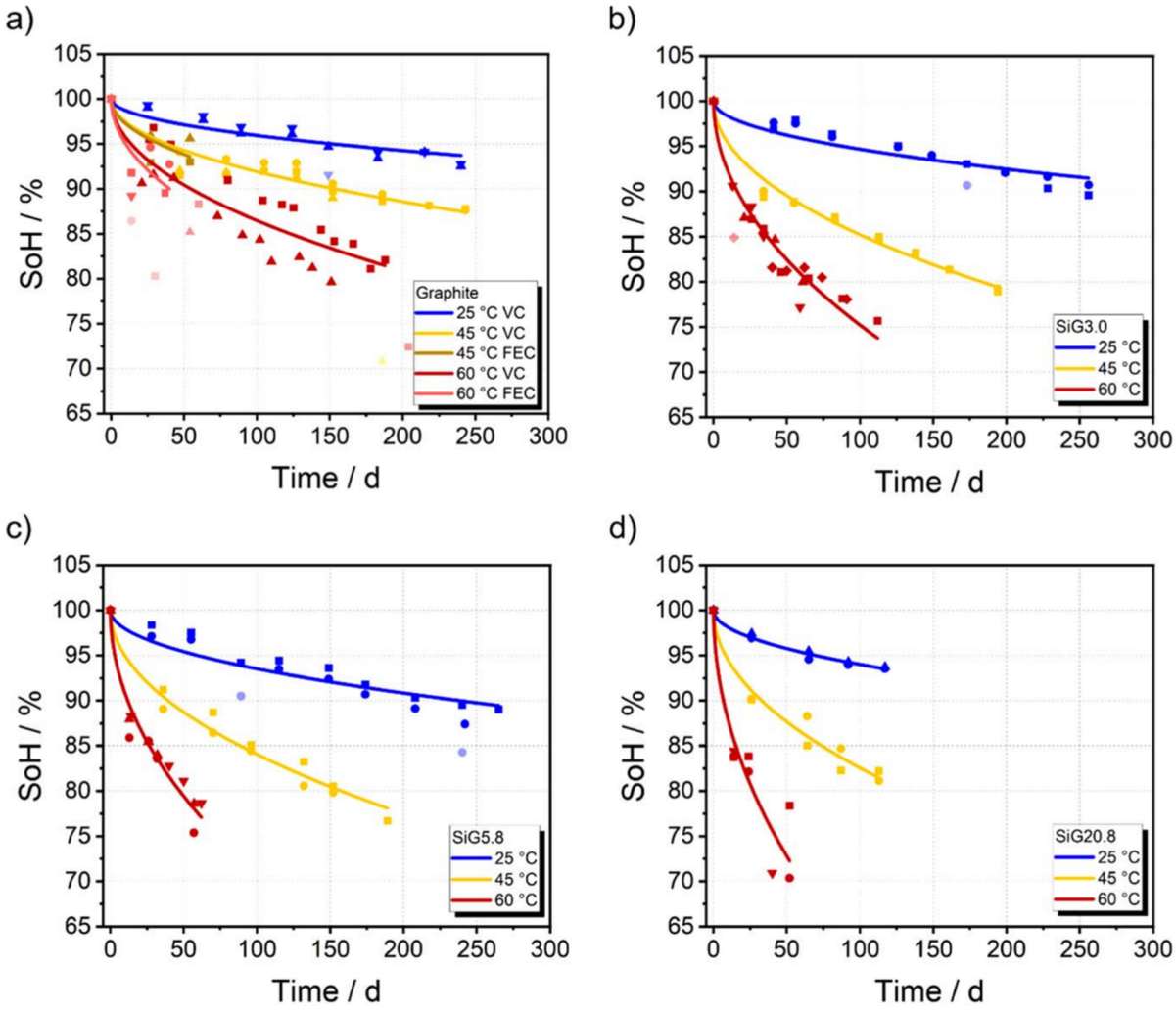

Figure 2. Capacity degradation for (a) graphite, (b) SiG3.0, (c) SiG5.8, and (d) SiG20.8 based cells at a storage SoC of 100% over calendar aging time. The points correspond to the measured data and the lines to the fitting results obtained with Eq. 2. The bleached data points represent outliers and were not included in the fits.

Journal of The Electrochemical Society, 2024 **171** 010510

Table I. Summary of fit results with Eq. 2 for capacity decrease of cells aged at SoC of 100%.

Anode	Temperature	Fit parameter a	R^2
Graphite	25 °C	−0.41 ± 0.02	0.88
	45 °C	−0.81 ± 0.02	0.91
	60 °C	−1.35 ± 0.05	0.83
SiG3.0	25 °C	−0.53 ± 0.02	0.90
	45 °C	−1.48 ± 0.02	0.99
	60 °C	−2.48 ± 0.05	0.97
SiG5.8	25 °C	−0.65 ± 0.03	0.90
	45 °C	−1.59 ± 0.03	0.98
	60 °C	−2.91 ± 0.07	0.97
SiG20.8	25 °C	−0.60 ± 0.01	0.99
	45 °C	−1.74 ± 0.05	0.97
	60 °C	−3.84 ± 0.19	0.93

compared to the graphite cells with VC at both temperatures. This indicates an even slower aging of the graphite cells when using FEC as electrolyte additive in comparison with the Si-containing cells.

The shape of the capacity fading curves is very similar for all Si contents, temperatures, and SoCs and is characterized by a reduced slope over aging time. In order to mathematically describe the time dependence of the capacity degradation, the square-root function shown in Eq. 2 was used to describe the whole data set with only the parameter a. A similar approach was used in several empirical calendar aging models developed by other authors for cells with pure graphite anodes.[27–30] Individual data points that obviously do not follow the general trend were declared as outliers and not included in the fits.

As shown in Table I, the quality of the fitting curves at 100% SoC is in a good correlation with the experimental data with R^2 values mostly being ⩾0.90. Only the fit for the graphite based cells stored at 60 °C shows a slightly lower R^2 value (⩾0.83) due to strong scattering of the data points. Equation 2 also provides good fit results for the SoCs of 60% and 30%, with R^2 values (with one exception) of R^2 ⩾0.85 (see Tables S1 and S2).

In the literature, a square-root dependence of the capacity decrease over time is often attributed to the formation of an insulating SEI layer with gradually slower growth over time.[27,28,31–33] The cause of the continuously decreasing growth rate of SEI is thereby discussed via different approaches.[34] These include transportation mechanisms such as solvent diffusion,[32,35] electrical conductivity,[31,36] or diffusion of neutral Li-interstitials[37,38] through the SEI, which all conclude a $\sqrt{t}$-dependence for the long-term capacity fade.[34] The good agreement of the experimental data with the square-root function in Eq. 2, gives a hint that SEI growth may also be present in cells with Si/graphite anodes. Since this is associated with reductive decomposition of $LiPF_6$ from the electrolyte, LLI can be expected.[17,39,40]

Analysis of time and temperature dependence via 3D Arrhenius plots.—In order to investigate the influence of temperature on the rate of capacity degradation in more detail, the Arrhenius equation was applied

$$r = A \exp\left(-\frac{E_a}{k_B T}\right) \quad [4]$$

with A as the pre-exponential factor, the activation energy E_a, the Boltzmann constant k_B, and the absolute temperature T.

From the square-root function in Eq. 2, a continuous function for the aging rate (Eq. 3) can easily be derived analytically. For the Arrhenius plot, the aging rates r were first determined for the different aging conditions according to Eq. 3 using the parameters a resulting from the square-root fits (Eq. 2). Compared to Kucinskis et al.,[41] this procedure allows to simultaneously capture the temporal change of the aging rate. Therefore, Fig. 3 shows the logarithmic aging rates for the different SoCs as a function of both temperature and time in a 3D Arrhenius plot. We note that the Arrhenius-like behavior is not found along the plotted lines, but perpendicular to them for each time point t (see exemplary 2D projections in ln(r) vs $(k_BT)^{-1}$ plain in Fig. 3a).

The 3D Arrhenius plots are characterized by the $\sqrt{t}$-dependence of the capacity loss discussed earlier. For all combinations of temperature and SoC studied, the aging rates for the graphite based cells (black curves in Fig. 3) are lower than for their Si-containing counterparts. Thus, the presence of the Si component appears to have an accelerating effect on the aging rate. This could result from a different composition of the SEI compared to the pure graphite anodes and their different properties.[5,15]

Since all aging rates in Fig. 3 were determined by Eq. 3, their relative temperature dependence for one cell type does not change over time. To focus on the temperature influence in more detail, a 2D section through the 3D plots at t = 1 d was set as an example and the associated aging rates were fitted linearly over the investigated temperature range from 25 °C to 60 °C. The resulting 2D Arrhenius plots for the different SoCs are shown in Figs. 4a–4c.

The results of the linear fits are listed in Table II and are characterized by R^2 values ⩾ 0.97 for all cell types and aging conditions. The high R^2 values indicate that the temperature dependence of the capacity loss rates can be adequately described by the Arrhenius Eq. 4. The linearity shows additionally that there is most likely one dominating aging mechanism at all temperatures studied.[42] A different behavior reported in literature is for example the temperature dependent transition from SEI growth at high temperatures to Li plating at low temperatures under cycling aging conditions, leading to a slope change in the Arrhenius plot.[16,41,43–46] The only exception from the Arrhenius behavior in the present study on calendar aging is the fit for the SiG5.8 cells aged at 30% SoC. However, the deviating correlation coefficient is again caused by the unusually fast capacity loss of the cells aged at 45 °C discussed earlier (see yellow data points in Fig. S2c) and should therefore not be interpreted as a contradiction to the otherwise assumed Arrhenius-like behavior.

In the literature, Arrhenius-like behavior in the temperature range studied is attributed to the growth of the SEI, which was additionally verified by Waldmann et al. through Post-Mortem analyses.[16,47] Thus, the observed validity of the Arrhenius-like relationship between the aging rates and the storage temperature reinforces the hypothesis that the calendar aging results mainly from LLI.

The values of the activation barriers E_a obtained from the slopes of the linear fits from Figs. 4a–4c are plotted against the Si content of the anode in Fig. 4d. At 30% and 60% SoC there is a general decrease of the values of E_a observable with increasing Si content. The opposite trend is evident for 100% SoC. In this case, the value of E_a is lowest for the cell with the graphite anode and highest for the one with the SiG20.8 anode. Since the value of E_a describes the influence of temperature on the aging rate, it can be concluded that for 100% SoC there is a stronger temperature effect on the aging rate with increasing Si content, whereas this effect decreases with higher Si content for the lower SoCs. In this case, the temperature influence on the aging rate is strongest for the graphite cells. However, the observed trends in E_a cannot be interpreted directly regarding the aging mechanism. As these are complex processes, resulting from several different parallel and consecutive reactions,[17] it is not possible to assign the values of E_a shown here to a specific reaction. Rather, E_a should be seen as an overall apparent activation energy for the whole aging process. The exact values of the activation barriers are listed in Table II. The observed E_a values are in the same order of magnitude as found by others[48,49] and by our group.[16,47]

Differential voltage analysis.—DVA allows the differentiation of various aging mechanisms such as LAAM and LLI.[50–52] Since, a

Journal of The Electrochemical Society, 2024 **171** 010510

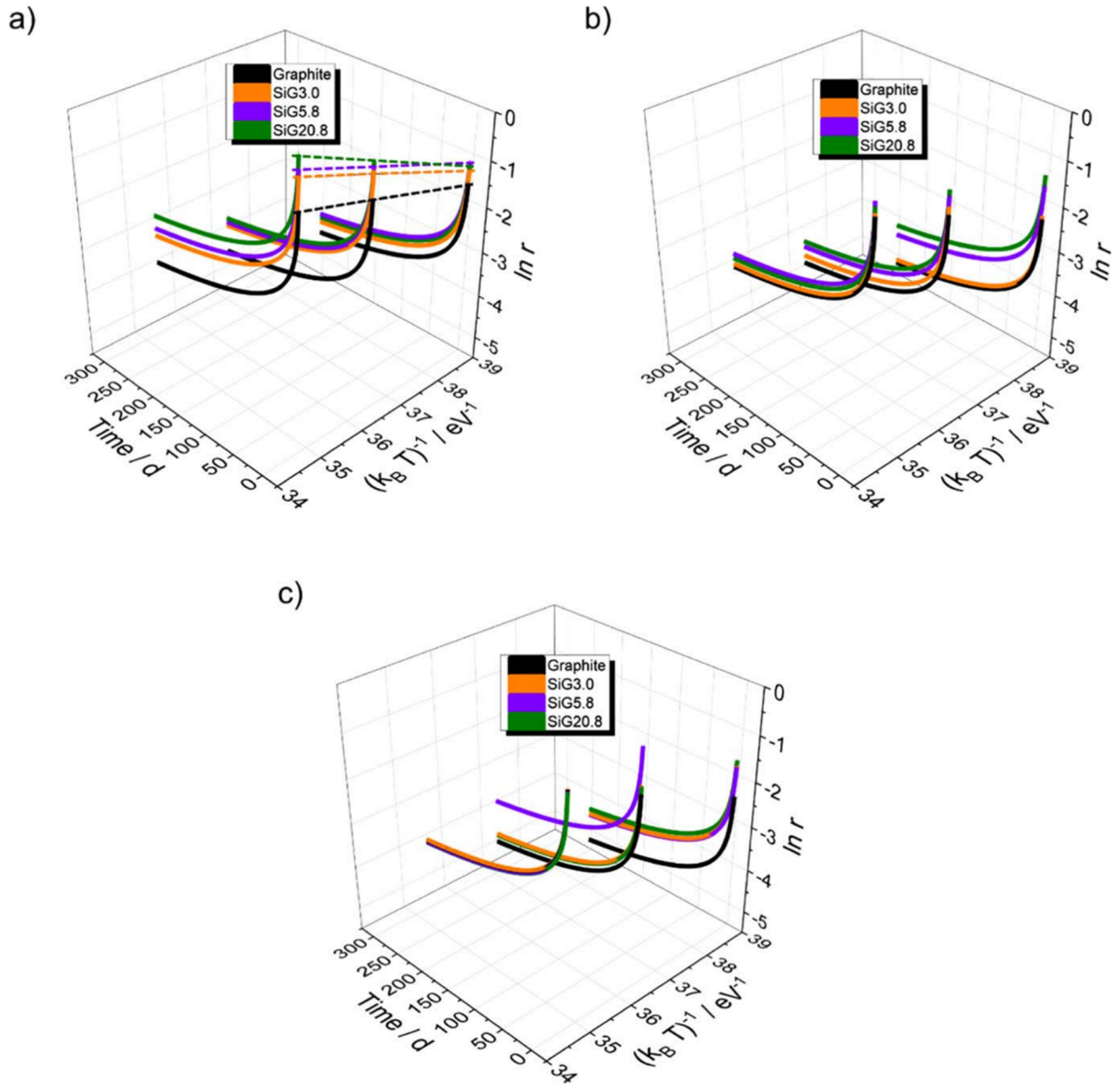

Figure 3. 3D Arrhenius plots for the calendar aging at (a) 100%, (b) 60% and (c) 30% SoC. The aging rates were calculated according to Eq. 3 as a function of time t for the three temperatures studied, 25 °C, 45 °C, and 60 °C. The error bars of the aging rates are so small that they cannot be seen in the plots. The exemplary 2D projections in the ln(r) vs $(k_BT)^{-1}$ plain in a) are cuts through the 3D data and correspond to the representation in Fig. 4a.

similar main aging mechanism can be assumed for all aging conditions, only the discharge curves of the cells aged at 45 °C and a storage SoC of 100% were analyzed here. The corresponding DVA results for one cell of each Si content are shown in Fig. 5. It should be noted that the capacities from all check-ups are normalized to a SoC of 100% for better comparability, i.e. 100% SoC corresponds to the fully charged state, independent from the aging state.

For the graphite based cell (Fig. 5a), two peaks, G_1 and G_2, are obtained in accordance with the literature.[8,50,51] The central graphite peak G_1 is located at a higher SoC than the G_2 peak and corresponds to the transition between the potential plateaus of the LiC_6 and LiC_{12} phases during the delithiation of the graphite anode.[53] In the discharge curves of Si/graphite cells, the presence of the Si component is manifested by a less steep voltage drop in the direction of delithiation due to the higher working potential of Si compared to graphite.[54,55] This results in two additional peaks in the DVAs of SiG3.0, SiG5.8, and SiG20.8 based cells (Figs. 5b–5d) at low SoCs which can be attributed to the Si component.[12,19] In consistence with Flügel et al. these peaks are referred to as S_1 and S_2.[8] With higher Si content, both the graphite and Si peaks are shifted to higher SoCs. As expected, no characteristic cathode peaks were observed for NMC622.[56,57]

With calendar aging, a shift of all identified peaks to higher SoCs is observed for all cell types. The largest change takes place between the formation and the first check-up, which is based on the strongest capacity decrease at the beginning of aging as explained above. The shift of the graphite peak G_1 is clearly more pronounced for the Si-containing cells than for the graphite cells, which indicates stronger aging with increasing Si content. This is consistent with the aging

Journal of The Electrochemical Society, 2024 **171** 010510

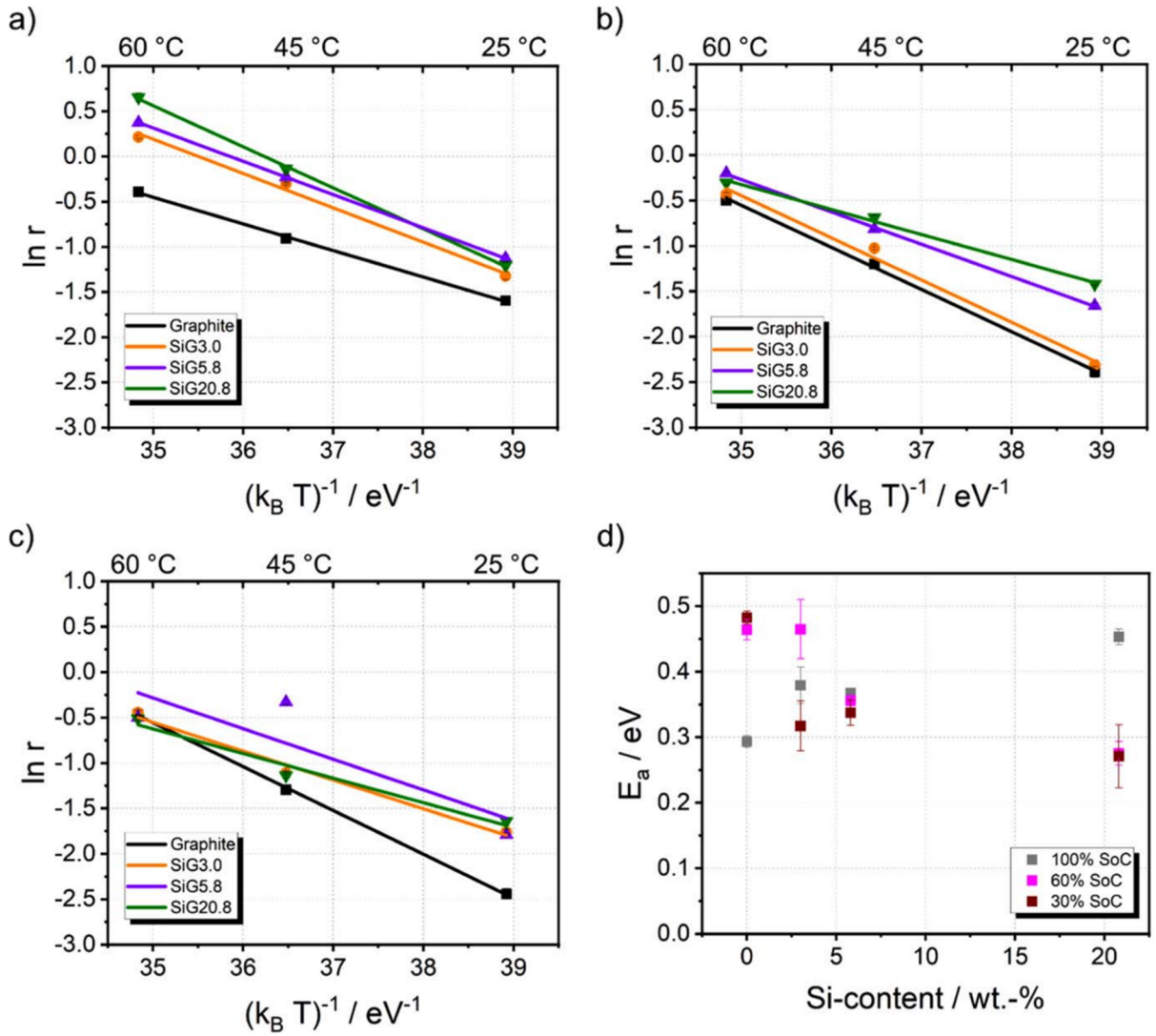

Figure 4. Arrhenius plots for calendar aging at a SoC of (a) 100%, (b) 60%, (c) 30% at the onset of aging. The aging rates were obtained from Fig. 3 by a cross-section at t = 1 d. The error bars are so small that they cannot be seen in this representation. The lines correspond to the linear fits of the aging rates over the temperature range from 25 °C to 60 °C. (d) Plot of the activation energies obtained from the linear fits from (a)–(c) versus the Si content of the cells.

Table II. Summary of fit results with Arrhenius equation (Eq. 4) for temperature dependence of capacity decrease rates.

Anode	SoC	E_a	R^2
Graphite	100%	0.29 ± 0.01 eV	1.00
	60%	0.46 ± 0.02 eV	1.00
	30%	0.48 ± 0.01 eV	1.00
SiG3.0	100%	0.38 ± 0.03 eV	0.99
	60%	0.46 ± 0.05 eV	0.99
	30%	0.32 ± 0.04 eV	0.98
SiG5.8	100%	0.37 ± 0.00 eV	1.00
	60%	0.36 ± 0.01 eV	1.00
	30%	0.34 ± 0.02 eV	0.76
SiG20.8	100%	0.45 ± 0.01 eV	1.00
	60%	0.28 ± 0.02 eV	1.00
	30%	0.27 ± 0.05 eV	0.97

results (see above). The intensity of the Si peaks decreases for all Si contents. Only for S_2 of the SiG20.8 cell no noticeable change in intensity can be observed, however, this peak is already very flat and broad at the beginning in the formation. In addition to the shift in S_1 and S_2, the decrease in intensity of these peaks implies a decrease in the Li storage capability in Si. Accordingly, the higher capacity loss of the SiG3.0, SiG5.8, and SiG20.8 based cells compared to the pure graphite cell could be caused by LAAM, a prominent aging mechanism in the Si-containing cells.[8,11]

For a differentiated consideration of the cause of the capacity decreases and to verify a possible LAAM, the total capacities shown in the DVAs (0% SoC–100% SoC) were each divided into two characteristic capacity fractions Q_1 and Q_2 (Fig. 5) following Keil et al.[50,51] A similar approach to interpret the DVA results for commercial Si/graphite cells was also adopted by Zilberman et al.[19] Here, Q_1 corresponds to the distance between 0% SoC and the G_1 peak and contains information about the storage capacity of the anode.[50,51] A decrease of Q_1 with aging can therefore be interpreted as a

Journal of The Electrochemical Society, 2024 **171** 010510

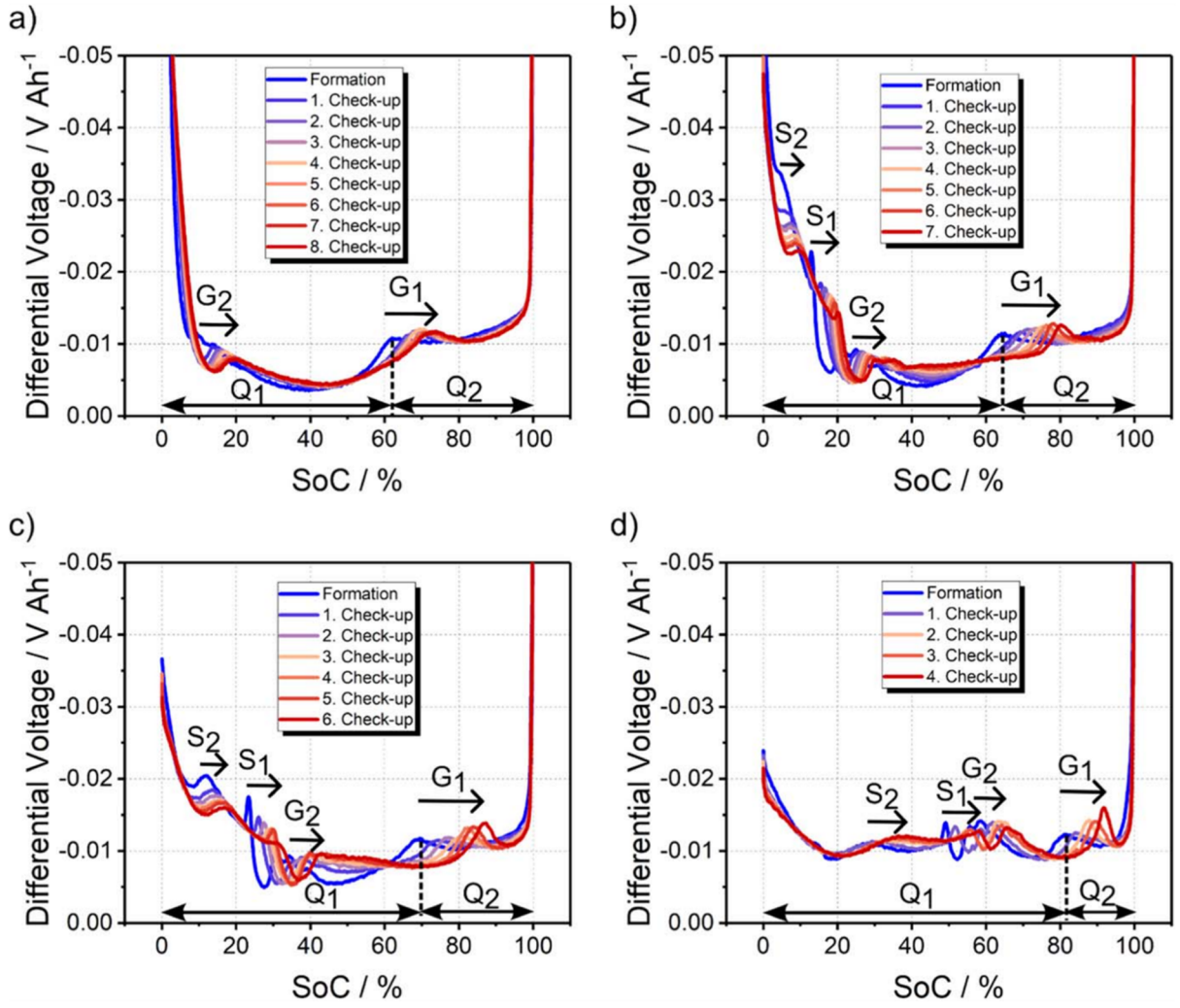

Figure 5. Comparative plot of DVA for one cell each calendar aged at 45 °C/100% SoC of (a) graphite, (b) SiG3.0, (c) SiG5.8, and (d) SiG20.8 for the discharge curves of the last formation cycle and the check-ups performed. The capacities are normalized to SoC = 100%. The arrows indicate the shift in Si peaks S_1 and S_2 and graphite peaks G_1 and G_2 due to calendar aging. The central graphite peak G_1 from the formation is highlighted by a dashed vertical line for each cell type and divides the capacity into two characteristic portions Q_1 and Q_2. These allow assignment of the calendar aging contributions into a LAAM (change Q_1) and a LLI (change Q_2).[50,51]

degradation of the anode, i.e. LAAM. The capacity fraction Q_2 is calculated from the distance between the graphite peak G_1 and 100% SoC. It contains information about the electrode balancing.[50,51] Absolute changes of Q_2 during aging without simultaneous changes of the anode and cathode capacities can be interpreted as LLI.[50,51] Figure 6 plots the Q_1 and Q_2 values calculated from the DVAs for the cells aged at 45 °C and 100% SoC, taking into account their actual SoHs. For each cell type, the corresponding ratio of the capacity fractions from the formation is compared with that from the last check-up performed in this study (Graphite) or before reaching the EoL criterion (SiG3.0, SiG5.8 and SiG20.8).

When comparing the Q_1 values of the aged cells with the respective reference values from the formation, differences can be observed between the pure graphite and the Si-containing cells. For the former, there is no evidence indicating degradation of the anode. Therefore, the overall decrease in capacity is attributed to the decrease of the Q_2 value and thus solely to LLI and not to a change in balancing (N/P ratio). The LLI is assumed to result from reductive decomposition of the electrolyte and the associated SEI growth, as explained above. In the presence of Si, however, not only the Q_2 value but also the fraction of the anode storage capability Q_1 decreases due to calendar aging, so that for the Si based cells an additional LAAM can be assumed with respect to the Si component. The reduction of the capacity fraction Q_1 increases with increasing Si content and is greatest for SiG20.8. Nevertheless, the dominant part of the capacity loss is due to the decrease in the Q_2 fraction for these cells. Thus, for the Si-containing cells, the mechanism of the calendar aging seems to consist mainly of LLI and complementary of LAAM which increases with increasing Si content.

Post-Mortem analysis.—In Fig. 7, SEM top views of graphite and SiG5.8 anode surfaces are compared exemplarily. After formation, the graphite particles in the pure graphite anode (Fig. 7a) have relatively smooth surfaces and clear edges. In contrast, the visible surfaces of the anode aged at 45 °C and 100% SoC (Fig. 7b) show a higher roughness. EDX-mappings of the unaged anode indicate no presence of either Fluorine or Phosphorous. In contrast, a Fluorine content of ∼3.4 wt−% and a Phosphorous content of ∼0.7 wt−% were detected in the electrode after calendar aging. Since Fluorine and Phosphorous are typical building blocks of the SEI layer formed on graphite

Journal of The Electrochemical Society, 2024 **171** 010510

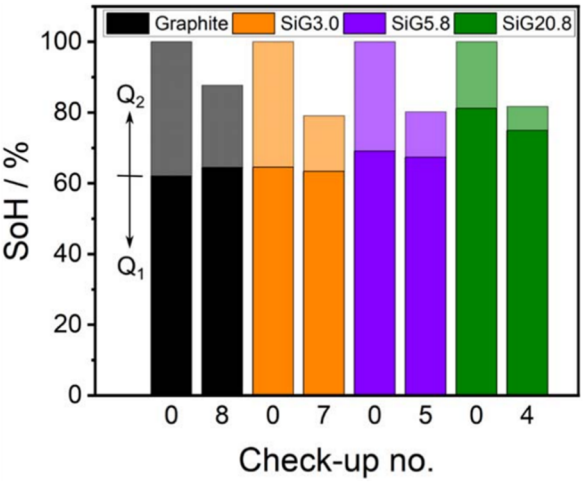

Figure 6. Evaluation of Q_1 and Q_2 from DVA. Each column corresponds to the average of two cells.

particles,[16,31] it can be assumed that the structures visible on the surface of the graphite particles in the SEM image are most likely electrolyte decomposition products as part of the SEI. This is consistent with the indications based on the electrochemical analysis suggesting SEI growth with LLI aging mechanism for the pure graphite anodes.

The SiG5.8 anode (Fig. 7c) is also characterized by smooth graphite particles after formation. In contrast to the pure graphite anode, there is no film formation observable on the surfaces of the graphite particles of the calendar aged SiG5.8 anode (Fig. 7d). However, we note that this might be due to the different electrolyte additives for graphite (VC) and Si/graphite (FEC). The SEI growth in the Si/graphite cells suggested by the electrochemical data therefore probably mainly affects the Si component.

In order to better characterize the Si particles, SEM images of electrode cross-sections were carried out. The corresponding sections of a representative particle of the SiG5.8 anodes after formation and after calendar aging (45 °C and 100% SoC) are compared in Fig. 8. It is important to note that the visible μm-scaled Si compounds are themselves composed of nm-scaled Si particles. The Si particles are embedded in a carbon matrix with a carbon coating surrounding the entire μm-sized structure (see e.g. film of darker grey indicated in Fig. 8d). While the nm-size of the Si particles decreases the diffusion paths of Li in Si,[58] the observed

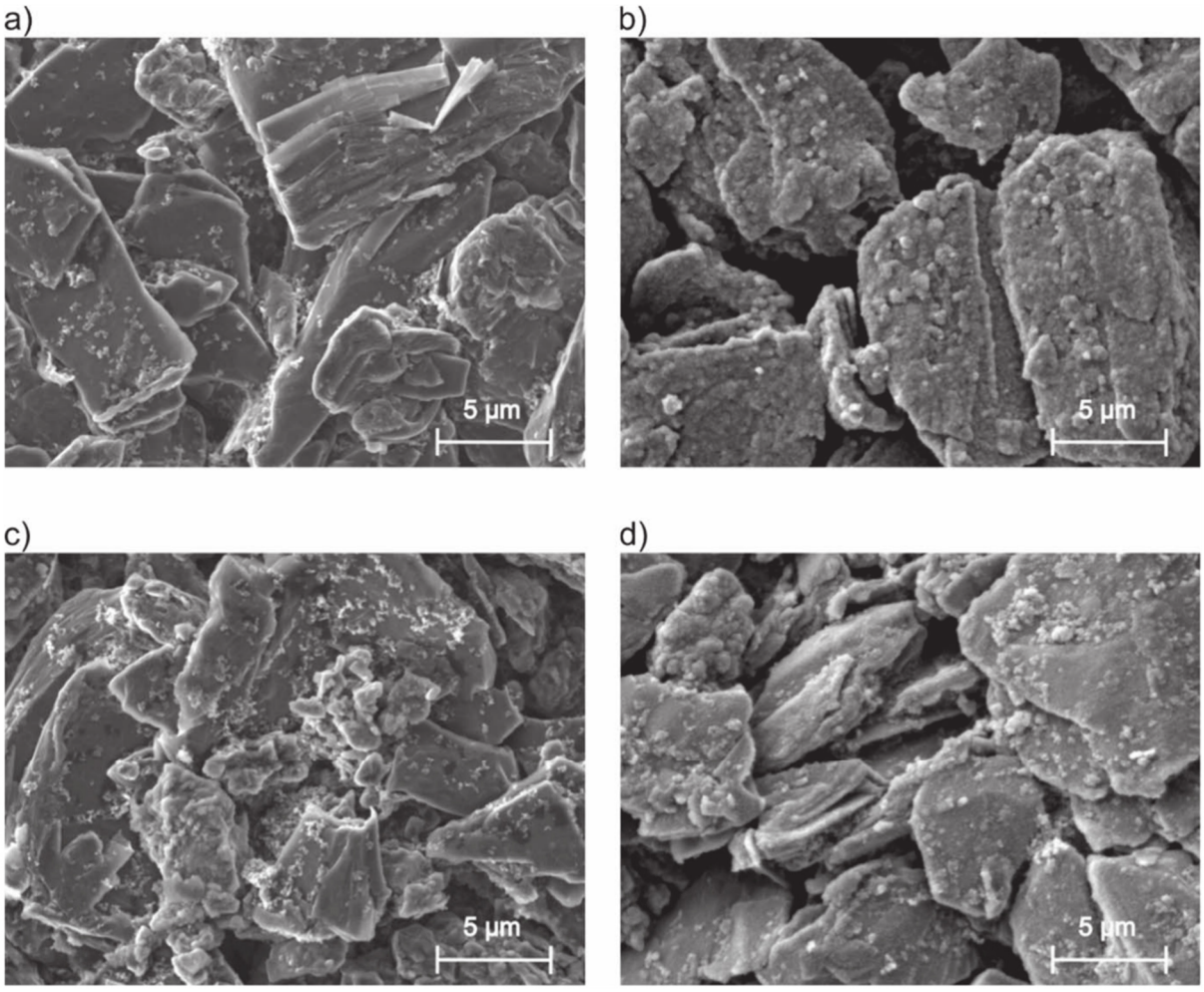

Figure 7. SEM measurements of anodes from (a)-(b) graphite based and (c)-(d) SiG5.8 based cells at 5000x magnification. Anodes a) and c) are from cells after formation and anodes (b) and (d) are from calendar aged cells at 45 °C/100% SoC.

Journal of The Electrochemical Society, 2024 **171** 010510

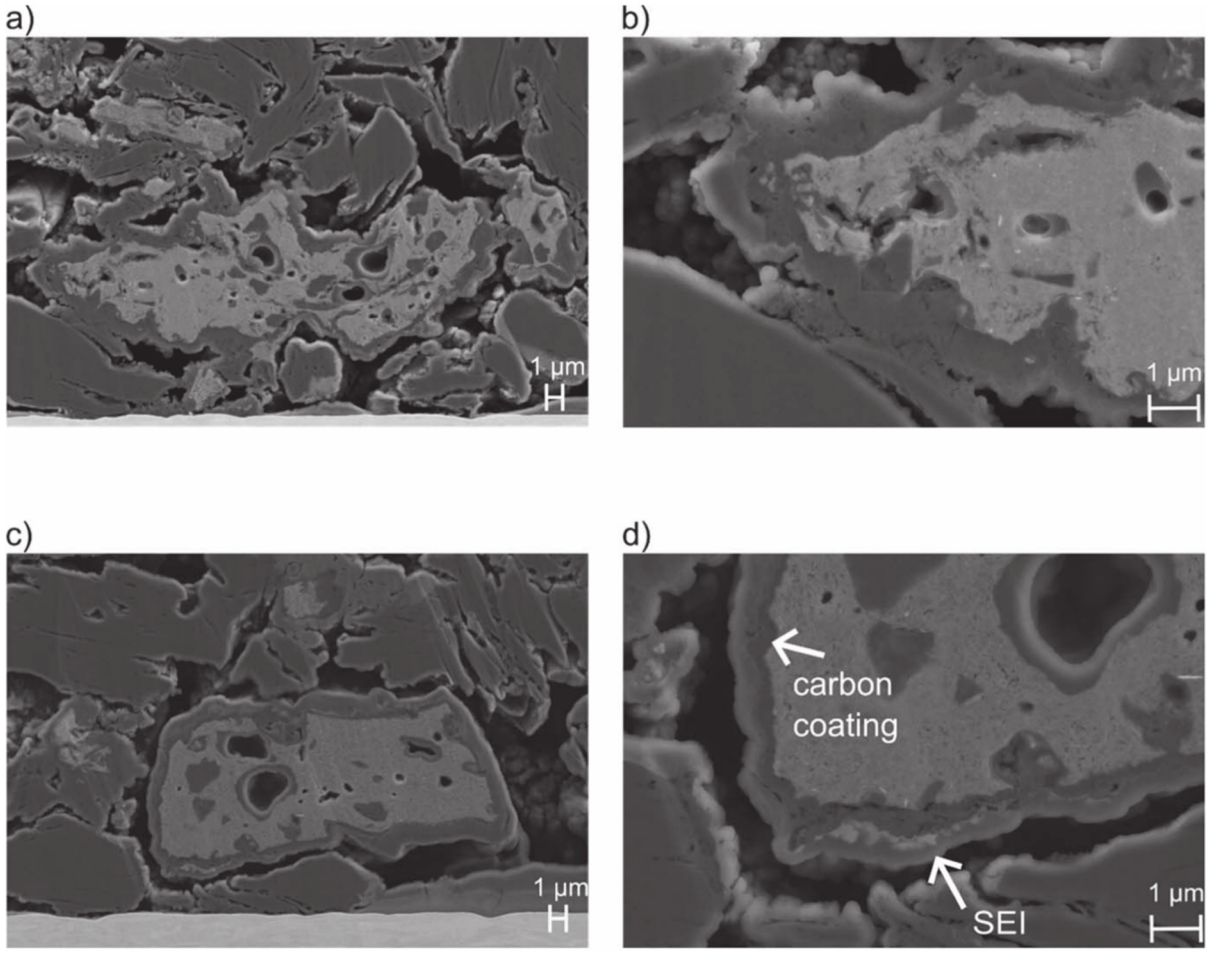

Figure 8. Comparative SEM cross-sections of representative Si particles of SiG5.8 anodes from a cell (a)-(b) after formation and (c)-(d) after calendar aging at 45 °C and the storage SoC of 100%. Images (a) and (c) were recorded at 10000x magnification and images (b) and (d) at 30000x magnification. The arrows in (d) indicate the intrinsic carbon coating and the SEI layer.

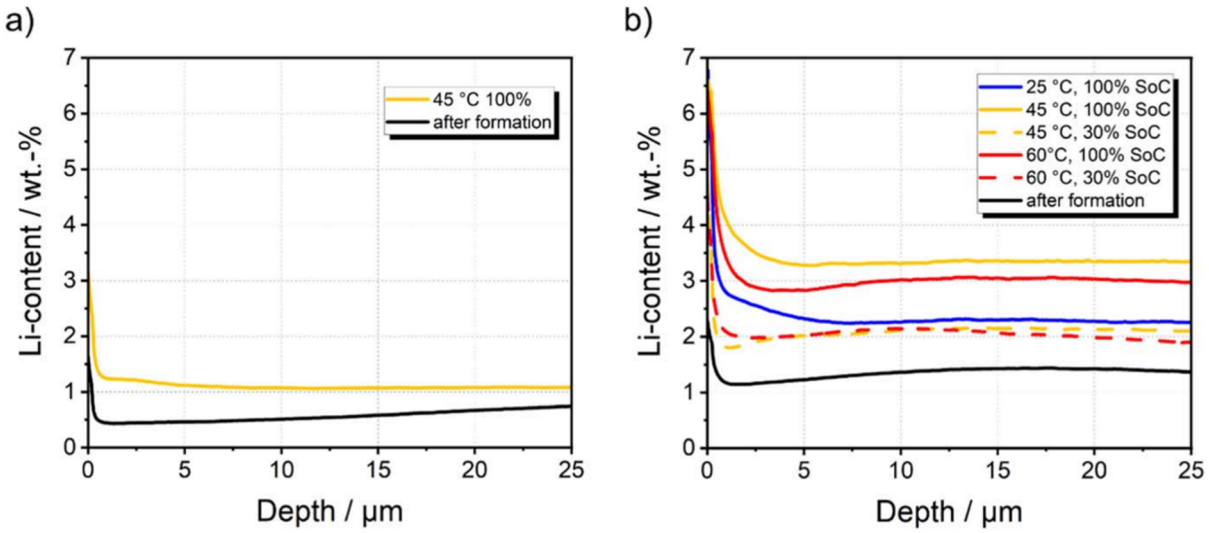

Figure 9. Comparative plot of the GD-OES depth profile of the Li content of anodes from (a) graphite based and (b) SiG5.8 based cells.

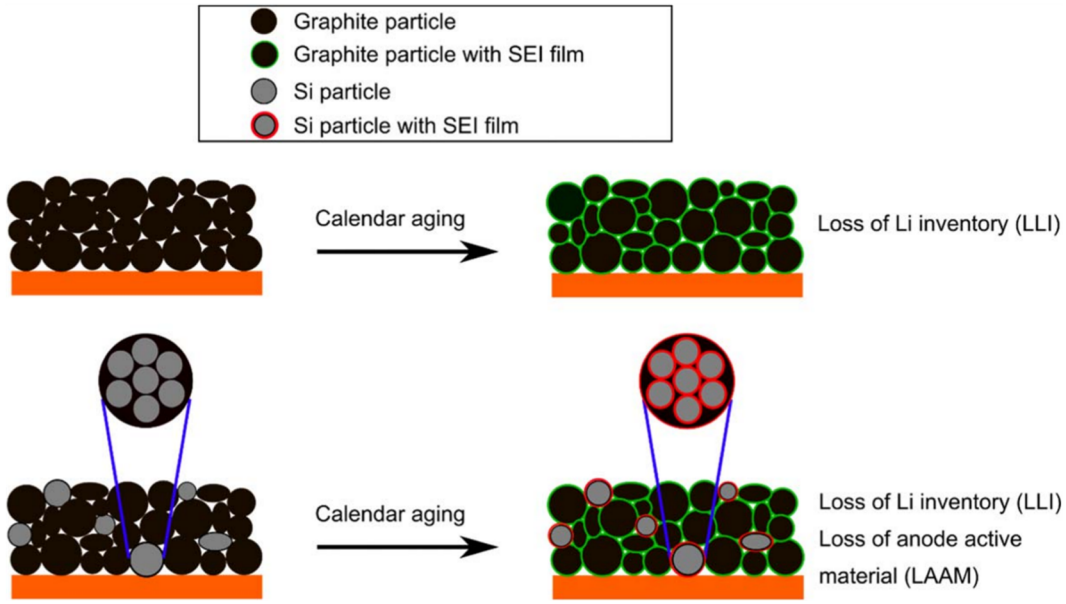

Figure 10. Schematic representation of the calendar aging mechanism in the pure graphite cells (top) and the Si/graphite cells (bottom).

Table III. Summary of the calendar aging behavior of cells with graphite and Si/graphite anodes.

Graphite		Si/graphite
	square-root decrease of capacity with time faster aging with higher temperature (Arrhenius-like) fastest aging at highest SoC of 100%	
aging of pure graphite slower than with Si SEI growth on graphite –> LLI		faster aging with higher Si content SEI growth on graphite –> LLI SEI growth on Si –> LLI + LAAM

particle composite architecture is commonly used to minimize the volume expansion of Si particles during lithiation[9] and was also found in commercial cells.[8]

In addition to the intrinsic carbon coating of the μm-sized Si/carbon particles, the surface of these particles appears to be covered by another very thin film after formation (film of lighter grey in Figs. 8a–8b), which is most likely a SEI layer formed during formation. After calendar aging, the additional surface film around the Si/carbon secondary microparticle (film of lighter grey in Figs. 8c–8d) is still very thin compared to our earlier observation with commercial cells (cell type C in Ref. 8). Thus, no significant aging-induced SEI growth can be observed for the μm-scaled composite as a whole. In contrast, the SEI formation suggested by the electrochemical analysis most likely takes place on the surfaces of the embedded nano-sized primary Si particles. However, this cannot be observed by SEM due to resolution limitations. In the literature it is reported, that Li- and O-rich SEI components form especially on Si particles.[59,60] According to Philippe et al.,[59] such components are Li silicates with the general formula of $Li_xSi_yO_z$, which were also found by Richter et al.[11] for Si/graphite anodes in commercial cells. Therefore, it is conceivable that such species might also be formed during calendar aging with the active material used in this study, thereby consuming both cyclable Li^+-ions and the Si active material itself. This leads to the suggested combination of LLI and LAAM as the main aging mechanism for the Si-containing cells.

The Li contents in graphite and SiG5.8 anodes were quantified by GD-OES depth profiling. When comparing the unaged and calendar aged anodes in Fig. 9 it can be noted that the Li content is lower both at the surface and in the bulk material for the unaged cells. The increase in Li content in the electrodes due to calendar aging can be taken as an indication of an irreversible loss of cyclable Li^+-ions in favor of the growth of the SEI layer.

For the SiG5.8 anodes calendar aged at 45 °C and 60 °C (Fig. 9b) a higher amount of Li was determined in the corresponding anodes for the cells aged at 100% SoC compared to their analogues aged at 30% SoC. This finding correlates well with the highest capacity losses found for the highest SoC studied. Moreover, the quantified Li contents in the Si-containing anodes are higher than in the graphite based counterparts. Accordingly, the presence of Si seems to enhance irreversible Li accumulation in the anode, which could explain the higher irreversible capacity losses of the Si/graphite cells compared to the graphite-only cells.

Table III summarizes all characteristics of the calendar aging behavior found for the investigated cell types. These indications suggest a different main aging mechanism for the Si/graphite anodes in comparison to the pure graphite anodes. As shown schematically in Fig. 10, calendar aging results from SEI growth in both cases, but leads to pure LLI for the graphite anodes, while it additionally consumes the Si active material itself in the Si/graphite cells, leading to LLI and LAAM as the main aging mechanism.

Journal of The Electrochemical Society, 2024 **171** 010510

Conclusions

In this detailed study with 121 Li-ion pouch full cells containing pure graphite as well as Si/graphite anodes, the main mechanisms for calendar aging were investigated. The following results on cell level can be reported:

- Capacity fade follows a square-root function with time for all cell types. The aging rate changes with time and can be described by the derivation of the square-root function.
- The aging rate increases with temperature following an Arrhenius-like behavior. Time-dependent 3D Arrhenius plots show the highest aging rates in the beginning of aging and an attenuation with aging time.
- The highest capacity losses were found after aging at 100% SoC followed by 60% SoC and 30% SoC.
- In general, a faster capacity decrease was identified for the Si/graphite cells compared to the pure graphite cells. With respect to the Si content a clear trend of increasing aging rates with increasing Si content was observed. However, this trend is not in the same direction for all aging conditions studied.

Post-Mortem analysis revealed the following trends on electrode level:

- An aging-induced film growth is detectable by SEM on the surface of the pure graphite anodes, however, not for the Si/graphite anodes. In this context, the structure of the Si/carbon secondary microparticles should be emphasized, which contain embedded nano-Si particles. The SEI growth occurs most likely on the surfaces of the Si nanoparticles, which is not visible by SEM.
- GD-OES depth profiling revealed an increased Li content for anodes from calendar aged cells compared to fresh cells. With increasing SoC, higher amounts of Li were detected in Si-containing anodes. Overall, the quantified Li contents are higher in aged cells with Si component compared to pure graphite anodes.

It can be concluded, that the main aging mechanism for the investigated cells containing graphite or Si/graphite anodes most likely is SEI growth, with the SEI irreversibly binding Li in the anode. In case of graphite anodes, SEI growth happens on the surface of the graphite particles only, leading only to LLI. Since SEI is a surface modification of graphite particles only and no bulk modification, LAAM does not play a significant role for graphite anodes.

In contrast, for Si/graphite anodes investigated in this paper, SEI growth leads to both LLI and LAAM. In case of the Si compound, SEI growth affects also the Si active material itself, leading not only to LLI as for graphite. The cause for such different behavior is still to be investigated and most likely will be also subject to the Si properties in the anode. This point is important since LAAM can change the N/P ratio and therefore influence the susceptibility to Li plating. Therefore, the mechanism in calendar aging is relevant for the safety in second-life applications. Further investigations on this direction are ongoing in our labs.

Acknowledgments

Funding of the projects CharLiSiKo (03XP0333A) and MiCha (03XP0317C) in the AQua-Cluster by the German Federal Ministry of Education and Research (BMBF) and project management by Projektträger Jülich (PtJ) are gratefully acknowledged. All investigations in this work were carried out at ZSW. The authors would like to thank A. Aracil Regalado and C. Pfeifer (ZSW) for SEM/EDX measurements and Prof. A. Latz (HIU, DLR) for fruitful discussions.

ORCID

Katharina Bischof https://orcid.org/0009-0004-0321-3252
Marius Flügel https://orcid.org/0000-0002-9792-0414
Margret Wohlfahrt-Mehrens https://orcid.org/0000-0002-5118-5215
Thomas Waldmann https://orcid.org/0000-0003-3761-1668

References

1. M. Dubarry, N. Qin, and P. Brooker, *Current Opinion in Electrochemistry*, **9**, 106 (2018).
2. C. Wang, C. Yang, and Z. Zheng, *Advanced Science*, **9**, 2105213 (2022).
3. F. Ozanam and M. Rosso, *Materials Science and Engineering: B*, **213**, 2 (2016).
4. F. Luo, B. Liu, J. Zheng, G. Chu, K. Zhong, H. Li, X. Huang, and L. Chen, *J. Electrochem. Soc.*, **162**, A2509 (2015).
5. J. D. McBrayer et al., *Nat. Energy*, **6**, 866 (2021).
6. X. Zuo, J. Zhu, P. Müller-Buschbaum, and Y.-J. Cheng, *Nano Energy*, **31**, 113 (2017).
7. M. Armand et al., *J. Power Sources*, **479**, 228708 (2020).
8. M. Flügel, K. Richter, M. Wohlfahrt-Mehrens, and T. Waldmann, *J. Electrochem. Soc.*, **169**, 50533 (2022).
9. F. Dou, L. Shi, G. Chen, and D. Zhang, *Electrochemical Energy Reviews*, **2**, 149 (2019).
10. M. Schindler, J. Sturm, S. Ludwig, A. Durdel, and A. Jossen, *J. Electrochem. Soc.*, **168**, 60522 (2021).
11. K. Richter, T. Waldmann, M. Kasper, C. Pfeifer, M. Memm, P. Axmann, and M. Wohlfahrt-Mehrens, *J. Phys. Chem.*, C**123**, 18795 (2019).
12. J. Schmitt, M. Schindler, and A. Jossen, *J. Power Sources*, **506**, 230240 (2021).
13. D. Anseán, G. Baure, M. González, I. Cameán, A. B. García, and M. Dubarry, *J. Power Sources*, **459**, 227882 (2020).
14. X. Li, A. M. Colclasure, D. P. Finegan, D. Ren, Y. Shi, X. Feng, L. Cao, Y. Yang, and K. Smith, *Electrochim. Acta*, **297**, 1109 (2019).
15. K. Kalaga, M.-T. F. Rodrigues, S. E. Trask, I. A. Shkrob, and D. P. Abraham, *Electrochim. Acta*, **280**, 221 (2018).
16. T. Waldmann, M. Wilka, M. Kasper, M. Fleischhammer, and M. Wohlfahrt-Mehrens, *J. Power Sources*, **262**, 129 (2014).
17. J. Vetter, P. Novák, M. R. Wagner, C. Veit, K.-C. Möller, J. O. Besenhard, M. Winter, M. Wohlfahrt-Mehrens, C. Vogler, and A. Hammouche, *J. Power Sources*, **147**, 269 (2005).
18. L. Y. Beaulieu, T. D. Hatchard, A. Bonakdarpour, M. D. Fleischauer, and J. R. Dahn, *J. Electrochem. Soc.*, **150**, A1457 (2003).
19. I. Zilberman, J. Sturm, and A. Jossen, *J. Power Sources*, **425**, 217 (2019).
20. L. de Sutter, G. Berckmans, M. Marinaro, J. Smekens, Y. Firouz, M. Wohlfahrt-Mehrens, J. van Mierlo, and N. Omar, *Energies*, **11**, 2948 (2018).
21. W. Lu, L. Zhang, Y. Qin, and A. Jansen, *J. Electrochem. Soc.*, **165**, A2179 (2018).
22. M. Flügel, M. Bolsinger, M. Marinaro, V. Knoblauch, M. Hölzle, M. Wohlfahrt-Mehrens, and T. Waldmann, *J. Electrochem. Soc.*, **170**, 60536 (2023).
23. D. Aurbach, K. Gamolsky, B. Markovsky, Y. Gofer, M. Schmidt, and U. Heider, *Electrochim. Acta*, **47**, 1423 (2002).
24. J. C. Burns, R. Petibon, K. J. Nelson, N. N. Sinha, A. Kassam, B. M. Way, and J. R. Dahn, *J. Electrochem. Soc.*, **160**, A1668 (2013).
25. I. A. Shkrob, J. F. Wishart, and D. P. Abraham, *The Journal of Physical Chemistry C*, **119**, 14954 (2015).
26. C. Xu, F. Lindgren, B. Philippe, M. Gorgoi, F. Björefors, K. Edström, and T. Gustafsson, *Chem. Mater.*, **27**, 2591 (2015).
27. M. Ecker, J. B. Gerschler, J. Vogel, S. Käbitz, F. Hust, P. Dechent, and D. U. Sauer, *J. Power Sources*, **215**, 248 (2012).
28. J. Schmitt, A. Maheshwari, M. Heck, S. Lux, and M. Vetter, *J. Power Sources*, **353**, 183 (2017).
29. J. Schmalstieg, S. Käbitz, M. Ecker, and D. U. Sauer, *J. Power Sources*, **257**, 325 (2014).
30. S. Käbitz, J. B. Gerschler, M. Ecker, Y. Yurdagel, B. Emmermacher, D. André, T. Mitsch, and D. U. Sauer, *J. Power Sources*, **239**, 572 (2013).
31. E. Peled, *J. Electrochem. Soc.*, **126**, 2047 (1979).
32. H. J. Ploehn, P. Ramadass, and R. E. White, *J. Electrochem. Soc.*, **151**, A456 (2004).
33. M. Broussely, S. Herreyre, P. Biensan, P. Kasztejna, K. Nechev, and R. Staniewicz, *J. Power Sources*, **97-98**, 13 (2001).
34. F. Single, A. Latz, and B. Horstmann, *ChemSusChem*, **11**, 1950 (2018).
35. M. B. Pinson and M. Z. Bazant, *J. Electrochem. Soc.*, **160**, A243 (2013).
36. J. Christensen and J. Newman, *J. Electrochem. Soc.*, **151**, A1977 (2004).
37. F. Single, B. Horstmann, and A. Latz, *J. Electrochem. Soc.*, **164**, E3132 (2017).
38. S. Shi, P. Lu, Z. Liu, Y. Qi, L. G. Hector, H. Li, and S. J. Harris, *J. Am. Chem. Soc.*, **134**, 15476 (2012).
39. C. R. Birkl, M. R. Roberts, E. McTurk, P. G. Bruce, and D. A. Howey, *J. Power Sources*, **341**, 373 (2017).
40. X. Han, L. Lu, Y. Zheng, X. Feng, Z. Li, J. Li, and M. Ouyang, *eTransportation*, **1**, 100005 (2019).
41. G. Kucinskis, M. Bozorgchenani, M. Feinauer, M. Kasper, M. Wohlfahrt-Mehrens, and T. Waldmann, *J. Power Sources*, **549**, 232129 (2022).
42. P. Atkins, J. De Paula, and J. Keeler, *Atkins' Physical Chemistry* (Oxford University Press, Oxford) (2023).
43. T. Waldmann, M. Kasper, and M. Wohlfahrt-Mehrens, *Electrochim. Acta*, **178**, 525 (2015).
44. X.-G. Yang and C.-Y. Wang, *J. Power Sources*, **402**, 489 (2018).
45. M. Feinauer, A. A. Abd-El-Latif, P. Sichler, A. Aracil Regalado, M. Wohlfahrt-Mehrens, and T. Waldmann, *J. Power Sources*, **570**, 233046 (2023).

46. M. Bozorgchenani, G. Kucinskis, M. Wohlfahrt-Mehrens, and T. Waldmann, *J. Electrochem. Soc.*, **169**, 30509 (2022).
47. T. Waldmann, N. Ghanbari, M. Kasper, and M. Wohlfahrt-Mehrens, *J. Electrochem. Soc.*, **162**, A1500 (2015).
48. B. Y. Liaw, E. P. Roth, R. G. Jungst, G. Nagasubramanian, H. L. Case, and D. H. Doughty, *J. Power Sources*, **119–121**, 874 (2003).
49. J. Wang, P. Liu, J. Hicks-Garner, E. Sherman, S. Soukiazian, M. Verbrugge, H. Tataria, J. Musser, and P. Finamore, *J. Power Sources*, **196**, 3942 (2011).
50. P. Keil, S. F. Schuster, J. Wilhelm, J. Travi, A. Hauser, R. C. Karl, and A. Jossen, *J. Electrochem. Soc.*, **163**, A1872 (2016).
51. P. Keil and A. Jossen, *J. Electrochem. Soc.*, **164**, A6066 (2017).
52. M. Dubarry, C. Truchot, and B. Y. Liaw, *J. Power Sources*, **219**, 204 (2012).
53. T. Ohzuku, Y. Iwakoshi, and K. Sawai, *J. Electrochem. Soc.*, **140**, 2490 (1993).
54. M. Ashuri, Q. He, and L. L. Shaw, *Nanoscale*, **8**, 74 (2016).
55. V. G. Khomenko, V. Z. Barsukov, J. E. Doninger, and I. V. Barsukov, *J. Power Sources*, **165**, 598 (2007).
56. R. Jung, M. Metzger, F. Maglia, C. Stinner, and H. A. Gasteiger, *J. Electrochem. Soc.*, **164**, A1361 (2017).
57. H.-J. Noh, S. Youn, C. S. Yoon, and Y.-K. Sun, *J. Power Sources*, **233**, 121 (2013).
58. M. Weiss et al., *Adv. Energy Mater.*, **11**, 2101126 (2021).
59. B. Philippe, R. Dedryvère, M. Gorgoi, H. Rensmo, D. Gonbeau, and K. Edström, *Chem. Mater.*, **25**, 394 (2013).
60. B. Philippe, R. Dedryvère, J. Allouche, F. Lindgren, M. Gorgoi, H. Rensmo, D. Gonbeau, and K. Edström, *Chem. Mater.*, **24**, 1107 (2012).

3.5. 3D-Printed Testing Plate for the Optimization of High C-Rates Cycling Performance of Lithium-Ion Cells

Reprinted with permission from:

Gilberto Carbonari, R.-G. Scurtu, T. Waldmann, S. Radloff, **M. Flügel**, A. Hoffmann, M. Wohlfahrt-Mehrens, 2021 *J. Electrochem. Soc.* **168** 050508

© 2021 The Author(s). Published on behalf of The Electrochemical Society by IOP Publishing Limited. This is an open access article distributed under the terms of the Creative Commons Attribution Non-Commercial No Derivatives 4.0 License (CC BY-NC-ND, http://creativecommons.org/licenses/by-nc-nd/4.0/), which permits non-commercial reuse, distribution, and reproduction in any medium, provided the original work is not changed in any way and is properly cited. For permission for commercial reuse, please email: permissions@ioppublishing.org.

DOI: https://doi.org/10.1149/1945-7111/abfab9

Individual Contribution

C. Carbonari	Conceptualization, Methodology, Validation, Formal Analysis, Investigation, Writing - Original Draft, Visualization
R.G. Scurtu	Conceptualization, Methodology, Validation, Formal Analysis, Investigation, Writing – Review & Editing, Visualization
T. Waldmann	Conceptualization, Methodology, Validation, Formal Analysis, Investigation, Writing – Review & Editing, Visualization, Project Administration
S. Radloff	Conceptualization, Methodology, Validation, Formal Analysis, Investigation, Visualization
M. Flügel	Conceptualization, Methodology, Validation, Formal Analysis, Investigation, Visualization
A. Hoffmann	Conceptualization, Supervision, Writing – Review & Editing
M. Wohlfahrt-Mehrens	Conceptualization, Supervision, Writing - Review & Editing, Project Administration, Funding Acquisition

Summary

In this work, a strategy to avoid Li deposition in graphite anodes was developed using a reference electrode to monitor the anode potential. Novel 3-D printed testing plates (PP3D plates) with a Li-reference electrode were used to create well-designed 3-electrode pouch cells. The newly developed setup was used to investigate the electrochemical behavior of NMC811 cathodes and graphite anodes at discharge C-rates up to 7C and charge C-rates up to 2C. The introduction of the PP3D plate provided insight into the optimal cycling conditions for the best cell performance, safety and cycle life for this specific anode/cathode combination, allowing the optimization of the aging procedure.

The presence of the PP3D plate did not negatively affect stack performance and provided an opportunity for the implementation of additional sensors. The plate enabled the monitoring of the anode potentials against a Li reference during C-rate tests. The observed potential trends were consistent with the behavior observed during long-term cycling at different charge currents and temperatures. All cells exhibited substantial performance and cycle stability, which can be attributed to optimized manufacturing and proper electrode design, such as slurry formulation, loading, and density. The use of pouch cell holders ensured the reproducibility of the results.

During the fast-charging test, the anode potential shifted towards a potential of 0 V vs. Li/Li^+ at the end of charge, due to the polarization, which is influencing the N/P ratio. The anodes charged at 25 °C only reached a potential below 0 V vs. Li/Li^+ during the 2C CC charging step. When a CV step was included, the anode potential rose to positive potentials, implicating, that deposited Li re-intercalates during the CV step.

The cells charged at 1C and 2C CCCV at 25 °C reached 80% SOH after 1000 cycles. However, when charged at 2C CCCV at 40 °C, the cells reached 80% SOH after approximately 650 cycles. Additionally, the GD-OES depth profiling further supported these findings. The only SLPCs showing lithium deposition were those charged at 2C rate at 25 °C, aligning with the negative anode potentials observed in the PP3D cell results.

The development of 3D-printed testing plates with Li-reference electrodes facilitated the creation of a well-designed 3-electrode pouch cell. This setup enabled the identification of the best high C-rate cycling procedure, leading to improved performance and cycling life of lithium-ion cells. The 3D printing versatility of the PP3D plates allows the easy implementation of more stable reference electrodes, such as $Li_4Ti_5O_{12}$ or $LiFeO_4$ or various sensors for further electrochemical studies.

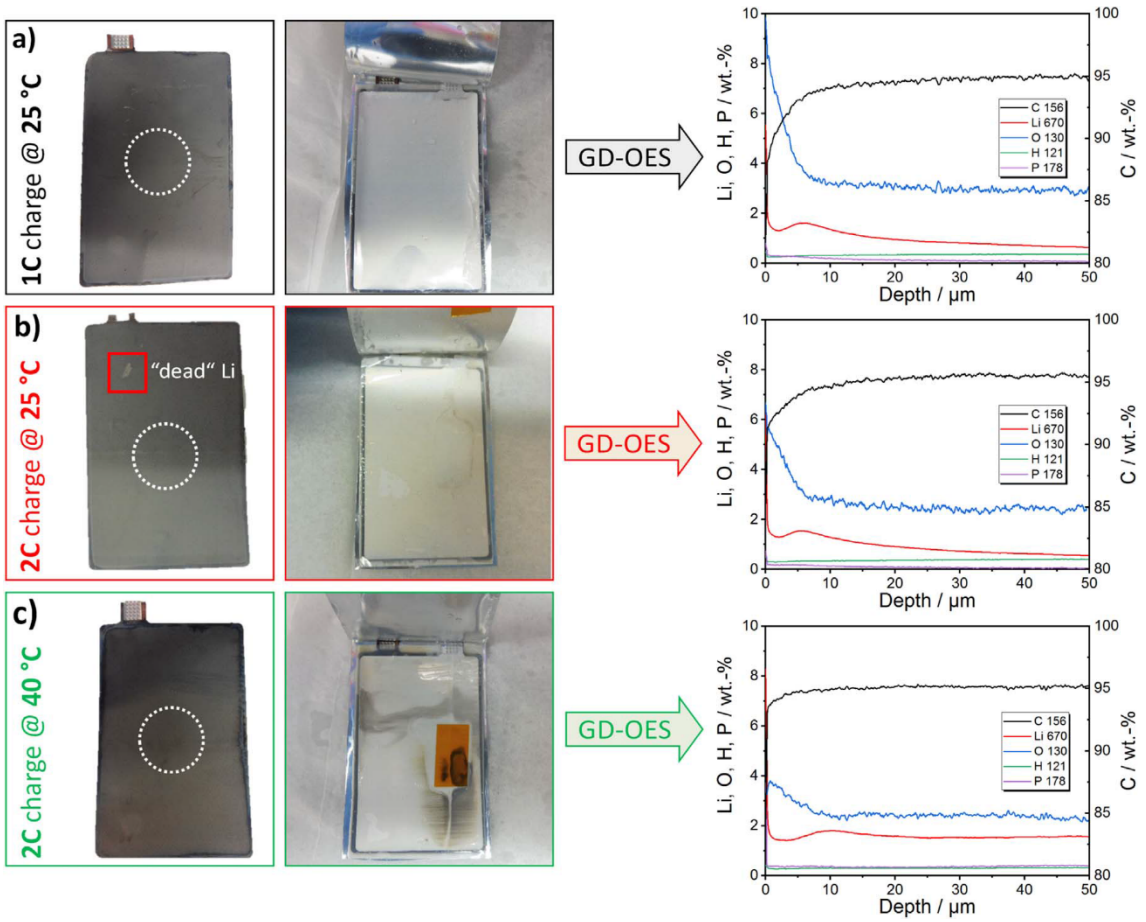

Figure 13: Post-Mortem analysis of the cells aged at different C-rates and temperatures [172].

Journal of The Electrochemical Society, 2021 **168** 050508

3D-Printed Testing Plate for the Optimization of High C-Rates Cycling Performance of Lithium-Ion Cells

Gilberto Carbonari, Rares-George Scurtu,[z] Thomas Waldmann, Sonja Radloff,[*] Marius Flügel, Alice Hoffmann, and Margret Wohlfahrt-Mehrens[**]

Zentrum für Sonnenenergie- und Wasserstoff-Forschung Baden-Württemberg, 89081 Ulm, Germany

Nowadays, long charging times have become one of the main limitations to a greater worldwide spread of electric vehicles (EV). Enabling high C-rates charging is a promising approach to eliminate this problem and alleviate range anxiety. When a battery is charged at high currents, several factors have to be taken into account. Temperature is certainly a key parameter because when it is too high this can lead to degradation of components (binder, electrolyte, active material, etc), however, when it is too low intercalation kinetics becomes sluggish. Using 3D-printed testing plates (PP3D plates) with Li-reference electrode, we developed a tool for electrochemical investigations of pouch cells. These plates enabled to build a new well-designed 3-electrode pouch cell. This setup allows the identification of the best high C-rate cycling procedure to improve the performance and cycling life of the lithium ion cells. We explored the electrochemical behavior of NMC811 cathodes and graphite anodes, during high discharge C-rates test up to 7 C and charge C-rates up to 2 C. Moreover, the temperature influence on charging performance and longtime cycling stability is investigated. The cells cycled at 25 °C using optimized procedures reached an 80% state of health after more than 1000 cycles.

© 2021 The Author(s). Published on behalf of The Electrochemical Society by IOP Publishing Limited. This is an open access article distributed under the terms of the Creative Commons Attribution Non-Commercial No Derivatives 4.0 License (CC BY-NC-ND, http://creativecommons.org/licenses/by-nc-nd/4.0/), which permits non-commercial reuse, distribution, and reproduction in any medium, provided the original work is not changed in any way and is properly cited. For permission for commercial reuse, please email: permissions@ioppublishing.org. [DOI: 10.1149/1945-7111/abfab9]

Manuscript submitted February 24, 2021; revised manuscript received April 19, 2021. Published May 3, 2021.

Supplementary material for this article is available online

The last few years have seen a dizzying increase in the worldwide demand for electric vehicles (EV) and portable electronics.[1] Both of them share a common energy source: rechargeable lithium-ion batteries (LIBs). Their development follows the market demands for higher energy density as well as safer, cheaper, and more environmentally friendly batteries.[2] These tasks can be accomplished by pursuing different approaches but several of them could be fulfilled simultaneously. The traditional strategy to improve the battery-specific energy suggests increasing the average cell potential[2] and/or improving the specific capacity of the material. This can be easily estimated by applying Eq. 1.

$$Specific\ Energy\ (Wh\ Kg^{-1}) = \frac{nominal\ voltage\ (V)\ \cdot\ capacity\ rating\ (Ah)}{battery\ weight\ (Kg)} \quad [1]$$

One solution to these challenges is the use of layered lithium oxides also known as NMCs. Their general formula is $Li_{1+x}(Ni_yMn_zCo_{1-y-z})_{1-x}O_2$ and their names depend on the relative ratio of the three different transition metals (TM). NMC111 with a relatively low nickel content has been and still is used in LIBs because of its cycle life, stability, and capacity. On the other hand, Ni-rich materials such as NMC532, NMC622, and NMC811 seem to be reasonable choices for the future of the battery producers.[3] In particular, NMC811 provides high capacities of ~200 mAh g^{-1} and an average discharge potential of ~3.80 V together with a substantial decrease of the Co content.[4,5] Cobalt amount reduction is important in cutting down the costs and reducing the dependence on suppliers with a questionable supply chain.[6] These advantages come at the expense of its cycling stability and safety, both mainly originating from a high nickel content.[7] Several solutions have been taken into consideration such as the tailored coating on the active material surface[8,9] and electrolyte additives.[10–12] In terms of cost reduction and environmental sustainability, one further challenge for these materials is the implementation of aqueous processing. In fact, NMCs are sensitive to water and air exposure during storage and processing.[13] Nevertheless, several research groups have already obtained promising results from water-based cathode formulations.[14,15]

In order to minimize inactive material thus increasing battery energy density, an optimal capacity balancing ($Q_{negative\ electrode}/Q_{positive\ electrode}$ = N/P ratio) of the electrodes used in the cell must be defined.[16,17] A N/P ratio < 1 is not beneficial for cell-specific capacity and leads to anode overcharge and metallic lithium deposition on the anode side, whereas an N/P ratio ≫ 1 leads to cathode over-discharge and possibly cathodic material degradation. Ideally, an N/P ratio equal to 1 should be chosen to minimize these effects, but due to intrinsic defects in the electrodes and to avoid edge effect phenomena, N/P ratios slightly over 1 are used (e.g. 1.1–1.2). It should be noted that in the case of cells for high-energy applications, the ratio could be closer to 1, but in the case of quick charge application, the adopted N/P ratio is usually higher.

In a classical laboratory approach, the N/P ratio is usually determined by testing separately anode and cathode in coin half-cells. These capacity values are often obtained at low C-rates (e.g. C/10) and they do not reflect the ratio that can be obtained at relatively high C-rates.[18] On the other hand, when high currents are applied in coin half-cells, polarization phenomena can affect the results. The low lithium surface area leads to a large electrode polarization affecting its potential and capacity. Moreover, if we consider relatively high currents, every single coating defect (e.g. active material A.M. agglomerations, edge effect, edge cutting defects, etc.) starts to play a role, and often non-homogeneous coatings heavily affect the electrochemical results of small electrodes. For these reasons, pouch full-cells were used in this work to study especially the crosstalk of the paired electrodes, which gives more useful information about their electrochemical performances in real working conditions.

The development of additional strategies to overcome these issues can be facilitated by an accurate analysis of the processes leading to cell aging. Parameters such as anode and cathode potentials, cycling temperature, and stack pressure could be extremely helpful for a deep understanding of the cell behavior. Particularly, the usefulness of a reference electrode (RE) has never been questioned. An ideal RE should be non-polarizable and should exhibit a stable and reproducible potential during the electrochemical test. Since in full-cells voltage is

*Electrochemical Society Student Member.
**Electrochemical Society Member.
[z]E-mail: rares-george.scurtu@zsw-bw.de

Journal of The Electrochemical Society, 2021 **168** 050508

given by the difference of the cathode and anode potential (two-electrode setup), the introduction of a RE allows measuring the individual electrode contribution, which is a key parameter for an in-depth understanding of cell aging and degradation mechanisms.[19]

A significant work[20–22] was done in the case of small-sized electrodes on the lab scale. In case of larger electrode area and full-cells, most of the published works insert the RE inside the jelly roll or the electrode stack.[23,24] In this case, the RE surely is in the best position taking into account the electrical field and equipotential lines,[25] however, its presence in the stack will influence the cell behavior.[26] Different groups tried to minimize its dimension to avoid any side effects.[23,27] In commercial batteries, a certain stack pressure is always present and the minimal defect, as in the case of a RE, quickly results in lithium plating[28] even at moderate C-rates. For the sake of clarity, we would like to point out that in commercial batteries thin polymeric and ceramic coated separators are used. In this case, the presence of an internal RE will result in an even greater problem since the buffer ability of the glass fiber separator (e.g. Whatman GF/A) is lost.

Here is proposed a simple solution that involves a 3D printed plate (Fig. 1a). This device has proven to be cheap, easy to print, and non-invasive. Besides, it can be easily up-scaled and used to monitor larger electrode stacks. Its versatility allows the introduction of even more sensors (temperature, strain, etc) to gain a more complete understanding of cell aging mechanisms. Custom models can be realized thanks to the ease of the 3D design. In particular, the implementation of other sensors would help in a more complete mapping of cell aging.

In this paper, graphite||NMC811 single-layer pouch cells were tested to assess their discharge capabilities. In order to improve their charging step, 3D printed plates with an integrated lithium reference electrode (Li-RE) were used to follow anode and cathode potentials. Setup validation was investigated electrochemically by the means of pouch cells without 3D plate as well as optical visualization and Glow Discharge—Optical Emission Spectroscopy (GD-OES) depth profiling. Remarkable results in terms of performance, reproducibility, and reliability were obtained using this setup. The purpose of this work is to develop a tool able to predict and find the optimal cycling operation of a cell in terms of customized cycling procedures for extending the cell's lifetime.

Experimental

3D plate design.—The 3D plate was designed with free CAD software (Blender) and printed with a Fused Deposition Modeling (FDM) 3D printer (Ultimaker3, Ultimaker). Aside from a good extrusion accuracy, the choice of the material is fundamental since it needs to be electrolyte resistant. The most used in commercially available test cells is the expensive polyether ether ketone (PEEK) thanks to its superior mechanical and chemical properties. Since the extrusion process of this polymer requires high temperatures and high-end 3D printers, we have opted for a cheaper and easy to print polymer such as polypropylene (PP). Figure 1a shows its simple design. The electrodes´ tabs are fixed in two guides (see Fig. 1a—I) allowing the electrodes stack to stay in the desired position. The reference electrode (RE) position is well defined by design: to avoid short circuits and limit measurement's artifacts, the Li-RE (0.2 mm^2 surface) is placed at a horizontal distance of 300 μm from the stack (see Fig. S1). Single-layer pouch cells assembled in the 3D plate setup will be named PP3D cells (Fig. 1c).

Coatings and electrodes preparation.—All materials were used as received. Anode and cathode slurries were prepared in a planetary mixer where active materials portions were kept as high as possible to match industrial targets and good coating performance in terms of mechanical and electrochemical stability. The used materials were Graphite (Hitachi Chemical), $LiNi_{0.8}Mn_{0.1}Co_{0.1}O_2$ (NMC 811, Targray), Na-CMC (Sunrose), PVdF (Solvay Solexis), SBR emulsion (Zeon), Super C65 (SC65, Imerys) and SFG6L graphite (Imerys).

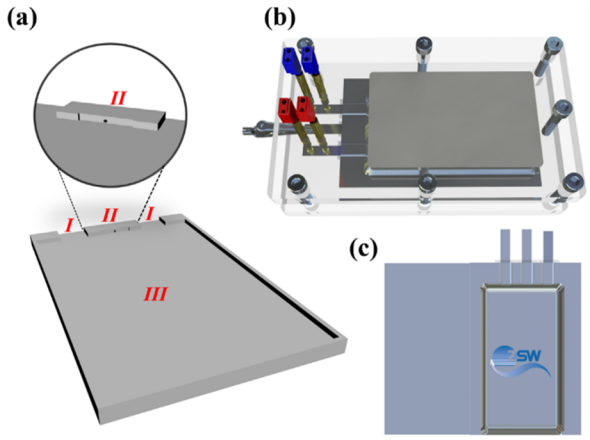

Figure 1. PP3D plate design with a magnified vision of the reference electrode area (II), channels for the electrodes' tabs and the surface where the stack is placed (III) (a); b) Pouch cell holder design (b); Assembled PP3D cells (c).

Distilled water and *N*-methylpyrrolidone (NMP, Sigma Aldrich) were used as solvents respectively for anode and cathodes. The slurries were then cast in a pilot line (LACOM Gmbh, Germany) equipped with a comma bar system, four drying ovens (total length: 8 m), and a Kr online mass scanner to ensure a uniform loading throughout the coatings. All electrodes were prepared by single-side coating and calendering to a specific density. The most important parameters of the electrodes are shown in Table I.

Cells assembly.—Where not specified, all the cells were assembled with the materials and components listed in Table I. For single-layer pouch cells (SLPCs), electrodes were punched with a customized mechanical puncher (anode area: 26 cm^2; cathode area: 23.94 cm^2), dried overnight at 130 °C under vacuum and stored in a dry cabinet. A tri-layered polymeric separator (Celgard 2325) was

Table I. Anode and cathode characteristics.

Anode	94 wt% SMG-HT1(Hitachi Chemical)
	2 wt% Super C65 (Imerys)
	2 wt% Na-CMC (Sunrose)
	2 wt% SBR (Zeon)
	Cu current collector: 10 μm
	Coating Thickness: 50 μm
	Density: 1.4 g cm^{-3}
	AM loading: 8 mg cm^{2}
	Capacity (@ C/10): 2.9 mAh cm^{-2}
	2 wt% Super C65 (Imerys)
Cathode	93 wt% NMC811 (Targray)
	2 wt% Super C65 (Imerys)
	2 wt% SFG6L graphite (Imerys)
	3 wt% PVdF (Solvay Solexis)
	Al current collector: 14 μm
	Coating thickness: 44 μm
	Density: 3.2 g cm^{-3}
	AM loading: 13.3 mg cm^{-2}
	Capacity (@ C/10): 2.7 mAh cm^{-2}
Separator	Celgard 2325
	Thickness: 25 μm
	Porosity: 39%
Electrolyte	1.4 M $LiPF_6$ in EC:DMC
	(3:7 wt%) + 2% VC (LP40)
	Conductivity @25 °C ≈ 12 mS cm^{-1}
	Conductivity @40 °C ≈ 15 mS cm^{-1}

Journal of The Electrochemical Society, 2021 **168** 050508

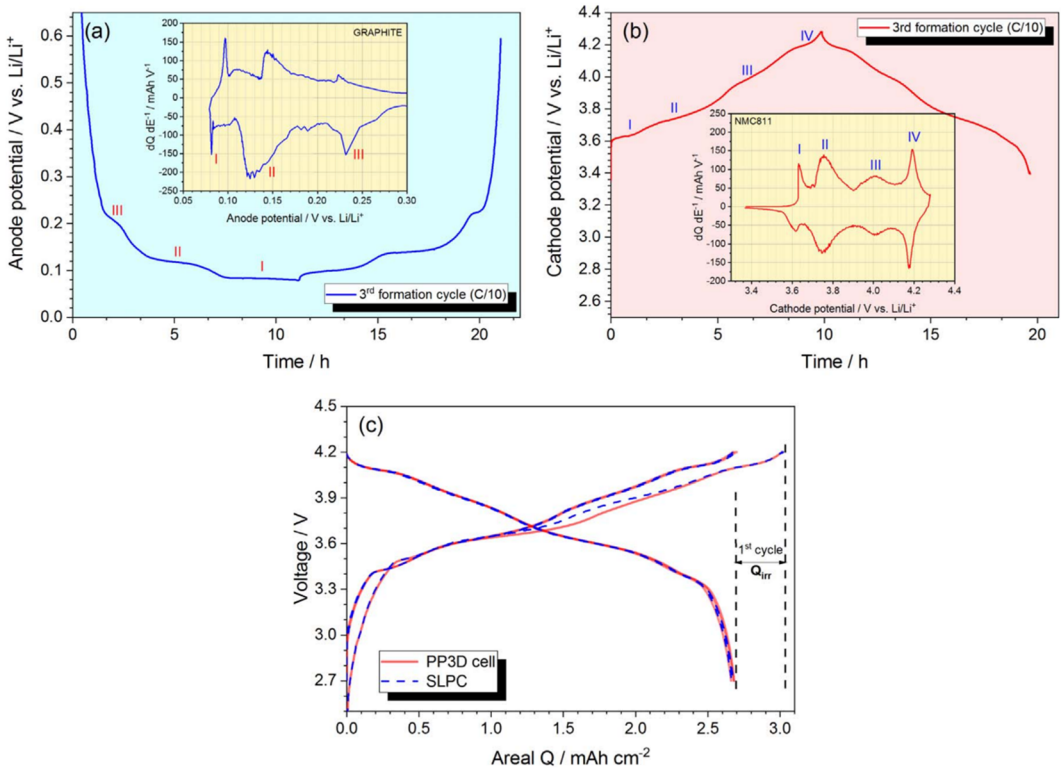

Figure 2. Galvanostatic profiles during the formation step of the graphite-based anode (a) and NMC811-based cathode (b) in a PP3D cell. Comparison of the first 3 cycles between a SLPC and a PP3D cell (c).

used and Al and Ni tab collectors were ultrasound-welded respectively to cathode and anode. Before electrolyte filling, the cell was furthermore dried at 80 °C overnight under vacuum.

Unlike regular single-layer pouch cells, when the PP3D plate is used, Celgard 2325 separator (26 cm^2) was stacked between anode and cathode and not rolled around them as in the SLPCs. A small piece of freshly cleaned metallic lithium (PI-KEM) was filled inside the channel where a thin copper wire was inserted. Anode and cathode were aligned on the reference electrode side and held in position by Kapton tape. Both cell types were assembled in a dry room (dew point < -65 °C), then they were vacuum-dried overnight at 80 °C. SLPC and PP3D cells were filled respectively with 0.9 ml and 1.2 ml of electrolyte and vacuum-sealed in a glovebox (MBraun, O_2, and H_2O levels < 0.5 ppm).

Electrochemical characterization.—All the electrochemical procedures listed in Table SI (Supporting Info available online at stacks.iop.org/JES/168/050508/mmedia) were carried out on a VMP-3 (Biologic) system connected to a climate chamber (VB-4004, Vötsch) where the cells were tested at controlled temperatures (25 °C and 40 °C). The resulting capacities are always normalized with respect to the first discharge value after the formation or the cathode active material weight. SLPCs and PP3D cells were cycled using an in-house designed pouch cell holder (Fig. 1b) equipped with pogo pins to test cells in a 4-points configuration. Thanks to the knowledge gained from previous tests on this anode/cathode combination, the bolts of the holder were tightened applying a defined torque momentum resulting in an average force of 100 N on the surface of the pouch cell. The holder assures a homogenous pressure on the cells and it is minimizing the electrical contact resistance between VMP probes and the tabs of the cells.

Post-mortem and glow discharge optical emission spectroscopy (GD-OES).—Aged cells were opened in an Ar-filled glovebox (MBraun, O_2, and H_2O levels < 0.5 ppm), and pictures of the graphite anodes were taken. The absence or presence of lithium deposition was further confirmed by GD-OES analysis according to the method published earlier.[29] lithium deposition quantification was conducted using reference samples.

Aged anode samples were washed three times in Dimethyl Carbonate (DMC), left to dry, and eventually mounted on airtight sample holders. An additional test was performed on the pristine anode coating to evaluate its binder distribution following the sodium relative concentration (from the Na-CMC binder) throughout the coating thickness. GD-OES analyses were conducted using a GDA750 device (Spectruma). The measurements on the anodes were performed in RF mode at a discharge voltage of 550 V, a gas pressure of 2 hPa, and a pulse rate of 50% at a frequency of 2500 Hz. A mixture of H_2 6.0 and Ar 6.0 (1:99 vol. %) was used as a discharge gas. The following emission lines were used for detection: Cu (327.4 nm), C (156.1 nm), O (130.2 nm), Li (670.7 nm), P (178.3 nm), H (121.6 nm), Na (589.0 nm). The sputtered craters in the samples produced by the measurement have a diameter of 2.5 mm.

Results and Discussion

Cell formation and validation.—The formation protocol in Table SI (supporting Info) was applied to SLPCs and PP3D cells. Figure 2a shows the three formation cycles for the two different setups. Charge/discharge profiles are overlapped leading to the same capacities. The use of the PP3D plate did not influence the electrochemical performance of the stack tested in a state-of-the-art SLPC. Firstly, both showed an initial irreversible capacity loss (ICL)

Journal of The Electrochemical Society, 2021 **168** 050508

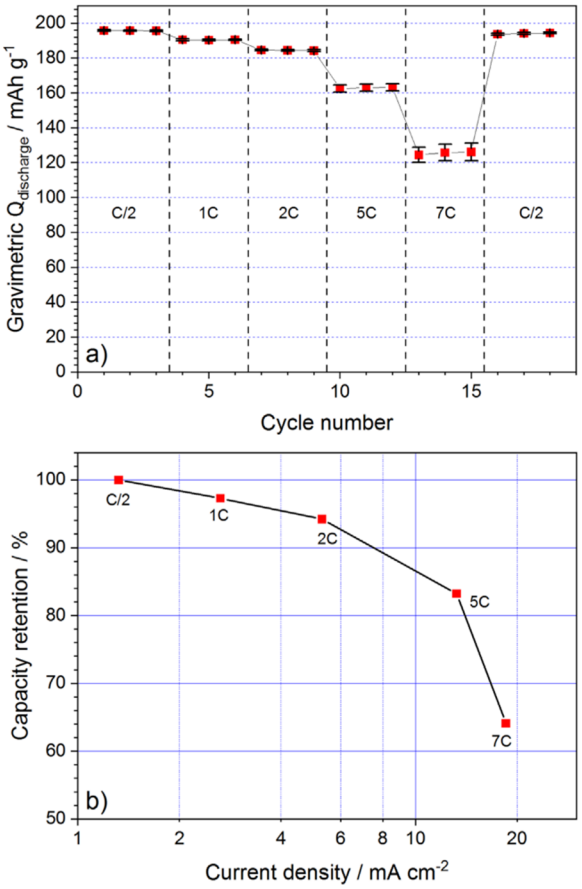

Figure 3. SLPCs performance at different discharge current rates (a)–(b) ranging from C/2 to 7 C. Charge steps were conducted with C/2 in constant current-constant voltage (CCCV) mode until a current lower than C/20 is reached.

of 11.5%, a value in perfect agreement with the ICL values found in the literature (10% < ICL < 20%).[30,31]

The presence of the Li-RE in PP3D cells affords us to separate anode and cathode contributions. Figures 2b–2c report the third formation cycle for the anode and cathode, respectively. In Fig. 2b it is possible to distinguish the lithium intercalation process in the graphite anode. The dQ dE^{-1} vs. E plot in the inset allows for better visualization of the graphite staging. The redox peaks around 230 (III), 120 (II), and 80 mV (I) correspond to the formation of LiC_{36}, LiC_{12}, and LiC_6 graphite intercalation compounds (GICs), respectively.[32–35] In Fig. 2c, it is possible to observe the respective $dQ \times dE^{-1}$ vs. E plot for the cathode side. The typical redox peak at 3.76 V is present together with three other oxidation peaks at 3.64 V, 4.02 V, and 4.20 V corresponding to the multiphase transition from hexagonal to monoclinic (H1 → M), monoclinic to hexagonal (M → H2) and hexagonal to hexagonal (H2 → H3).[7,36,37]

Graphite is certainly the most used anode material in LIBs and the lithium is inserted in its structure by an intercalation reaction. Because of several factors such as temperature, electrodes structure, electrolyte, charging current, etc, lithium plating can compete with the main Li storage mechanism.[38] This alternative faradaic reaction becomes thermodynamically possible when the anode potential falls below the Li/Li^+ couple potential (−3.04 V), where Li^+ ions get reduced preferably on the graphitic surface leading to poor performance and safety issues. This phenomenon is exacerbated especially in the case of low temperatures, electrolytes with poor Li transport properties,[39] high C-rates, and not optimized anode structures. Since the N/P ratio changes with the applied current depending on the capacity retention and the different kinetics of anode and cathode, it would be faster to detect single electrode potentials in a full-cell at different C-rates. This is done by introducing a RE that allows monitoring the anode and cathode potentials individually. Its positioning can be internal or external relative to the electrode stack and despite the investigation of both geometries by several groups,[21,22,40,41] it is still hard to select the best setup.[19] To minimize the measurements artifacts, we deliberately used an external reference electrode to avoid shielding errors due to WE surface area coverage by RE[26] and application of inhomogeneous stack pressure. The ohmic drop due to relatively poor conductive organic electrolytes was minimized by placing the RE as close as possible to the stack edge previously aligned to avoid misalignment. Thanks to the near point-like design, the copper wire used as an electric connection to the RE was completely isolated from the electrolyte avoiding mixed surface potentials.

Good cell performance and reproducibility were achieved by the application of an external pressure onto the electrode stack since it can greatly influence the cell performance during formation and cycling steps.[42] Materials undergoing big volume expansions during cycling (e.g. silicon)[43,44] can benefit from the application of specific and tailored pressure. This is also true in the case of traditional materials such as graphite, where a better electrical contact can be obtained. Nevertheless, if excessive mechanical compression is applied especially to anodes and separators, their pores can close[45] leading to a decrease of active area and consequently an increase of the current density on the anode surface. A pouch cell holder was designed and used to ensure homogeneous pressure distribution all

Journal of The Electrochemical Society, 2021 **168** 050508

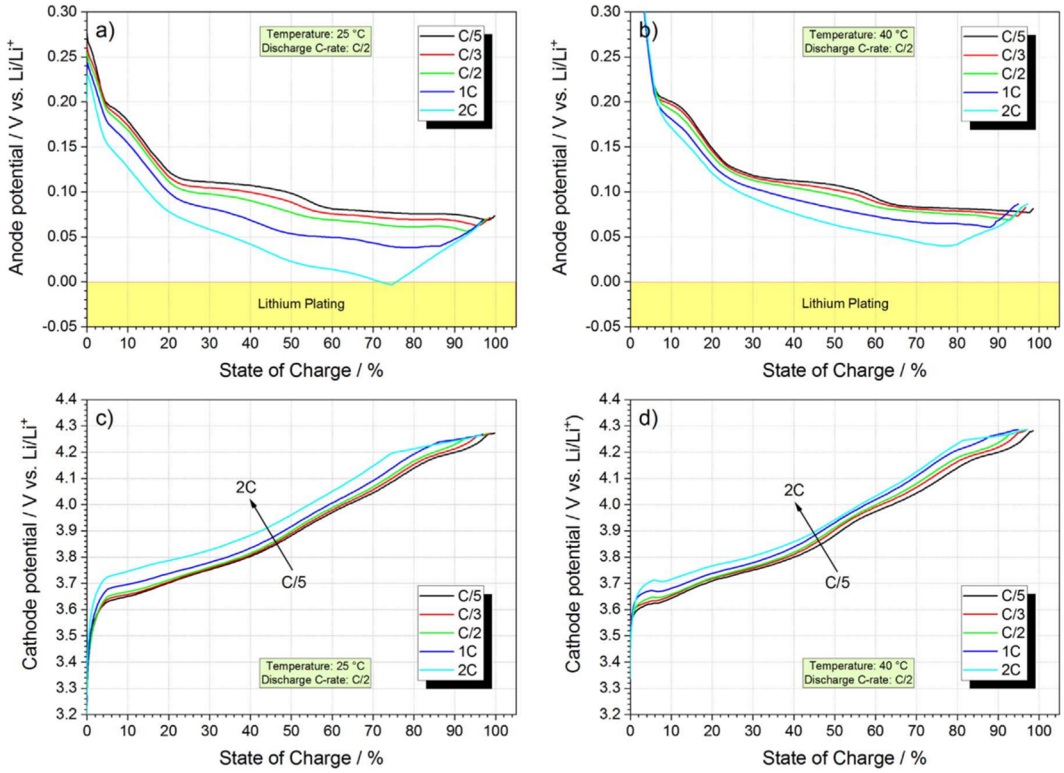

Figure 4. Anode and cathode potentials at different charge current rates and temperatures in a PP3D cell: anode potential vs. SOC % at 25 °C (a) and 40 °C (b); cathode potential vs. SOC % at 25 °C (c) and 40 °C (d).

over the cell surface providing better and more reproducible results. The holder can squeeze out all the gas bubbles potentially formed during electrolyte degradation in the first cycles. When pressure is not applied, gas bubbles can prevent full utilization of the active material, which often leads to lithium deposition in its surrounding.[28,46] Figure 1b shows its design where a different pressure can be applied simply using a torque wrench to tighten the bolts. In the case of small pouch cells (single- and bi-layer), pressure differences play a bigger role than in the stacked pouch cells. In the latter case, the higher number of layers attenuates the pressure inhomogeneities experienced by single electrodes acting as a buffer. In the following measurements, the pressure distribution is furtherly ensured by soft polymeric pads on both lateral sides of the cells.

Charge/discharge C-rate Tests.—The electrode specifications (AM type, AM content, loading, density) were chosen for achieving good performance with high discharge currents (high power). As can be seen from Fig. 3, single-layer pouch cells were discharged up to a rate of 7 C ($\approx$ 19 mAcm^{-2}). The discharge steps were conducted in constant current mode leading to remarkable capacity retentions (see Table II). The final discharge step at C/2 (Fig. 3a) confirmed that the high current discharge did not damage the cells allowing for a full recovery of the initial discharge capacity. Electrodes loadings and charge/discharge conditions greatly affect cell performance. Nevertheless, the obtained results proved to be noteworthy, especially, when taking into consideration full- and half-cells studies with the same electrode materials.[9,12,47]

To investigate the charging behavior PP3D cells were utilized, where anode and cathode potentials were monitored separately. High-charging current densities can greatly influence battery behavior since different phenomena can occur mainly at the graphite/electrolyte interface. Because of high charging currents and low temperatures, the anode surface potential can drop below 0 V (vs Li$^+$/Li) and lithium

Table II. Capacity retention values for several discharge currents. The values are calculated relatively to the 1st discharge capacity value after the formation step. Charge steps were conducted with C/2 in constant current-constant voltage (CCCV) mode until a current lower than C/20 is reached.

Capacity retention at different discharge C-rates					
C/2	1 C	2 C	5 C	7 C	C/2
100%	97.2%	94.2%	83.3%	64.3%	99.2%

plating becomes the thermodynamically favorable process over the intercalation. This can often lead to important safety concerns since lithium dendrites can pierce the separator and cause internal short circuits[38] and deposited lithium can react exothermically with electrolyte.[48–50] Using the PP3D plate, we investigated how our cathode/anode couple behaves in different charging conditions. The charge C-rate protocols denoted in Table SI (Supporting Info) were applied.

Figure 4 shows anode and cathode potentials at different charge C-rates as a function of the state of charge (SOC) at 25 °C and 40 °C, respectively. Most battery producers recommend an operating charging temperature ranging from 0 °C to 40 °C. These values depend on several factors such as electrodes' chemistry, electrolyte type, and cell design. Based on literature data and personal experience, it was decided to use a controlled cycling temperature of 40 °C to stress the cells and partially simulate the thermal behavior of bigger cell formats (stacked pouch cells, prismatic cells, cylindrical cells).[51] As can be seen from Figs. 4a–4b, at both temperatures the anode end-of-charge potential is progressively shifted toward zero because of the increasing polarization influencing the N/P ratio. When cells were cycled at 25 °C the anode

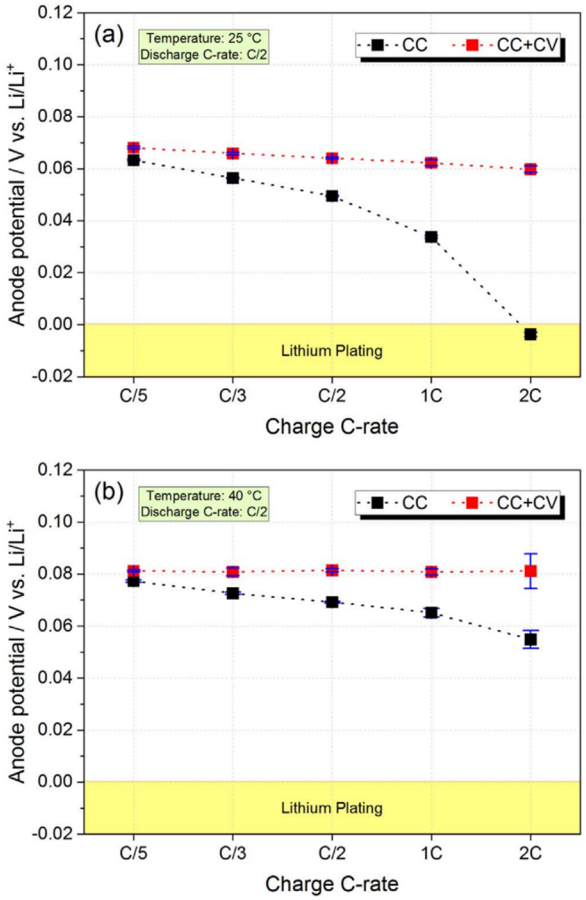

Figure 5. Charging C-rate's influence on the anode potential at the end of lithiation (CC + CV in red) at 25 °C (a) and 40 °C (b). The black squares represent the anode potential at the end of the CC step.

potential reached the lithium deposition limit only when a 2 C current was applied in the CC charging step. After the application of the CV step, the potential increased to around 70 mV as in the other C-rates. This behavior was present in each 2C-charging cycle in different cells. This leads to the hypothesis that despite the negative potential at the end of the CC step, lithium re-intercalation occurred during the CV step. For the sake of clarity, we cannot exclude that extended cycling in these conditions could lead to heavy a more pronounced lithium deposition. As already mentioned, the temperature during charge and discharge plays a fundamental role in the electrodes kinetics. If the electrolyte and the electrodes are able to withstand and do not degrade at such a temperature, then a beneficial effect on the cell performance should be observed.

When the same charging protocol was applied at 40 °C, the rate capability improved, and as expected the temperature contribution was particularly relevant at higher C-rates. The increase in Li^+ ions mobility due to the electrolyte lower viscosity had a beneficial effect on the cell performance. The SOC reached right after the CC step in charge (Table III) increased from 86.2% to 88% at 1 C (+ 2%) and from 74.6% to 81.3% at 2 C (+ 9%). Potentials shifts were observed at the cathode side as well (Figs. 4c–4d). As it can be seen clearly from Fig. 5, the anode potentials at the end of the CC charge steps at 40 °C (Fig. 5b) are higher than those at 25 °C (Fig. 5a). These more positive potential values are the result of the smaller polarization associated with the temperature increase.

Long-term cycling protocols.—To confirm the obtained results, we tested single-layer pouch cells. Long-term cycling tests were carried out at different combinations of temperature and charging C-rate. Their results are shown in Fig. 6. As already mentioned above, the cycling temperature is important since it can directly affect the lithiation/delithiation kinetics, and based on the previous result, a symmetrical 1 C/1 C cycling at 25 °C should have not showed a fast capacity decay due to Li plating. 2 C charging at 25 °C showed an anode potential slightly below 0 V, followed by an anode potential increase during the CV step (Fig. 5a). Lithium deposition does not lead always to dendrites and electrically isolated lithium ("dead" lithium) formation. Depending on the conditions, these lithium deposits can re-intercalate in the graphite.[52–55] This reversible Li deposition usually does not lead to a large amount of capacity loss through cycling, however, it can be anyway a safety concern[48] and should be avoided when possible. The results obtained in Fig. 4a

Table III. SOC values reached after the CC step in the charging C-rate protocol (see Table SI).

	SOC after CC step	
Charge C-rate	$T = 25$ °C	$T = 40$ °C
C/5	98.1%	97.7%
C/3	95.5%	94.8%
C/2	92.9%	92.8%
1 C	86.2%	88.0%
2 C	74.6%	81.3%

Journal of The Electrochemical Society, 2021 **168** 050508

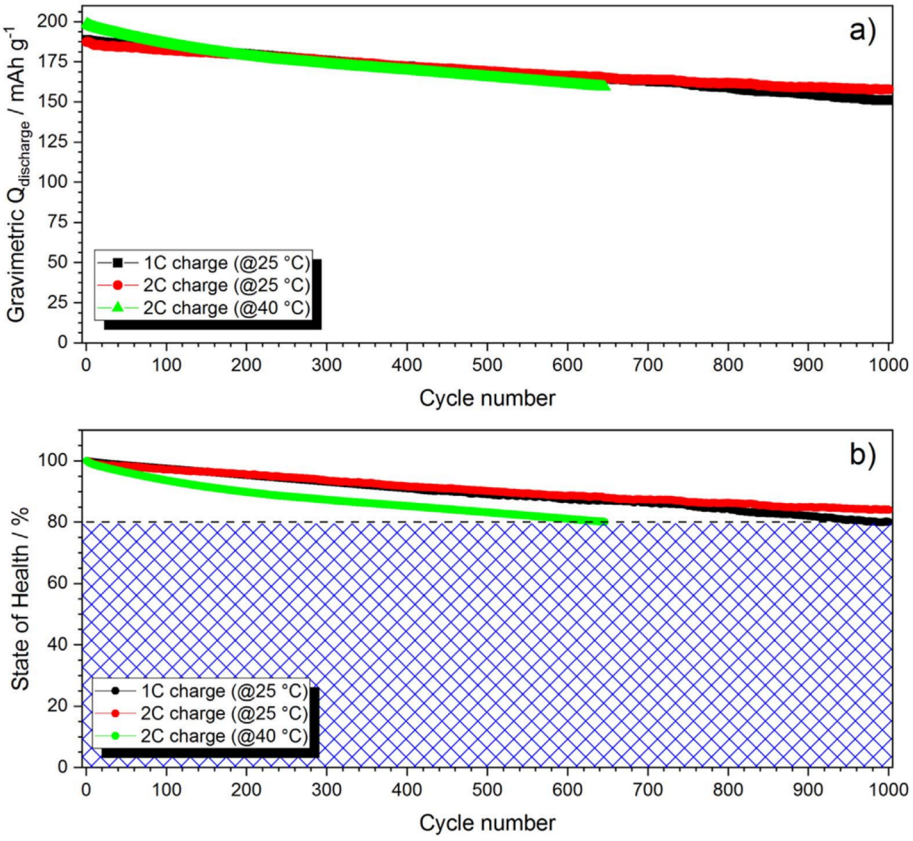

Figure 6. SLPCs cycling performance at different charge current rates and temperatures.

suggest that perhaps we are dealing mostly with a reversible form of lithium deposition since no plateau is observed below 0 V and in the CV step the potential increases rapidly to ≈70 mV.

At the same time, other cells were cycled at a rate of 2 C at 40 °C. As shown in Figs. 4b and 5b, the anode potential in these pouch cells never dropped below 0 V. If the electrolyte and the NMC811 cathode would not degrade because of the cycling temperature, better results could have been expected compared to the pouch cells cycled at 25 °C. Several studies point out that temperatures higher than 30 °C can accelerate NMC-based cathodes degradation.[7] Moreover, electrolyte decomposition products such as HF can trigger NMC dissolution.[56] The dissolution of transition metals can pose a problem also to the anode since they can be included in the SEI structure worsening cell stability and cycling life.

Post-mortem and GD-OES depth profiling.—After long-term cycling, the SLPCs were discharged at 2.7 V and disassembled in a glove box. In Fig. 7, it is possible to observe anodes and separators appearances after they reached 80% state of health (SOH). As predicted by the previous experiments (Figs. 4 and 5), pouch cells cycled with a charge rate of 1 C at 25 °C (Fig. 7a) and with a charge rate of 2 C at 40 °C (Fig. 7c) did not show any presence of dead lithium on their surface. When the temperature is raised to 40 °C better performance was expected due to an improvement of the intercalation kinetics, however the thermal stability of the electrolyte must be taken into consideration as well. Since the temperature was applied continuously throughout the cycling procedure, this can have affected the electrolyte stability resulting in faster cell aging. SLPCs cycled at 40 °C (Fig. 6) reached 80% SOH earlier than the cells cycled at 25 °C and no clear sign of gas evolution was observed. A sign of the electrolyte degradation can be seen in Fig. 7c where the polymeric separator showed local black areas and brownish spots. Taking a closer look at Fig. 7b, it is possible to notice a small "dead" lithium spot near the tabs. During the CV charging step, this region provides the shortest path for charge transport phenomena, therefore is more prone to be overcharged. This behavior was already detected in the PP3D cells where the anode potential was going slightly below 0 V. Nevertheless, the pouch cells cycled in these conditions showed comparable performance to those cycled with a 1 C charge current (see Fig. 6). The negative potential in the first cycles probably led to "dead" lithium that remained in that position without affecting further cycles.

In order to assess the presence of deposited lithium by GD-OES depth profiling, it is assumed that the measured amount of lithium is composed of lithium in the SEI and metallic lithium, as defined by Ghanbari et al.[29] The cell has been completely discharged, therefore the amount of intercalated lithium is negligible.

$$Li_{detected} = Li_{metallic} + Li_{SEI} \quad [2]$$

Furthermore, it is presumed, that the SEI consists only of lithium oxide (Li_2O). Li_2O has the highest Li-content (46.5 wt %) of all known SEI species, therefore this assumption gives the minimum amount of metallic lithium. The detected oxygen is used to calculate the amount of Li_2O in the SEI. If Eq. 2 gives a positive value for $Li_{metallic}$, Li deposition has been detected. A negative value means that all Li is bound in the SEI.[29] Figure 7 shows all the GD-OES results performed at the center of the anode for each cell (white dotted circle in Fig. 7). Using this calculation, none of the investigated samples have shown lithium deposition. In Fig. 7a,

Journal of The Electrochemical Society, 2021 **168** 050508

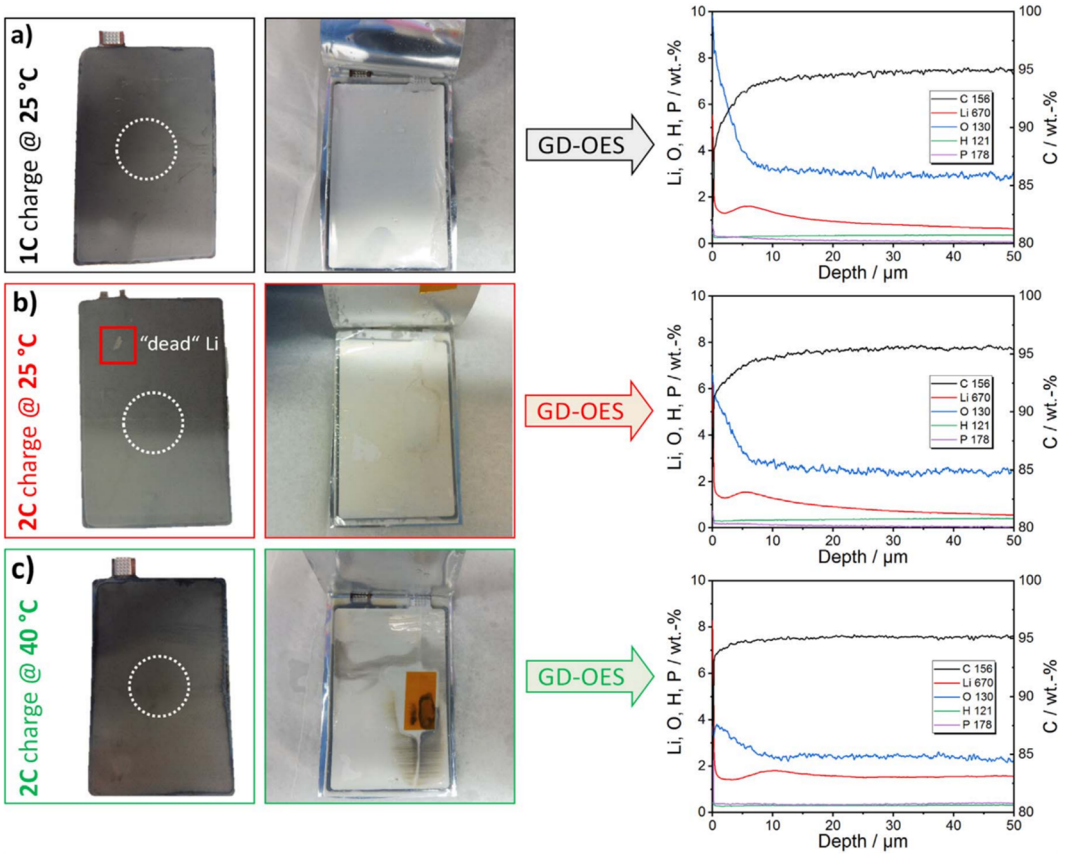

Figure 7. Post-mortem studies of the SLPCs cycled at different charge-currents and temperatures: anodes and separators appearances (on the left) and respective GD-OES depth profiling results (on the right). The analyzed samples were harvested inside the white dotted circle.

the cell, which has been charged with a 1 C current at 25 °C shows a lithium gradient throughout the depth of the electrodes. This result is consistent with previous findings[57] showing that the SEI is more pronounced at the electrode surface. In Fig. 7b is shown the GD-OES result from the area highlighted by the white dotted circle as in the other two anodes. Nevertheless, since a small lithium deposition was visible, a sample was harvested from the red square and analyzed to confirm the presence of metallic lithium. The GD OES results from this area can be seen in Fig. 8a, where the Li distribution shows a plateau at the anode surface with a higher mass percentage than the other analyzed samples in Fig. 7. Furthermore, Eq. 2 was applied and the calculated $Li_{metallic}$ weight percentages have shown positive values only in this sample. The comparison between the calculated $Li_{metallic}$ weight percentages of these different samples is presented in Fig. S2 (Supporting Info). The cell charged with a 2 C current at 40 °C (Fig. 7c) shows a steady Li content, which could originate from the electrolyte decomposition at elevated temperatures that leads to an enhanced SEI formation.[58,59]

GD-OES analysis was also used to assess the binder distribution. Slurry preparation, electrodes coating, and the drying step greatly influence the electrode homogeneity. In particular, binder migration toward the electrode surface can occur when high thermal gradients are present during electrode drying.[60] This phenomenon can lead to poor mechanical stability together with poor electrochemical performance of the electrode. By the detection of sodium which is present in the Na-CMC, the binder distribution was monitored. The results can be seen in Fig. 8b. The homogeneous sodium distribution throughout the whole pristine anode coating is shown by the flat course of the Na intensity. For the sake of comparison, an aged anode coating was analyzed as well. The Na distribution resulted to be the same as in the pristine anode. Since it was not detected a binder gradient, these results are the index of a successful anode drying step that resulted in a homogeneous binder distribution. The good performance in the C-rate discharge tests is also supporting these findings.

Conclusions

Graphite and NMC811 electrodes were manufactured and tested in SLPCs and PP3D cells with remarkable results especially at high discharge rates (64.3% capacity retention at 7 C $\approx$ 19 mA cm^{-2} discharge rate). The use of a novel 3D printed testing plate allowed us to investigate and understand under which cycling conditions we can obtain the best outcome in terms of cell performance, safety, and cyclic life for this specific anode/cathode combination.

In particular, the following results were obtained:

1) All the cells showed significant power performance and cycling stability, especially due to the optimized production and proper design of electrodes (slurry recipe, loading, density). Results reproducibility was furthermore assured by the use of pouch cell holders (Fig. 1b).
2) The presence of the PP3D plate does not affect stack performance (Fig. 2c) and could be optimal support for the implementation of other sensors.
3) The PP3D plate enables us to record the anode potentials vs. Li reference measured during C-rate tests. Potentials trends are supported by the SLPCs behavior observed during long-term cycling at different charge currents and temperatures.

Journal of The Electrochemical Society, 2021 **168** 050508

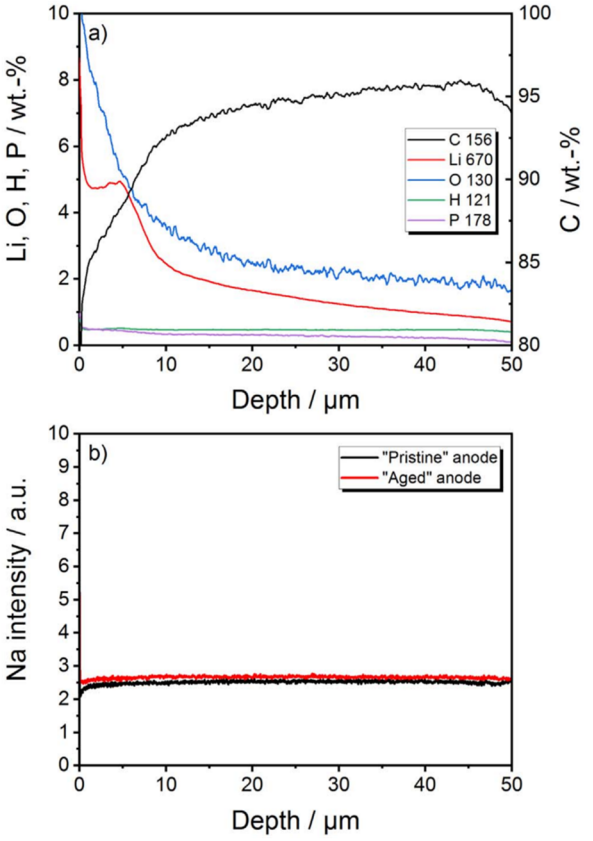

Figure 8. GD-OES depth profiling: a) Li, O, H, P, and C intensity from the red square area in Fig. 7b (SLPC: 2 C charge rate at 25 °C); b) Intensity of the Na line at 588.995 nm in the pristine (black line) and in an aged (red line) anode (left: anode surface, right: Cu current collector). The Na intensity was related to the Ar line at 763.511 nm to compensate for the small variations of the sputtering rate.

4) 80% SOC is reached after 1000 cycles when the cells are charged at 1 C and 2 C at 25 °C, and around 650 cycles when charged at 2 C at 40 °C.

These findings were furtherly supported by the GD-OES depth profiling. The only SLPCs showing lithium deposition (Fig. 6) were those charged with a 2 C rate at 25 °C. These cycling conditions were the only ones showing negative anode potentials in the PP3D cell results. Also, GD-OES depth profiling can be used as a valid ally to detect coatings homogeneity after electrode production.

Lithium metal is one of the most used reference electrodes in the academic world, however, there are concerns about its stability over time. With few modifications of the plate design, other materials such as $Li_4Ti_5O_{12}$ (LTO)[61] or $LiFePO_4$ (LFP) can replace lithium metal as a reference electrode. Because of the 3D printing versatility, several sensors could be easily implemented inside the plate. Implementation of other sensors and further electrochemical studies are currently under investigation and they will be discussed in a further paper.

Acknowledgments

This work was financially supported by project DigiBattPro 4.0 BW (3-4332.62-IPA/69) by the Ministerium für Wirtschaft, Arbeit und Wohnungsbau Baden-Württemberg and by the European Union's H2020 Framework Program under Grant agreement n° 814106 (TEESMAT). The authors wish to thank Hitachi Chemical for the SMG-HT1 anode material they provided. The authors would like to thank G. Zettisch (ZSW) for the 3D printing process.

ORCID

Gilberto Carbonari https://orcid.org/0000-0002-0634-9508
Rares-George Scurtu https://orcid.org/0000-0003-1635-4930
Thomas Waldmann https://orcid.org/0000-0003-3761-1668

References

1. X. G. Yang and C. Y. Wang, *J. Power Sources*, **402**, 489 (2018).
2. M. Armand et al., *J. Power Sources*, **479**, 228708 (2020).
3. S. T. Myung, F. Maglia, K. J. Park, C. S. Yoon, P. Lamp, S. J. Kim, and Y. K. Sun, *ACS Energy Lett.*, **2**, 196 (2017).
4. X. Wang, Y. L. Ding, Y. P. Deng, and Z. Chen, *Adv. Energy Mater.*, **10**, 1903864 (2020).
5. A. Manthiram, B. Song, and W. Li, *Energy Storage Mater.*, **6**, 125 (2017).
6. E. A. Olivetti, G. Ceder, G. G. Gaustad, and X. Fu, *Joule.*, **1**, 229 (2017).
7. T. Li, X.-Z. Yuan, L. Zhang, D. Song, K. Shi, and C. Bock, *Degradation Mechanisms and Mitigation Strategies of Nickel-Rich NMC-Based Lithium-Ion Batteries* (Springer, Berlin) 3, 43 (2020).
8. A. Mauger and C. Julien, *Ionics (Kiel).*, **20**, 751 (2014).
9. F. Xin, H. Zhou, X. Chen, M. Zuba, N. Chernova, G. Zhou, and M. S. Whittingham, *ACS Appl. Mater. Interfaces*, **11**, 34889 (2019).
10. A. Tornheim, M. He, C.-C. Su, and Z. Zhang, *J. Electrochem. Soc.*, **164**, A6366 (2017).
11. R. Petibon, L. M. Rotermund, and J. R. Dahn, *J. Power Sources*, **287**, 184 (2015).
12. J. V. Laveda, J. E. Low, F. Pagani, E. Stilp, S. Dilger, V. Baran, M. Heere, and C. Battaglia, *ACS Appl. Energy Mater.*, **2**, 7036 (2019).
13. R. Jung, R. Morasch, P. Karayaylali, K. Phillips, F. Maglia, C. Stinner, Y. Shao-Horn, and H. A. Gasteiger, *J. Electrochem. Soc.*, **165**, A132 (2018).
14. M. Wood, J. Li, R. E. Ruther, Z. Du, E. C. Self, H. M. Meyer, C. Daniel, I. Belharouak, and D. L. Wood, *Energy Storage Mater.*, **24**, 188 (2020).
15. A. Kazzazi, D. Bresser, A. Birrozzi, J. Von Zamory, M. Hekmatfar, and S. Passerini, *ACS Appl. Mater. Interfaces*, **10**, 17214 (2018).
16. F. Reuter, A. Baasner, J. Pampel, M. Piwko, S. Dörfler, H. Althues, and S. Kaskel, *J. Electrochem. Soc.*, **166**, A3265 (2019).
17. J. Kasnatscheew, T. Placke, B. Streipert, S. Rothermel, R. Wagner, P. Meister, I. C. Laskovic, and M. Winter, *J. Electrochem. Soc.*, **164**, A2479 (2017).
18. C. Mao, R. E. Ruther, J. Li, Z. Du, and I. Belharouak, *Electrochem. Commun.*, **97**, 37 (2018).
19. R. Raccichini, M. Amores, and G. Hinds, *Batteries.*, **5**, 12 (2019).
20. D. P. Abraham, S. D. Poppen, A. N. Jansen, J. Liu, and D. W. Dees, *Electrochim. Acta*, **49**, 4763 (2004).
21. S. Solchenbach, D. Pritzl, E. J. Y. Kong, J. Landesfeind, and H. A. Gasteiger, *J. Electrochem. Soc.*, **163**, A2265 (2016).
22. J. Costard, M. Ender, M. Weiss, and E. Ivers-Tiffée, *J. Electrochem. Soc.*, **164**, A80 (2017).
23. L. H. J. Raijmakers, M. J. G. Lammers, and P. H. L. Notten, *Electrochim. Acta*, **259**, 517 (2018).
24. J. R. Belt, D. M. Bernardi, and V. Utgikar, *J. Electrochem. Soc.*, **161**, A1116 (2014).
25. D. W. Dees, A. N. Jansen, and D. P. Abraham, *J. Power Sources*, **174**, 1001 (2007).
26. Z. Chu, X. Feng, B. Liaw, Y. Li, L. Lu, J. Li, X. Han, and M. Ouyang, *J. Electrochem. Soc.*, **165**, A3240 (2018).
27. E. McTurk, C. R. Birkl, M. R. Roberts, D. A. Howey, and P. G. Bruce, *ECS Electrochem. Lett.*, **4**, A145 (2015).
28. T. Waldmann, B. I. Hogg, and M. Wohlfahrt-Mehrens, *J. Power Sources*, **384**, 107 (2018).
29. N. Ghanbari, T. Waldmann, M. Kasper, P. Axmann, and M. Wohlfahrt-Mehrens, *J. Phys. Chem. C*, **120**, 22225 (2016).
30. J. Shim and K. A. Striebel, *J. Power Sources*, **119–121**, 934 (2003).
31. V. Aravindan, Y. S. Lee, and S. Madhavi, *Adv. Energy Mater.*, **7**, 1 (2017).
32. T. Ohzuku, Y. Iwakoshi, and K. Sawai, *J. Electrochem. Soc.*, **140**, 2490 (1993).
33. M. S. Dresselhaus and G. Dresselhaus, *Adv. Phys.*, **30**, 139 (1981).
34. F. Dinkelacker, P. Marzak, J. Yun, Y. Liang, and A. S. Bandarenka, *ACS Appl. Mater. Interfaces*, **10**, 14063 (2018).
35. M. D. Levi, C. Wang, J. S. Gnanaraj, and D. Aurbach, *J. Power Sources*, **119–121**, 538 (2003).
36. H. J. Noh, S. Youn, C. S. Yoon, and Y. K. Sun, *J. Power Sources*, **233**, 121 (2013).
37. H. A. Gasteiger, M. Metzger, C. Stinner, F. Maglia, and R. Jung, *J. Electrochem. Soc.*, **164**, A1361 (2017).
38. Q. Liu, C. Du, B. Shen, P. Zuo, X. Cheng, Y. Ma, G. Yin, and Y. Gao, *RSC Adv.*, **6**, 88683 (2016).
39. Z. Du, D. L. Wood, and I. Belharouak, *Electrochem. Commun.*, **103**, 109 (2019).
40. S. Klink, D. Höche, F. La Mantia, and W. Schuhmann, *J. Power Sources*, **240**, 273 (2013).
41. C. Delacourt, P. L. Ridgway, V. Srinivasan, and V. Battaglia, *J. Electrochem. Soc.*, **161**, A1253 (2014).
42. V. Müller, R. G. Scurtu, M. Memm, M. A. Danzer, and M. Wohlfahrt-Mehrens, *J. Power Sources*, **440**, 227148 (2019).
43. A. J. Louli, J. Li, S. Trussler, C. R. Fell, and J. R. Dahn, *J. Electrochem. Soc.*, **164**, A2689 (2017).

44. H. Yang, F. Fan, W. Liang, X. Guo, T. Zhu, and S. Zhang, *J. Mech. Phys. Solids*, **70**, 349 (2014).
45. J. Cannarella and C. B. Arnold, *J. Power Sources*, **226**, 149 (2013).
46. B. P. Matadi et al., *J. Electrochem. Soc.*, **164**, A1089 (2017).
47. K. Beltrop et al., *Chem. Mater.*, **30**, 2726 (2018).
48. T. Waldmann and M. Wohlfahrt-Mehrens, *Electrochim. Acta*, **230**, 454 (2017).
49. M. Fleischhammer, T. Waldmann, G. Bisle, B. I. Hogg, and M. Wohlfahrt-Mehrens, *J. Power Sources*, **274**, 432 (2015).
50. T. Waldmann, J. B. Quinn, K. Richter, M. Kasper, A. Tost, A. Klein, and M. Wohlfahrt-Mehrens, *J. Electrochem. Soc.*, **164**, A3154 (2017).
51. T. Waldmann, G. Bisle, B.-I. Hogg, S. Stumpp, M. A. Danzer, M. Kasper, P. Axmann, and M. Wohlfahrt-Mehrens, *J. Electrochem. Soc.*, **162**, A921 (2015).
52. C. Uhlmann, J. Illig, M. Ender, R. Schuster, and E. Ivers-Tiffée, *J. Power Sources*, **279**, 428 (2015).
53. C. Hogrefe, S. Hein, T. Waldmann, T. Danner, K. Richter, A. Latz, and M. Wohlfahrt-Mehrens, *J. Electrochem. Soc.*, **167**, 140546 (2020).
54. C. von Lüders, V. Zinth, S. V. Erhard, P. J. Osswald, M. Hofmann, R. Gilles, and A. Jossen, *J. Power Sources*, **342**, 17 (2017).
55. V. Zinth, C. Von Lüders, M. Hofmann, J. Hattendorff, I. Buchberger, S. Erhard, J. Rebelo-Kornmeier, A. Jossen, and R. Gilles, *J. Power Sources*, **271**, 152 (2014).
56. R. Jung, F. Linsenmann, R. Thomas, J. Wandt, S. Solchenbach, F. Maglia, C. Stinner, M. Tromp, and H. A. Gasteiger, *J. Electrochem. Soc.*, **166**, A378 (2019).
57. N. Ghanbari, T. Waldmann, M. Kasper, P. Axmann, and M. Wohlfahrt-Mehrens, *ECS Electrochem. Lett.*, **4**, A100 (2015).
58. M. Dubarry, C. Truchot, B. Y. Liaw, K. Gering, S. Sazhin, D. Jamison, and C. Michelbacher, *J. Electrochem. Soc.*, **160**, A191 (2013).
59. T. Waldmann, M. Wilka, M. Kasper, M. Fleischhammer, and M. Wohlfahrt-Mehrens, *J. Power Sources*, **262**, 129 (2014).
60. L. S. Kremer, A. Hoffmann, T. Danner, S. Hein, B. Prifling, D. Westhoff, C. Dreer, A. Latz, V. Schmidt, and M. Wohlfahrt-Mehrens, *Energy Technol.*, **8**, 1 (2020).
61. B. Epding, A. Broda, B. Rumberg, H. Jahnke, and A. Kwade, *J. Electrochem. Soc.*, **166**, A1550 (2019).

4. Conclusion

The present dissertation aimed to investigate the aging behavior of state-of-the-art Li-ion cells with Si/graphite anodes and to study the influence of Si content on the susceptibility of Li plating on Si/graphite anodes. Si as an anode active material offers a significant advantage in terms of specific capacity, which is almost ten times higher than that of conventional graphite anodes. This attribute enables a considerable reduction in anode thickness. However, the diffusion coefficient of Li in Si is reported to be lower than that of graphite, which may result in opposing effects in terms of fast-charging capability and the occurrence of Li plating. The bulk diffusion length in the electrode pores is reduced with higher Si contents, however, the diffusion coefficient of Li in the active material particles is reduced as well. Moreover, Si has other drawbacks, including a high irreversible capacity during formation and volume change, leading to particle fractures or SEI thickening.

This work provides important and novel insights into the Li plating phenomenon occurring on Si/graphite anodes that were published in three separate papers and whose results are related in this concluding chapter.

In the first publication **"Detection of Li Deposition on Si/Graphite Anodes from Commercial Li-Ion Cells: A Post-Mortem GD-OES Depth Profiling"** [2], a novel technique for Post-Mortem GD-OES depth profiling was presented to determine the minimum amount of metallic Li on graphite and Si/graphite anodes. This enhanced method (eq. (3) in [2]), unlike the previous method that could only be applied to graphite anodes, differentiates between O from the SEI and SiO_x, allowing a corridor to be calculated that contains the minimum amount of metallic Li:

$$Li_{met} = Li_{det} - \left(O_{det} - Si_{det}\frac{x \bullet M(O)}{M(Si)}\right) \bullet \frac{2 \bullet M(Li)}{M(O)} \tag{19}$$

The objective of the study was not only to quantify Li plating on Si/graphite anodes, but also to determine the conditions under which Li plating occurs on these anodes. Therefore, the operating conditions that lead to Li plating in fresh cells were determined and examined to determine if these conditions also result in Li plating in aged cells. In this work, the combination of GD-OES, SEM/EDX, DVA and electrode analysis in coin half-cells, a set of complementary methods, is used to elucidate the aging mechanisms. It was found that two cell types aged predominantly due to loss of active Li inventory and one cell type aged due to loss of anode active material. Loss of anode active material was caused by inactivation of Si by a thick SEI layer around the Si particles. Pre-aged cells that aged due to LLI as the primary degradation mechanism no longer exhibited Li plating when subsequently aged under conditions that resulted in Li plating in fresh cells. In

contrast, cells pre-aged with LAAM as the main degradation mechanism are still prone to Li plating under the original Li plating conditions. An altered N/P ratio due to the irreversible consumption of the Si compound in the anode active material is most likely the root-cause. In addition, a linear relationship between anode thickness and specific energy of cylindrical cells was determined in this first part of the thesis. By adding Si to the anode, its thickness can be reduced while keeping the specific energy constant. However, as this investigation has shown, Si tends to form a thick SEI during aging, which contributes to the deactivation of Si.

The second publication **"Onset Shift of Li Plating on Si/Graphite Anodes with increasing Si content"** [3] investigated whether decreasing the anode thickness by increasing the Si content at the same areal capacity and N/P ratio shifts the charging C-rate, which leads to Li plating. To this end, five series of anodes with different Si contents (0.0 wt.-%, 3.0 wt.-%, 3.5 wt.-%, 5.8 wt.-%, 20.8 wt.-%) and corresponding cathodes were coated on pilot scale with constant anode areal capacities and tailored cathode areal capacity to compensate for irreversible capacity losses, yielding the same N/P ratio. Evaluation of the voltage relaxation curves following fast charging tests at different C-rates provided hints of the occurrence of Li plating at 0 °C, which was confirmed during Post-Mortem analysis using SEM and GD-OES. To compare the different performance of the cells, the notion of a critical C-rate was introduced, referring to the C-rate, at which Li plating was first detected. The critical C-rate was found to increase with increasing Si content, making cells with reduced thickness and higher Si content more tolerant to Li plating at high charging C-rates. Similarly, project partners at the Aalen University of Applied Sciences found that the SOC at which Li plating is observed increases with increasing Si content using a half-cell setup in which the different anodes are lithiated to different SOCs at 1C.

The third manuscript **"Observation of preferential sputtering on Si/Graphite anodes for Li-ion cells by GD-OES and its validation by neutron depth profiling"** entails a method comparison between post-mortem GD-OES depth profiling and neutron depth profiling. The initial goal of validating and improving the GD-OES method has been achieved. First, it was experimentally found that Li has a higher sputter rate than graphite, which results in the faster sputtering of the Li layer on the anode surface compared to the graphite particles. As a result, the original method, which was based on the assumption of a constant sputter rate, was improved in terms of the depth accuracy. The previous result that Li plating occurs mostly on the anode surface, i.e. near the separator, is still valid with the improved method. The adapted method, which takes into account the variable sputter rate with eq. (20), was developed to more accurately convert the sputter time into sputter depth.

$$d = D \frac{\int_0^z I_{Ar}(t)dt}{\int_0^t I_{Ar}(t)dt} \quad (20)$$

In addition, it was observed that the higher sputter rate of Li causes the phenomenon of preferential sputtering on the anode surface. In this case, the Li-rich SEI is preferably sputtered off, which leads to an excessively high detected Li concentration on the anode surface.

To date, Li plating remains a prominent and concerning phenomenon in LIBs due to its rapid capacity degradation and the potential risk of internal short circuits. The identification of a voltage plateau during voltage relaxation has proven to be an effective method for detecting the reversible intercalation of Li plating on graphite anodes. In this thesis, the voltage relaxation analysis is employed to detect reversible Li plating specifically on Si/graphite anodes. Notably, voltage plateaus in both commercially available and custom-built cells after charging at low temperatures were detected. However, these voltage plateaus were only discernible at low temperatures and for anodes containing less than 6 wt.-% of Si. The validity of the voltage relaxation analysis was confirmed by post-mortem analysis utilizing GD-OES and SEM, which successfully detected irreversibly deposited Li. At higher temperatures and greater Si contents, voltage plateaus were no longer detectable after rapid charging, despite Li depositions being observed during post-mortem analysis. Investigating the reasons behind the absence of voltage plateaus and determining the maximum Si content at which voltage relaxation analysis becomes invalid would be of significant interest for future studies.

Given the complementary nature of voltage relaxation analysis, GD-OES, and SEM for detecting Li plating on Si/graphite anodes, the subsequent focus shifted toward improving the quantification of metallic Li. To achieve this, a method to estimate the proportion of Li bound in the SEI on Si/graphite anodes and determine the minimum fraction of metallic Li was developed. The main challenge lays in accurately determining the O content within the SiO_x particles. Hence, a range encompassing the minimum and maximum values within which the real O content lies was identified. Employing Focused Ion Beam-Scanning Electron Microscopy (FIB-SEM) along with Energy Dispersive X-ray Spectroscopy (EDX) or Time-of-Flight Secondary Ion Mass Spectrometry (ToF-SIMS) can lead to more precise determination of the O content. However, it is anticipated that there will be a gradient in the particle, with an increasing O content observed during aging.

Further enhancement in quantification accuracy was achieved by improving the precision of depth measurements. It is well-known that carbon exhibits a much lower sputter rate compared to metals. Consequently, it is apparent that the sputter rate of Li plating would exceed that of the bulk graphite

due to these disparate sputter rates. This discrepancy in sputter rates precludes the assumption of a homogeneous removal rate. However, quantifying these sputter rates proved challenging. Through comparison with NDP, we have now determined the actual depth of Li plating and developed a new method to enhance the accuracy of GD-OES depth determination. Unfortunately, the comparison of methods was made at a later stage of this dissertation, so that the findings on the precise depth calculation were not yet applied in the first two publications.

Subsequent to the establishment of methodologies for the detection and quantification of Li plating, investigations were undertaken to address the prevention of Li plating. Exploiting the advantageous high capacity characteristics of Si, efforts were made to reduce the thickness of the anode while maintaining a constant anode area capacity. It was observed that as the Si content increased, resulting in decreased anode thickness, the propensity for Li plating exhibited a corresponding decrease.

The identification, quantification and mitigation of Li plating is of significant practical importance due to the critical safety requirements of battery cells. In-situ voltage relaxation analysis provides a valuable means of determining the acceptable temperature range and maximum current rates, thereby aiding in the prevention of Li plating. Li plating can be avoided by careful selection of appropriate operating conditions, while the likelihood of its occurrence can be further reduced by strategic electrode design. Furthermore, in cases where Li plating has already occurred, the quantification of metallic Li can be used to assess the associated risk of dendrite formation and draw valid conclusions.

This research also focused on addressing the issue of repurposing aged batteries in second-life applications. Due to the projected large number of aged batteries from electric vehicles in the near future, it is crucial to determine whether these cells can continue to be used or should be recycled. This study utilized three cells as examples to demonstrate that the aging mechanism during the initial application significantly impacts the performance of the cell in subsequent applications. The aging mechanisms of these cells were determined using DVA, reverse engineering of the electrodes in coin half-cells, GD-OES and SEM. These techniques are applicable for investigating the aging mechanisms of other cell types as well. The objective was to develop methodological workflows suitable for analyzing aging and, thereby, encourage further exploration of the potential second-life applications of cells.

Future developments of Li-ion batteries will be driven by efforts to achieve higher energy densities and further increased fast-charging capability, but also to reduce costs, guarantee safety and reduce

dependencies. Emerging developments in cell chemistry and electrochemical energy storage are expected to introduce new aging mechanisms and alter the tendency of Li plating.

The current trend is expected to continue, favoring an increase in Si content in the anode composition. While the majority of anodes analyzed during this thesis only contain less than 10 wt.-% Si in the active material, higher Si contents will be feasible in the future. The inclusion of Si in the anode offers the potential to decrease its thickness to improve fast charging and enhance energy density due to its considerable specific capacity and low operational potential. Furthermore, the abundance of Si as a resource can reduce reliance on naturally occurring graphite deposits. However, overcoming certain challenges related to irreversible losses during formation and accelerated aging rates caused by volume changes remains imperative, even though the risk of Li plating is expected to decrease.

In addition, further advances in cell design and cell chemistry may also reduce the risk of Li plating. Such advancement in LIBs is the development of all-solid-state batteries (ASSBs), where the electrolyte is in a solid state, providing several advantages. The adoption of solid-state electrolytes significantly reduces the risk associated with Li dendrite formation and separator piercing, which is why Li metal anodes can be employed. Moreover, the occurrence of side reactions is minimized, leading to improved cycle stability. Additionally, the use of solid-state electrolytes in ASSBs enhance safety by eliminating the risks associated with electrolyte leakage and flammability. However, the implementation of ASSBs currently faces challenges, including the identification and development of suitable solid electrolytes, ensuring interfacial stability between electrodes and the solid-electrolyte, and achieving scalability to industrial levels.

Moreover, Na-ion batteries have significant potential due to the natural abundance of Na and lower cost compared to Li batteries. In addition, Na-ion batteries are perceived as a safer alternative due to their ability to be safely stored at 0 V. However, the lower energy density of sodium-ion batteries compared to lithium-ion batteries makes them more suitable for stationary applications.

In battery research, GD-OES is becoming an increasingly popular method as it allows a quantitative elemental depth profile to be obtained comparatively quickly over the entire thickness of the electrode. The depth-resolved determination of the sample composition provides GD-OES with an advantage over laser induced breakdown spectroscopy (LIBS) and induced coupled plasma optical emission spectroscopy (ICP-OES). Compared to Tof-SIMS coupled with FIB-SEM, GD-OES measurement is also faster and less expensive. For these reasons, GD-OES is likely to be used more extensively in the Post-Mortem analysis of batteries in the coming future. Future applications of GD-OES in the field of LIBs will include Si anodes with increased Si content, the

study of anode pre-lithiation, and the characterization of cathodes. In addition, as Na-ion batteries become more widely adopted, GD-OES will be useful in studying aging phenomena in these new cell designs.

Overall, this dissertation contributes to the understanding of the aging behavior of state-of-the-art Li-ion cells with Si/graphite anodes and the influence of Si content on the susceptibility to Li plating on Si/graphite anodes. The new semi-quantitative method based on Post-Mortem GD-OES depth profiling has demonstrated to be a valuable tool for the accurate determination of the minimum amount of metallic Li on Si/graphite anodes which is critical for the safe and reliable operation of Li-ion batteries.

5. References

[1] First ‘Fit for 55’ proposal agreed: the EU strengthens targets for CO2 emissions for new cars and vans, 2023, https://www.consilium.europa.eu/en/press/press-releases/2022/10/27/first-fit-for-55-proposal-agreed-the-eu-strengthens-targets-for-co2-emissions-for-new-cars-and-vans/, accessed 30 March 2023.

[2] M. Flügel, K. Richter, M. Wohlfahrt-Mehrens, T. Waldmann, J. Electrochem. Soc. 169 (2022) 50533. https://doi.org/10.1149/1945-7111/ac70af.

[3] M. Flügel, M. Bolsinger, M. Marinaro, V. Knoblauch, M. Hölzle, M. Wohlfahrt-Mehrens, T. Waldmann, J. Electrochem. Soc. 170 (2023) 60536. https://doi.org/10.1149/1945-7111/acdda3.

[4] I. Pivarníková, M. Flügel, N. Paul, A. Cannavo, G. Ceccio, J. Vacík, P. Müller-Buschbaum, M. Wohlfahrt-Mehrens, R. Gilles, T. Waldmann, Journal of Power Sources 594 (2024) 233972. https://doi.org/10.1016/j.jpowsour.2023.233972.

[5] J.B. Goodenough, Accounts of Chemical Research 46 (2013) 1053–1061. https://doi.org/10.1021/ar2002705.

[6] M.S. Whittingham, Science (New York, N.Y.) 192 (1976) 1126–1127. https://doi.org/10.1126/science.192.4244.1126.

[7] M. Whittingham, F.R. Gamble, Materials Research Bulletin 10 (1975) 363–371. https://doi.org/10.1016/0025-5408(75)90006-9.

[8] K. Mizushima, P.C. Jones, P.J. Wiseman, J.B. Goodenough, Materials Research Bulletin 15 (1980) 783–789. https://doi.org/10.1016/0025-5408(80)90012-4.

[9] A. Yoshino, K. Sanechika, Nakajima, Secondary Battery.

[10] NobelPrize.org, The Nobel Prize in Chemistry 2019, 2023, https://www.nobelprize.org/prizes/chemistry/2019/summary/, accessed 28 March 2023.

[11] M. Li, J. Lu, Z. Chen, K. Amine, Advanced Materials 30 (2018) e1800561. https://doi.org/10.1002/adma.201800561.

[12] Y. Nishi, Chemical record (New York, N.Y.) 1 (2001) 406–413. https://doi.org/10.1002/tcr.1024.

[13] J.B. Quinn, T. Waldmann, K. Richter, M. Kasper, M. Wohlfahrt-Mehrens, J. Electrochem. Soc. 165 (2018) A3284-A3291. https://doi.org/10.1149/2.0281814jes.

[14] M.S. Ziegler, J.E. Trancik, Energy Environ. Sci. 14 (2021) 1635–1651. https://doi.org/10.1039/d0ee02681f.

[15] BloombergNEF, EVO Report 2022 | BloombergNEF | Bloomberg Finance LP, 2023, https://about.newenergyfinance.com/electric-vehicle-outlook/, accessed 14 April 2023.

[16] IEA, Global EV Outlook 2023 – Analysis - IEA, 2023, https://www.iea.org/reports/global-ev-outlook-2023, accessed 5 May 2023.

[17] C.G. Zoski, Handbook of Electrochemistry, Elsevier Science & Technology, Oxford, 2007.

[18] J.O. Besenhard, C. Daniel (Eds.), Handbook of battery materials, 2., completely rev. and enl. ed., 1. Reprint, Wiley-VCH-Verl., Weinheim, 2012.

[19] B. Scrosati, J. Hassoun, K.M. Abraham, W.A. van Schalkwijk (Eds.), Lithium batteries: Advanced technologies and applications, John Wiley & Sons Inc, Hoboken, New Jersey, 2013.

[20] J.B. Goodenough, Nat Electron 1 (2018) 204. https://doi.org/10.1038/s41928-018-0048-6.

[21] M.N. Obrovac, V.L. Chevrier, Chemical Reviews 114 (2014) 11444–11502. https://doi.org/10.1021/cr500207g.

[22] S. Goriparti, E. Miele, F. de Angelis, E. Di Fabrizio, R. Proietti Zaccaria, C. Capiglia, Journal of Power Sources 257 (2014) 421–443. https://doi.org/10.1016/j.jpowsour.2013.11.103.

[23] M. Winter, J.O. Besenhard, M.E. Spahr, P. Novák, Adv. Mater. 10 (1998) 725–763. https://doi.org/10.1002/(SICI)1521-4095(199807)10:10<725:AID-ADMA725>3.0.CO;2-Z.

[24] L.Y. Beaulieu, K.W. Eberman, R.L. Turner, L.J. Krause, J.R. Dahn, Electrochem. Solid-State Lett. 4 (2001) A137. https://doi.org/10.1149/1.1388178.

[25] C. Julien, A. Mauger, K. Zaghib, H. Groult, Inorganics 2 (2014) 132–154. https://doi.org/10.3390/inorganics2010132.

[26] J. Asenbauer, T. Eisenmann, M. Kuenzel, A. Kazzazi, Z. Chen, D. Bresser, Sustainable Energy Fuels 4 (2020) 5387–5416. https://doi.org/10.1039/D0SE00175A.

[27] G.E. Blomgren, J. Electrochem. Soc. 164 (2017) A5019-A5025. https://doi.org/10.1149/2.0251701jes.

[28] P.W. Atkins, J. de Paula, J.J. Keeler, Atkins' physical chemistry, Eleventh edition, Oxford University Press, Oxford, New York, 2018.

[29] S. Passerini, D. Bresser, A. Moretti, A. Varzi (Eds.), Batteries: Present and future energy storage challenges, Wiley-VCH Verlag GmbH & Co. KGaA, Weinheim, 2020.

[30] M. Armand, P. Axmann, D. Bresser, M. Copley, K. Edström, C. Ekberg, D. Guyomard, B. Lestriez, P. Novák, M. Petranikova, W. Porcher, S. Trabesinger, M. Wohlfahrt-Mehrens,

H. Zhang, Journal of Power Sources 479 (2020) 228708. https://doi.org/10.1016/j.jpowsour.2020.228708.

[31] F. Luo, B. Liu, J. Zheng, G. Chu, K. Zhong, H. Li, X. Huang, L. Chen, J. Electrochem. Soc. 162 (2015) A2509-A2528. https://doi.org/10.1149/2.0131514jes.

[32] M. Li, J. Lu, Z. Chen, K. Amine, Advanced Materials 30 (2018) e1800561. https://doi.org/10.1002/adma.201800561.

[33] N. Nitta, F. Wu, J.T. Lee, G. Yushin, Materials Today 18 (2015) 252–264. https://doi.org/10.1016/j.mattod.2014.10.040.

[34] D.D.L. Chung, Journal of Materials Science 37 (2002) 1475–1489. https://doi.org/10.1023/A:1014915307738.

[35] H. LIPSON, A.R. STOKES, Nature 149 (1942) 328. https://doi.org/10.1038/149328a0.

[36] Proc. R. Soc. Lond. A 106 (1924) 749–773. https://doi.org/10.1098/rspa.1924.0101.

[37] T. Tran, K. Kinoshita, Journal of Electroanalytical Chemistry 386 (1995) 221–224. https://doi.org/10.1016/0022-0728(95)03907-X.

[38] K. Persson, V.A. Sethuraman, L.J. Hardwick, Y. Hinuma, Y.S. Meng, A. van der Ven, V. Srinivasan, R. Kostecki, G. Ceder, J. Phys. Chem. Lett. 1 (2010) 1176–1180. https://doi.org/10.1021/jz100188d.

[39] X.Y. Song, K. Kinoshita, T.D. Tran, J. Electrochem. Soc. 143 (1996) L120-L123. https://doi.org/10.1149/1.1836896.

[40] J.R. Dahn, Physical review. B, Condensed matter 44 (1991) 9170–9177. https://doi.org/10.1103/PhysRevB.44.9170.

[41] U. Hofmann, W. Rüdorff, Trans. Faraday Soc. 34 (1938) 1017–1021. https://doi.org/10.1039/TF9383401017.

[42] W. Rüdorff, U. Hofmann, Z. Anorg. Allg. Chem. 238 (1938) 1–50. https://doi.org/10.1002/zaac.19382380102.

[43] N. Daumas, A. Herold, Comptes Rendus Hebdomadaires Des Seances De L Academie Des Sciences Serie C 5 (1969) 373.

[44] C. Sole, N.E. Drewett, L.J. Hardwick, Faraday Discuss. 172 (2014) 223–237. https://doi.org/10.1039/C4FD00079J.

[45] M.D. Levi, D. Aurbach, Journal of Electroanalytical Chemistry 421 (1997) 79–88. https://doi.org/10.1016/S0022-0728(96)04832-2.

[46] M. Heß, P. Novák, Electrochimica Acta 106 (2013) 149–158. https://doi.org/10.1016/j.electacta.2013.05.056.

[47] C. Uhlmann, J. Illig, M. Ender, R. Schuster, E. Ivers-Tiffée, Journal of Power Sources 279 (2015) 428–438. https://doi.org/10.1016/j.jpowsour.2015.01.046.

[48] T. Waldmann, B.-I. Hogg, M. Wohlfahrt-Mehrens, Journal of Power Sources 384 (2018) 107–124. https://doi.org/10.1016/j.jpowsour.2018.02.063.

[49] J.C. Arrebola, A. Caballero, L. Hernán, J. Morales, J. Electrochem. Soc. 156 (2009) A986. https://doi.org/10.1149/1.3231489.

[50] K. Zaghib, F. Brochu, A. Guerfi, K. Kinoshita, Journal of Power Sources 103 (2001) 140–146. https://doi.org/10.1016/S0378-7753(01)00853-9.

[51] R. Dominko, M. Gaberscek, M. Bele, D. Mihailovic, J. Jamnik, Journal of the European Ceramic Society 27 (2007) 909–913. https://doi.org/10.1016/j.jeurceramsoc.2006.04.133.

[52] M. Gaberšček, M. Bele, J. Drofenik, R. Dominko, S. Pejovnik, Journal of Power Sources 97-98 (2001) 67–69. https://doi.org/10.1016/S0378-7753(01)00589-4.

[53] E. Peled, C. Menachem, D. Bar-Tow, A. Melman, J. Electrochem. Soc. 143 (1996) L4-L7. https://doi.org/10.1149/1.1836372.

[54] T. Takamura, K. Sumiya, J. Suzuki, C. Yamada, K. Sekine, Journal of Power Sources 81-82 (1999) 368–372. https://doi.org/10.1016/S0378-7753(98)00220-1.

[55] M. Mundszinger, S. Farsi, M. Rapp, U. Golla-Schindler, U. Kaiser, M. Wachtler, Carbon 111 (2017) 764–773. https://doi.org/10.1016/j.carbon.2016.10.060.

[56] M. Yoshio, H. Wang, K. Fukuda, T. Umeno, T. Abe, Z. Ogumi, J. Mater. Chem. 14 (2004) 1754. https://doi.org/10.1039/B316702J.

[57] C. Wurm, O. Oettinger, S. Wittkaemper, R. Zauter, K. Vuorilehto, in: Lithium-Ion Batteries: Basics and Applications, Springer, Berlin, Heidelberg, 2018, pp. 43–58.

[58] S.L. Glazier, J. Li, A.J. Louli, J.P. Allen, J.R. Dahn, J. Electrochem. Soc. 164 (2017) A3545-A3555. https://doi.org/10.1149/2.0421714jes.

[59] C.J. Wen, R.A. Huggins, Journal of Solid State Chemistry 37 (1981) 271–278. https://doi.org/10.1016/0022-4596(81)90487-4.

[60] W.-J. Zhang, Journal of Power Sources 196 (2011) 13–24. https://doi.org/10.1016/j.jpowsour.2010.07.020.

[61] M.N. Obrovac, L. Christensen, Electrochem. Solid-State Lett. 7 (2004) A93. https://doi.org/10.1149/1.1652421.

[62] W.-J. Zhang, Journal of Power Sources 196 (2011) 877–885. https://doi.org/10.1016/j.jpowsour.2010.08.114.

[63] C.-M. Park, J.-H. Kim, H. Kim, H.-J. Sohn, Chemical Society Reviews 39 (2010) 3115–3141. https://doi.org/10.1039/B919877F.

[64] F. Ozanam, M. Rosso, Materials Science and Engineering: B 213 (2016) 2–11. https://doi.org/10.1016/j.mseb.2016.04.016.

[65] F. Wang, G. Chen, N. Zhang, X. Liu, R. Ma, Carbon Energy 1 (2019) 219–245. https://doi.org/10.1002/cey2.24.

[66] M. Ashuri, Q. He, L.L. Shaw, Nanoscale 8 (2016) 74–103. https://doi.org/10.1039/C5NR05116A.

[67] J. Li, J.R. Dahn, J. Electrochem. Soc. 154 (2007) A156. https://doi.org/10.1149/1.2409862.

[68] X.H. Liu, L. Zhong, S. Huang, S.X. Mao, T. Zhu, J.Y. Huang, ACS Nano 6 (2012) 1522–1531. https://doi.org/10.1021/nn204476h.

[69] Y. Fan, Q. Zhang, Q. Xiao, X. Wang, K. Huang, Carbon 59 (2013) 264–269. https://doi.org/10.1016/j.carbon.2013.03.017.

[70] Q. Xu, J.-Y. Li, J.-K. Sun, Y.-X. Yin, L.-J. Wan, Y.-G. Guo, Adv. Energy Mater. 7 (2017) 1601481. https://doi.org/10.1002/aenm.201601481.

[71] M. Ko, S. Chae, J. Ma, N. Kim, H.-W. Lee, Y. Cui, J. Cho, Nat Energy 1 (2016) 1–8. https://doi.org/10.1038/nenergy.2016.113.

[72] Z. Zhang, Y. Wang, W. Ren, Q. Tan, Y. Chen, H. Li, Z. Zhong, F. Su, Angewandte Chemie International Edition 53 (2014) 5165–5169. https://doi.org/10.1002/anie.201310412.

[73] H. Wu, G. Zheng, N. Liu, T.J. Carney, Y. Yang, Y. Cui, Nano Letters 12 (2012) 904–909. https://doi.org/10.1021/nl203967r.

[74] H. Ma, F. Cheng, J.-Y. Chen, J.-Z. Zhao, C.-S. Li, Z.-L. Tao, J. Liang, Advanced Materials 19 (2007) 4067–4070. https://doi.org/10.1002/adma.200700621.

[75] H. Jia, P. Gao, J. Yang, J. Wang, Y. Nuli, Z. Yang, Adv. Energy Mater. 1 (2011) 1036–1039. https://doi.org/10.1002/aenm.201100485.

[76] J. Yang, Solid State Ionics 152-153 (2002) 125–129. https://doi.org/10.1016/S0167-2738(02)00362-4.

[77] M. Miyachi, H. Yamamoto, H. Kawai, T. Ohta, M. Shirakata, J. Electrochem. Soc. 152 (2005) A2089. https://doi.org/10.1149/1.2013210.

[78] Z. Liu, Q. Yu, Y. Zhao, R. He, M. Xu, S. Feng, S. Li, L. Zhou, L. Mai, Chemical Society Reviews 48 (2019) 285–309. https://doi.org/10.1039/C8CS00441B.

[79] S.C. Jung, H.-J. Kim, J.-H. Kim, Y.-K. Han, J. Phys. Chem. C 120 (2016) 886–892. https://doi.org/10.1021/acs.jpcc.5b10589.

[80] K. Mizushima, P.C. Jones, P.J. Wiseman, J.B. Goodenough, Materials Research Bulletin 15 (1980) 783–789. https://doi.org/10.1016/0025-5408(80)90012-4.

[81] R. Chebiam, A. Kannan, F. Prado, A. Manthiram, Electrochemistry Communications 3 (2001) 624–627. https://doi.org/10.1016/S1388-2481(01)00232-6.

[82] S. Venkatraman, Y. Shin, A. Manthiram, Electrochem. Solid-State Lett. 6 (2003) A9. https://doi.org/10.1149/1.1525430.

[83] A. Manthiram, K. Chemelewski, E.-S. Lee, Energy Environ. Sci. 7 (2014) 1339. https://doi.org/10.1039/C3EE42981D.

[84] W. Li, E.M. Erickson, A. Manthiram, Nat Energy 5 (2020) 26–34. https://doi.org/10.1038/s41560-019-0513-0.

[85] M.M. Thackeray, W. David, P.G. Bruce, J.B. Goodenough, Materials Research Bulletin 18 (1983) 461–472. https://doi.org/10.1016/0025-5408(83)90138-1.

[86] A. Manthiram, Nat Commun 11 (2020) 1550. https://doi.org/10.1038/s41467-020-15355-0.

[87] Q. Zhong, A. Bonakdarpour, M. Zhang, Y. Gao, J.R. Dahn, J. Electrochem. Soc. 144 (1997) 205–213. https://doi.org/10.1149/1.1837386.

[88] A.K. Padhi, K.S. Nanjundaswamy, J.B. Goodenough, J. Electrochem. Soc. 144 (1997) 1188–1194. https://doi.org/10.1149/1.1837571.

[89] K. Xu, Chemical Reviews 104 (2004) 4303–4417. https://doi.org/10.1021/cr030203g.

[90] E. Peled, J. Electrochem. Soc. 126 (1979) 2047–2051. https://doi.org/10.1149/1.2128859.

[91] D. Guyomard, J.M. Tarascon, J. Electrochem. Soc. 140 (1993) 3071–3081. https://doi.org/10.1149/1.2220987.

[92] J. TARASCON, D. Guyomard, Solid State Ionics 69 (1994) 293–305. https://doi.org/10.1016/0167-2738(94)90418-9.

[93] M.S. Ding, K. Xu, S.S. Zhang, K. Amine, G.L. Henriksen, T.R. Jow, J. Electrochem. Soc. 148 (2001) A1196. https://doi.org/10.1149/1.1403730.

[94] S. Zhang, T. Jow, K. Amine, G. Henriksen, Journal of Power Sources 107 (2002) 18–23. https://doi.org/10.1016/S0378-7753(01)00968-5.

[95] M. Dahbi, F. Ghamouss, F. Tran-Van, D. Lemordant, M. Anouti, Journal of Power Sources 196 (2011) 9743–9750. https://doi.org/10.1016/j.jpowsour.2011.07.071.

[96] K. Xu, S. Zhang, T.R. Jow, W. Xu, C.A. Angell, Electrochem. Solid-State Lett. 5 (2002) A26. https://doi.org/10.1149/1.1426042.

[97] S.S. Zhang, K. Xu, T.R. Jow, J. Electrochem. Soc. 149 (2002) A586. https://doi.org/10.1149/1.1466857.

[98] J.B. Goodenough, Y. Kim, Chem. Mater. 22 (2010) 587–603. https://doi.org/10.1021/cm901452z.

[99] S. Leroy, F. Blanchard, R. Dedryvère, H. Martinez, B. Carré, D. Lemordant, D. Gonbeau, Surf. Interface Anal. 37 (2005) 773–781. https://doi.org/10.1002/sia.2072.

[100] A. Patil, V. Patil, D. Wook Shin, J.-W. Choi, D.-S. Paik, S.-J. Yoon, Materials Research Bulletin 43 (2008) 1913–1942. https://doi.org/10.1016/j.materresbull.2007.08.031.

[101] R. Jung, M. Metzger, D. Haering, S. Solchenbach, C. Marino, N. Tsiouvaras, C. Stinner, H.A. Gasteiger, J. Electrochem. Soc. 163 (2016) A1705-A1716. https://doi.org/10.1149/2.0951608jes.

[102] C. Xu, F. Lindgren, B. Philippe, M. Gorgoi, F. Björefors, K. Edström, T. Gustafsson, Chem. Mater. 27 (2015) 2591–2599. https://doi.org/10.1021/acs.chemmater.5b00339.

[103] M. Broussely, P. Biensan, F. Bonhomme, P. Blanchard, S. Herreyre, K. Nechev, R.J. Staniewicz, Journal of Power Sources 146 (2005) 90–96. https://doi.org/10.1016/j.jpowsour.2005.03.172.

[104] X. Han, L. Lu, Y. Zheng, X. Feng, Z. Li, J. Li, M. Ouyang, eTransportation 1 (2019) 100005. https://doi.org/10.1016/j.etran.2019.100005.

[105] T. Waldmann, M. Wilka, M. Kasper, M. Fleischhammer, M. Wohlfahrt-Mehrens, Journal of Power Sources 262 (2014) 129–135. https://doi.org/10.1016/j.jpowsour.2014.03.112.

[106] M. Dubarry, V. Svoboda, R. Hwu, B. Yann Liaw, Electrochem. Solid-State Lett. 9 (2006) A454. https://doi.org/10.1149/1.2221767.

[107] M. Dubarry, B.Y. Liaw, M.-S. Chen, S.-S. Chyan, K.-C. Han, W.-T. Sie, S.-H. Wu, Journal of Power Sources 196 (2011) 3420–3425. https://doi.org/10.1016/j.jpowsour.2010.07.029.

[108] C.R. Birkl, M.R. Roberts, E. McTurk, P.G. Bruce, D.A. Howey, Journal of Power Sources 341 (2017) 373–386. https://doi.org/10.1016/j.jpowsour.2016.12.011.

[109] J. Christensen, J. Newman, J Solid State Electrochem 10 (2006) 293–319. https://doi.org/10.1007/s10008-006-0095-1.

[110] J. Vetter, P. Novák, M.R. Wagner, C. Veit, K.-C. Möller, J.O. Besenhard, M. Winter, M. Wohlfahrt-Mehrens, C. Vogler, A. Hammouche, Journal of Power Sources 147 (2005) 269–281. https://doi.org/10.1016/j.jpowsour.2005.01.006.

[111] M.M. Kabir, D.E. Demirocak, Int J Energy Res 41 (2017) 1963–1986. https://doi.org/10.1002/er.3762.

[112] G. Kucinskis, M. Bozorgchenani, M. Feinauer, M. Kasper, M. Wohlfahrt-Mehrens, T. Waldmann, Journal of Power Sources 549 (2022) 232129. https://doi.org/10.1016/j.jpowsour.2022.232129.

[113] M. Bozorgchenani, G. Kucinskis, M. Wohlfahrt-Mehrens, T. Waldmann, J. Electrochem. Soc. 169 (2022) 30509. https://doi.org/10.1149/1945-7111/ac580d.

[114] S. Watanabe, M. Kinoshita, T. Hosokawa, K. Morigaki, K. Nakura, Journal of Power Sources 260 (2014) 50–56. https://doi.org/10.1016/j.jpowsour.2014.02.103.

[115] X.-G. Yang, C.-Y. Wang, Journal of Power Sources 402 (2018) 489–498. https://doi.org/10.1016/j.jpowsour.2018.09.069.

[116] T. Guan, S. Sun, Y. Gao, C. Du, P. Zuo, Y. Cui, L. Zhang, G. Yin, Applied Energy 177 (2016) 1–10. https://doi.org/10.1016/j.apenergy.2016.05.101.

[117] T. Guan, S. Sun, F. Yu, Y. Gao, P. Fan, P. Zuo, C. Du, G. Yin, Electrochimica Acta 279 (2018) 204–212. https://doi.org/10.1016/j.electacta.2018.04.197.

[118] A.H. Whitehead, M. Perkins, J.R. Owen, J. Electrochem. Soc. 144 (1997) L92-L94. https://doi.org/10.1149/1.1837564.

[119] M.W. Verbrugge, B.J. Koch, Journal of Electroanalytical Chemistry 436 (1997) 1–7. https://doi.org/10.1016/S0022-0728(97)00031-4.

[120] M. Bauer, C. Guenther, M. Kasper, M. Petzl, M.A. Danzer, Journal of Power Sources 283 (2015) 494–504. https://doi.org/10.1016/j.jpowsour.2015.02.130.

[121] J. Fan, S. Tan, J. Electrochem. Soc. 153 (2006) A1081. https://doi.org/10.1149/1.2190029.

[122] S. Tippmann, D. Walper, L. Balboa, B. Spier, W.G. Bessler, Journal of Power Sources 252 (2014) 305–316. https://doi.org/10.1016/j.jpowsour.2013.12.022.

[123] V. Zinth, C. von Lüders, M. Hofmann, J. Hattendorff, I. Buchberger, S. Erhard, J. Rebelo-Kornmeier, A. Jossen, R. Gilles, Journal of Power Sources 271 (2014) 152–159. https://doi.org/10.1016/j.jpowsour.2014.07.168.

[124] A. Latz, J. Zausch, Journal of Power Sources 196 (2011) 3296–3302. https://doi.org/10.1016/j.jpowsour.2010.11.088.

[125] K. Jalkanen, J. Karppinen, L. Skogström, T. Laurila, M. Nisula, K. Vuorilehto, Applied Energy 154 (2015) 160–172. https://doi.org/10.1016/j.apenergy.2015.04.110.

[126] N. Ghanbari, T. Waldmann, M. Kasper, P. Axmann, M. Wohlfahrt-Mehrens, J. Phys. Chem. C 120 (2016) 22225–22234. https://doi.org/10.1021/acs.jpcc.6b07117.

[127] R. Arunachala, C. Parthasarathy, A. Jossen, J. Garche, ECS Trans. 73 (2016) 201–212. https://doi.org/10.1149/07301.0201ecst.

[128] Y. Krämer, C. Birkenmaier, J. Feinauer, A. Hintennach, C.L. Bender, M. Meiler, V. Schmidt, R.E. Dinnebier, T. Schleid, Chemistry – A European Journal 21 (2015) 6062–6065. https://doi.org/10.1002/chem.201406606.

[129] B. Rieger, S.F. Schuster, S.V. Erhard, P.J. Osswald, A. Rheinfeld, C. Willmann, A. Jossen, Journal of Energy Storage 8 (2016) 1–5. https://doi.org/10.1016/j.est.2016.09.002.

[130] M. Dollé, S. Grugeon, B. Beaudoin, L. Dupont, J.-M. Tarascon, Journal of Power Sources 97-98 (2001) 104–106. https://doi.org/10.1016/S0378-7753(01)00507-9.

[131] M. Dollé, L. Sannier, B. Beaudoin, M. Trentin, J.-M. Tarascon, Electrochem. Solid-State Lett. 5 (2002) A286. https://doi.org/10.1149/1.1519970.

[132] M. Jäckle, A. Groß, J. Chem. Phys. 141 (2014) 174710. https://doi.org/10.1063/1.4901055.

[133] K. Nishikawa, T. Mori, T. Nishida, Y. Fukunaka, M. Rosso, T. Homma, J. Electrochem. Soc. 157 (2010) A1212. https://doi.org/10.1149/1.3486468.

[134] T. Ohsaki, T. Kishi, T. Kuboki, N. Takami, N. Shimura, Y. Sato, M. Sekino, A. Satoh, Journal of Power Sources 146 (2005) 97–100. https://doi.org/10.1016/j.jpowsour.2005.03.105.

[135] R. Payling, Glow Discharge Optical Emission Spectroscopy: A Practical Guide, 1st ed., Royal Society of Chemistry, Cambridge, 2002.

[136] R.K. Marcus, J.A.C. Broekaert (Eds.), Glow discharge plasmas in analytical spectroscopy, J. Wiley, Chichester, England, 2003.

[137] W. Grimm, Spectrochimica Acta Part B: Atomic Spectroscopy 23 (1968) 443–454. https://doi.org/10.1016/0584-8547(68)80023-0.

[138] C. J. Belle, J. D. Johnson, Appl. Spectrosc., AS 27 (1973) 118–124.

[139] A. Bengtson, Spectrochimica Acta Part B: Atomic Spectroscopy 40 (1985) 631–639. https://doi.org/10.1016/0584-8547(85)80110-5.

[140] R.K. Marcus, T.R. Harville, Y. Mei, C.R. Shick, Anal. Chem. 66 (1994) 902A-911A. https://doi.org/10.1021/ac00090a719.

[141] Y. Saito, M.K. Rahman, Journal of Power Sources 174 (2007) 877–882. https://doi.org/10.1016/j.jpowsour.2007.06.223.

[142] H. Takahara, H. Miyauchi, M. Tabuchi, T. Nakamura, J. Electrochem. Soc. 160 (2013) A272-A278. https://doi.org/10.1149/2.061302jes.

[143] H. Takahara, M. Shikano, H. Kobayashi, Journal of Power Sources 244 (2013) 252–258. https://doi.org/10.1016/j.jpowsour.2013.01.109.

[144] H. Takahara, A. Kojyo, K. Kodama, T. Nakamura, K. Shono, Y. Kobayashi, M. Shikano, H. Kobayashi, J. Anal. At. Spectrom. 29 (2014) 95–104. https://doi.org/10.1039/C3JA50183C.

[145] H. Takahara, Y. Kobayashi, K. Shono, H. Kobayashi, M. Shikano, T. Nakamura, J. Electrochem. Soc. 161 (2014) A1716-A1722. https://doi.org/10.1149/2.1011410jes.

[146] N. Ghanbari, T. Waldmann, M. Kasper, P. Axmann, M. Wohlfahrt-Mehrens, ECS Electrochem. Lett. 4 (2015) A100-A102. https://doi.org/10.1149/2.0041509eel.

[147] K. Richter, T. Waldmann, M. Kasper, C. Pfeifer, M. Memm, P. Axmann, M. Wohlfahrt-Mehrens, J. Phys. Chem. C 123 (2019) 18795–18803. https://doi.org/10.1021/acs.jpcc.9b03873.

[148] K. Richter, T. Waldmann, N. Paul, N. Jobst, R.-G. Scurtu, M. Hofmann, R. Gilles, M. Wohlfahrt-Mehrens, ChemSusChem 13 (2020) 529–538. https://doi.org/10.1002/cssc.201903139.

[149] T. Nelis, R. Payling, Glow discharge optical emission spectroscopy: A practical guide, Royal Society of Chemistry, Cambridge, 2003.

[150] B. Chapman, B.N. Chapman, Glow discharge processes: Sputtering and plasma etching, Wiley, New York, NY, 1980.

[151] R. Payling, D.G. Jones, S.A. Gower, Surface and Interface Analysis 23 (1995) 1–11. https://doi.org/10.1002/sia.740230102.

[152] R. Payling, D.G. Jones, S.A. Gower, Surface and Interface Analysis 20 (1993) 959–966. https://doi.org/10.1002/sia.740201206.

[153] A. Martín, A. Menéndez, R. Pereiro, N. Bordel, A. Sanz-Medel, Anal Bioanal Chem 388 (2007) 1573–1582. https://doi.org/10.1007/s00216-007-1291-2.

[154] P. Šmíd, E. Steers, Z. Weiss, J. Pickering, V. Hoffmann, J. Anal. At. Spectrom. 23 (2008) 1223. https://doi.org/10.1039/B803812K.

[155] A. Bogaerts, J. Anal. At. Spectrom. 23 (2008) 1476. https://doi.org/10.1039/B810599E.

[156] J.F. Ziegler, G.W. Cole, J.E.E. Baglin, Journal of Applied Physics 43 (1972) 3809–3815. https://doi.org/10.1063/1.1661816.

[157] R.G. Downing, G.P. Lamaze, J.K. Langland, S.T. Hwang, Journal of Research of the National Institute of Standards and Technology 98 (1993) 109–126. https://doi.org/10.6028/jres.098.008.

[158] D.I. Thwaites, Radiat Res 95 (1983) 495. https://doi.org/10.2307/3576096.

[159] S.C. Nagpure, R.G. Downing, B. Bhushan, S.S. Babu, L. Cao, Electrochimica Acta 56 (2011) 4735–4743. https://doi.org/10.1016/j.electacta.2011.02.037.

[160] F. Linsenmann, M. Trunk, P. Rapp, L. Werner, R. Gernhäuser, R. Gilles, B. Märkisch, Z. Révay, H.A. Gasteiger, J. Electrochem. Soc. 167 (2020) 100554. https://doi.org/10.1149/1945-7111/ab9b20.

[161] M. Wetjen, M. Trunk, L. Werner, H.A. Gasteiger, R. Gernhäuser, R. Gilles, B. Märkisch, Z. Révay, J. Electrochem. Soc. 166 (2019) A1408-A1411. https://doi.org/10.1149/2.0581908jes.

[162] E. Moyassari, L. Streck, N. Paul, M. Trunk, R. Neagu, C.-C. Chang, S.-C. Hou, B. Märkisch, R. Gilles, A. Jossen, J. Electrochem. Soc. 168 (2021) 20519. https://doi.org/10.1149/1945-7111/abe1db.

[163] I. Tomandl, J. Vacik, T. Kobayashi, Y. Mora Sierra, V. Hnatowicz, V. Lavreniev, P. Horak, G. Ceccio, A. Cannavo, M. Baba, R. Ye, Radiation Effects and Defects in Solids 175 (2020) 394–405. https://doi.org/10.1080/10420150.2019.1701471.

[164] I. Tomandl, T. Kobayashi, A. Cannavó, J. Vacík, G. Ceccio, T. Sassa, V. Hnatowicz, Journal of Power Sources 542 (2022) 231719. https://doi.org/10.1016/j.jpowsour.2022.231719.

[165] M. Petzl, M.A. Danzer, Journal of Power Sources 254 (2014) 80–87. https://doi.org/10.1016/j.jpowsour.2013.12.060.

[166] C. von Lüders, V. Zinth, S.V. Erhard, P.J. Osswald, M. Hofmann, R. Gilles, A. Jossen, Journal of Power Sources 342 (2017) 17–23. https://doi.org/10.1016/j.jpowsour.2016.12.032.

[167] C. Uhlmann, J. Illig, M. Ender, R. Schuster, E. Ivers-Tiffée, Journal of Power Sources 279 (2015) 428–438. https://doi.org/10.1016/j.jpowsour.2015.01.046.

[168] M. Bauer, B. Rieger, S. Schindler, P. Keil, M. Wachtler, M.A. Danzer, A. Jossen, Journal of Energy Storage 10 (2017) 1–10. https://doi.org/10.1016/j.est.2016.11.006.

[169] S. Schindler, M. Bauer, M. Petzl, M.A. Danzer, Journal of Power Sources 304 (2016) 170–180. https://doi.org/10.1016/j.jpowsour.2015.11.044.

[170] X.-G. Yang, S. Ge, T. Liu, Y. Leng, C.-Y. Wang, Journal of Power Sources 395 (2018) 251–261. https://doi.org/10.1016/j.jpowsour.2018.05.073.

[171] K. Bischof, M. Flügel, M. Hölzle, M. Wohlfahrt-Mehrens, T. Waldmann, J. Electrochem. Soc. 171 (2024) 10510. https://doi.org/10.1149/1945-7111/ad1b7c.

[172] G. Carbonari, R.-G. Scurtu, T. Waldmann, S. Radloff, M. Flügel, A. Hoffmann, M. Wohlfahrt-Mehrens, J. Electrochem. Soc. 168 (2021) 50508. https://doi.org/10.1149/1945-7111/abfab9.

6. List of figures

Figure 1: Historical development and projection of global sales of battery electric vehicles (BEV) and plug-in hybrid electric vehicles from 2015 to 2030. Reproduced with data adapted from reference [16]. 2

Figure 2: Schematic battery cell based on a graphite anode and a layered oxide cathode during discharge. Reproduced with permission from Springer Nature: How we made the Li-ion rechargeable battery, J.B. Goodenough, Copyright (2018) [20]. 3

Figure 3: Schematic illustration of the (A) Rüdorff and (B) Daumas-Hérold models of Li intercalation in graphite. Reproduced with permission from Royal Society of Chemistry: In-situ Raman study of lithium-ion intercalation into microcrystalline graphite, C. Sole, N.E. Drewett, L.J. Hardwick, Copyright (2014) [44]. 7

Figure 4: Lithium intercalation stages and stage transitions of graphite. Reprinted from Electrochimica Acta 106, M. Heß, P. Novák, Shrinking annuli mechanism and stage-dependent rate capability of thin-layer graphite electrodes for lithium-ion batteries, 149-158, Copyright (2013) with permission from Elsevier [46]. 8

Figure 5: Crystal structure of the layered oxide $LiCoO_2$, the spinel $LiMn_2O_4$ and the olivine $LiFePO_4$. Reprinted with permission from MDPI, Comparative Issues of Cathode Materials for Li-Ion Batteries, C.M. Julien, A. Mauger, K. Zaghib, H. Groult, Copyright (2014) [25]. 11

Figure 6: Energetic illustration of the decomposition of the electrolyte and formation of the SEI and CEI. Illustration modified from [98]. 13

Figure 7: Side-reactions inside a LIB. Reprinted from Journal of Power Sources 341, C.R. Birkl, M.R. Roberts, E. McTurk, P.G. Bruce, D.A. Howey, Degradation diagnostics for lithium ion cells, 373-386, Copyright (2016) with permission from Elsevier [108]. 14

Figure 8: Schematic representation of the glow discharge source and the Rowland circle. 17

Figure 9: Schematic illustration of the results obtained in the publication [2]. 26

Figure 10: Schematic illustration of the thicknesses of the anodes and cathodes which have been paired together [3]. 40

Figure 11: GD-OES and neutron depth profile of a Si/graphite anode with Li plating on the anode surface [4]. 55

Figure 12: Illustration of the calendar aging mechanism of a graphite anode (left) and Si/graphite anode (right) [171]. 69

Figure 13: Post-Mortem analysis of the cells aged at different C-rates and temperatures [172]. . 84

IV. Appendix

a) Curriculum vitae

Removed for online publication.

b) List of Publications

i. Articles in Peer-Reviewed Scientific Journals

2024

A7) K. Bischof, **M. Flügel**, M. Hölzle, M. Wohlfahrt-Mehrens, T. Waldmann. "Aging mechanism for calendar aging of Li-ion cells with Si/Graphite anodes". 2024 *J. Electrochem. Soc.* **171** 010510 https://doi.org/10.1149/1945-7111/ad1b7c

A6) I. Pivarníková; **M. Flügel**; N. Paul; A. Cannavo; G. Ceccio; J. Vacík; P. Müller-Buschbaum; M. Wohlfahrt-Mehrens; R. Gilles; T. Waldmann. "Observation of preferential sputtering of Si/graphite anodes from Li-ion cells by GD-OES and its validation by neutron depth profiling". 2024 *J. Power Sources* **594** 233972. https://doi.org/10.1016/j.jpowsour.2023.233972

2023

A5) **M. Flügel**; M. Bolsinger; M. Marinaro; V. Knoblauch; M. Hölzle; M. Wohlfahrt-Mehrens; T. Waldmann. „Onset Shift of Li plating on Si/Graphite Anodes with increasing Si content". *J. Electrochem. Soc.* **2023**, *170* (6), 060536. https://doi.org/10.1149/1945-7111/acdda3

2022

A4) **M. Flügel**; K. Richter; M. Wohlfahrt-Mehrens; T. Waldmann. "Detection of Li Deposition on Si/Graphite Anodes from Commercial Li-Ion Cells: A Post-Mortem GD-OES Depth Profiling Study". *J. Electrochem. Soc*. **2022**, *169* (5), 050533. https://doi.org/10.1149/1945-7111/ac70af/meta

2021

A3) G. Carbonari; R.-G. Scurtu; T. Waldmann; S. Radloff; **M. Flügel**; A. Hoffmann; Margret Wohlfahrt-Mehrens. "3D-printed testing plate for the optimization of high C-rates cycling performance of lithium-ion cells". *J. Electrochem. Soc.* **2021**, *168* (5), 050508. https://doi.org/10.1149/1945-7111/abfab9

A2) **M. Flügel**; M. Kasper; C. Pfeifer; M. Wohlfahrt-Mehrens; T. Waldmann. "Cu dissolution during over-discharge of Li-ion cells to 0 V: a post-mortem study". *J. Electrochem. Soc.* **2021**, *168* (2), 020506. https://doi.org/10.1149/1945-7111/abdc5f

2020

A1) **M. Flügel**; T. Waldmann; M. Kasper; M. Wohlfahrt-Mehrens. "Detection of Copper Deposition on Anodes of Over-Discharged Lithium Ion Cells by GD-OES Depth Profiling". *ChemPhysChem* **2020**, *21* (18), 2047-2050. https://doi.org/10.1002/cphc.202000333

ii. Contribution to conferences and meetings

Oral presentations

2023

T9) **M. Flügel**. „Workflows zur Charakterisierung von Li-Abscheidungen auf Graphitanoden und Si/Graphit Kompositanoden“. BMBF-Kompetenzcluster AQua – 2. Industrietag, July 5, 2023 in Ulm

T8) **M. Flügel**; M. Wohlfahrt-Mehrens; M. Kasper; M. Hölzle; T. Waldmann. „Quantification of Lithium in Anodes of Lithium Ion Batteries using GD-OES“. International Workshop on the Characterization and Quantification of Lithium, from the Micro- to the Nano-Scale, from Mining to Energy, June 26 – 27, 2023 in Paris

T7) **M. Flügel**; M. Bolsinger, M. Marinaro; V. Knoblauch; M. Wohlfahrt-Mehrens; M. Hölzle; T. Waldmann. „Characterization and general trends of Li deposition in full cells with Si/graphite anodes“. Advanced Battery Power Conference 2023, April 27 – 28, 2023 in Aachen

T6) L. Boveleth; **M. Flügel**; M. Bolsinger; I. Pivarnikova; N. Paul; T. Danner; A. Latz. “Simulation of Li plating in Si/Graphite composite electodes”. Modval 2023, March 21 – 23, 2023 in Duisburg

2022

T5) **M. Flügel**; K. Richter; M. Wohlfahrt-Mehrens; T. Waldmann. “Detection of Li deposition on Si/Graphite anodes from commercial Li-ion cells – A Post-Mortem GD-OES depth profiling study”. 242nd ECS Meeting, October 9 – 13, 2022 in Atlanta

T4) **M. Flügel**; K. Richter; M. Wohlfahrt-Mehrens; T. Waldmann. “Detection of Li deposition on Si/Graphite anodes with GD-OES”. 19. Deutsches Anwendertreffen “Analytische Glimmentladungsspektroskopie”, September 26 – 27, 2022 in Dresden

T3) **M. Flügel**. “GD-OES depth profiling and in situ optical microscopy for deep insights onto Li-ion batteries”. TEESMAT Webinar series, June 23, 2022

2021

T2) **M. Flügel**; M. Kasper; M. Wohlfahrt-Mehrens; T. Waldmann. “Cu Dissolution and re-deposition during Over-Discharge of Li-Ion Cells – A Post-Mortem Study”. Advanced Battery Power Conference, April 28 – 29, 2021, online

2019

T1) T. Waldmann; J.B. Quinn; K. Richter; **M. Flügel**; M. Kasper; M. Wohlfahrt-Mehrens. “Specific energy and fast-charging capability of commercial Li-ion cells of the new 21700 format”. Kraftwerk Batterie 2019 in Aachen

Poster presentations

2023

P6) **M. Flügel**; M. Bolsinger, M. Marinaro; V. Knoblauch; M. Wohlfahrt-Mehrens; M. Hölzle; T. Waldmann. „Investigation of the Effect of the Si Content on the Onset of Li Plating on Si/Graphite Anodes". Ulm Electrochemical Talks 2023, June 14 – 15, 2023 in Ulm

2022

P5) **M. Flügel**; M. Wohlfahrt-Mehrens; T. Waldmann. "Characterization and General Trends of Li Deposition in Full Cells with Si-/Graphite Anodes". Aqua Industrietag 2022

2021

P4) **M. Flügel**, M. Kasper, M. Wohlfahrt-Mehrens, T. Waldmann. "Cu Dissolution and Re-Deposition during Over-Discharge of Li-Ion Cells – A Post-Mortem Study". Ulm Electrochemical Talks (UECT) 2021, Ulm

P3) T. Waldmann; **M. Flügel**; M. Kasper; M. Wohlfahrt-Mehrens. "GD-OES Depth Profiling – A valuable new Technique to Study varios Aging Effects in Li-ion Cells". Advanced Battery Power Conference, April 28 – 29, 2021, online.

2019

P2) T. Waldmann, J.B. Quinn, K. Richter, **M. Flügel**, M. Kasper, M. Wohlfahrt-Mehrens. "Commercial 18650 vs. 21700 cells – a first comparison of energy density, performance, and production effort". Batterieforum Berlin 2019

2018

P1) T. Waldmann, J.B. Quinn, K. Richter, **M. Flügel**, M. Kasper, M. Wohlfahrt-Mehrens. "Energy density and heating behavior of commercial 18650 vs. 21700 cells – high energy vs. high power cells". Ulm Electrochemical Talks (UECT) 2018, Ulm

V. Acknowledgement

Removed for online publication.